Experimental and Model-based Approaches to Directional Thalamic Deep Brain Stimulation

A DISSERTATION
SUBMITTED TO THE FACULTY OF
UNIVERSITY OF MINNESOTA
BY

YiZi Xiao

IN PARTIAL FULFILLMENT OF THE REQUIREMENTS
FOR THE DEGREE OF
Doctor of Philosophy

Matthew D. Johnson

September, 2016

Acknowledgements

I am grateful to all who have given me knowledge, confidence, opportunities and motivation.

Dedication

To my wife, who shared a tiny apartment with me and picked me up after work every day.

Contents

List of Tables

List of Figures

List of Abbreviations

AC	Anterior commissure
AChE	Acetylocholinesterase
AF	Activating function
ANN	Artificial neural network
ANOVA	Analysis of variance
APul	Anterior pulvinar
ATP	Adenosine triphosphate
Bsc	Brachium of the superior colliculus
CL	Central lateral nucleus of thalamus
CM	Centre median nucleus of thalamus
COM	Center of mass
CT	Corticothalamic
CTC	Cerebellothalamocortical
CTT	Cerebellothalamic tract
DBS	Deep brain stimulation
DBSA	Directionally segmented DBS array
DTI	Diffusion tensor imaging
DWI	Diffusion-weighted imaging
EAP	Equal-area projection
eEPF	Excitatory effective pulse fraction
EPF	Effective pulse fraction
ET	Essential tremor
FEM	Finite-element model
FOV	Field of view
FPM	Firing pattern modulation
FRM	Firing rate modulation
GABA	Gamma-Aminobutyric acid
GOF	Goodness of fit
GP	Globus pallidus
GPe	Globus pallidus externa
GPi	Globus pallidus interna

H	Entropy
IC	Internal capsule
iEPF	Inhibitory effective pulse fraction
ION	Inferior olivary nucleus
IPG	Implantable pulse generator
LP	Linear programming
Lpo	Nucleus lateropolaris of thalamus
MD	Maximum deviation
MGN	Medial geniculate nucleus
ML	Medial lemniscus
MLS	Moving-least-squares
MPTP	1-methyl-4-phenyl-1,2,3,6-tetrahydropyridine
MR	Magnetic resonance
MRI	Magnetic resonance imaging
M1	Primary motor cortex
NHP	Non-human primate
PBS	Phosphate buffered saline
PC	Posterior commissure
PD	Parkinson’s disease
PF	Pallidofugal
PO	Nucleus posterior oralis of thalamus
PPN	Pedunculopontine nucleus
PSA	Posterior subthalamic area
PSO	Particle swarm optimization
PSTH	Peri-stimulus time histogram
QP	Quadratic programming
rDBSA	Radially-segmented DBS array
RF	Radio frequency
SCP	Superior cerebellar peduncle
SMA	Supplementary motor area
SNr	Substantia nigra pars reticulata
STN	Subthalamic nucleus
SWI	Susceptibility-weighted imaging
TC	Thalamocortical
TCT	Thalamocortical tract
TIN	Thalamic interneuron
TRN	Thalamic reticular nucleus
VA	Nucleus ventralis anterior of thalamus
Vce	Nucleus ventralis caudalis externus of thalamus
Vim	Ventral intermediate nucleus of thalamus
VL	Nucleus ventralis lateralis of thalamus
VLc	Nucleus ventralis lateralis pars caudalis of thalamus
VLo	Nucleus ventralis lateralis pars oralis of thalamus

VLps	Nucleus ventralis lateralis pars postrema of thalamus
Vo	Nucleus ventrooralis of thalamus
Vop	Nucleus ventralis oralis posterior of thalamus
VPI	Nucleus ventroposterior inferior of thalamus
VPL	Ventral posterolateral nucleus of thalamus
VPLc	Caudal ventral posterior lateral nucleus of thalamus
VPLo	Oral ventral posterior lateral nucleus of thalamus
VTA	Volume of tissue activated

Chapter 1

Introduction

- Chapter 1 introduces the background and goals pursued in this thesis.
- Chapter 2 describes a multimodal imaging approach to locate thalamic targets for deep brain stimulation.
- Chapter 3 describes an efficient computational algorithm to program high-density deep brain stimulation electrode arrays.
- Chapter 4 introduces a spherical statistical framework to quantify the spatial profile of neurons activated by deep brain stimulation.
- Chapter 5 discusses the spatial characterization of stimulation-induced neuronal activity around chronically implanted thalamic deep brain stimulation electrode arrays.
- Chapter 6 presents a final discussion of the analyses presented in the thesis.

1.1 Background

1.1.1 History of Essential Tremor

Essential tremor (ET) is the most prevalent adult movement disorder [1] and one of the most common adult neurological disorders [2], [3], [4], as much as 20 times more prevalent than Parksinson's Disease (PD) [5]. The disorder affects 4% of all adults over the age of 40 [6], and to a lesser extent children and young adults [7]. The tremor manifests as involuntary movements in the 4 – 12Hz range, which decreases in frequency but increases in amplitude over time [8]. The location and amplitude of tremor is variable among ET patients: kinetic and/or postural tremor is found predominantly in the upper extremities (90% of all cases), followed by the head (30%), voice (20%), jaw/face (10%) and lower extremities (10%) [9]. At least 50% of patients also have tandem abnormalities in gait [10]. These symptoms of ET compromises the quality of life of affected patients and affect their capability to work [11]. ET is also associated with a higher incidence (compared to healthy controls) of 'non-motor' symptoms that include mild cognitive changes, depression, anxiety, etc [12]. First-degree relatives of ET patients are five times more likely to develop ET compared to control subjects [13]. A family history of ET also appears to be correlated with younger reported age of tremor onset [14].

The exact pathogenesis of ET currently remains unresolved. Evidence supports the cerebellar involvement in ET including the discovery of axonal swellings ('torpedoes') in the Purkinje cells of some patients [15]. There is also evidence of greater loss of Purkinje cells in the cerebellum of ET patients compared to healthy controls [16]. Lesions in the Guillian-Mollaret Triangle (dentate, globose and emboliform nuclei, contralateral red nucleus, contralateral inferior olive, and their interconnecting fiber tracts) are known to cause a variety of action tremors [17]. In particular, the inferior olivary nucleus (ION) in conjunction with the cerebellum are hypothesized to produce ET. The ION and the

cerebellum have reciprocal connections. Climbing fibers originating from the ION make excitatory synapses onto the dendritic trees of Purkinje cells in the contralateral cerebellum [18]. The dentate and interposed nuclei of the cerebellum also project to the contralateral ION via two pathways: 1) direct inhibitory (gamma-Aminobutyric acid, GABAergic) projections that synapse close to the gap junctions between the dendrites of olivary neurons, and 2) indirect excitatory (glutamatergic) projections through midbrain nuclei (including parvocellular red nucleus) [19]. The olivary neurons oscillate between 0.5 – 12Hz and induces rhythmic activation of cerebellar Purkinje cells and nuclear cells [20]. Synchronous olivary activity is facilitated by gap junctions between olivary neurons, which is in turn mirrored in the cerebellum. Olivocerebellar oscillation is normally limited spatially and temporally [20], [21]. However, patients with ET have enhanced synchronization and 4 – 12Hz neuronal rhythmicity in their inferior olives [22]. This could be due to a variety of mechanisms [23], [24]: 1) altered olivary network properties (e.g. increased gap junctions), 2) altered excitatory/inhibitory modulation of the olivary network, 3) abnormal enhancement of the membrane conductances mediating oscillations, or a combination of these mechanisms [25], [26] [27]. This synchronous activity in the inferior olive may lead to widespread and sustained oscillations in the olivocerebellar network and produce tremor, as occurs with administration of serotonin precursors or harmaline [22]. Activation of inhibitory synapses from the cerebellum can decrease the coupling between olivary neurons and thereby reduce oscillation within the nucleus [19]. However, studies using ethanol and diazepam to suppress harmaline-induced tremor have found that tremor suppression was far more pronounced than suppression of olivary rhythmicity [28], [29]. This finding suggests the primary mechanism of tremor suppression is decoupling of the ION and its oscillatory activities from the rest of the motor network [30]. More importantly, the extrapolated lesson is that the target for effective therapy need not be the origin of tremor activity. This concept laid the foundation for effective treatment of ET through deep brain stimulation (DBS, Fig. 1), a therapy that will be the focus of this dissertation.

As progression of ET leads to interference with daily living, pharmacological treatment is the first line treatment option. This treatment will not cure the disease but may alleviate

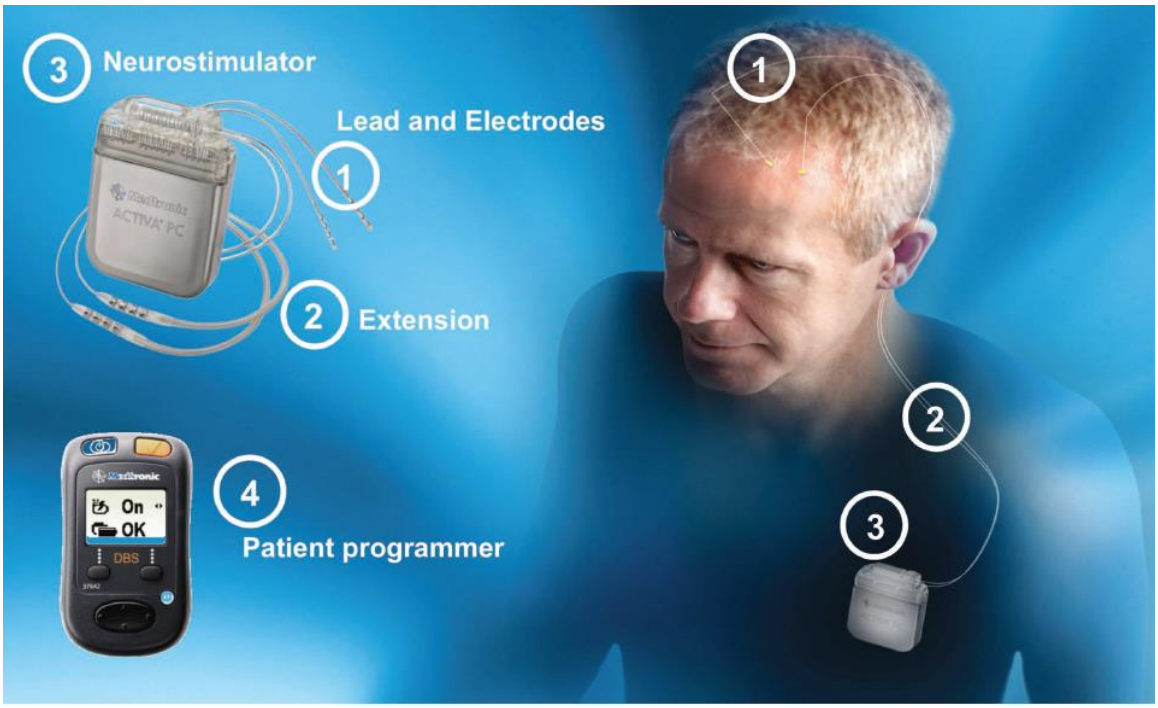

Figure 1. Schematic of an implantable DBS system
The system is consisted of: 1) electrode lead, 2) wire extensions connecting the lead with the implantable pulse generator (IPG), 3) the IPG and 4) the patient programmer. (Figure adapted from [31])

tremor [32]. Only two medications, propranolol and primidone, have substantial evidence to support their efficacy in reducing symptoms [33], [34], [35]. Propranolol is a nonselective beta-adrenergic receptor antagonist commonly used for treatment of hypertension. It is the only FDA-approved medication for the treatment of ET. Primidone is an anticonvulsant that has been shown to reduce tremor by approximately 50% [35]. Despite the benefits provided by these medications, approximately 30% of patients will not respond to either of these agents [8]. Surgical intervention is the next line treatment option for medication-refractory ET patients. The ventral intermediate nucleus (Vim) of the thalamus has been identified as a target for radio frequency (RF) lesion procedures (thalamotomy) in order to suppress tremor in PD, ET and cerebellar tremor [36], [37]. The thalamus is a relay hub with projections from the cerebellum [38] and basal ganglia [39], as well as extensive reciprocal and non-reciprocal connections with the cortex [40]. The anatomy of the thalamus and the role it plays as a target for the treatment of ET will be discussed in detail later in the chapter. Studies have reported that thalamotomies can

reduce tremor symptoms by 80% – 90% compared to baseline [41], [42], [43]. However, side effects caused by the procedure can occur in as many as 14% – 47% of patients, which include dysarthria (difficulty with speech), verbal/cognitive deficits, confusion, weakness, drowsiness and paralysis. These events may resolve over time, but it was shown in one study that hemiparesis and speech difficulties persisted in 16% of patients [44]. Due to the risk of adverse side effects and the irreversible nature of the procedure, bilateral thalamotomy is no longer used to treat ET. The surgical procedure of choice for treatment of ET is now DBS [45]. The advantage of DBS over thalamotomy is that it is reversible. Instead of doing permanent damage to the tissue, DBS delivers high frequency electrical stimulation via an implanted electrode array within a target region to arrest tremor. Parameters such as stimulation amplitude, frequency and pulse width can be adjusted for continued management of tremor. DBS has proven to be an effective treatment option for ET and other motor disorders, but challenges remain and so are opportunities for advancing the technology.

1.1.2 History of Deep Brain Stimulation

DBS and its efficacy in tremor suppression was first discovered during RF lesion surgeries [46]. Single pulses of high frequency electrical stimulation were used to identify the target for lesion and resulted in temporary and reversible therapeutic effects [47]. This observation led to the increasing adoption of electrical stimulation as a viable therapy for treatment of neurological disorders. For example, in 1960, stimulation electrodes were chronically implanted in the amygdaloid nucleus to treat schizophrenia [48]. In 1973, chronic stimulation of the thalamus was performed to control facial pain by inducing paresthesias [49]. In 1975, Bechtereva implanted 26-40 chronic stimulation electrodes in various brain structures and delivered bursts of 50Hz stimulation to treat hyperkinesia as well as phantom limb syndrome [50]. In 1987, Benabid and Siegfried were the first to report chronic stimulation in the Vim nucleus specifically for the treatment of movement disorders [51], [52] and found the procedure to produce similar therapeutic effects as thalamotomy [53], with the added advantage of being reversible

and adjustable. Subsequently, Benabid collaborated with medical devices manufacturer Medtronic to develop DBS as a technology for the treatment of severe, intractable tremor which culminated in a multicenter clinical trial and regulatory approval for the therapy [31]. The advent of the Medtronic Itrel I and Itrel II implantable pulse generators made continuous, chronic stimulation possible outside of the OR and clinic (Fig. 1). DBS of the globus pallidus interna (GPi) [54] and the subthalamic nucleus (STN) [55] were reported to improve multiple symptoms of PD. Regulatory approvals were granted for these two indications of PD after clinical studies in North American and Europe [56], [57]. DBS was also explored to treat other movement disorders such as dystonia [58], [59] and Tourette syndrome [60], [61], psychiatric disorders such as Obsessive Compulsive Disorder [62] and refractory depression [63], [64], as well as epilepsy [65], [66].

1.1.3 Targets of DBS for Essential Tremor

The Vim nucleus has traditionally been the preferred target for stereotactic thalamotomy and the gold standard in DBS for the treatment of ET [67]. Stimulation of the posterior subthalamic area (PSA, includes the cerebellothalamic tract (CTT), zona incerta, Forel field H2 and the prelemniscal radiation) [68] [69], [70] have also shown promise in treating ET. Recent studies using postoperative magnetic resonance imaging (MRI) to correlate electrode location with clinical effects have pointed to the PSA as the more effective and efficient site for stimulation [71], [72] compared to the Vim nucleus. However, the ‘optimal target’ for DBS to treat ET is variable among patients and not well established [72]. First, there are no randomized studies comparing the efficacy of stimulation in the Vim and PSA. Furthermore, factors including the quality of MRI, electrode localization using surgical atlases, variations in anatomy and heterogeneity in essential tremor as a clinical entity may also confound the results [72]. However, diffusion tractography has shown that effective DBS sites (albeit wide-ranging spatial coordinates) all share strong connections with the cerebellum and the ventral-lateral thalamus-motor cortex loop [71]. This is supported by another study which suggests that the dentate-thalamic fibers play a prominent role in mediating the beneficial effects of

Studies in Monkeys					Studies in Humans				
Walker	Olszewski	Ilinsky & Kultas-Ilinsky	Percheron, et al.	Jones & Hirai & Jones	Hassler	Dewulf	Van Buren & Borke	Walker	Ohye
VA	VA	VApc	LRpo LO	VA	dorsooralis (Do), internus (Doi), externus (Doe) lateropolaris (Lpo)	va	Lpo	Lpo	Lpo
VAmc	VAmc	VAmc	LRmc	VAmc	lateropolaris magnocellularis (Lpomc)	vom (a)	Lpo (mc)		
VM	VLm	VM	LRvm	VMp	ventrooralis medialis (Vom)				
VL	VLo	VAdc	LO	VLa	ventrooralis anterior (Voa); ventrooralis posterior (Vop)	voa + da(p) vop	Voe(a) Voe(p)	Vo	Voe(a) Voe(p)
VL	area X	VL	LIM	VLp (antero-medial part)	ventrooralis internus (Voi)	vom(p)	Voi	Vo	Voi
VL	VLc	VL	LI	VLp (dorsal part)	dorsointermedius externus (Dime) dorsointermedius internus (Dimi) dorsointermedius superior (Dims)	da(p)	Do	Vo	
LPpa	VLps	VL	LOd	VLp (postero-dorsal part)	dorsointermedius externus magnocellularis (Dimemc)				
VIM	VPLo	VL	LI/LIL	VLp (ventral part)	ventrointermedius internus (Vimi) ventrointermedius externus (Vime) zentrolateralis intermedius internus (Zimi) zentrolateralis intermedius externus (Zime)	vim	Vimi Vime	VIM	Vim
VPL	VPLc	VPL	LCL	VPLa	zentrolateralis caudalis internus (Zci) zentrolateralis caudalis externus (Zce) ventrocaudalis anterior externus (Vcae)	vpl	Vce	Vce	Vce
				VPLp	ventrocaudalis posterior externus (Vcpe)				

Table 1. Comparison of nomenclature on the divisions of the motor thalamus in both monkeys and humans from various researchers
(Table adopted from [73])

stimulation in the PSA for the treatment of ET [68]. There is considerable evidence implicating the cerebellothalamocortical (CTC) motor pathway in tremorgenesis [74], making it the focus of study in this dissertation. It is therefore important to understand the CTC pathway, the thalamus as the relay hub within this pathway, as well as its connections to the rest of the motor system.

1.2 The Motor Thalamus its Connections with the Motor System

1.2.1 Anatomy of the Motor Thalamus and its Nomenclature

The foundation of modern parcellation of the thalamus was laid down by Hasseler, who based his classification scheme on cytoarchitectonic and myeloarchitectonic criteria [75]. Since then, a multitude of researchers have performed independent studies in both monkeys [76], [77], [78], [79], [80], [81] and humans [82] [83], [84], [85] and developed their own sometimes overlapping classification systems. Macchi et al. [73] produced a comprehensive summary of these systems (Table 1) and pointed the path to a common system of terminology whereby subdivisions of the thalamus are based on distribution of the major afferent fiber pathways. However, the same study did not put forth a common

system of terminology, and therefore the issue remains of the use of a particular classification scheme. We have decided to the use the Olszewski system [77] and the Walker system [82] to describe the thalamus in monkeys and humans respectively, keeping in line with terminology traditionally employed by this laboratory. The motor thalamus receives three major motor-related afferent pathways with separate regions of termination, which forms the basis for its tripartite division [73] (Fig 2). The anterior region receives primarily inhibitory (GABAergic) afferent fibers from the substantia nigra pars reticulata (SNr), possibly with some overlap with pallidal afferents [86], [87], [88]. In the monkey, this region consists of Olszewski's nucleus ventralis anterior (which is subdivided into the parvocellular part VA and the magnocellular part VAmc) as well as the medial part of the nucleus ventralis lateralis (VL) – VLm. The human counterpart in the thalamus is Walker's nucleus lateropolaris (Lpo). The middle region receives afferent inhibitory (GABAergic) fibers from the GPi [89], [80], [90], [91]. In Olszewski's terminology, this corresponds to the anterior or oral sub-nucleus of the VL – pars oralis (VLo). The counterpart in Walker's terminology is the nucleus ventrooralis (Vo) in the human. The posterior region receives afferent fibers from the cerebellar nuclei [38], [86], [88], [92]. This region lies in the posterior portion Olszewski's VL, which includes an anteromedial sub-nucleus (Area X), a dorsal-caudal sub-nucleus (pars caudalis [VLc]), an extreme posterodorsal sub-nucleus (pars postrema [VLps]), and an oral ventral posterior lateral nucleus (VPLo). In Walker's terminology, this area includes the Vo as well as the Vim. Further posterior to the cerebellar receiving area of thalamus lies a 'non-motor' region. It consists of an anterodorsal shell and a large central core which receives proprioceptive and cutaneous lemniscal afferents, respectively [38], [91]. This division however was not distinguished by either Olszewski or Walker. The entire region was termed caudal ventral posterior lateral nucleus (VPLc) by Olszewski and nucleus ventralis caudalis externus (Vce) by Walker.

1.2.2 Cortical-Basal Ganglia-Thalamocortical Circuit

Stimulation of Vim nucleus can often result in electrical current spreading to adjacent nuclei, including the Vo. This is because implantation of the DBS lead often targets the

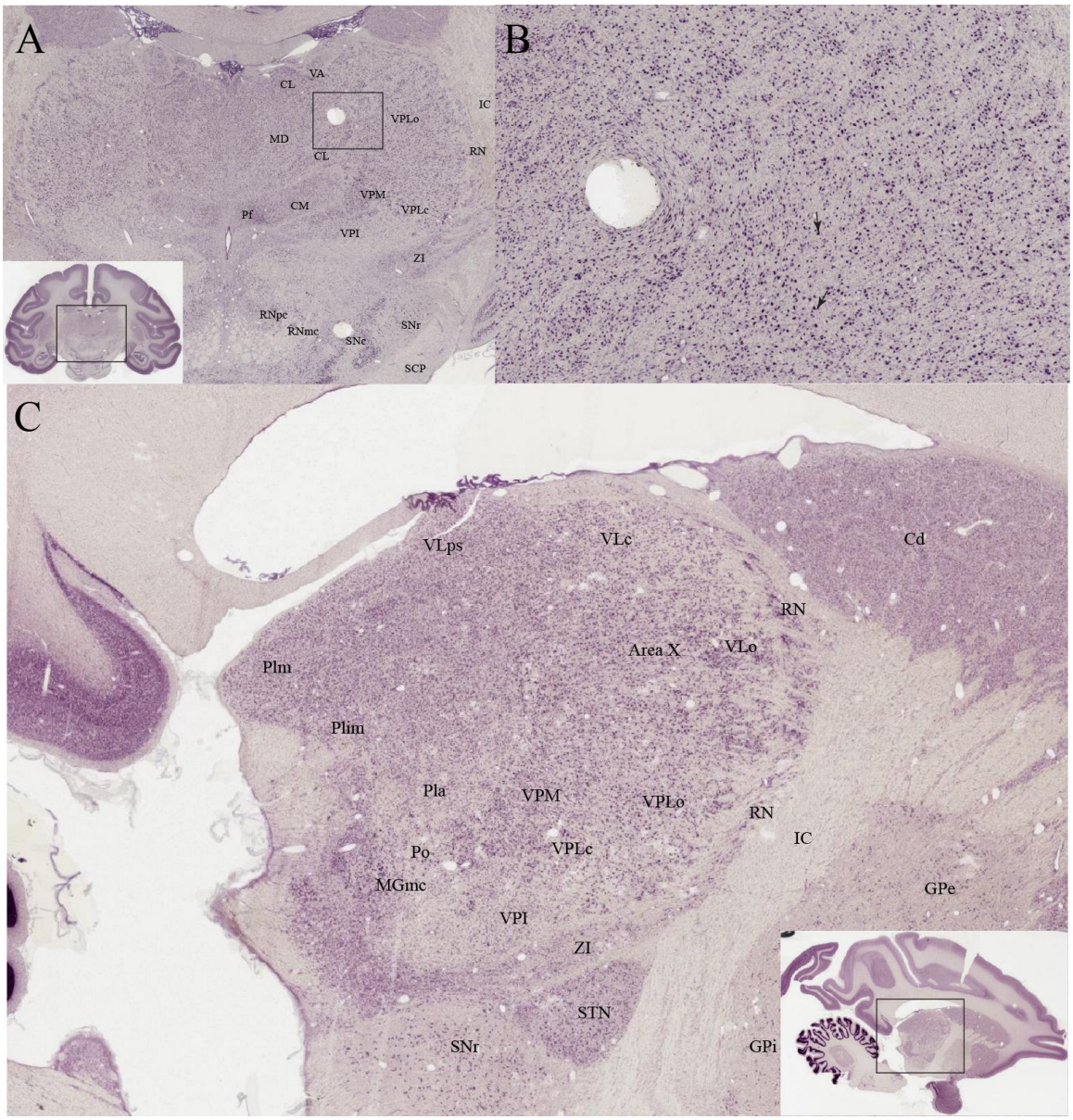

Figure 2. The motor and sensory thalamus and surrounding structures

Abbreviations are listed at the end. **(A)** Nissl-stained coronal section of the Rhesus Macaque monkey (*Macaca Mulatta*) brain focused on the thalamic area, with delineations of motor and sensory thalamic nuclei. Inset shows the entire brain slice. Boxed region in the inset is the enlarged region. Boxed region in the main image is magnified in B. (Figure adapted from [93]) **(B)** Magnified image of the boxed region in the main image in A. Arrows point to examples of stained neurons. **(C)** Nissl-stained sagittal section of the Rhesus Macaque monkey (*Macaca Mulatta*) brain focused on the thalamic area with delineations of motor and sensory thalamic nuclei. Inset shows the entire brain slice. (Figure adapted from [93]) **Abbreviations:** Cd – caudate nucleus, CL – central lateral nucleus of thalamus, CM – centromedian nucleus of thalamus, GPe – globus pallidus externa, GPi – globus pallidus interna, IC – internal capsule, MD – mediodorsal nucleus of thalamus, MGmc – magnocellular part of the medial geniculate nucleus, Pf – parafascicular nucleus of thalamus, Pla – anterior nucleus of pulvinar, Plim – medial division of the inferior nucleus of pulvinar, Plm – medial nucleus of pulvinar, Po – posterior nucleus of thalamus, RN – reticular nucleus of thalamus, STN – subthalamic nucleus, VA – nucleus ventralis anterior of thalamus, VLc – nucleus ventralis

lateralis pars caudalis of thalamus, VLo – nucleus ventralis lateralis pars oralis of thalamus, VLps – nucleus ventralis lateralis pars postrema of thalamus, VPI – nucleus ventroposterior inferior of thalamus, VPLo – oral ventral posterior lateral nucleus of thalamus, VPLc – caudal ventral posterior lateral nucleus of thalamus, VPM – ventral posterior medial nucleus of thalamus, ZI – zona incerta.

border between Vim and nucleus ventralis oralis posterior (Vop, part of Walker's Vo, homologue of VLo in monkeys) in order to avoid stimulating the sensory thalamus to the posterior [94]. Therefore it is important to understand the connections between the anterior portions of the motor thalamus with the rest of the motor network, which has been the subject of much research. The thalamus serves as a nexus between frontal cortical regions and the basal ganglia. Information flows from the cortex through basal ganglia structures to the thalamus, and back to the cortex [95]. Cortical inputs are received by the striatum (caudate and putamen) and then projected to the output structures of the GP and SNr, which is then relayed to the thalamus via two pathways: 1) the Direct Pathway, from the striatum to the GPi, from the GPi to the SNr and then to the thalamus, and 2) the Indirect Pathway, from the globus pallidus externa (GPe) to the STN, from the STN to the GPi, and from the GPi to the thalamus [96]. The regions of termination of these two pathways in the thalamus were discussed in the previous section. Striatal projections to both pathways are GABAergic and inhibitory. GPi/SNr projections to the thalamus are also GABAergic and inhibitory. The result is that activation of the Direct Pathway (via two inhibitory synapses) results in disinhibition of thalamic output to the cortex. The STN projection to the GPi is excitatory, therefore activation of the Indirect Pathway inhibits thalamic output to the cortex. The role of the Direct Pathway is to reinforce cortically driven behavior via positive feedback. The Indirect Pathway on the other hand modifies this behavior by inhibiting this positive feedback. It is important to note that the functional topography of the frontal cortex is maintained throughout the cortical-basal ganglia-thalamocortical loop [39] (Fig. 3A). The motor areas of the cortex (primary, supplementary, premotor, and cingulate motor areas) facilitate different

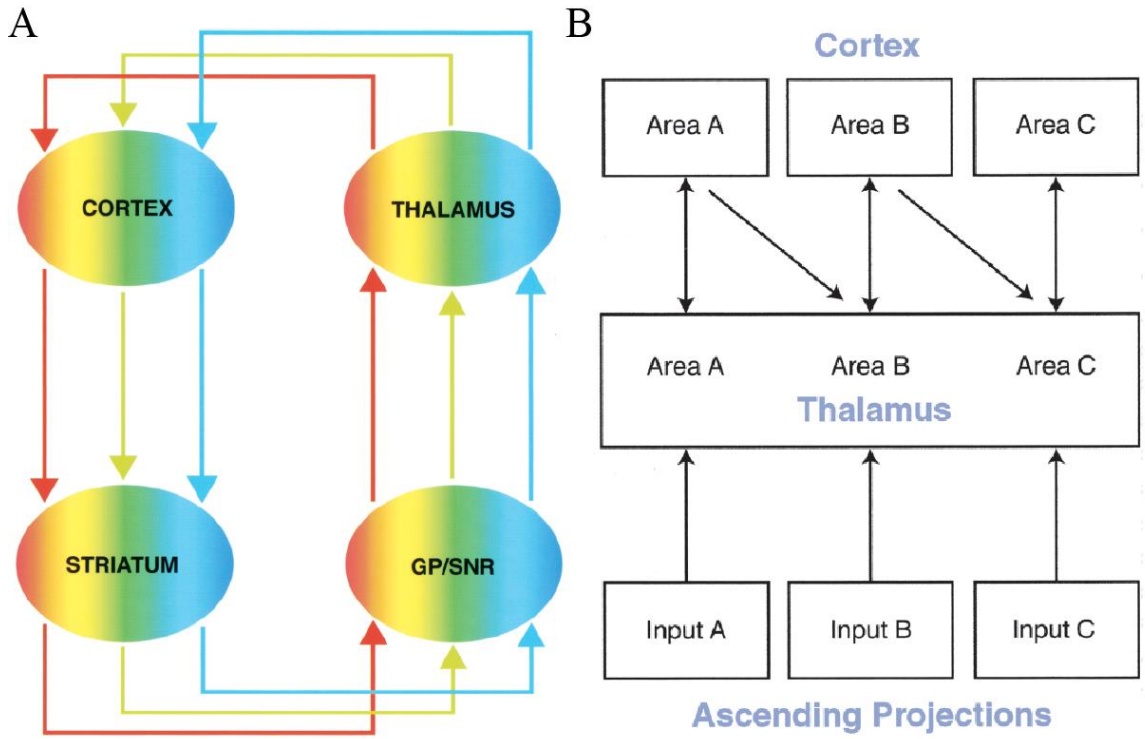

Figure 3. Functional connectivity in the cortico-basal ganglia-thalamocotrical network
(A) Schematic illustrating the preservation of functional topology within the cortico-basal ganglia-thalamocotrical network. Each color represents a functional region. GP – globus pallidus, SNR – substantia nigra pars reticulate. (Figure adopted from Figure 3 in [39]) **(B)** Schematic illustrating information transfer between cortical areas via thalamic relay nuclei. For instance, cortical area A has reciprocal connections with thalamic relay nucleus A, but also has non-reciprocal connections with thalamic relay nucleus B. In this way, cortical area A can also influence cortical area B via thalamic relay nucleus B. (Figure adopted from Figure 4 in [39])

aspects of motor control, such as movement execution, motor learning and sensorimotor integration [97], [98], [99]. These motor areas of the cortex project to the dorsolateral striatum, which includes the dorsal/postcommissural putamen and the dorsolateral head of the caudate [100], [101]. The dorsal lateral prefrontal association areas of the cortex are involved in executive functions such as working memory and switching between cognitive states [102], [103]. This area mainly projects to the head and body of the caudate and rostral putamen [104]. The orbital and medial prefronal cortex is involved in different aspects of reward and emotional response [105], [106]. This area projects mainly to ventral and medial striatum [107]. Studies in the monkey [108], [109], [86], [92] have revealed that the pallidothalamic projection consists of two parallel streams. The stream involved in the ‘motor circuit’ has its origins in the motor areas of the cortex,

which projects via the putamen to the lateral portions of the GPe and GPi, then travels through the ansa lenticularis and terminates in the anterior portion of VLo (Walker's Vo). The other stream involved in the 'associative circuit' originates in the dorsal lateral prefrontal association areas in cortex, which projects via the caudate to the medial portions of the GPe and GPi, then travels through the fasciculus lenticularis and terminates in the posterior region of the VA [73]. In this way, the functional topography is maintained from the cortex to the thalamus [39]. Furthermore, this functional topography is also present in the return path from the thalamus to cortex via thalamocortical (TC) projections. The VLo (Walker's Vo) projections primarily to the caudal cortical motor areas, which are closely involved in movement execution [92]. The VA projects primarily to the rostral motor areas, which mainly facilitate 'cognitive' aspects of motor control, including motor learning [110], [111]. Corticothalamic (CT) connections have both reciprocal and nonreciprocal components. The reciprocal component involves cortical areas receiving thalamic inputs projecting back to those same areas in the thalamus. The nonreciprocal component involves cortical areas that do not receive input from certain thalamic areas but projecting to those same areas in the thalamus [112], [113]. The reciprocal projections primarily arise from small cells in layer VI for the cortex, whereas the nonreciprocal projections primarily arise from large, rapidly conducing cells in layer V of cortex [114], [115]. The ventral lateral thalamic areas (VLo, VLc, area x in monkeys, Vo in humans) has reciprocal connections mainly with the caudal motor cortical areas, but also receive nonreciprocal projections from more rostral cortical motor areas [92], [116], [111]. The VA is reciprocally connected with the rostral motor cortical areas and dorsolateral prefrontal areas, but also receives nonreciprocal projections from lateral orbitofrontal areas [117] [39]. In this way, the information relayed from the thalamus to the cortex is not only derived from the parallel pathways through the basal ganglia, but is also modified by other cortical areas through the nonreciprocal CT projections. This also allows for information to flow across different functional regions of the cortex via the thalamus (Fig. 3B). Finally, the thalamus also projects directly to the striatum. This is most associated with midline and intralaminar thalamic nuclei [118], [119], but was also found to be true of thalamic relay

nuclei, which constitutes much of the thalamic afferent to the dorsal striatum. In particular, the VLo projects primarily to the dorsolateral postcommissural putamen, while the VAmc projects primarily to the dorsal head of the caudate nucleus [120]. Taken together, the thalamus plays a dual role in the cortical-basal ganglia-thalamocortical network: 1) Integrating basal ganglia output with cortical input and 2) directly modulating the activity of the striatum.

1.2.3 Thalamic Connections with the Cerebellum, Spinal Cord and Cortex

The thalamus is also a nexus between the cerebellum and the cortex (Fig. 4A). The cerebellum projects to the thalamus via the CTT, which originates in the dentate, interposed and fastigial cerebellar nuclei. The CTT ascends and becomes the superior cerebellar peduncle, decussates and passes anteriorly through and around the red nucleus into the thalamus [121]. The CTT terminates primarily in the ventral lateral thalamic complex, which includes Olszewski's Area X, VLc, VLps and VPLo (Walker's Vo and Vim) [73]. Injections of tracers and lesions in the three deep cerebellar nuclei have mapped out the thalamic termination zones for the afferent fibers [38]. The majority of the efferent fibers from the dentate nucleus terminate in the contralateral thalamus. The main fiber termination zones were found in the VPLo, VLc, Area X, some were also found in the VLps, the zone adjacent to the VLo as well as the central lateral nucleus (CL) of the intralaminar thalamic complex. Efferent fibers form the interposed nucleus terminated in the same areas as those for the dentate nucleus, although the amount of labeled fiber terminals were less for the interposed nucleus [38]. The foci of the fiber termination within those superimposable thalamic areas were segregated [122]. The efferent fibers from the fastigial nucleus were found in the VPLo, VLc and CL nuclei in both the contralateral and ipsolateral thalamus. However, the amount of fiber terminations were much smaller in the contralateral thalamus compared to those found for the dentate and interposed nuclei. The amount of fiber terminations in the ipsilateral thalamus was even sparser. A topographical trend exists in which the posterior parts of the cerebellar nuclei project to the anteromedial regions of the VL complex (area X) and anterior parts project to the posterolateral regions (VPLo, VLc) [38]. Studies using

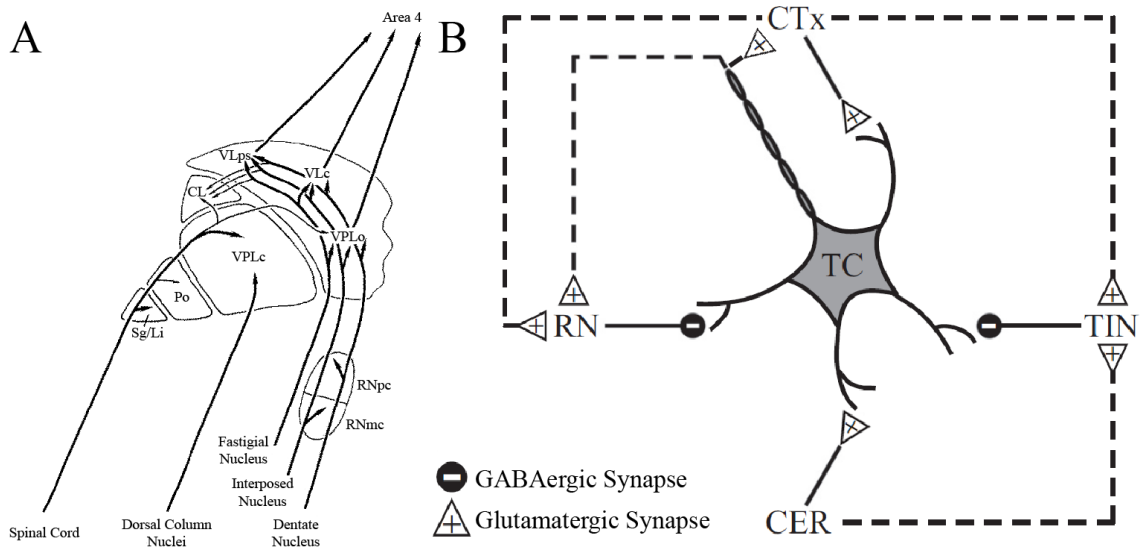

Figure 4. The motor and sensory thalamus and their afferent and efferent connections
Abbreviations are listed at the end. **(A)** Schematic in the prasagittal plane illustrating the afferent pathways to the motor and sensory thalamic nuclei, and the thalamocortical projections from the motor thalamus to the motor cortex (area 4). (Figure adapted from [38]) **(B)** Schematic of the various projections to and from the thalamocortical relay neuron. (Figure adapted from [123]). **Abbreviations:** CER – cerebellum, CTx – cortex, Li – limitans nucleus, RN – reticular nucleus of thalamus, RNmc – magnocellular part of the red nucleus, RNpc – parvocellular part of the red nucleus, SCP – superior cerebellar peduncle, SNc – substantia nigra pars compacta, SNr – substantia nigra pars reticulate, Sg – suprageniculate nucleus, TC – thalamocortical relay neuron, TIN – thalamic interneuron.

anterograde and retrograde labeling techniques have defined the cortical projections from the cerebellar receiving areas of thalamus. The VPLo, VLc and VLps project mainly to the primary motor cortex (M1) [124], [125], [126], but also have additional projections to the premotor areas [124], [125], [126] as well as the supplementary motor area (SMA) [124], [125], [126], [127], and even the prefrontal cortex [128]. The anteromedial region of Area X projects mainly to the premotor areas and SMA [124], [125], [126], [128], [129], [130] , with additional projections to M1 [124], [125], [126]. Injections of anterograde tracers in M1 have also revealed reciprocal projections back to the VPLo and through the extent of VLc [40].

The gracile and cuneate nuclei of the dorsal column of the spinal cord project via the lemniscal fibers (carrying proprioceptive and cutaneous information) into the dorsal thalamic mass through the posterior complex [131] and Olszewski's nucleus ventroposterior inferior (VPI). These fibers ascend along the posterior margin of VPLc and then mostly terminate within that nucleus [38]. The spinothalamic fibers carrying

sensory information from the periphery travel through the brainstem and project posterior to the medial lemniscus, entering the thalamus bilaterally.

Spinothalamic tract terminations were found within the posterior, lateral and dorsal aspects of the VPLc and VPLo, although contralateral fibers were found to be much sparser compared to the ipsilateral fibers [38]. Anterograde and retrograde tracing studies have found the VPLc to have extensive reciprocal connections with the primary somatosensory cortex (areas 1, 2 and 3), even directly linking CT fibers to spinothalamic fibers [40]. Taken together, the thalamus relays afferent information from the cerebellum, dorsal column nuclei and spinal cord to the various cortical areas and also receives feedback from those same cortical areas.

1.2.4 Thalamic Reticular Nucleus and Thalamic Interneurons

It is not possible to leave out the thalamic reticular nucleus (TRN) when discussing projections between the thalamus and the cortex (Fig. 4B). The TRN envelops the anterior and lateral parts of the thalamus, as well as some of its dorsal and ventral parts [132]. The nucleus lies at the thalamus-white-matter interface, which is between the internal capsule (IC) and the external medullary lamina where the TC and CT tracts intersect [133] before reaching their respective destinations. Both tracts innervate the TRN and give off excitatory (glutamatergic) collaterals, and the TRN neurons send inhibitory (GABAergic) fibers back to the thalamus [134], [135] (Fig. 5A). Studies have also found strong evidence that synaptic interactions between TRN neurons are mainly inhibitory [136], [137]. At least seven sectors (auditory, gustatory, somatosensory, visceral, visual, motor and limbic) are found to occupy distinct regions of the TRN [138], [139]. The motor sector in particular was located to the rostral part of the TRN in rats [140], [141]. Each sector has its own somatotopic organization and receives inputs from distinct but functionally related thalamic nuclei and cortical areas [142]. The only source of CT inputs to the TRN is from layer VI [143], [144], while the TRN projects to nearly all the anterior, dorsal, intralaminar, posterior and ventral thalamic nuclei in a loosely parallel pattern [141], [145], [132]. It is important to note that CT fibers are

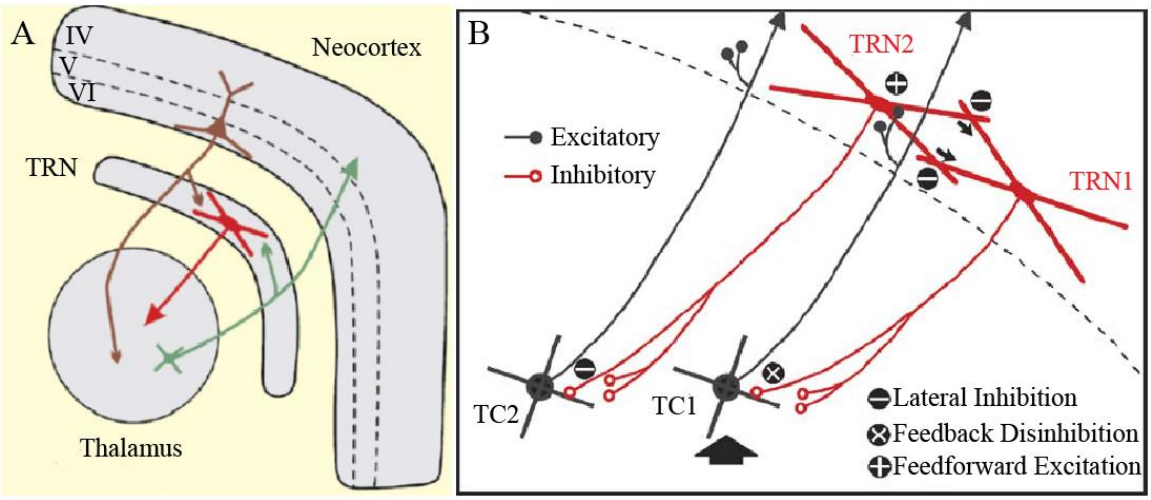

Figure 5. The reticular nucleus of thalamus and its afferent and efferent projections
(A) The place of the reticular nucleus of thalamus (TRN) between the neocortex and the rest of thalamus. Arrows point in the direction of efferent projections. **(B)** Schematic illustrating the possible connections between the neurons of the reticular nucleus (TRN, in red) and thalamocortical replay neurons (TC, in black), as well as the excitatory/inhibitory mechanisms that can arise from these connections. Excitatory and inhibitory synaptic connections are drawn in black and red circles, respectively. For example, neuron TC1 is activated following an afferent discharge on a specific prethalamic input (black arrow). This cell projects to and excites cell TRN2, which then inhibits cell TC2 (lateral inhibition). The neuron TRN2 then inhibits cell TRN1 (via dendrodendritic GABAergic synapses), which then would disinhibit the neuron TC1 (feedback disinhibition). (Figures adapted from [146])

approximately 10 times more numerous than TC fibers [147], [135], which means the number of CT synapses within the TRN are much greater compared to TC synapses. Layer VI neurons can also more effectively generate large excitatory synaptic conductances in TRN neurons than in TC neurons [148], pointing to the important role that the TRN plays in modulating the activities of TC neurons. Studies have shown that TC and TRN neurons form both closed-loop as well as open-loop connections, giving rise to possible complex mechanisms such as feedback inhibition, lateral inhibition, feed-forward excitation and feedback dis-inhibition (Fig. 5B). These mechanisms facilitate ‘cross-talk’ between different thalamic nuclei and the integration of information from various sources. There exists two distinct functional TRN cell types based on their firing pattern: ‘tonic’ and ‘burst’ mode [149]. The firing patterns of the two can be interchanged. Neurons in the ‘tonic’ mode are thought to be responsible for linear transfer of information from the thalamus to the cortex. While neurons in the ‘burst’ mode are considered to react to changes in input activity patterns. A change from the ‘burst’ mode

to the ‘tonic’ mode facilitates transfer of the new stimuli to the cortex [142]. Taken together, the TRN is in a unique position to receive both inputs from the periphery as well as the cortex, and it is likely involved in both bottom-up and top-down information processing [146]. Thalamic interneurons (TINs) are GABAergic and reside in the midst of relay neurons, composing of between 20% – 30% of the total thalamic neuronal population [150]. The TINs receive excitatory inputs from the cortex as well as inhibitory inputs from the TRN [150]. Projections from the TINs are local to the thalamus, innervating relay neurons as well as other TINs, facilitating intrathalamic inhibition [135]. TINs play a key role in local thalamic circuitry and in controlling the flow of information to the cortex.

1.2.5 Electrophysiological Properties of the Motor and Sensory thalamus

Vitek et al. thoroughly studied the physiological properties and somatotopy [151] of the motor and sensory thalamus, as well as the response of subnuclei to microstimulation [152]. The firing rates of the neurons in the VLc, VLo, VA and Area X were 12 ± 8, 13 ± 8, 15 ± 8, 12 ± 8Hz respectively. The VPLo and VPLc fired at higher frequencies of 22 ± 11 and 26 ± 8Hz respectively. The proportion of cells that responded to passive somatosensory examination (joint rotation, muscle palpation, tendon taps, cutaneous stimulation) across these nuclei decreased in the following order: VPLc (96%), VPLo (93%), VLc (77%), VLo (37%), Area X (22%) and VA (12%). The order in which neurons responded only to active movement (reaching/grasping) was somewhat reversed: VLo (44%), VA (45%), Area X (40%), VLc (11%), VPLo (3%) and VPLc (0%). VPLo (77%) neurons were the most responsive to applications of torque to the joints, followed by VLc (73%) and VLo (44%). The studies revealed a well-defined somatotopic organization in the VLo, VPLo and VPLc, and strongly implicated its existence in the VLc, but not for the VA or Area X. Within nuclei with this somatotopy, representation of body regions is organized in a laminar fashion like the layers of skin on an onion. The leg, trunk, arm and orofacial regions are represented in successively deeper lamellae. Microstimulation of the motor thalamus at less than $40\mu A$ was able to evoke movement in the contralateral limb, trunk or face. Microexcitability of the motor thalamus (as

measured by the percentage of stimulated sites that induces movement) was found to be 93% in VPLo, 21% in VLo, 11% in VLc, 1% in VA. Area X was not found to be microexcitable. 44% of stimulated sites within the VPLc were also found to be microexcitable, but this may have been a result of current spreading to the adjacent VPLo. Microexcitable responses within motor thalamic nuclei followed a somatotopic organization that was consistent with that found through somatosensory examination. Namely, evoked responses shifted from the leg, to the arm and then face as the stimulation sites moved progressively inward in each nucleus. Microexcitable zones ranging from 500 - 1500μm exist within the VPLo, in which microstimulation evoked the same motor response. This finding suggests that the thalamus preserves the fundamental unit of motor organization (i.e. single muscle or joint) and may contribute the modular organization of the cortex. Knowledge of the electrophysiological and somatotopic organization of the motor thalamus is crucial for identifying both motor thalamic targets for DBS as well as sensory thalamic regions in which stimulation induces adverse side-effects.

1.3 Mechanisms of DBS for Essential Tremor

Despite the effectiveness of DBS in treating ET (and other hypo/hyperkinetic disorders), its mechanisms of action are still under debate. The similarity in clinical outcomes between lesions and DBS led to early hypotheses that high-frequency DBS works through inhibition and reduced neuronal output near the stimulated site [153]. This was observed during both STN and GPi DBS [154], [155], [156] and hypothesized to be due to the activation of presynaptic inhibitory afferents to neurons near the site of stimulation. However, other studies [157], [158], [159], [160] have shown an increase in overall firing in nuclei downstream of where the stimulation was taking place, suggesting that output from the stimulated nucleus was actually increased. Modeling studies suggested that this paradox could be explained by the simultaneous direct activation of axons and suppression of cell bodies [161]. Supra-threshold stimulation initiated action potentials in the axon rather than the cell body, suppressing intrinsic firing in the soma while generating efferent output in the axon that was time-locked to the stimulus, leading to a

regularization of neuronal activity [161], [157]. Studies have also shown that this regularization effect spreads downstream throughout the cortico-basal ganglia-thalamocortical network. Examples include STN DBS regularizing activities in the pallidal- and cerebellar-receiving areas of the thalamus [162] and GPi DBS inducing firing pattern changes in the motor cortex [163]. These findings led to the hypothesis that an 'informational lesion' effect was taking place where pathological activities in the stimulated target and in downstream structures were replaced by (stimulation-induced) regularized neuronal activity [164]. This hypothesis is supported by computational modeling studies which showed that model neurons demonstrated frequency and amplitude dependent regularization of activity in response to stimulation [165]. This regularization of model neuron activity was also found to be strongly correlated with the therapeutic effects of DBS, including tremor reduction in ET patients [165] and alleviation of bradykinesia in PD patients [166]. The same correlation was observed *in-vivo* in the 1-methyl-4-phenyl-1,2,3,6-tetrahydropyridine (MPTP) monkey model of Parkinson's disease during STN DBS [167]. Effective high-frequency stimulation that reduced motor symptoms regularized neuronal firing patterns in the pallidum and motor thalamus, as indicated by decreases in firing pattern entropy. On the other hand, ineffective low-frequency stimulation actually increased firing pattern entropy, in effect creating more randomness in neuronal activity. The frequency dependent effects of DBS on neuronal firing patterns were further studied using computational models of thalamic nerve fiber stimulation [168]. The results indicated that at between 2 – 80Hz, stimulation increased the firing pattern entropy in the fibers (compared to no stimulation) by superimposing stimulus induced activity on top of intrinsic burst activity. Stimulation frequencies between 80 – 1000Hz reduced firing pattern entropy in the fibers to zero, effectively masking the intrinsic activity with regularized firing. Stimulation above 1000Hz induced irregular firing patterns (increasing firing pattern entropy) or conduction block in the majority of fibers. These results aligned with previous reports of frequency ranges in which DBS was found to be effective [53], again in support of the 'informational lesion' hypothesis – effective DBS masks the intrinsic activity of stimulated neurons and replaces it with regularized firing. This lesion of information in

the neural circuitry was also observed experimentally, although the effect was shown to be incomplete [169]. In a set of experiments, repetitive joint articulations were performed in monkeys while unit spike activity was recorded in the sensorimotor GP and VLo before, during and after GP-DBS. The results showed that despite highly regularized firing patterns, cells in GP and VLo still responded to one or more aspects of joint movement during GP-DBS. Other studies have also shown that DBS may in fact improve information content in the network by enhancing information processing [170], [171]. Evidence of axonal or synaptic failure from high-frequency stimulation also prompted the proposal of a 'functional lesion' effect [172]. Regardless of the exact mechanism, therapeutic DBS acts through modulation of relevant pathways within the motor circuit. In the case of ET, DBS is thought to disrupt pathological activity in the CTT [68] and/or thalamocortical tract (TCT) [153]. Stimulation of fiber pathways adjacent to the stimulated site may also play an important role in the observed clinical effects. An example is STN DBS activating the CTT ventral and posterior to the STN and the reported beneficial effects on ET symptoms [173], [174]. Stimulation of the PSA has been demonstrated to produce good tremor control at lower stimulation intensities (compared to the Vim proper) [175]. This is presumably because the afferent CTT fibers are bundled together as they enter the ventrolateral thalamus and therefore stimulation is able to activate a larger proportion of these fibers. The larger intensities required to stimulate the Vim proper is supported by the finding of topographically organized 'tremor clusters' within that nucleus [176]. Therefore it is possible that stimulation in the Vim involves a volumetric effect in which tremor suppression results from electrical current sufficiently capturing these tremor clusters via the mechanisms discussed previously. The theories discussed above have mostly focused on neuronal or network mechanisms of DBS. A study by Bekar et al. [177] have discovered that nonsynaptic release of adenosine triphosphate (ATP) during high-frequency DBS and the subsequent accumulation of its metabolic product – adenosine, is crucial for reduction of tremor as well as DBS-induced side-effects. The mechanism involves activation of adenosine A1 receptors during high-frequency stimulation, which reversibly inhibits excitatory transmission in the thalamus. In summary, great inroads have been made in the effort to

understand the mechanisms of DBS at multiple levels, and continued research is needed to link these pieces together into a comprehensive picture. In the meantime, DBS remains a potent therapy with very present challenges that remain to be tackled.

1.4 Challenges and Opportunities for Thalamic DBS

1.4.1 Lead Placement for Effective Therapy

Although DBS is an effective treatment for ET, a survey shows that approximately 10% of patients with DBS implants receive inadequate tremor control due to poorly placed leads [178]. The Vim nucleus of thalamus is the primary DBS target for the treatment of ET. Lead placement within the Vim nucleus is very important in order to avoid inducing adverse side-effects. The DBS lead is usually placed along Vim's anterior border with the Vop in order to avoid current spreading posterior to the sensory thalamic nucleus of Vo [94], which can result in persistent paresthesias during stimulation [179]. Placing the lead too anterior will result in stimulation of the Vop, which will be less effective [180]. Leads placed too medial or too lateral will likely result in intraoral and leg paresthesias, respectively. Stimulation of the corticospinal tract that lies in the IC ventral and lateral of the Vim can result in tonic muscle contractions [181], [182]. Speech and swallowing problems can also result from thalamic DBS, however the exact mechanisms are unknown. The general assumption is that placing the lead within the head somatotopic region of the Vim (more medial) is more likely to evoke these side-effects. However, thalamic lesions studies have also pointed to damage in the pallidal afferent areas of the thalamus as a potential cause for dysarthria [183]. In addition, given the somatotopic organization of the thalamus [151], it is also important to direct stimulation in a focused manner in order to achieve the desired effect. For example, leg tremor can be difficult to suppress with thalamic DBS because the leg region is located in the lateral portion of the Vim near the IC. Clinical studies have also noted two different target regions for effective tremor suppression. One is within the Vim proper [53], [184], stimulation in which could be modulating the TCT from Vim to M1 [185], [186]. The other region is slightly ventral to the Vim [173], [175], [72], stimulation in which could be modulating CTT entering the Vim. Stimulation of the Vim proper usually requires a larger volume of activation [187],

[151], likely in order to encompass the somatotopic regions involved in tremor [188]. Stimulation of the region ventral to the Vim can achieve tremor suppression with lower stimulation amplitudes [173], [175], [72], but the target area is also harder to locate. The above analysis strongly suggests that there is little room for error in thalamic DBS in order to avoid adverse side-effects. Considering neurosurgical targeting error for DBS lead implantation has been estimated at 2mm from the intended target (with the combined use of MRI and intraoperative microelectrode recordings) [189], it is important to develop technologies that can 1) clearly visualize DBS target areas and 2) provide flexibility in terms of the directionality of stimulation and shaping the region of activation.

1.4.2 DBS Programming

Postoperative DBS programming is a process to determine the parameters of stimulation, which include electrode configuration/polarity, frequency of stimulation, pulse width and amplitude (current or voltage). The goals of DBS programming are to 1) maximize symptom suppression, 2) minimize side-effects and 3) maximize stimulator battery-life [190]. The basic programming algorithm is a 'monopolar review' performed under off-drug conditions [190]. Stimulation should be set to, for example, 60μs in pulse width and 130Hz in frequency (for thalamic DBS) and kept constant for the remainder of the test. Monopolar stimulation is delivered through each electrode on the DBS lead at a stepwise increment of 0.2 – 0.5V (for voltage controlled stimulation) in order to determine the amplitude threshold for inducing a clinical response or side-effect. If the clinical response is observed without inducing side-effects, then the stimulation amplitude is further increased until the threshold for side-effects is reached. The goal is to find the electrode with the largest 'therapeutic window' (i.e. the difference in stimulation amplitude between therapeutic threshold and sustained side-effect threshold [191]) to use for chronic stimulation. In case of persistent side-effects, the results from the monopolar review can also provide a basis for adding adjacent electrodes to form bipolar or multipolar configurations that are more likely to yield good results [192]. DBS programming is usually performed by nurse-practitioners and is a time-consuming

process. It has been estimated that the mean time spent programming a DBS stimulator can range from 18 – 36.2 hours per patient [193], with some patients significantly more difficult to program than others. Programming sessions are usually limited to 1 – 3 hours each time due to patient fatigue, which means multiple visits are needed before programming can be completed [193]. This approach, although feasible (albeit time-consuming) with traditional DBS leads which only have four cylindrical contacts (e.g. Medtronic model 3387 and 3389), will become more difficult to implement as the number of available electrodes increases. Additionally, the standard programming process relies on patient feedback and assessment of symptoms, which may not be feasible for disorders such as dystonia and Tourette's syndrome, for example, in which the therapeutic effects may not appear for weeks or months after beginning stimulation [194], [195]. Experience and intuition with DBS programming as well as the amount of time allotted to each patient also play important roles in the outcome of the therapy [196]. Compounding the issue is the problem of habituation of therapy. Studies have shown that the therapeutic effects from Vim-DBS fades in at least 40% of ET patients after 1 – 2 years, especially in the case of action tremor [197], [198]. A recent study [199]found that in a cohort of ET patients with Vim DBS implants, 73% reported waning benefits during a 56 months follow-up period, suggesting the prevalence of DBS habituation may be far higher than reported previously. Potential mechanisms may involve an increase in the volume of pathological thalamic tissue with disease progression or development of synaptic plasticity that impedes therapeutic electrical stimulation in or near the Vim. Case studies have shown patients who take 12-48 hours of 'DBS-holiday' every month can avoid developing tolerance to stimulation [200], [201]. Reprogramming DBS settings have also been shown to yield short-term (<10 weeks) improvements from unmanaged tremor due to habituation [199]. Taken together, there's a strong need to simplify the DBS programming process, making it efficient and intuitive, yet still achieve the desired therapeutic results. Direct visualization of targets of interest as well as regions responsible for side-effects will be an important feature, as well as computational algorithms that can infer or back-calculate the stimulation parameters for optimal therapy. Furthermore, programming should be adaptive and able to react to the changing

therapeutic landscape, possibly by cycling through configurations that can target different pathways (e.g. CTT vs. TCT).

1.4.3 Validation of Computational Models of DBS

The development of computational models has been instrumental in understanding and replicating the way the nervous system is influenced by electrical stimulation [202], [203], [204]. Studies have reconstructed realistic model neurons [205] with dedicated software [206] to understand mechanisms of DBS [161], [207], [208]. Integrating imaging data has allowed for the development of subject-specific computational models of DBS, with targets including the STN [209], [210], GP [211], ventral striatum [212], pedunculopontine nucleus (PPN) [213], [214] and thalamus [215], [201]. Of particular importance is the concept of volume of tissue activated (VTA) (which will be elaborated in later chapters) [216], [217], which allows for direct visualization of the extent of modulation through DBS. As VTA-based technologies are increasingly making its way to guide programming in DBS [218], [219], it is important to validate model predictions based on neurophysiological outcome measures. Validation of model predicted results in humans has relied on indirect measures of motor and perceptual observations related to side-effects of stimulation. Examples include calibrating model predicted DBS activation of the IC with electromyogram recordings of distal muscle groups [210] or activation of the Vc with patient reports of sensory paresthesias [201]. However, there is an obvious disconnect in terms of the scale of analysis between the computational VTA (cellular level, based on activation profile of neuronal elements, e.g. axons or cell bodies) and the behavioral outcome measures (systems level). What is needed is characterization of *in-vivo* activation profiles of tissue within target regions during DBS using electrophysiological recording techniques. These types of validation are logistically difficult to accomplish in humans and must therefore rely on animal models.

1.4.4 Opportunities and Emerging Technologies in DBS

The challenges facing DBS therapy also presents opportunities for the development and utilization of emerging technologies. The issue of accuracy of lead placement for

effective therapy can be addressed in two different directions: 1) develop the ability to clearly visualize the DBS target, and 2) develop the ability to directly stimulate and rescue therapy in cases of poorly targeted DBS leads. Traditionally, DBS implantation is guided by frame-based stereotaxy or frameless neuronavigational software, both of which require fusion of preoperative MRI and CT imaging to define the 'stereotactic space'. This space is the reference space in which DBS implantation takes place and is assumed to remain immobile relative to the brain targets. A new advancement that shifts away from this paradigm is the use of interventional (or intraoperative) MRI to guide the placement of DBS leads [220], [221]. This technique uses a frameless MRI compatible aiming device in conjunction with real-time direct visualization of patient imaging data to verify implant location. This eliminates the need for preoperative acquisition of MRI and CT data and also reduces complexity of the procedure as well as errors that might be introduced in the process. Furthermore, patients no longer need to be awake for the implant surgery and can instead undergo general anesthesia. This is both desirable for most patients and can also speed up the overall process. The procedure is limited however by the availability of interventional MR machines as well as the field strength that it can provide, which is important for visualizing small anatomical targets or targets with low contrast. High-field MRI ($\geq$ 7T) can provide improved visualization of anatomical targets [222], [223], [224] and reveal fine anatomical details (e.g. sub-nuclei within thalamus) [225], [226] due to its superior signal-to-noise ratio. Image contrast can be improved with the combined use of novel imaging modalities such as susceptibility-weighted imaging (SWI) [224], [227], [228]. In addition, high-field imaging can also assist in improving the fit of anatomical atlases to imaging data (to delineate sub-structures) [229] by providing detailed landmarks. Finally, diffusion tensor imaging (DTI) combined with the use of probabilistic tractorgraphy has shown great promise in mapping and visualizing the white-matter pathways of the brain [230], [223], [231]. Together, these emerging technologies have the potential to delineate entire circuits within the brain (e.g. cerebellothalamocortical pathway) on a subject-specific basis and provide valuable anatomical information for both DBS neuronavigation and computational models.

Rescue of therapy in the case of poorly targeted DBS leads is another area in which exciting research and development is taking place. The design of DBS leads has not changed since the 1970s, largely following the work of Hosobushi et al. [49]. The traditional design (e.g. Medtronic model 3387, 3389) consists of a linear stack of cylindrical electrodes along the length of the lead. This design is particularly sensitive to surgical targeting errors in the direction tangential to the length of the lead, because the cylindrical electrodes deliver electrical current axisymmetric to the lead shank. This makes it more difficult to stimulate small or oblong structures such as the PPN [213] or STN [232] as the large size of electrodes will like modulate a larger area than intended. These shortcomings motivated the development of radially-segmented DBS arrays (rDBSAs) [233], [191], which segments each cylindrical electrode into three or more smaller electrodes that face different directions around the lead body. This design allows for independent control of stimulation through each electrode and can therefore enable directional steering of electrical current around [232] and along [234] the lead. Computational models of rDBSAs have demonstrated their effectiveness in shifting the electric field as well as the VTA in the preferred direction [235], [232], [236], [215], [237]. Clinical studies have also demonstrated that directional stimulation through rDBSAs can increase the 'therapeutic window' [191], [238]. An added benefit to the rDBSA design is the finer spatial resolution of local-field potential recordings that can be achieved compared to cylindrical electrodes [233]. However, the increased number of electrodes on the rDBSAs further complicates the difficult task of manual DBS programming. Researchers are addressing this issue by coupling computational models of DBS with patient-specific imaging data to develop programming algorithms that allow for visualization and control of the extent of modulation [219], [239], [240]. A well-developed approach is to pre-compute large amounts of VTAs from many different stimulation configurations and store them in a database, which serves as a look-up table [219], [218]. Researchers can then use surgical navigation software [241] to define target volumes for stimulation, prompting the algorithm to search through the VTA database and find the solution with the largest overlap with the target volume. A more recent approach was developed by Chaturvedi et al. that trained artificial neural networks

(ANNs) to predict the shape of VTAs resulting from stimulation, using a set of 4620 unique stimulation configurations. This method benefits from the ability of the ANNs to generalize the complex relationship between stimulation parameters and the shape of the resulting VTA. However, it still required substantial pre-computation and the underlying concept of using pre-computed data for prediction is somewhat unchanged. Additionally, the VTA predictions have yet to be fully validated experimentally.

The goal of this dissertation is to utilize these emergent technologies and develop new tools and methodologies to engage the challenges facing DBS, as outlined in the previous sections. More specifically, we will **1) couple high-field SWI with DTI/tractography to segment DBS targets within thalamus (Chapter 2), 2) develop computational model-based programming algorithms for rDBSAs (Chapter 3), 3) apply statistical tools to quantify computational VTAs resulting from directional stimulation (Chapter 4) and 4) characterize *in-vivo* the DBS-induced spatial neuronal activation profiles adjacent to chronically implanted thalamic rDBSAs (Chapter 5).**

Chapter 2

Multimodal Imaging of Thalamic Nuclei

This chapter was reprinted with permission from Frontiers Media.

YiZi Xiao, Laura M. Zitella, Yuval Duchin, Bejamin Teplitzky, Daniel Kastl, Gregor Adriany, Essa Yacoub, Noam Harel, and Matthew D. Johnson, "Multimodal 7T imaging of thalamic nuclei for preclinical deep brain stimulation applications," *Front in Neurosci,* 10(2016): p.264.

2.1 Overview

2.1.1 Objective

Precise neurosurgical targeting of electrode arrays within the brain is essential to the successful treatment of a range of brain disorders with deep brain stimulation (DBS) therapy. Here, we describe a set of computational tools to generate *in vivo*, subject-specific atlases of individual thalamic nuclei thus improving the ability to visualize thalamic targets for preclinical DBS applications on a subject-specific basis.

2.1.2 Approach

A sequential nonlinear atlas warping technique and a Bayesian estimation technique for probabilistic crossing fiber tractography were applied to high-field (7T) susceptibility-weighted and diffusion-weighted imaging (SWI, DWI), respectively, in seven rhesus macaques. Image contrast, including contrast within thalamus from the susceptibility-weighted images, informed the atlas warping process and guided the seed point placement for fiber tractography. The thalamic substructure boundaries were validated through *in vivo* electrophysiological recordings and post-mortem blockface tissue sectioning.

2.1.3 Main Results

The SWI resulted in relative hyperintensity of the intralaminar nuclei and relative hypointensity in the medial dorsal nucleus, pulvinar, and the medial/ventral border of the ventral posterior nuclei, providing context to demarcate borders of the ventral nuclei of thalamus, which are often targeted for DBS applications. Additionally, ascending fiber tractography of the medial lemniscus (ML), superior cerebellar peduncle (SCP), and pallidofugal pathways into thalamus provided structural demarcation of the ventral nuclei of thalamus.

2.1.4 Significance

Together, these imaging tools for visualizing and segmenting thalamus have the potential to improve the neurosurgical targeting of DBS implants and enhance the selection of stimulation settings through more accurate computational models of DBS.

2.2 Background

Structural brain imaging has become a valuable tool to guide the implantation and programming of deep brain stimulation (DBS) systems for the treatment of many brain disorders [216], [242], [243]. Current clinical magnetic resonance imaging (MRI) (1.5-3T) provides reasonable image contrast to identify, for example, the borders of the globus pallidus (GP) and to some extent the borders of the subthalamic nucleus [244] for

treatment of Parkinson's disease. Such visualization abilities have enabled new opportunities for interventional MRI guided stereotactic neurosurgery [220]. However, clearly demarcating targets within the thalamus (another surgical target of DBS) at these field strengths remains a considerable challenge for both clinical [222, 245] and preclinical DBS studies. Improvement in structural imaging of intra-thalamic nuclei would have important implications given that interventional stereotactic procedures within thalamus have shown marked promise for the treatment of pain [246], essential tremor [53, 247], epilepsy [248, 249], Tourette syndrome [250], disorders of consciousness [251], as well as other brain disorder indications on the horizon, including schizophrenia [252, 253]. This is especially important because favorable behavioral outcomes with thalamic DBS hinge upon the accuracy of stimulating the desired thalamic pathway, while avoiding modulation of neuronal pathways implicated in the emergence of adverse side effects [44, 201, 215, 254, 255]. Thalamic nuclei can be difficult to visualize with traditional (1.5-3T) scanners, thus requiring the identification of fixed coordinates based on an internal reference, such as the anterior commissure (AC) and posterior commissure (PC) plane [256-260]. However, several imaging approaches have been used to demarcate various thalamic nuclei beyond typical clinical imaging protocols. These include functional imaging [261-264], high-field MRI [223, 265-267], parcellation utilizing corticothalamic DWI with probabilistic tractography [230, 268], and other signal processing techniques [269, 270]. Another approach to capture subtle thalamic anatomy is using histologically derived brain atlases [271] based on acetylocholinesterase (AChE) [272] and calcium-binding protein (e.g. parvalbumin) [273] labeling of thalamus [274] to match and overlay upon individual MR images [269, 270]. However, inter-subject variability in thalamic anatomy has been widely demonstrated [275-277], and a 'one-size-fits-all' method for linear registration of histological brain atlases to structural imaging data has proven to be imprecise amongst subjects [244]. The need to identify anatomical information within individual MRI data has prompted the development of deformable digital atlases [278-291], numerous image processing techniques [229, 292-295], and intraoperative microelectrode mapping procedures to verify and expand upon the interpretation of the imaging data [296, 297].

Here, we show that a multi-modal imaging approach using 7T *in vivo* MRI enables demarcation of intra-thalamic nuclei as confirmed with histology in two subjects. The acquired dataset enabled: 1) investigation of what contrast exists in the non-human primate (NHP) thalamus in high-field 7T SWI, 2) development of methods to identify structures not directly visible even with high-field MRI, 3) construction of afferent fibers to the thalamus via probabilistic fiber tractography, and 4) comparison of the constructed nuclei and fiber tract to post-mortem histology.

2.3 Methods

2.3.1 Data Acquisition

High-field MRI (7T, Magnex Scientific) was performed on seven rhesus macaque primates (*macaca mulatta*, 6 female and 1 male, Table 2) at the University of Minnesota's Center for Magnetic Resonance Research using a Siemens console and head gradient insert capable of 80 mT/m with a slew rate of 333 mT/m/s. A customized head coil was developed with 16-channel transmit and 16+6 receive channels, in which 4 coils mounted on top of each subject's head and 2 ear-loop coils were added to enhance signal detection from subcortical structures [298]. All procedures were approved by the Institutional Animal Care and Use Committee of the University of Minnesota and complied with United States Public Health Service policy on the humane care and use of laboratory animals. Animals were anesthetized (isoflurane, 2.5%) during the imaging sessions and monitored continuously for depth of anesthesia. Animals were individually housed in a Primate Products Enhanced Environment Housing System (dark/light cycle of 12/12) in the University of Minnesota's Research Animal Resources facility. The animals were given a range of environmental enrichment (e.g. toys, foraging baskets, mirrors, TV), provided with water ad libitum, and given a range of food options including fresh fruit and vegetables. All efforts were made to provide good care and alleviate unnecessary discomfort, and no adverse events occurred. At the conclusion of the study and in order to validate the MRI data, two animals were deeply anesthetized with sodium pentobarbital and perfused with phosphate buffered saline followed by a 4%

Subject	Gender	Age	SWI Resolution	DWI	EM	BFS	Description
1	F	22	0.4 mm iso				
2	F	22	0.4 mm iso				
3	F	14	0.33 mm iso				
4	F	13	0.4 mm iso	«	«		EM validation of SWI and DWI
5	F	10	0.4 mm iso	«		«	BFS validation of SWI and DWI
6	F	9	0.4 mm iso	«		«	BFS validation of SWI and DWI
7	M	4	0.33 mm iso				

Table 2. Subject characteristics and imaging protocols
(*iso: isometric, EM: electrophysiological mapping, BFS: blockface sectioning*)

paraformaldehyde fixative solution, consistent with the recommendations of the Panel on Euthanasia of the American Veterinary Medical Association.

SWI was collected in all subjects (n=7) and consisted of a 3D flow-compensated gradient echo sequence using a field of view (FOV) of 128 x 96 x 48 mm^3, matrix size of 384 x 288 x 144 (0.3 - 0.4 mm isotropic resolution), TR/TE of 35/29 msec, flip angle of 15°, BW of 120 Hz/pixel, and acceleration factor of 2 (GRAPPA) along the phase-encoding direction. SWI is sensitive to a difference in magnetic susceptibility in tissues and can be used to measure iron content [299], in the form of ferritin and hemosiderin, found in oligodendrocytes [300-303] and regions of the basal ganglia and thalamus [304]. In this case, a local difference in iron concentration manifests in a difference in local magnetic susceptibility, causing a deviation in the induced magnetization, translating into a difference in phase [299]. Studies have shown that the phase shift is linearly correlated with iron concentration [305, 306]. Here, we used a T2*-weighted gradient echo sequence and combined the magnitude and phase information by multiplying a 'phase mask' to the magnitude image. Values in the phase image above zero were assigned to 1 in the phase mask (i.e. negated), while those between 0 and $-\pi$ were linearly scaled from 1 to 0. The phase mask was then raised to a power of 4 and multiplied to the magnitude image. The choice of raising the phase mask to the power of 4 was based on optimizing the contrast-to-noise ratio of the SW image [299]. In this way, regions in the magnitude image with large phase shifts had their magnitudes severely attenuated and appeared hypointense in the SWI data [299]. Whole-brain SWI scans required approximately 30 minutes per animal.

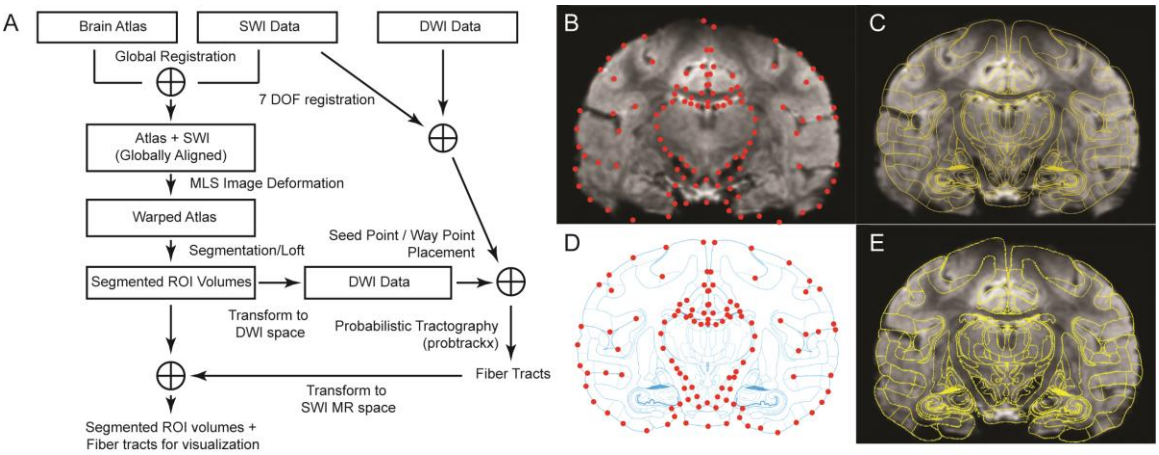

Figure 6. Brain atlas registration and warping process to SWI from Subject 3
(A) Schematic of the methodological analysis process combining SWI and DWI data. **(B)** Coronal image with 94 manually selected control points in red (q points). **(C)** Overlay of MRI with the corresponding atlas plate after global alignment. **(D)** Atlas plate after global alignment with MRI. Matching control points in red (p points). **(E)** Warped atlas plate superimposed on top of the original MR image.

Additionally, DWI was collected and analyzed in a subset of subjects (n=3). DWI consisted of a single refocused 2D single-shot spin echo EPI sequence [307] using a FOV of 128 x 84 x 99 mm^3, matrix size of 128 x 84 x 50 (1 mm isotropic resolution), TR/TE of 3500/53 msec, flip angle of 90°, BW of 1860 Hz/pixel, and an acceleration factor of 3 (GRAPPA). Diffusion-weighted images (b-value = 1500 s/mm^2) were collected with diffusion gradients applied along 55-143 uniformly distributed directions [308]. Fifteen additional non-diffusion-weighted images (b=0 s/mm^2) were acquired for every 10 diffusion-weighted images. We utilized TOPUP [309] in FSL to correct for geometric distortions in the EP images due to magnetic field inhomogeneities. This approach used multiple non-diffusion-weighted (b0) scans with bidirectional (posterior-anterior and anterior-posterior) phase-encoding directions to calculate and counteract the deformation field. Whole-brain DWI scans required approximately 30 minutes per animal.

2.3.2 Atlas Registration

To assist with identification of thalamic nuclei, a rhesus macaque brain atlas [310] was registered and nonlinearly deformed to the MRI volumes of each of the seven subjects. In preparation, MRI volumes were aligned in AC-PC space (Analyze 11.0,

AnalyzeDirect) and then resliced into serial coronal images. A set of 40 coronal images, spanning the entire thalamic region, was extracted from each subject's imaging dataset. First, a non-uniform rational B-spline modeling program (Rhinoceros) was used to create a proportional grid system, as developed by Talairach [256] for the human brain, to identify equivalent slices between the MRI and brain atlas (n = 30 slices between AC and PC) [310]. The distance (variable over 7 subjects, average: 0.482mm, minimum: 0.429mm, maximum: 0.517mm) between each slice was then used to generate 10 further images posterior to the PC. An initial global registration of the interpolated MR images to the brain atlas [310] was performed using both a global rigid transformation and a local affine transformation [311], such that the cortical outlines and the inter-hemispheric fissures in the atlas section were aligned with those on the MR image (Fig. 6B,C). To further warp the atlas to individual MR images, control points p and q were manually placed on each atlas section and the corresponding MR image, respectively, such that p_i and q_i represent the same spatial location. Common locations for control points were located on the boundaries of the cortex, major sulci, lateral and third ventricles, interpeduncular cistern, and the borders of thalamus [311, 312]. Spatial selection of control points across MR images with thalamus was consistent with those control points shown in Fig. 6B,D. We then used a nonlinear atlas warping approach that adapted a moving-least-squares (MLS) image deformation algorithm [313]. For each pixel *v* in the undeformed image, the algorithm solved for the best transformation function $f(x)$ that satisfied:

- $f(p_i) = q_i$
- *f produces a smooth deformation*
- *if* $p_i = q_i \rightarrow f(v) = v$

and minimized

$$\sum_{i=0}^{n} w_i |f(p_i) - q_i|^2,$$

where $w_i = \frac{1}{|p^i - v|^{2\alpha}}$ (α=2 was found to be suitable in this case).

In other words, the handles p_i should map directly to q_i under deformation, and if the deformed handles q_i are the same as p_i, then *f* should be the identity function. Since the

weights w_i were dependent on the location of each pixel, the algorithm solved for a different $f(x)$ for each pixel. $f(x)$ in the most general case was an affine function of the form: $f(x) = xM + T$, where M and T were rotation and translation matrices, respectively. The affine transformation allowed for rotation, translation, anisotropic scaling, and anisotropic shearing in two-dimensions. For more conservative *similarity* and *rigid* deformations, restrictions were put on the rotational matrix M to ensure isotropic shearing and scaling. Closed-form solutions were derived for all three cases. In cases of large deformations, the sign of the Jacobian of $f(x)$ can change and the one-to-one mapping of pixels may be violated, causing the image to fold back on itself. To eliminate such fold-backs, we implemented an approach by Tiddeman et al. to break up the entire warp into a series of smaller partial deformations, ensuring in each step the Jacobian of $f(x)$ does not change sign [314]. In each stage, the partially warped image serves as the starting point for a new round of deformation until all the control point restraints $f(p_i) = q_i$ are satisfied (Fig. 6D, E).

2.3.3 Diffusion Tensor Imaging

Fiber tractography was performed in FSL [315-317] for three subjects (M4, M5, and M7) to extract several fiber tract pathways projecting into thalamus. SW images were converted into NIfTI files (dcm2nii) and imported into the brain imaging analysis software platform, FSL (v5.0.2.1). The FSL automated brain extraction tool [318] was used to remove the skull in the images. A 7-DOF *flirt* [319-321] linear transformation in FSL was used to obtain registration between the SWI data and mean B_0 DWI volume. The transformation was necessary because even with image distortion correction due to field inhomogeneity, slight image distortion can still exist. Since these two imaging modalities differ, inter-modal cost functions (correlation ratio or mutual information-based options) were applied depending on which produced the best alignment as assessed visually. Before computation of tractography, the diffusion data was pre-processed using *bedpostx* to estimate the diffusion parameters. The bedpostx function was run with 3 fibers per voxel (n=3) to model crossing fibers. All other parameters were by default: w =1, b = 1000, j = 1250, s = 25, model = monoexponential. Seed point and waypoint

masks, based upon the warped atlas, were defined in the SW images to extract the following white mater tracts: the medial lemniscus (ML) projecting into the ventralis posterior lateralis pars caudalis (VPLc) nucleus of thalamus, the superior cerebellar peduncle (SCP) projecting into ventralis posterior lateralis pars oralis (VPLo) nucleus of thalamus, and the pallidofugal (PF) tract projecting into ventralis lateralis pars oralis (VLo) and ventralis anterior (VA) nuclei of thalamus [322]. To estimate the ML tract, seed points were placed in the ML representation of the caudal pons, and a waypoint was introduced as the entire region of the thalamus anterior to the pulvinar. Similarly, the SCP tract was extracted by placing seed points in the posterior pons, with waypoints at the decussation of SCP, and the entire thalamus. Two subjects (M5 and M7) required an additional seed point in the red nucleus. The PF tract was reconstructed using masks over the entire globus pallidus interna (GPi) with a waypoint in the thalamus. These masks were transformed into DWI space using the previously calculated transformation and were used for computing the probabilistic tractography (*probtrackx*, number of samples: 5000, curvature threshold: 0.2, number of steps: 2000). Once completed, the resulting tracts were inversely transformed back into SWI space for 3D visualization using the biomedical computer aided design software, Amira.

2.3.4 Evaluation of Atlas Warping and Diffusion Tensor Imaging

2.3.4.1 **Electrophysiological Mapping**

Electrophysiological recordings in the thalamus were performed in subject 4, as described previously [169]. Briefly, a 19-mm diameter cranial window was made over the right hemisphere close to the midline, keeping the dura intact. A sagittal recording chamber (Crist Instruments) was attached over this cranial window to provide microelectrode access to the ventral nuclei of thalamus. Reconstructed volumes of VPLo and VPLc from the lofted atlas deformation process were imported into a surgical navigation software, Monkey Cicerone [241], to guide the electrophysiological mapping of the ventral nuclei of thalamus. A post-operative CT scan was co-registered manually to the MRI in Monkey Cicerone using linear translation and rotation so that microelectrode recording locations

could be viewed in the context of reconstructed thalamic nuclei. Single channel tungsten microelectrodes (145-250 µm/diameter) were acutely inserted through the ventral nuclei of thalamus in increments of 10 µm, and electrophysiological spike recordings were performed along each track (n=5 tracks). Neuronal responses to passive manipulation [169] and low-threshold microstimulation [323] were used to identify regions of VPLo, while responses to tactile brushing of the limbs were used to identify regions of VPLc.

2.3.4.2 **Blockface Tissue Sectioning**

At the conclusion of the study, subjects 5 and 6 were deeply anesthetized and euthanized (sodium pentobarbital, 100 mg/kg, i.v.). Transcardial perfusion of room temperature phosphate buffered saline (PBS, pH 7.4) occurred at 50 ml/min for 40 min followed by perfusion of 4% paraformaldehyde in PBS at 4°C at the same rate for 20 min. The brain was post-fixed in PFA for 4 hours at 4°C then placed in 15% sucrose in PBS at 4°C for 1-3 days in order to cryoprotect. Sections, which were 50 µm thick, were cut in the coronal direction using a freezing microtome. During sectioning, serial images were acquired from a fixed distance using a Canon EOS Rebel T3i with EF-S 18-55mm IS II lens. Pitch (dorsal-ventral) and yaw (medial-lateral) angles from the AC-PC line were 17.59° and 4.3° for subject 5 and 6.85° and 1.72° for subject 6. Image resolution was approximately 62x62 µm.

2.4 Results

2.4.1 Visualization of Thalamus using SWI at 7T

2.4.1.1 **Hypointensity in the Medial and Posterior Thalamus**

SWI intensity was normalized to the AC image intensity in each subject so as to mitigate potential variations in MRI scanner sensitivity amongst subjects (see section 3.1.2). Image intensity was then compared between and within the thalamic nuclei by superimposing the nonlinearly deformed atlas onto the corresponding susceptibility-weighted images (Fig. 7). Using this method, several regions of thalamus, especially in

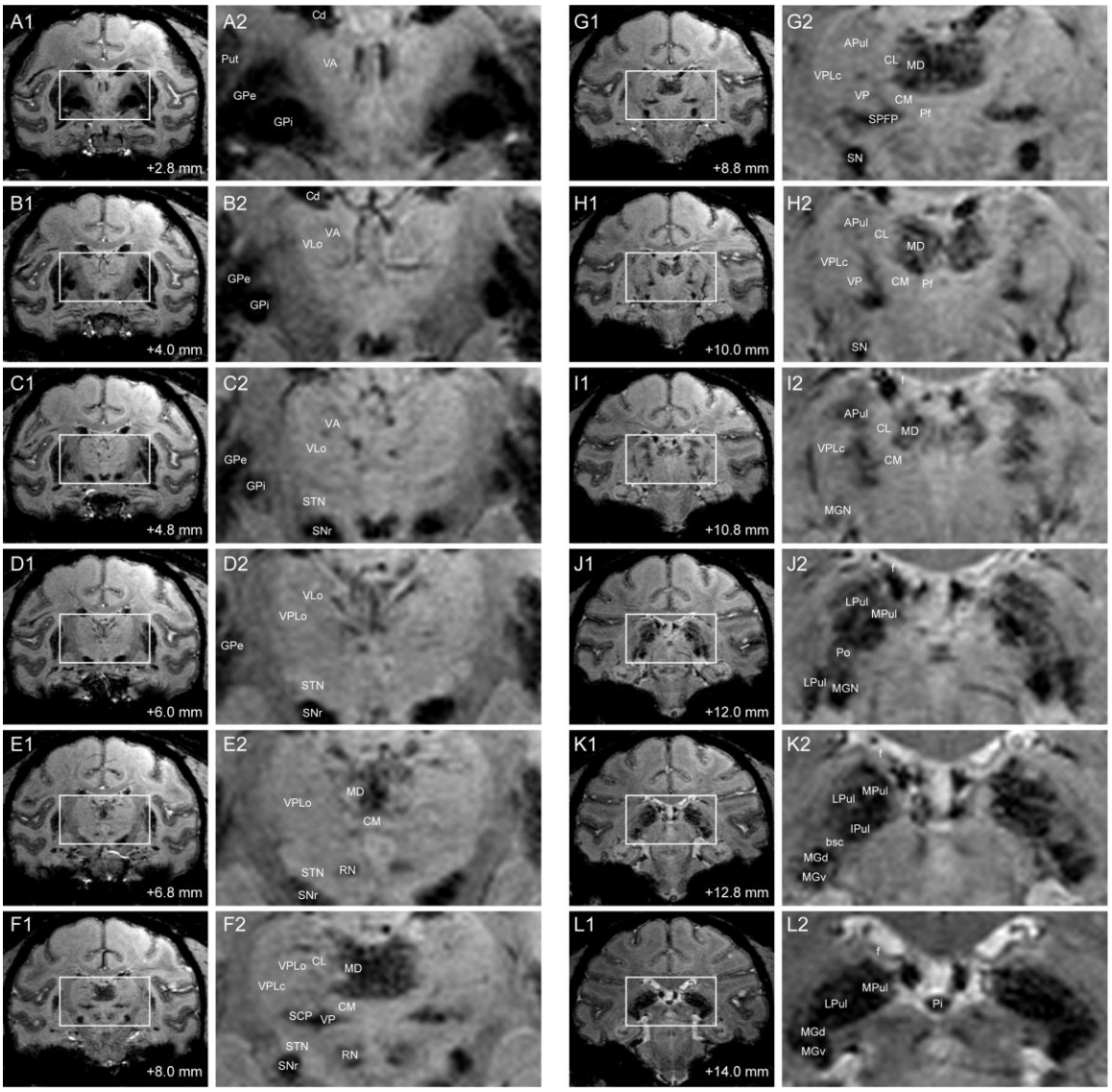

Figure 7. SWI of coronal slices through thalamus in Subject 2
Distance demarcations are relative to the midline crossing of the anterior commissure. (APul: anterior pulvinar, bsc: brachium of the superior colliculus, Cd: caudate nucleus, CL: central lateral nucleus of thalamus, CM: centre médian nucleus of thalamus, f: fornix, GPe: globus pallidus externus, GPi: globus pallidus internus, IPul: inferior pulvinar, MGd: dorsal medial geniculate nucleus, MGv: ventral medial geniculate nucleus, MPul: medial pulvinar, LPul: lateral pulvinar, Pf: parafascicular nucleus, Pi: pineal gland, Po: posterior thalamic nuclear group, Put: putamen, RN: red nucleus, SPFP: parvocellular part of the sub-parafascicular nucleus, STN: subthalamic nucleus)

the posterior portion of thalamus, were found to exhibit increased contrast relative to other regions of thalamus and regions external to thalamus. We tested for a significant difference in normalized SWI intensity between anterior and posterior thalamic nuclei. We grouped pixel values from VA and VLo together into one group and those from

pulvinar and medial geniculate nucleus (MGN) together into another group. We performed two-sample t-test between the normalized intensity values between the two groups and found that the difference was significant ($p = 3.67\times 10^{-13}$). Posterior thalamic nuclei including the pulvinar and MGN exhibited hypointensity in the susceptibility-weighted images, which in some subjects showed further demarcations of subregions within each nucleus (Fig. 7, I-L). The dorsal and ventral aspects of the anterior pulvinar were visible as clustered bands of hypointense regions that extended along the dorsomedial to ventrolateral plane. The anterior pulvinar was bordered by the relatively hyperintense CL nucleus on its medial border, the VPLc nucleus on its lateral border, and the posterior oralis (PO) nucleus on its ventral border. The PO nucleus was further demarcated by the brachium of the superior colliculus (bsc), which bisects the pulvinar from the MGN (Fig. 7, K2). Regions within the MD nucleus also exhibited hypointense contrast relative to the centre median (CM) nucleus on its ventral border, the CL nucleus on its lateral border, and the paraventricular and habenular nuclei on the dorsal border (Fig. 7, E-I). Additionally, the putative medial (magnocellular) division of the MD nucleus exhibited greater hypointensity than the lateral division, with the latter exhibiting finger-like projections extending into the CL nucleus. The ventral posterior nucleus, which lies ventrolateral to the CM nucleus, also exhibited hypointensity that spread medial into the ventral medial nucleus, lateral into the ventral posterior inferior nucleus, and dorsolateral between the CM nucleus and the VPLc (Fig. 7, F-H). However, there was relatively little contrast evident between the other ventral nuclei, albeit for a clear demarcation by the relatively hypointense internal capsule on the lateral border and the MD nucleus on the medial border.

2.4.1.2 **Age-Dependent Normalized Image Intensity**

The contours of pulvinar, medial geniculate nucleus (MGN), VPLc, VPLo, MD, VLo, and VA were segmented and the mean image intensity for each nucleus was calculated by averaging all pixels within relevant contours. The intensity values for seven thalamic nuclei were analyzed and compared amongst all seven subjects, with the images normalized by the subject-specific image intensity of the midline AC. The AC tract was

	VLo	MD	VPLo	VPLc	Pulvinar	MGN	LGN
r	-0.29	-0.59	-0.38	-0.8	-0.74	-0.92	-0.55
p	0.5251	0.1677	0.3973	0.0324	0.0484	0.0035	0.1987

Table 3. Age-related intensity correlations
Pearson correlation coefficient / p-value (df = 5, p<0.05)

	Subject 1	Subject 2	Subject 3	Subject 4	Subject 5	Subject 6	Subject 7
Pulvinar	0.78/0.35	0.52/0.23	1.55/0.26	0.81/0.34	1.05/0.19	1.31/0.23	1.42/0.24
MGN	0.65/0.23	0.57/0.19	1.11/0.17	0.76/0.24	1.09/0.17	1.14/0.28	1.28/0.28
VPLc	1.08/0.22	0.82/0.14	1.30/0.19	1.07/0.14	1.14/0.09	1.22/0.22	1.38/0.18
VPLo	1.29/0.16	0.98/0.11	1.70/0.16	1.32/0.15	1.21/0.11	1.21/0.28	1.45/0.19
MD	1.26/0.32	0.74/0.23	1.68/0.24	1.12/0.29	1.22/0.15	1.31/0.29	1.54/0.21
VLo	1.37/0.11	0.92/0.11	1.67/0.24	1.36/0.19	1.14/0.11	1.40/0.30	1.34/0.24
VA	1.34/0.14	0.90/0.12	1.65/0.20	1.36/0.15	1.10/0.13	1.44/0.25	1.35/0.26

Table 4. Normalized SWI intensity values
(Mean/Standard Deviation)

chosen for normalization since its intensity did not correlate with age (linear regression analysis, $r^2 = 0.0456$, slope = 0.4477, p = 0.64567). AC intensity was calculated from the widest coronal strip of the AC in each subject (Fig. 8A). Several nuclei exhibited trends of increased hypointensity level with age. Correlation analysis (Pearson correlation, df = 5, $p<0.05$) showed that the normalized mean intensity for nuclei in the posterior half of thalamus had a statistically significant dependence on age (VPLc: $r = -0.8$, Pulvinar: $r = -0.74$, and MGN: $r = -0.92$) (Fig. 8B, Table 3). However, this was not the case for the anterior portion of thalamus including the ventral nuclei and MD.

2.4.2 Probabilistic Tractography of Ascending Tracts to Ventral Nuclei in Thalamus

While most regions of thalamus exhibited contrast sufficient to segment manually or to guide the placement of markers for the nonlinear atlas deformation algorithm, the internal borders of the ventral nuclei were not clearly distinguishable from the SWI. In this case, fiber tractography was used to estimate the ventral nuclei demarcations based upon thalamic afferents coursing along the ML (to VPLc), SCP (to VPLo), and GP (to VLo/VA) in three subjects (subjects 4, 5, and 7). The resulting fiber tracts were spatially co-registered to the SWI data and the reconstructed thalamic nuclei. In the case of the ML and PF tracts, the fiber tractography was able to identify the ventral entry point to VPLc

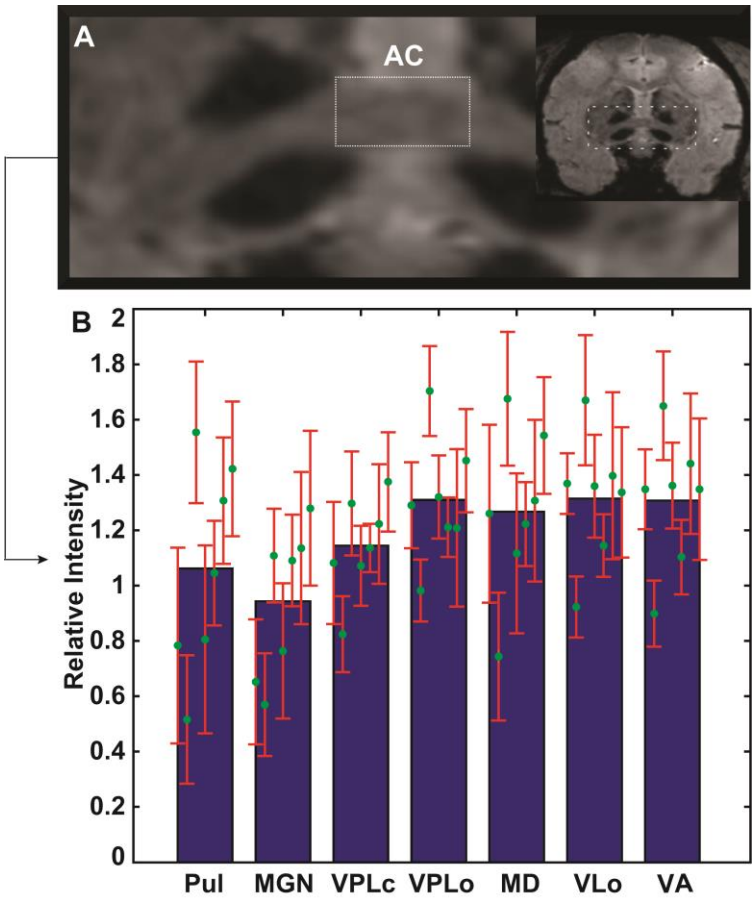

Figure 8. Age-related changes in thalamic image intensity with SWI
(A) Anterior commissure in each subject was used to normalize susceptibility-weighted image intensity for each subject. **(B)** Normalized mean intensity of thalamic nuclei (n=7 subjects). Green circles and red error bars mark the mean and standard deviation of normalized intensity for each subject. The mean and standard deviation values for each structure are arranged from left to right from oldest to youngest age.

and VLo in all three subjects (Fig. 9). In the case of the SCP tract, the tractography reconstructions were found to project into or just ventrally adjacent to the VPLo.

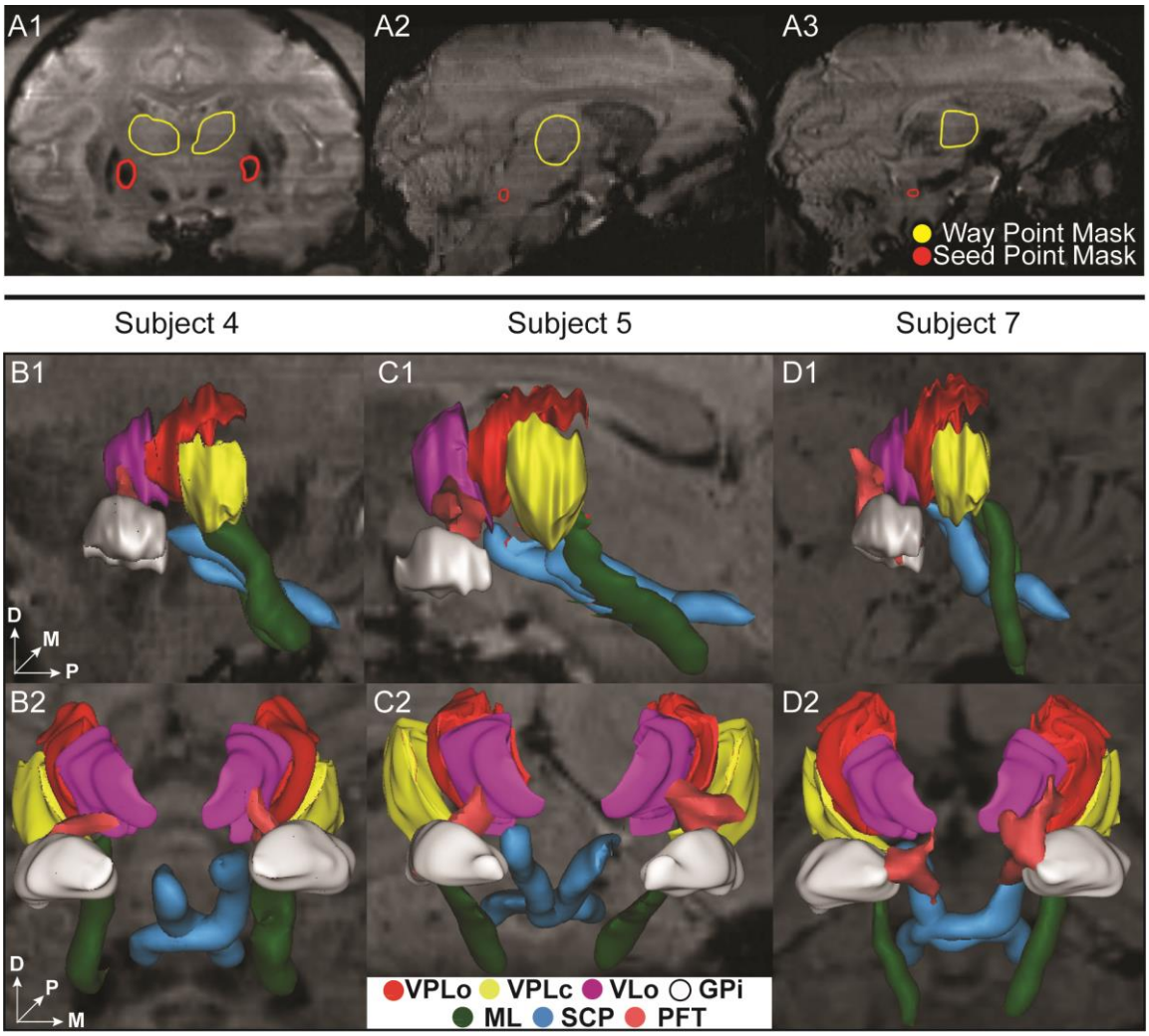

Figure 9. Ascending fiber tractography to the ventral nuclei of thalamus in three subjects
(A1-A3) Examples of seed point (red) and waypoint (yellow) masks used in the probabilistic tractography. (**A1)** Seed point mask in GPi and waypoint mask in thalamus for reconstruction of the PF tract. (**A2)** Seed point mask of SCP in brainstem and waypoint mask in thalamus for reconstruction of SCP. **(A3)** Seed point mask of ML in brainstem and waypoint mask in thalamus for reconstruction of ML. (**B-D)** Bilateral probabilistic fiber tractography reconstructions for the PF, SCP, and ML tracts and their corresponding thalamic nuclei. The nuclei of the oral (VPLo) and caudal (VPLc) parts of the ventral posterolateral nucleus are reconstructed from series of warped atlas plates. A: anterior, V: ventral, M: medial, D: dorsal, P: posterior.

2.4.3 Evaluation of Nuclei Reconstructions

2.4.3.1 Electrophysiological Microelectrode Mapping of Ventral Nuclei in Thalamus

To validate borders between the ventral nuclei, microelectrode spike recordings were performed through a cranial chamber chronically implanted in subject 4.

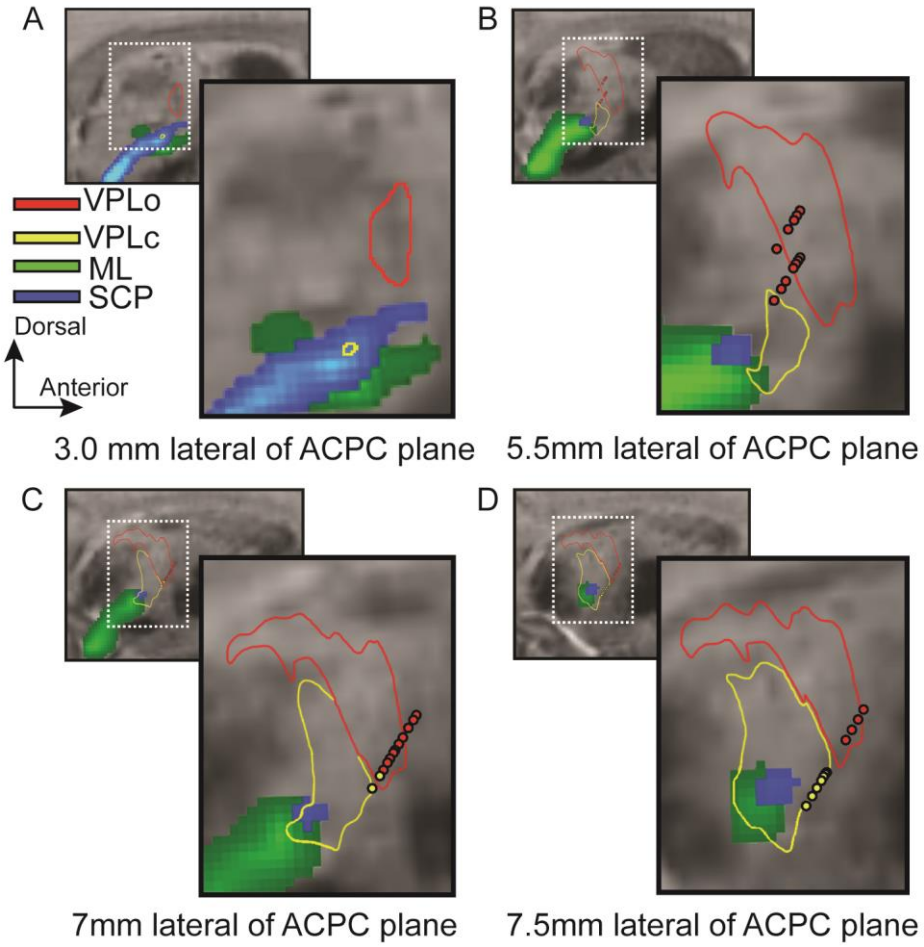

Figure 10. Superposition of microelectrode recordings with reconstructed thalamic nuclei and probabilistic tractography (subject 4)
Red and yellow spheres are the locations of VPLo (oral part of the ventral posterolateral nucleus of thalamus) and VPLc (caudal part of the ventral posterolateral nucleus of thalamus) cells, respectively. Red and yellow contours denote the boundaries of VPLo and VPLc, respectively, as defined by the warped brain atlas process. The resultant probabilistic tractography of ML (green) and SCP (blue) are also superimposed on each slice.

Electrophysiologically identified VPLo and VPLc cells matched closely with the segmented contours and probabilistic tractography predictions across multiple sagittal planes (Fig. 10). Small discrepancies at the border regions were observed, possibly due to the spatial spread of the recorded electric fields or slight inaccuracies in the atlas deformation process.

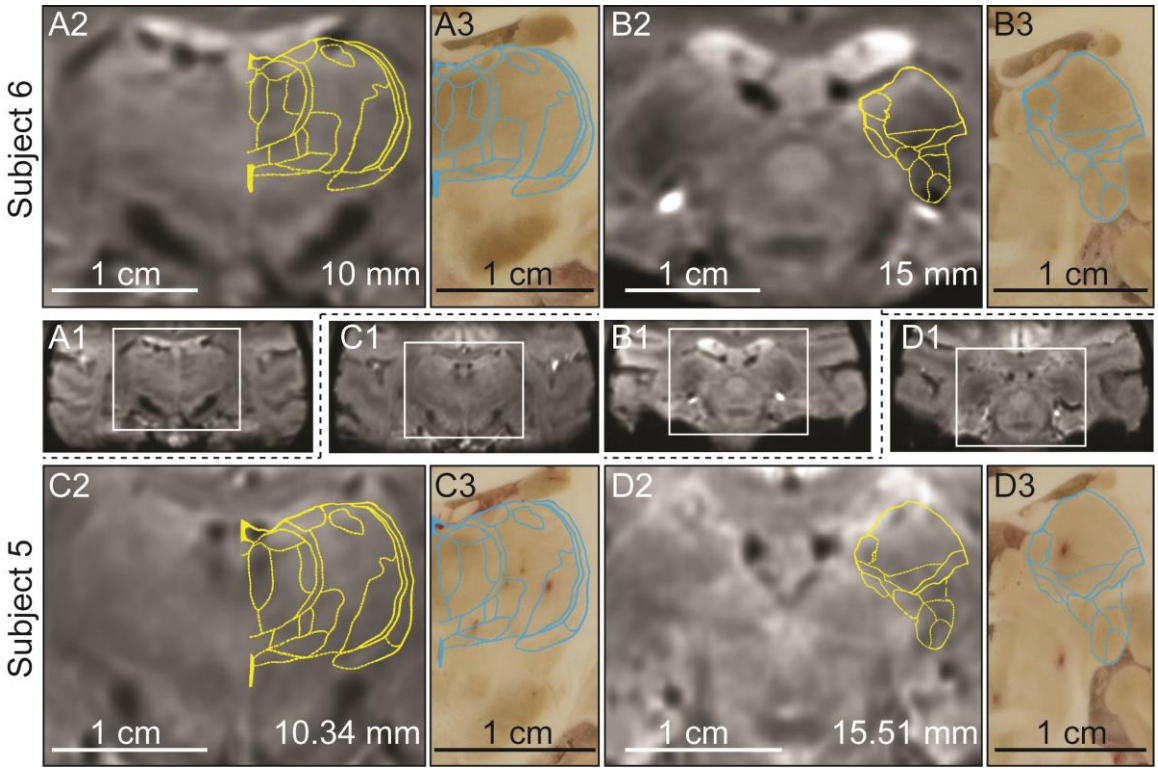

Figure 11. Relationship between hypointensity in the in vivo SWI and ex vivo blockface sectioned thalamic nuclei in the same non-human primates (subjects 5 and 6)
(A1-D1) Full brain coronal plane SWI with boxed region enlarged in A2-D2. **(A2/C2)** SWI of the thalamus in subjects 6 and 5 at 10.34mm and 10mm posterior to AC, respectively. **(A3/C3)** Blockface tissue sections aligned with the images shown in A2/C2. **(B2/D2)** SWI of the thalamus in subjects 6 and 5 at 15mm and 15.51mm posterior to AC, respectively. **(B3/D3)** Blockface tissue sections aligned with images shown in B2/D2. The yellow and blue contours show the SWI-deformed atlas plates overlaid on top of the SWI and blockface tissue sections, respectively.

2.4.3.2 **Tissue Sectioning-Based Identification of Hypointense Thalamic Nuclei in SWI**

Post-mortem blockface tissue sectioning was performed on subjects 5 and 6 to further validate that the atlas-based warping algorithm results were consistent with anatomical features observed in the *ex vivo* sectioned brain tissue (Fig. 11). Two representative sections at the level of the MD/VPLo/VPLc and the Pulvinar/MGN were found in each subject. The MD (Fig. 11, A2, C2, A3, C3), pulvinar and MGN (Fig. 11, B2, D2, B3, D3) all appeared hypointense in both the susceptibility-weighted images as well as the tissue section images. Atlas plates were warped to the susceptibility-weighted images and the

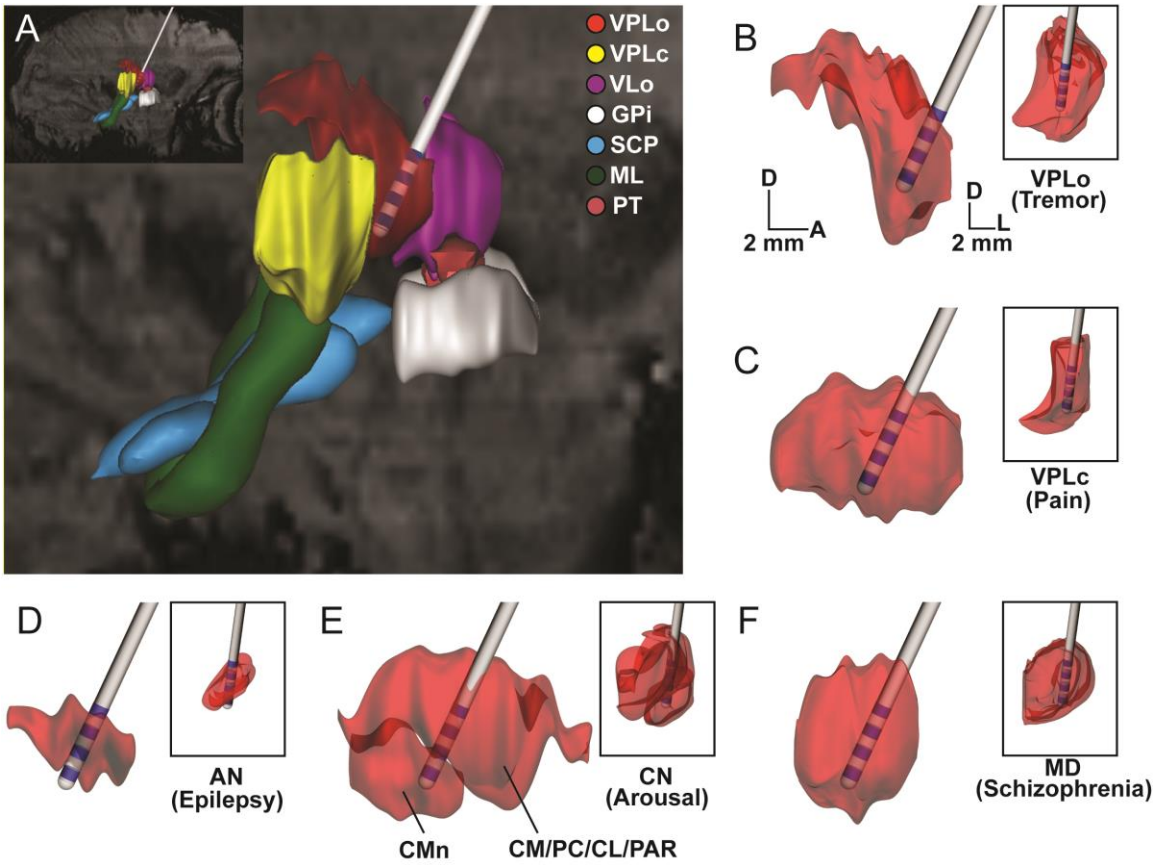

Figure 12. Subject-specific reconstructions of thalamic nuclei for DBS targeting
Scaled-down version of the clinical DBS lead shown in the context of thalamic nuclei reconstructed from the susceptibility-weighted images of Subject 4. **(A)** Sagittal view of reconstructed thalamic volumes, afferent fibers, and DBS lead for targeting VPLo to treat tremor disorders. **(B–F)** Large images show sagittal view of thalamic nuclei. Inset shows the coronal view of the same nucleus. Large and small scale bars are for sagittal and coronal images, respectively. D: dorsal, A: anterior, L: lateral.

resulting deformed plates were then linearly scaled (maintaining aspect ratio), slightly rotated (less than 2° in either counterclockwise or clockwise directions) and overlaid onto the matching tissue section images. The deformed atlas plates were found to align well with their matching tissue sections, especially in the hypointense pulvinar, MGN, and medial nuclei of the MD (Fig. 11A3, B3, C3, D3).

2.5 Discussion

In vivo visualization and demarcation of individual thalamic nuclei is critical for many preclinical and clinical stereotactic neurosurgical procedures targeting thalamus, including implantation of DBS leads (Fig. 12). In this study, we show the utility of an *in*

vivo multimodal imaging approach using high field 7T SWI and DWI to segment and identify nuclei within the NHP thalamus. The results were subsequently validated using electrophysiological recordings and post-mortem tissue sectioning.

2.5.1 Atlas-Based Reconstructions

A rich array of 2D or 3D registration methods exist to deform a brain atlas to MR images to identify structures not clearly visible on MR images [292]. Most 3D methods work to deform a source surface to fit a target surface by either minimizing difference in distance or energy of the deformation [281, 324-329]. This can be achieved by extracting ventricular and cortical surfaces from MR images and matching them to corresponding surfaces on a 3D atlas. The computed deformation based on matching these surfaces is then propagated throughout the entire volume. Although such methods may be appropriate for matching cortical surfaces, they essentially relegate the deformation of deep structures such as the thalamus to be a by-product of cortical and ventricular deformation [324]. One 2D solution well suited for atlas-based localization of structures lacking contrast in MR images involves the MLS method embodying the idea of ‘as rigid as possible’ image deformation [330, 331] which minimizes the amount of local scaling and shearing once certain constraints are satisfied. This more conservative approach incorporates the most reliable anatomical information contained in the MRI for the deformation process, and does not require defining features of an image and guessing for model parameters [327, 332]. Instead, the process requires setting a set of identical control points between the atlas and MR image to guide the deformation process. When coupled with high field imaging approaches with higher spatial resolution [223], the user can simply crop out all but the region of interest (e.g. thalamus) and perform a very local deformation. This approach is computationally efficient on top of an already fast and easy-to-implement algorithm. The result of the deformation is smooth and more realistic than the popular thin-plate spline approach [313, 333]. For these reasons we implemented the MLS method to take advantage of the increased contrast within thalamus at 7T to help further demarcate borders between thalamic nuclei.

2.5.2 Susceptibility-Weighted Imaging of Thalamus

Analysis of the SWI data across the seven subjects showed: (1) relative hypointensity in internal capsule compared with the ventral nuclei of thalamus, (2) thalamic regions of hypointensity were most notably in the posterior half of thalamus and in the medial dorsal nucleus, and (3) positive correlations of image hypointensity in the posterior half of thalamus with age. SWI is sensitive to a difference in magnetic susceptibility in tissues and can be used to measure iron content [299]. Regions with higher iron content exhibit larger, linearly correlated phase shifts and will appear hypointense in the SWI data [305, 306]. Iron in the form of ferritin and hemosiderin is stored in oligodendrocytes [300-303, 334] and has been found in relatively rich deposits in certain brain regions [304]. Consistent with our results in the posterior half of thalamus, brain iron has been shown to accumulate with age [335], and an elevation in iron concentration in certain regions is known to occur in neurodegenerative diseases, including for example the substantia nigra and GP in Parkinson's disease [336-339] and hippocampus in Alzheimer's disease and Parkinson's disease [340, 341]. In order to detect potential outliers in our data, we calculated Cook's distance [342] for each nuclei using the age of the seven subjects as the independent variable and the average normalized SWI intensity values as the explanatory variable. A data point is considered an outlier if its Cook's distance value exceeded three times the average Cook's distance across all seven subjects (for a given nucleus). This analysis indicated that subject 2 is an outlier in all nuclei except pulvinar and MGN. These two posterior also demonstrated statistical significance in correlation between normalized SWI intensity and age. It should also be noted that SWI is not exclusive in its ability to demarcate nuclei within thalamus, and other approaches including low-field T1 and T2-weighted imaging have also been used [269, 343].

2.5.3 Cross-Validation of the Computationally Segmented Thalamic Nuclei Derived from SWI

In this study, we applied multiple tools to cross-validate the segmentation of thalamic nuclei based on 7T SWI data, including probabilistic fiber tractography,

electrophysiology, and *ex vivo* blockface tissue sectioning. This multi-modal approach was feasible given the animal model preparation used.

2.5.4 **Demarcation of the Ventral Nuclei using Probabilistic Tractography**

Previous studies have found considerable variability in the location of generic atlas-based target points in thalamic nuclei in relation to major neighboring fiber tracts in individual patients, suggesting the need for individualized methods that can target structures not directly visible on conventional MRI [344]. One approach to subject-specific mapping of thalamic nuclei includes probabilistic fiber tractography for reconstructing white matter pathways [345] into the thalamus, including those originating from GPi (PF tracts) [223] and cortex [230]. Here, we extend these studies showing nearly complete demarcation of the ventral nuclei utilizing ascending ML, SCP, and PF fiber tracts. This approach provided important data to verify the atlas plate to SWI slice alignment for the anterior portion of the thalamus. The trajectories of the fiber tracts projecting into the subject-specific ventral nuclei reconstructions (i.e. VPLc, VPLo, and VLo/VA) were consistent across the three subjects.

2.5.5 **Electrophysiological Cross-Validation**

The accuracy of the warping process was also verified by *in vivo* electrophysiological recording in the ventral thalamic nuclei. Cells were categorized based on their responsiveness to proprioceptive and microstimulation excitable (VPLo) and tactile (VPLc) input. While the locations of these cell types aligned well with both the deformed atlas and fiber tractography results, there were small discrepancies at the border between the nuclei. In this case, additional deformation methods can be applied to further reduce these small discrepancies [346].

2.5.6 **Blockface Tissue Sectioning Cross-Validation**

To avoid deformation of the tissue during histological processing, we chose to take blockface photographs of the brain during sectioning. Two types of deformations may still occur during the preparation of brain sections: 3D deformation caused by extraction

of the brain from the skull and 2D deformation caused by the sectioning process [347]. The three-dimensional deformation stems from loss of cerebrospinal fluid and blood and subsequent mechanical effects from gravity. Two-dimensional deformation results from shearing and tearing during cutting of the brain tissue and shrinkage due to changes in tissue temperature and hydration. Natural shade differences of frozen brain tissue were found to be sufficient for identifying many of the major thalamic nuclei. Based on this analysis, the relative positions of the thalamic nuclei on the blockface photographs resulted in consistent registration, where only linear scaling (no change in aspect ratio) and slight rotations (less than 1°) were needed when overlaying the SWI-warped atlas plates onto the blockface sections. This registration was most visible for MD, pulvinar, and MGN borders with their respective hypointense regions in the MR images. In addition, the borders of the thalamus in the medial/lateral and dorsal/ventral directions also aligned well. The tissue sectioning validation demonstrated that the image warping approach could in the future utilize contrast not only between gray/white matter boundaries, but also between different thalamic nuclei to guide accurate segmentation of nuclei within thalamus.

2.5.7 **Limitations**

There are several points to consider in the interpretation of the results. First, the dataset included six females and only one young male rhesus macaque. These subjects were selected in part because their cranial musculature was minimal allowing for the receiver coils to be placed closer to the brain [227]. Another limitation is the use of an atlas that is particular to one NHP, along with its own nomenclature and criteria of demarcation [348]. However, the approach itself is one that can be extended to other brain atlases based on cytoarchitectonic features. While the fiber tractography and warping methodology results aligned reasonably well with the histological blockface images and electrophysiological results, there was some degree of misalignment especially in the caudate and substantia nigra regions with the histological images. This registration error likely stemmed in part from nonlinear deformations that occurred as part of the perfusion, fixation, and freezing processes. Further, the histological coronal sections were sliced at

a slight pitch and yaw from the AC-PC line. Future studies that utilize 3D rendering of histology-based fiber tracts would be useful to further validate tractography and atlas warping methods. Lastly, we are limited by the relatively small sample size in the number of subjects with 7T SWI data. The analysis of correlation between normalized SWI intensity and subject age would benefit from a larger sample size. However, we are confident based on the outlier detection analysis that the posterior nuclei show significant correlation between average SWI intensity and age.

2.5.8 **Applications to DBS Targeting**

The multimodal imaging approaches shown here provided enhanced visualization of thalamic nuclei, which can be critical for preclinical and clinical stereotactic neurosurgery procedures [222] (Fig. 12). Defining thalamic nuclei through non-invasive means is especially important given that most nuclei have been targets for deep brain stimulation therapies and the precise locations, shapes, and sizes of these nuclei vary amongst subjects. In this way, the combined use of imaging techniques described in this study can assist in neurosurgical navigation of DBS targets in a given subject [349-351]. Additionally, the segmented nuclei reconstructions can also aid in the development of more accurate computational models of DBS [161, 201, 213, 215] to retrospectively quantify the neural pathways modulated by thalamic DBS therapy [352] or prospectively predict the stimulation settings necessary to target those pathways on a subject-specific basis [353].

2.6 Acknowledgements

This study was supported by the College of Science and Engineering, the Institute for Translational Neuroscience at the University of Minnesota, and an NIH grant (NS081118). We thank Allison Connolly and Filippo Agnesi for helpful discussion.

Chapter 3

Programming Algorithms for Deep Brain Stimulation Electrode Arrays

This chapter was reprinted with permission from IEEE.

YiZi Xiao*, Edgar Peña* and Matthew D. Johnson, "Theoretical Optimization of Stimulation Strategies for a Directionally Segmented Deep Brain Stimulation Electrode Array," *IEEE Transactions on Biomedical Engineering,* 63.2 (2016): p.359-371.

3.1 Overview

3.1.1 Objective

Programming deep brain stimulation (DBS) systems currently involves a clinician manually sweeping through a range of stimulus parameter settings to identify the setting that delivers the most robust therapy for a patient. With the advent of DBS arrays with a higher number and density of electrode sites, this trial and error process will become unmanageable in a clinical setting. Here, we describe a computationally efficient, model-based algorithm to identify an electrode configuration that will most strongly activate tissue within a volume of interest.

3.1.2 Approach

The cerebellar-receiving area of motor thalamus, the target for treating essential tremor with DBS, was rendered from imaging data and discretized into grid points aligned in approximate afferent and efferent axonal pathway orientations. A finite-element model (FEM) was constructed to simulate the volumetric tissue voltage during DBS. We leveraged the principle of voltage superposition to formulate a convex optimization-based approach to maximize activating function (AF) values at each grid point (via three different criteria), hence increasing the overall probability of action potential initiation and neuronal entrainment within the target volume.

3.1.3 Main Results

The algorithm achieved global optima of AF values within several seconds both efferent and afferent pathways. The optimal electrode configuration and resulting AF values differed across each optimization criteria and between axonal orientations.

3.1.4 Significance

This approach only required a set of FEM simulations equal to the number of DBS array electrodes, and can readily accommodate anisotropic/inhomogeneous tissue conductances or other axonal orientations. Together, the algorithm enabled efficient, flexible determination of a computationally optimal electrode configuration for DBS electrode arrays.

3.2 Background

Deep brain stimulation (DBS) is an effective surgical procedure for the treatment of a number of neurological and neuropsychiatric disorders, including medication-refractory Parkinson's disease (PD), essential tremor (ET), dystonia, and severe obsessive compulsive disorder [354]. The procedure involves the placement of a lead of electrodes into a precise brain region to modulate abnormal neuronal activity with various forms of pulsatile electrical stimulation. Successful treatment is characterized by both symptom suppression and lack of side-effects. Such success requires accurate lead placement as

well as spatially targeted stimulation settings to avoid activating regions that elicit, for example, adverse motor [355], sensory [178], and cognitive [356] side-effects for the patient. Traditional designs of the DBS lead implant (for example, the Medtronic model 3387/3389) use four cylindrical electrodes to deliver current in an omnidirectional fashion around the lead. A major improvement to this existing design would be enabling one to direct or steer current both along and around the DBS lead. This feature would be especially useful in cases of off-target DBS implants [215], [357] and for small or complex-shaped brain targets, such as the pedunculopontine nucleus [358], [213] for treating freezing of gait in patients with PD.

Several designs for high-density directionally segmented DBS arrays (DBSAs) with circumferentially-segmented electrodes have been advanced in recent years through computational studies [215], [213], [359] and *in-vivo* studies in non-human primates (NHPs) [357] and humans [360], [238], [361]. Here, we modeled DBS leads with 32 oval shaped electrodes arranged in 8 rows of 4 electrodes each, radially separated by 90° [357], [215], [213]. The surface areas of the DBSA electrodes were a fraction of the size of cylindrical electrodes found on commercial leads and have potential for improving the spatial resolution of targeting modulation of neuronal activity within the brain to improve overall therapy.

The safety and efficacy of current shaping technology has recently been investigated clinically using leads with annular [361] and circumferentially-segmented [360], [238] designs. In the latter case, therapeutic current thresholds were 43% lower with a radially directed stimulation scheme compared to the omnidirectional scheme [360]. Further, the ‘therapeutic window’ (difference in current thresholds to produce a meaningful symptom suppression and to sustain a side-effect) was the widest when using radially directed stimulation [360], [238]. Current shaping along the length of the DBS lead in patients with ET has also been shown to better alleviate stimulation-induced dysarthria while preserving tremor control [361]. The challenge with such current shaping approaches, however, especially in the case of DBSAs, is the number of possible electrode configurations and size of the stimulation amplitude, frequency, and pulse width parameter space [215].

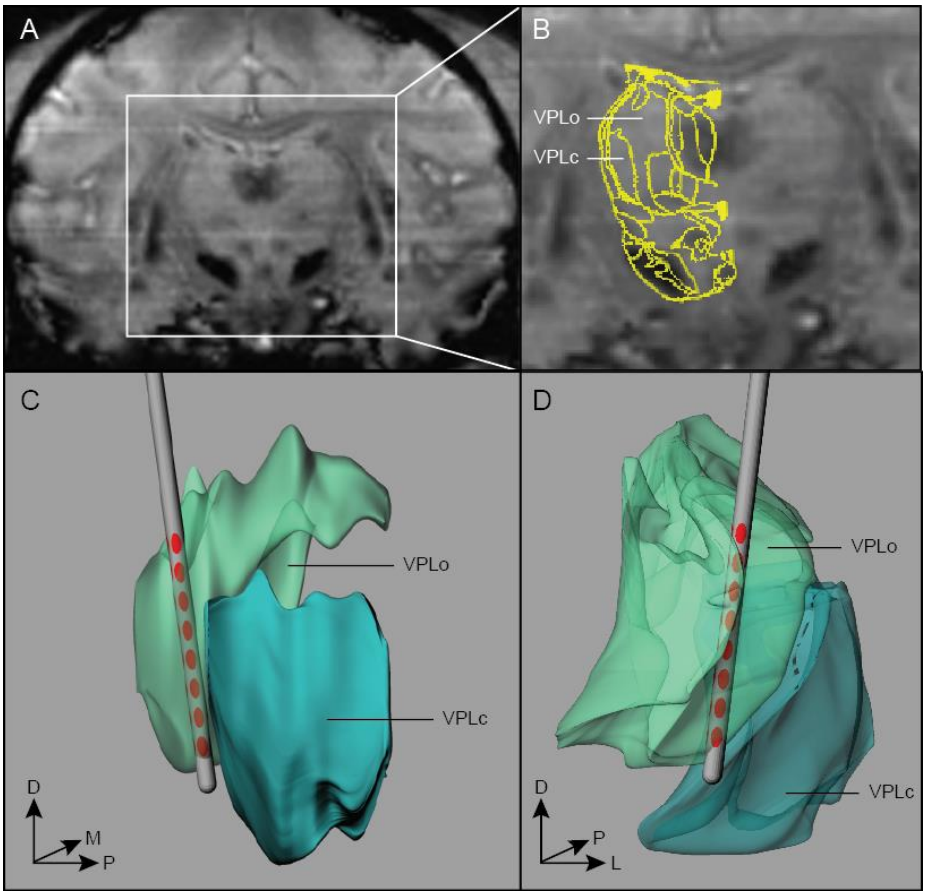

Figure 13. Three-dimensional thalamic nuclei reconstructions
Three-dimensional thalamic nuclei reconstructions were generated from **(A)** NHP susceptibility-weighted imaging and **(B)** warped brain atlas overlays. **(C)** Sagittal and **(D)** coronal view of the reconstructed VPLo and VPLc with the implanted DBSA.

Optimal programming of a DBSA has potential to improve treatment benefit and expedite the programming process. The current framework for programming the stimulation settings of DBS leads with four annular electrodes typically begins with evaluation of each contact using monopolar stimulation at fixed frequencies and pulse widths [362], [363]. The setting that requires the lowest stimulation amplitude to maximize therapy and/or has the widest therapeutic window is set for chronic stimulation unless persistent adverse side-effects are observed, in which case bipolar or multipolar stimulation configurations may be explored by combining the chosen contact with adjacent contact(s). The programming process can be time consuming [193], especially in cases when low-threshold side-effects appear. Furthermore, relying on direct patient

feedback for programming may not be feasible for disorders in which the therapeutic benefits may not emerge for weeks to months after starting stimulation [194], [195]. The efficacy of this programming method is also influenced by other factors, such as the intuition and experience of the DBS programmer, as well as the time allotted to each patient [196]. To explore the vast parameter space of the DBSA using this manual method of programming would not be feasible, since each additional electrode would prolong programming time in a nonlinear fashion and also pose a steeper learning curve. In addition, this method of programming four-electrode leads may underutilize the full potential of the DBSA to deliver optimal stimulation through a combination of active electrodes [364], [234]. Alternative programming approaches have been proposed aimed at increasing the efficiency of the process. One such approach uses a probabilistic efficacy atlas derived from intraoperative microstimulation response data [365]. The atlas is nonlinearly warped onto the pre-operative magnetic resonance imaging (MRI) data (co-registered to post-operative CT) to guide programming. This approach requires substantial accumulation of intraoperative patient data which is not readily accessible to the larger neuromodulation community. In addition, individual brain anatomy can vary substantially [366] and an entirely empirical approach may not be adequate.

Another proposed method estimates the volume of tissue activated (VTA) [367], [368], [369] from a particular DBS setting by simulating an activating function [370] derived from a finite element model solution of the tissue voltages along the neuron membrane compartments during DBS. In this case, DBS lead positions within the nucleus or fiber tract are dictated by the co-registration of a patient's pre-operative magnetic resonance (MR) brain imaging with post-operative MR imaging or computed tomography scan data. The benefit of this approach is that it provides direct visualization of the neuronal pathways that are modulated for a given stimulation setting [218].

The second spatial derivative of the extracellular voltage potential, or activating function (AF), generated through the DBS lead is the driving force behind action potential initiation in neuronal processes [370] and can be used to predict the VTAs [371]. However, AF thresholds for neuronal activation depend on axon orientation and distance from the stimulation source [372]. An alternative approach is to apply the AF to

compartment neuron models [373] in a target region, which can have detailed morphologies and biophysical parameters, and then find the stimulus amplitudes to initiate an action potential [371]. Such biophysical models, usually performed in the NEURON programming environment [374], can provide additional information about neuronal activation that AF alone may not describe, but this process can be time consuming and computationally intensive. In order to obtain the patient-specific stimulation strategy solutions, thousands of such simulations using different electrode configurations, axon orientations and locations must be run ahead of time, and the VTA solutions must be precompiled and stored [218]. Due to the resource-intensive and time consuming nature of this approach, it may not be readily accessible to the broader research and clinical community.

In this study, we propose an algorithm that leverages the superposition of the activating function, thus requiring only a set number (equal to the number of electrodes) of anatomical FEM simulations to be run. By combining this with the principles of convex optimization, we formulate an approach that maximizes the AF values in the volume of interest. We consider three separate optimization criteria that may be used with this approach. Overall, the methods presented here bypass the need to run extensive simulations of neuronal activation, providing an automated, computationally efficient way to patient-specific programming of a DBSA implant.

3.3 Methods

3.3.1 Algorithm Overview

We constructed a computational model of motor thalamic DBS using current-controlled stimulation using non-human primate MRI data (Fig. 13). High frequency stimulation of the ventral intermediate nucleus of thalamus (Vim) in humans can suppress tremor, while persistent paresthesias is thought to emerge from activation of the adjacent sensory thalamic nucleus (ventral posterolateral nucleus of thalamus/VPL) [53]. In the non-human primate, the equivalent nuclei to Vim and VPL are the oral (VPLo) and caudal (VPLc) ventral posterior lateral nuclei of thalamus, respectively [348]. We reconstructed

Figure 14. Procedural flowchart for optimization algorithm
Three different optimization criteria (MD, QP, LP) were considered separately.

both VPLo and VPLc and modeled independent current-controlled stimulation through each DBSA electrode (n=32). Volumes were discretized into points arranged in a grid pattern, with anatomically realistic afferent and efferent fiber orientations. We show a theoretical maximum AF value for each grid point, which forms a theoretical maximum curve (Max Curve) that cannot be surpassed. We take advantage of the principle of voltage superposition to achieve AF values as close as possible to this Max Curve through the use of convex optimization algorithms (Fig. 14).

3.3.2 Reconstruction of Thalmic Nuclei

High field magnetic resonance imaging (7T, Magnex Scientific) was performed on a female rhesus macaque monkey (*macaca mulatta*) under isoflurane anesthesia at the University of Minnesota's Center for Magnetic Resonance Research using a Siemens

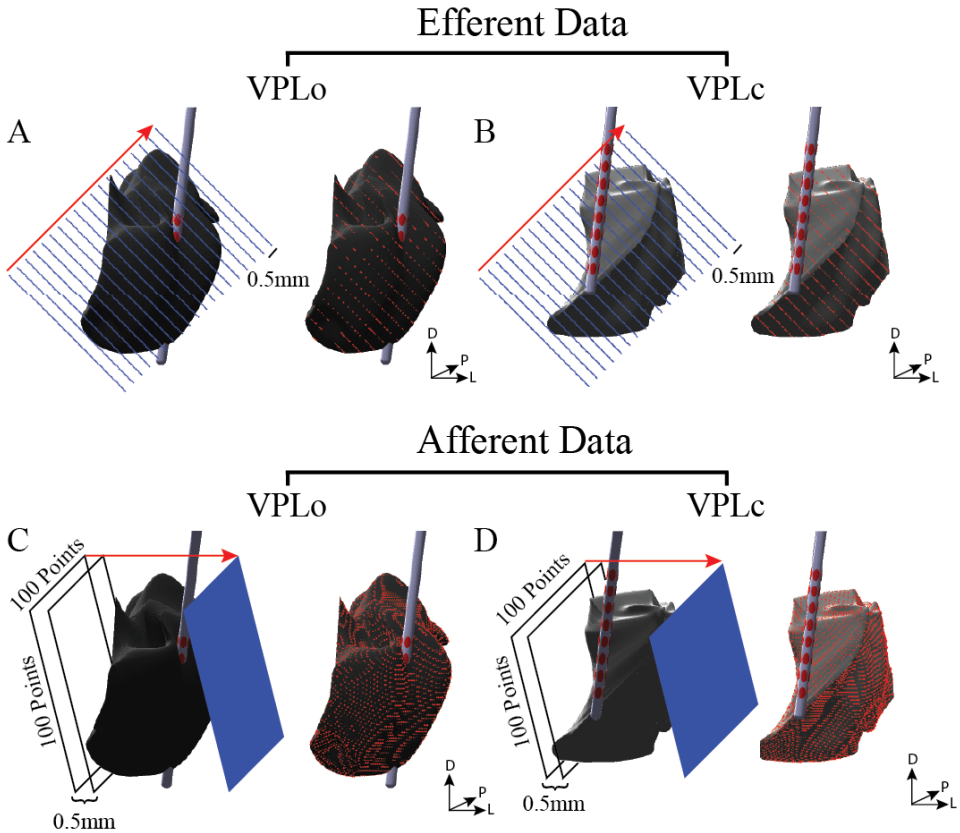

Figure 15. Discretization of thalamic volumes
The top row (**A,B**) shows the discretization process for the efferent direction while the bottom row (**C,D**) shows the process in the afferent direction. Both the VPLo and VPLc are shown in coronal orientation. In either case, the left image shows grid points arranged in serial layers spanning either volumes. The red arrow indicates the orientation of the neuronal processes. The right image shows only those grid points that fall within the volume (red points). The internodal distance between successive layers of grid points are shown. (A) and (C): VPLo. (B) and (D): VPLc.

console. All procedures were approved by the University of Minnesota's Institutional Animal Care and Use Committee and complied with United States Public Health Service policy on the humane care and use of laboratory animals. A customized head coil was developed with 16-channel transmit and 16+6 receive channels, in which 4 coils mounted on top of the subject's head and 2 ear-loop coils were added to enhance signal detection from subcortical structures [298]. Susceptibility-weighed imaging (SWI) data was acquired with a 3D flow-compensated gradient echo sequence. SWI data was aligned to the anterior commissure (AC)-posterior commissure (PC) plane (Analyze 11.0, AnalyzeDirect) and resliced into serial coronal sections with 40 coronal images spanning the thalamus. Matching plates from a rhesus macaque brain atlas [310] were nonlinearly

deformed [313], [314] to the coronal MR images, and the contours of VPLo and VPLc within each were extracted. These contours were imported into a B-spline modeling program (Rhinoceros) and arranged serially at an interval of 0.4 mm (voxel size) along the anterior-posterior direction. The contours were then lofted into 3D surfaces.

3.3.3 Finite Element Model of Stimulation through the DBSA

The DBSA (NeuroNexus, Ann Arbor, Michigan) consisted of 8 rows of 4 elliptical electrodes (semi-major axis: 0.265 mm; semi-minor axis: 0.14 mm). The lead was 0.5 mm in diameter and 40 mm in length. The angular distance between adjacent electrodes in the same row was 90° and

the distance between two adjacent rows of electrodes was 0.75 mm. A 0.1×40 mm (thickness × height), 0.18 S/m homogeneous encapsulation layer and a 100×100 mm (diameter × height), 0.3 S/m cylinder of homogeneous bulk tissue surrounded the lead [375], [376], [377]. The DBSA electrodes and insulation were assigned conductance values of 10^{6} S/m and 10^{-12} S/m, respectively. The electrode surfaces were designated as boundary current sources and the walls of the bulk tissue

cylinder were set to ground. The voltage distributions resulting from electrical stimulus perturbations were calculated via the finite element method solving Poisson's equation in COMSOL Multiphysics (v4.3b). Simulations of monopolar cathodic (-1 mA) stimulation were performed with each of the electrodes acting as the cathode (n=32).

3.3.4 Discretization of Thalamic Volumes

A 3D reconstruction of the DBSA geometry was created in Rhinoceros and placed within the VPLo close to its lateral border with VPLc such that the electrodes spanned the length of the VPLo. The trajectory of the lead was 77° above the horizontal plane and 10° from the sagittal plane [184] (Fig. 13). The electrodes were assigned indices from 1 to 32, such that the contacts facing posterior, medial, anterior, and lateral were labeled 1, 2, 3 and 4, respectively. This order of labeling was maintained in every row, with indices increasing along the vertical direction. The lead, VPLo, and VPLc were then rotated together such that the center of the first row of electrodes was consistent with the FEM

Efferent Data		
	Total Grid Points	Number of Grid Points in C matrix
VPLo	17×10^4	27173
VPLc	17×10^4	34059
Afferent Data		
	Total Grid Points	Number of Grid Points in C matrix
VPLo	11×10^4	20836
VPLc	14×10^4	25010

Table 5. Volume discretization data

model. The rotation matrix (T_{AF}) was stored for this change in a coordinate system from AC-PC to FEM model coordinates.

The afferent fiber orientations into VPLo and VPLc are about 45° from the intercommissural line in the coronal plane and 60° in the sagittal plane [322]. The efferent fiber orientation from VPLo and VPLc to cortex follows a ventral-medial to dorsal-lateral direction approximately 45° from the intercommissural plane in the coronal direction [378, 379]. At the scale of the grid spacing used in this study, the thalamus is generally considered to be an isotropic structure [377]. The surfaces of the DBSA, VPLo, and VPLc were generated in Rhinoceros and the vertices of these surfaces were imported into the Matlab programming environment (v2013b, MathWorks) using the AC-PC coordinate system. The vertices of thalamic volumes were rotated (rotation matrix T_f) such that either the afferent or efferent fiber directions were oriented in the z-direction. A 3D rectangular grid consisting of multiple layers spanning the z-direction was constructed for each volume. Each layer spanned the maximal extent of the volume in the x and y directions and consisted of 10,000 points (100 x 100) in total. An additional layer was added to either side of the existing grid for calculating AF values. These grid points were arranged in this way to represent axonal node compartments. The distance between layers of grid points was 0.5 mm in both the efferent and afferent directions, consistent with internodal distances of myelinated axons used in previous studies [364]. The coordinates of these grid points were transformed into AC-PC space by multiplying T_f^{-1} (Fig. 15) and then were transformed into the FEM model space by multiplying T_{AF}. Data regarding the discretization process are listed in Table 5.

3.3.5 Activating Function Values and Construction of the Max Curve

Using each FEM model solution stored previously, the activating function values for each grid point along the fiber direction was calculated using the following formula:

$$\frac{\partial^2 V}{\partial x^2} = \frac{V(x+\Delta x)-2V(x)+V(x-\Delta x)}{\Delta x^2} \tag{3.1}$$

where x is a position along the direction of fibers, V is the voltage value as a function of position, and Δx is the internodal distance. The AF values for grid points within the layers at either end cannot be calculated and these points are therefore discarded. Points that overlap spatially with the DBSA are also discarded. The AF values for the remaining n points can be stored in a 32×n matrix C:

$$C = \begin{pmatrix} \nabla^2_{1,1} & \cdots & \nabla^2_{1,n} \\ \vdots & \ddots & \vdots \\ \nabla^2_{32,1} & \cdots & \nabla^2_{32,n} \end{pmatrix} \tag{3.2}$$

where the ith row contains the AF values resulting from stimulation through the ith electrode alone, delivering -1mA monopolar cathodic current. Poisson's equation in electrostatics dictates that the tissue voltage distribution is related to the current by:

$$\nabla \cdot \sigma \nabla V = -I \tag{3.3}$$

where σ is the tissue conductance, and I is the current. From (Eqn. 3.3) it is possible to derive that $\frac{\partial^2 V}{\partial x^2} \propto I$. Along with (Eqn. 3.1), it can be shown that the AF values resulting from multiple voltage sources can be linearly superimposed. To find the maximum possible AF value at a given grid point from any possible electrode con mentioned thought experiment.uration (subject to a 1 mA power constraint), we can consider the following thought experiment: suppose there are n different categories of items that can be manufactured, each with the same cost but different profit margins. For a given manufacturing budget, the highest profit achievable occurs when the entire budget goes into manufacturing the most profitable item. Likewise, it can be readily shown that the highest possible AF value achievable at each grid point is obtained when stimulating through a single electrode using the entire 1mA of current. Therefore the maximum value in each column (j) of the C matrix is the theoretical maximum AF value possible for grid

Efferent VPLo				
	Mean (V/mm^2)	Std (V/mm^2)	Max (V/mm^2)	Min (V/mm^2)
MD	7.763×10^{-4}	0.022	0.445	-0.287
QP	15×10^{-4}	0.04	1.362	-1.172
LP	22×10^{-4}	0.091	3.573	-2.953
Efferent VPLc				
	Mean (V/mm^2)	Std (V/mm^2)	Max (V/mm^2)	Min (V/mm^2)
MD	-9.31×10^{-4}	0.002	0.009	-0.046
QP	-8.867×10^{-4}	0.007	0.049	-0.186
LP	-8.605×10^{-4}	0.012	0.119	-0.381
Afferent VPLo				
	Mean (V/mm^2)	Std (V/mm^2)	Max (V/mm^2)	Min (V/mm^2)
MD	-15×10^{-4}	0.027	0.576	-0.342
QP	14×10^{-4}	0.045	1.599	-0.809
LP	39×10^{-4}	0.069	3.912	-0.785
Afferent VPLc				
	Mean (V/mm^2)	Std (V/mm^2)	Max (V/mm^2)	Min (V/mm^2)
MD	-8.835×10^{-5}	0.003	0.043	-0.022
QP	2.174×10^{-4}	0.001	0.012	-0.004
LP	4.975×10^{-4}	0.001	0.009	-0.003

Table 6. Activating function values

point *j*. The maximum AF values are sorted in ascending order and arranged into the Max Curve. Each grid point represents the center of a membrane compartment. Positive AF values are responsible for directly depolarizing the cell membrane and considered here as potential initiation sites for action potential generation [370]. Negative AF values represent direct hyperpolarization of the cell membrane and thus limit the likelihood of generating action potentials. The goal as defined in this study was to obtain the highest AF value possible at each grid point within VPLo. This corresponds to maximizing proximity to the Max Curve.

3.3.6 Convex Optimization

The volume activation problem can thus be framed conceptually as follows: “How do we bring as many of the grid points as close as possible to their corresponding maximum AF

values on the Max Curve?" To formulate this problem mathematically, we applied the principle of superposition to denote the AF values due to a given electrode configuration:

$$AF_j = C_j^T I \tag{3.4}$$

where I is the 32×1 vector of currents through each electrode, and AF_j and C_j are the AF value and column of C corresponding to grid point *j*. Together, the AF values resulting from stimulation at each grid point can form another curve called the Actual Curve. At each grid point *j*, the difference between the maximum AF value and the actual AF value from stimulation with I is given by the following:

$$AF_{j,max} - AF_j = C_{j,max} - C_j^T I \tag{3.5}$$

Using (Eqn. 3.5) as a measure of discrepancy between the Max Curve and the Actual Curve, we can set the objective to minimize discrepancy. Specifically, we considered three different optimization criteria using three different measures of discrepancy between the two curves. For simplicity, we have used constraints in all three cases that the currents through any of the 32 electrodes be greater or equal to zero and that the sum of all currents through the electrodes be equal to 1mA. The latter constraint was arbitrarily defined and can be adjusted as necessary in the context of using total current amplitudes that do not express stimulation-evoked side effects. Using only the difference between the Max Curve and Actual Curve as a measure, the problem can be solved by linear programming (LP) as follows:

minimize: $\sum(C_{j,max} - C_j^T I)$
subject to: $\sum I_k = 1$ and $I_k \geq 0$, for all k

Using the square of the difference between the two curves, the problem can be solved by quadratic programming (QP):

minimize: $\sum(C_{j,max} - C_j^T I)^2$
subject to: $\sum I_k = 1$ and $I_k \geq 0$, for all k

Finally, the maximum deviation (MD) between the two curves as a criterion to minimize is given by:

minimize: $max_j(C_{j,max} - C_j^T I)$
subject to: $\sum I_k = 1$ and $I_k \geq 0$, for all k

For linear programming, quadratic programming, and maximum deviation minimization via convex optimization, the problem is well-posed and has a unique, global minimum. Here, we considered all three of these criteria separately (LP, QP, and MD), and implemented the optimization in MATLAB (v2013b) using the cvx package for solving convex optimization problems [380]. All computations and performance assessments were run on a PC with eight cores, 64-bit operating system, 24.0 GB RAM, and an Intel Core i7 processor at 3.40 GHz. To verify optima were reached, one million random electrode configurations were generated, and their corresponding discrepancy measures were obtained to construct noise histograms for each of the three methods.

3.3.7 Runtime and Sampling Robustness

We ran the algorithms on random subsets of grid points to assess (1) the algorithm's runtime with respect to number of grid points used, and (2) the robustness of electrode configuration solutions with respect to sampling. Each of the three optimization criteria (MD, QP, LP) was used on random subsets of the efferent VPLo grid points. The random subsets consisted of eight sampling levels: 1/2, 1/4, 1/8, 1/16, 1/32, 1/64, 1/128, and 1/256 of the total number of grid points within the volume. We obtained and ran 31 random subsets of grid points for each sampling level. The resulting electrode configurations were assessed based on the average height and angle of the active electrodes. The runtime was also measured. This yielded 31 measurements of height, angle, and runtime for each sampling level.

3.4 Results

3.4.1 Electrode Configurations

The optimal current output in the efferent and afferent cases is shown graphically in Figs. 16 and 17, respectively. In both cases, MD had the most active contacts, while LP had the least (contacts delivering 1 μA or more current were considered active). The distribution of current amongst the active contacts was fairly uniform in the MD criterion solutions and less so in the QP criterion solutions. In the efferent case, the mean current output was

0.067±0.037 mA per electrode (mean ± std) for the MD solution and 0.091±0.104 mA per electrode for the QP solution. In the afferent case, the mean current output was 0.072±0.043 mA per electrode for the MD solution and 0.2±0.147 mA per electrode for the QP solution. In the efferent case, the active electrode contacts faced the anterior or posterior directions primarily. In the afferent case, most active electrodes faced medially or laterally. In the case of the LP solution, for both efferent and afferent cases, the entire 1 mA current was applied through only one contact, as expected from the previously mentioned thought experiment.

3.4.2 Activating Function Values

The algorithm AF solutions were based on grid points in VPLo and were optimized to achieve proximity to the VPLo Max Curve. The resulting AF values for both VPLo and VPLc are summarized in Table 6 and shown graphically in Fig. 18. Not surprisingly, higher AF values were concentrated near the active electrodes. In both the efferent and afferent cases, the MD, QP and LP solutions produced successively tighter concentrations of larger AF values along the length of the thalamic nuclei. The MD solution AF values exhibited the least amount of spread both spatially and numerically. The LP solution, on the other hand, exhibited the most spread, the largest mean, and the largest maximum AF values, but also produced the lowest AF values within VPLo. Fig. 18 illustrates the proximity of the actual AF values to the Max Curve for VPLo grid points. The LP solution had many points that achieved their maximum value, though a relatively large variation in AF values was once again evident across grid points. In contrast, very few grid points from the MD and QP solutions achieved their maximum values, but there was relatively less variation in AF values compared to the results using the LP criterion.

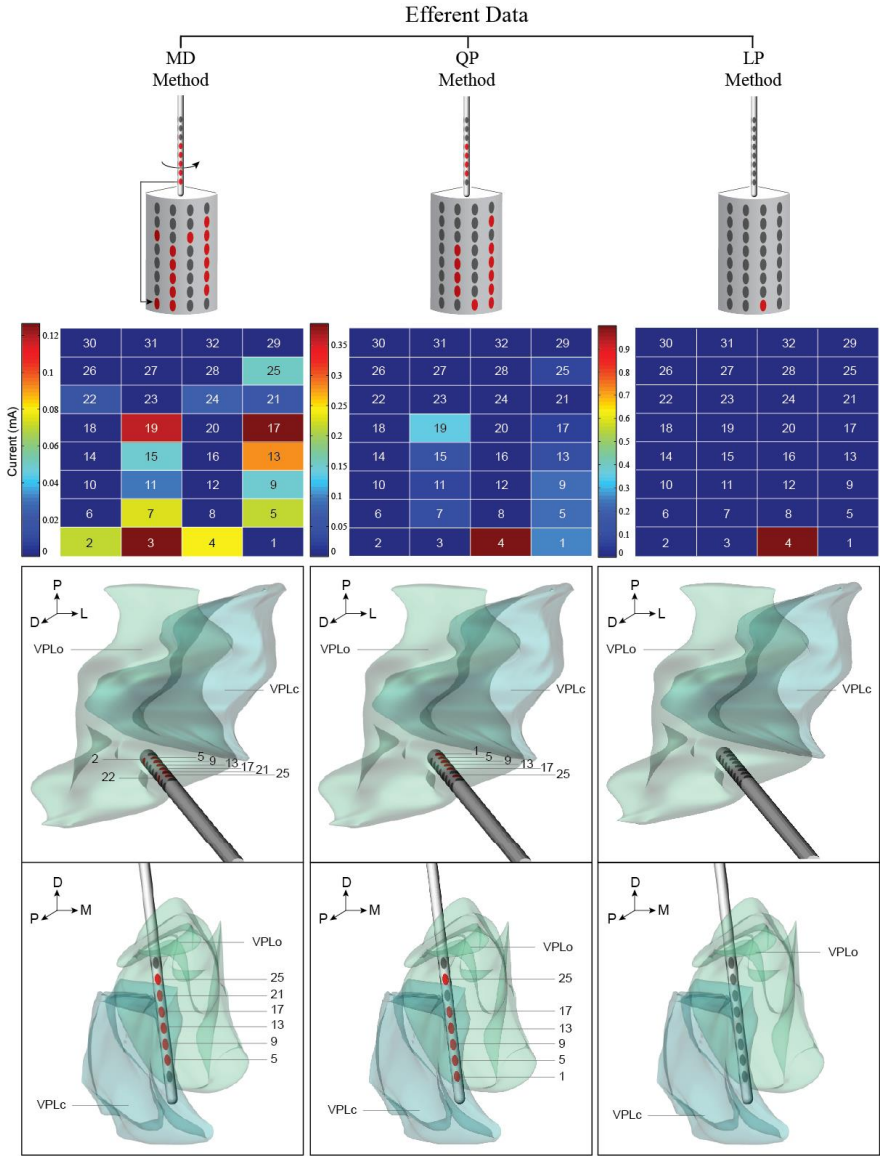

Figure 16. Algorithm-generated electrode configurations for the thalamic efferent pathway approximations

The left, middle, and right columns show outcomes from the MD, QP and LP optimization criteria, respectively. Active contacts (> 1 μA) in each case are shown in red (top row) with the precise amount of current calculated by the algorithm shown in indexed colors (second row). Axial views (third row) and oblique views (fourth row) of VPLo and VPLc are shown in the context of the DBSA with active contacts shown in red.

3.4.3 Optimization Results

Fig. 20 shows three different measures comparing the performances of the MD, QP, and LP solutions to one million random (chance) electrode configurations. Stimulating electrode configurations *I* (three separate criteria solutions and 1 million random

Efferent Data			
	Max Deviation	Sum of Square of Differences	Sum of Differences
MD	< 0.001	< 0.001	0.001
QP	0.8348	< 0.001	< 0.001
LP	0.8593	0.0037	< 0.001
Afferent Data			
	Max Deviation	Sum of Square of Differences	Sum of Differences
MD	< 0.001	<0.001	0.0583
QP	0.2758	< 0.001	< 0.001
LP	0.2758	< 0.001	< 0.001

Table 7. Probability of algorithms performing better than randomly generated results

solutions) were used to calculate the model predicted actual AF values using (Eqn. 3.4). The results were arranged into the Actual Curve. The maximum deviation, sum of differences, and square of the sum of differences between the Actual Curve and the Max Curve were calculated. As expected, the MD solution achieved the lowest maximum deviation, the QP solution achieved lowest sum of square of deviations, and LP solution achieved the lowest sum of deviations. Furthermore, within each of these categories, the best-performing solution performed significantly better than chance. While no single optimization solution yielded better-than-chance results across all three measures, MD tended to perform better relative to chance in all categories. QP and LP showed better-than-chance performance for all except the maximum deviation category. The p-values for each category are listed in Table 7.

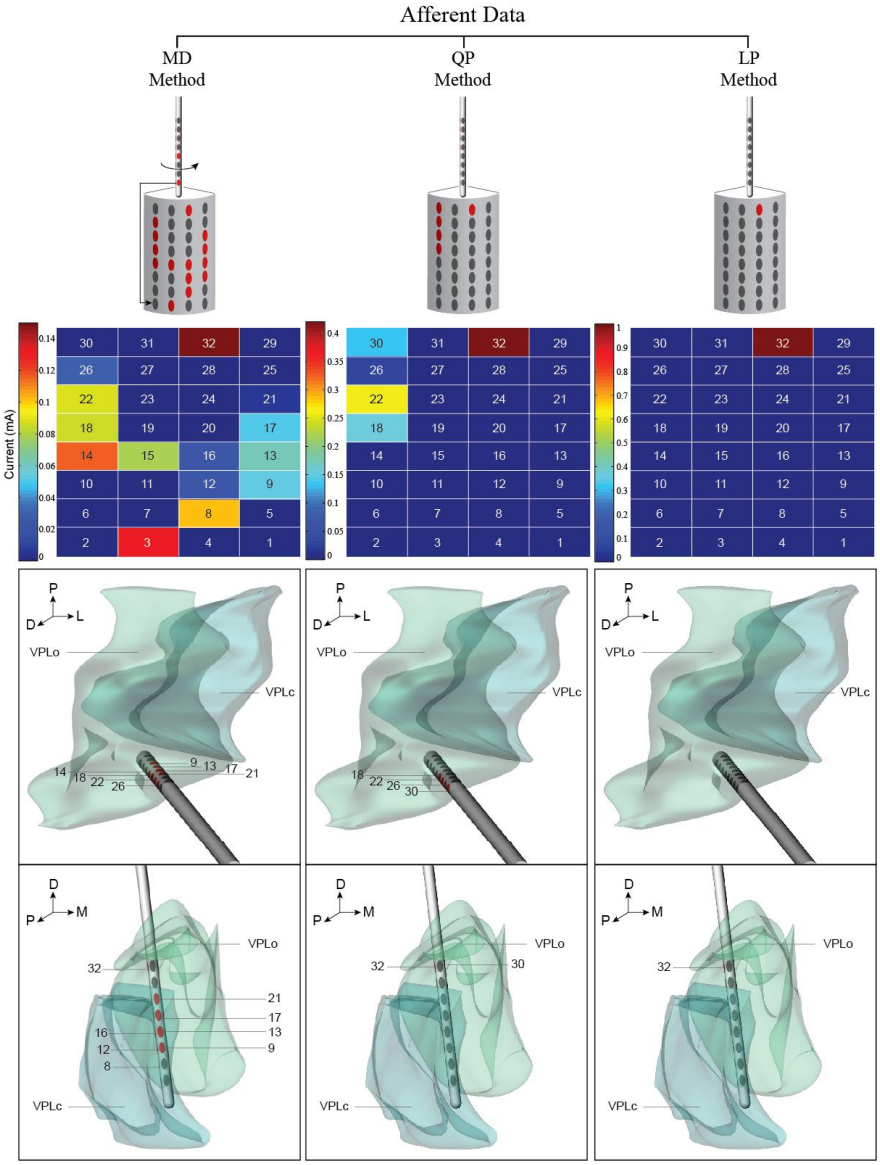

Figure 17. Algorithm-generated electrode configurations for the thalamic afferent pathway approximations
Labeling is identical to that described for Figure 16.

3.4.4 Runtime and Sampling Robustness

In terms of runtime (Fig. 21C,F,I), mean duration for 27,173 efferent VPLo grid points was 3.0 seconds for the MD solution, 3.4 seconds for the QP solution, and 0.2 seconds for the LP solution. Runtime scaled nonlinearly with respect to number of grid points, such that sampling half the grid points reduced runtime by more than half. Using subsets of the full grid points for the computation yielded active electrodes with similar mean

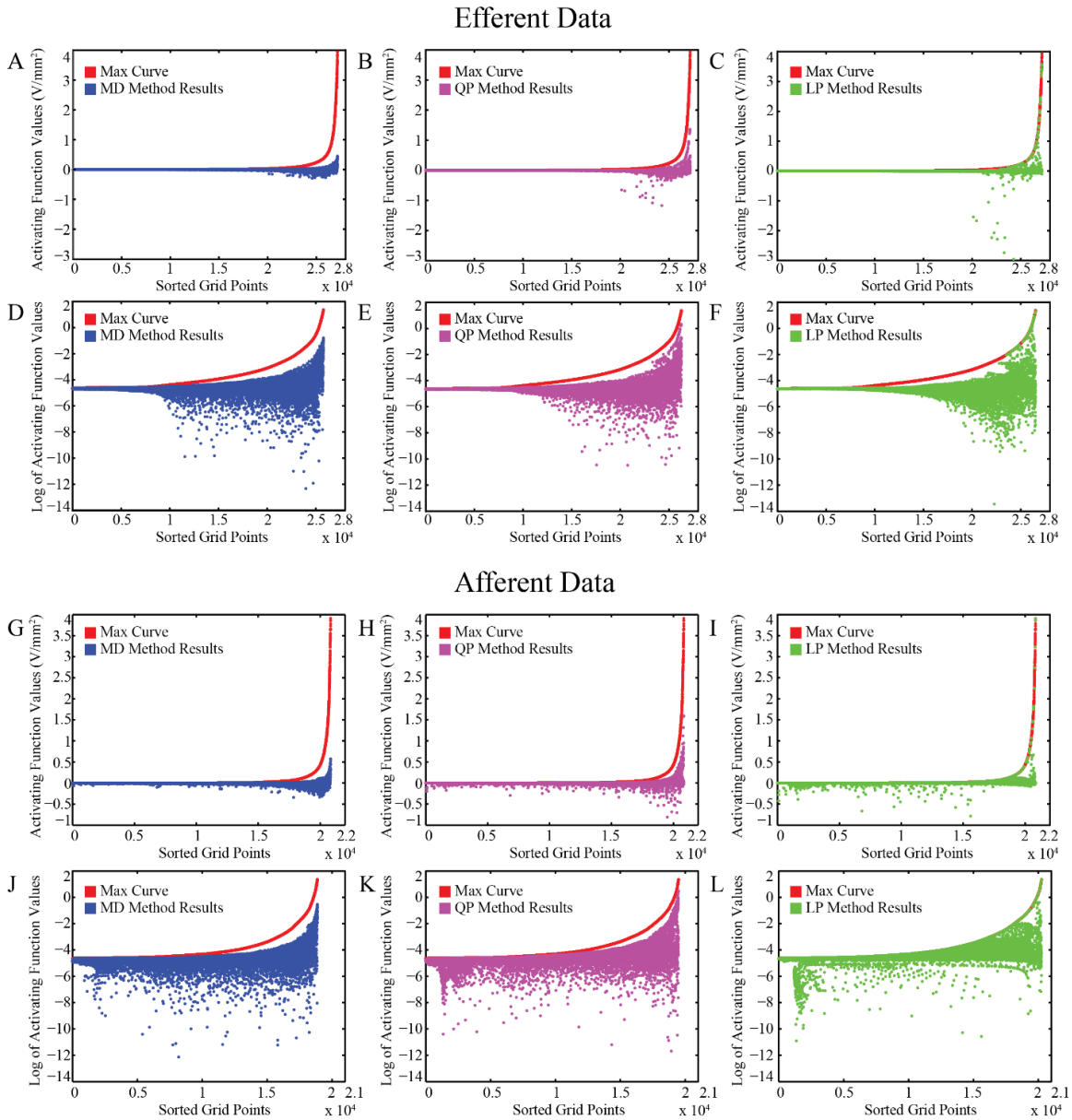

Figure 18. Comparison of Max Curve to solutions obtained by MD, QP, and LP for efferent and afferent data

Grid points in the region of interest are sorted based on their maximum achievable values. For each optimization criterion, the actual value at each grid point is plotted underneath its maximum possible value. Therefore, the closeness of the grid points to the Max Curve is a measure of optimization performance. (**A-C**) and (**G-I**): AF values at all grid points are presented in units of V/mm^2. (**D-F**) and (**J-L**): Grid points with AF values less than -0.01 V/mm^2 were omitted in these plots. The remaining AF values were made positive by adding 0.01 and the natural logarithm of the resulting values was computed.

height (Fig. 21A, D, G) and mean angular direction (Fig. 21B, E, H). However, smaller subsets yielded larger standard deviations of the active electrode heights and directions.

3.5 Discussion

3.5.1 Predicting Neuronal Activation

Several computational methods have been used to predict neuronal activation. The first spatial derivative along the neuronal process has been shown to be appropriate for modeling activation near the vicinity of the soma [381]. However, computational studies have also shown that the waveforms used in DBS applications are likely to elicit action potentials first in the axons [382], [161] based upon the second spatial derivative of the extracellular voltage along the axonal processes [370], [383]. Such calculations can be performed using spatially distributed multi-compartment neuron models [384] to obtain a VTA. However, this process is computationally intensive. A more efficient approach, as described in this study, is to use the AF values along the estimated direction of neuronal processes to predict the VTA. This method is widely used [357], [371], [385], [386] but still requires large amounts of simulations to be run and the results stored in order to account for different orientations and displacements of neuronal processes from the source(s) of stimulation [364]. Studies have pointed out the limitations to this approach [387] and a novel method for VTA prediction using artificial neural networks (ANN) has been proposed [388], although substantial amounts of simulations are still needed to generate different stimulation scenarios to train the ANN.

Our goal here was to increase the probability of neuronal activation instead of determining the exact activation profile using VTA prediction. We do this by maximizing AF values, taking advantage of well-established theories associating higher AF values with neuronal activation [370] [383]. It is not straightforward to set an exact threshold AF value due to the variation in reported values [357] [359], and the dependence on factors such as fiber orientation and distance of compartments to the active electrode(s) [372]. Nevertheless, the method presented here circumvents such limitations by determining a theoretical maximum AF value at each grid point (Max Curve) given a current input limit. These grid points represent neuronal compartments, each with the ability to initiate an action potential. The goal of our superposition and optimization-based framework is to achieve proximity between the stimulation-induced AF values and the Max Curve. This

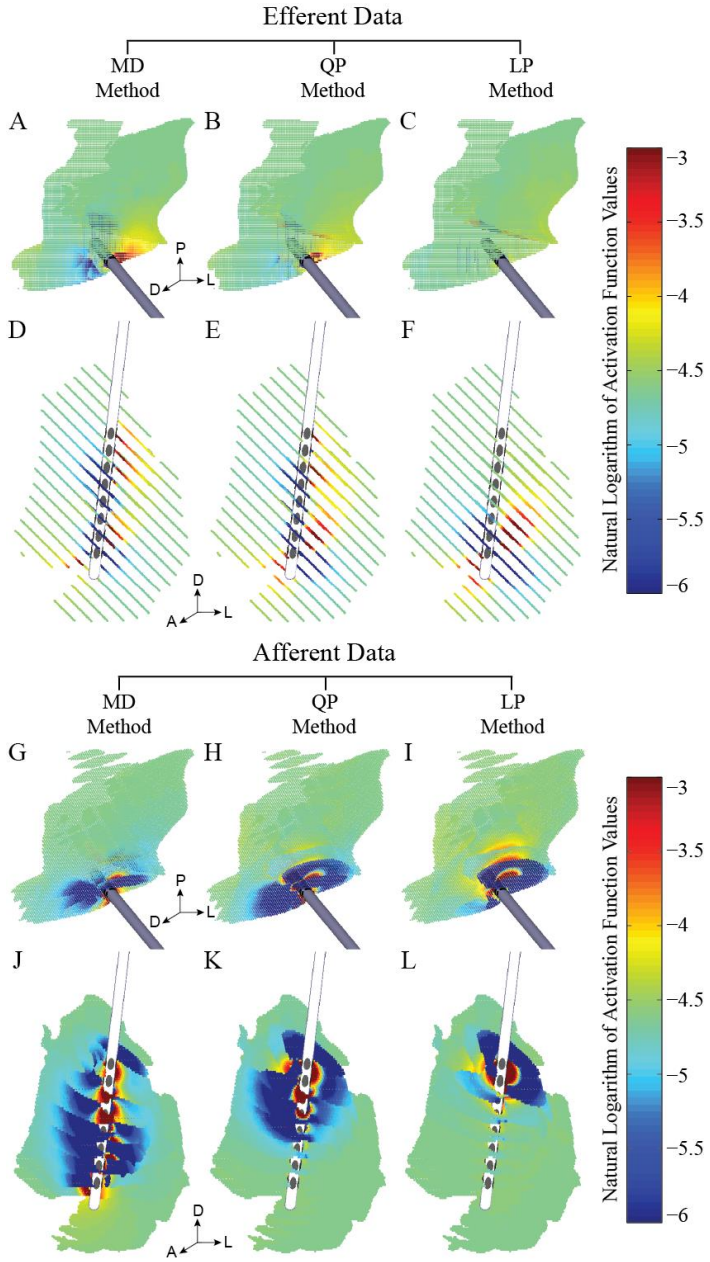

Figure 19. Activating function values resulting from DBSA stimulation using algorithm-generated electrode configurations

(**A-C**): Efferent data, axial view of the AF values resulting from stimulation configurations generated using the MD, QP, and LP criteria, respectively. (**D-F**): Coronal view of the AF values shown in (a-c). (**G-I**): Afferent data, axial view of the AF values resulting from stimulation configurations generated using the MD, QP, and LP criteria, respectively. (**J-L**): Coronal view of the AF values shown in (j-l). For visualization purposes, all AF values greater than -0.01V/mm^2 were made positive by adding 0.01 and the natural logarithm of the resulting values was computed. The logarithm values were used as indexed colors. The color bar in this figure ranges from -6 to -3 in logarithm values. Points with values outside of this range were directly assigned the values of -6 or -3. Points with AF values less than -0.01V/mm^2 were assigned logarithm values of -6. Refer to Figure 13(D) for borders between VPLo and VPLc in the coronal view. Refer to Figure 16 or 17 for the border in the axial view.

ultimately aims to increase the probability for action potential initiation or other forms of sub-threshold modulation.

While we used the Max Curve, the algorithm can be readily adapted to activation thresholds, such as a constant AF threshold used in some studies [357], [359], [371] or a nonlinear AF threshold fall-off with respect to distance from the stimulating electrode [372]. Here we selected the Max Curve as the target criteria to compare each grid point against its own theoretical maximum AF value. This avoids certain issues that constant AF thresholds may introduce, such as weighting the discrepancies due to grid points far from the electrodes too heavily. Furthermore, it is possible that certain AF values on the Max Curve are negative, which means that the hyperpolarizing effect would elicit an indirect depolarizing influence on the axons. These points can be omitted from the C matrix so that the algorithm can focus on the remaining points with positive AF values on the Max Curve. Here, we chose to keep these points in this study.

3.5.2 Algorithm and Performance

Finding the optimal stimulation strategy for high-density electrode arrays remains a challenge in various electrical stimulation technologies. Manipulation of the amounts of current delivered through each electrode has been shown to shape the spatial distribution of voltage potentials, their gradients [389], and ultimately the VTA [390].

Algorithms for automatic generation of stimulating electrode configurations require well-defined neuronal response measures and an understanding of the underlying mechanisms of action. In cochlear implant studies, the goal is to minimize current spread from activating multiple electrodes so as to reduce the effects of interfering stimulation. Studies have proposed using psychophysical measurements to find the optimal electrode configuration in order to selectively activate a particular neural site [391], [392]. In DBS, the goal has been viewed as one to maximize modulation of neuronal spike activity within a target brain region, while avoiding activation of pathways implicated in the manifestation of side effects. In terms of the former, one of the established approaches is to search through pre-compiled solutions to find the settings that give the most overlap between the VTA and the target volume [216]. For DBS arrays, this approach would

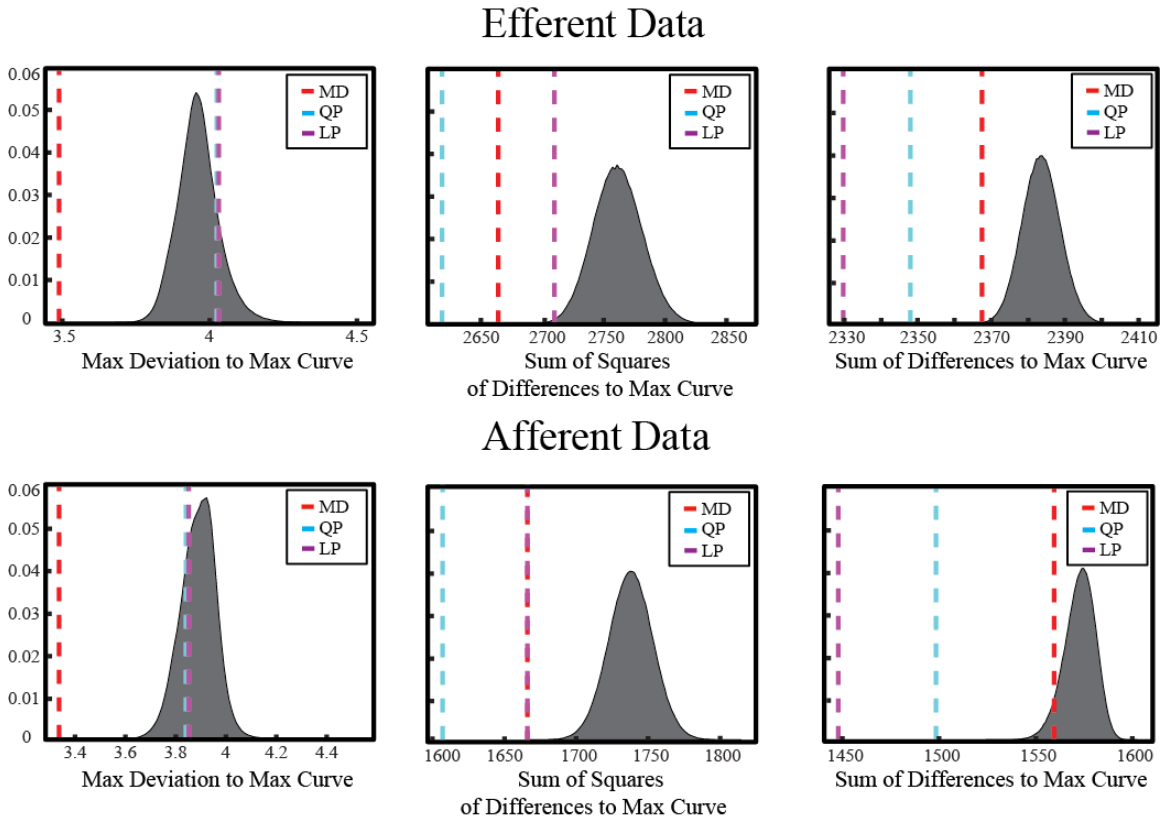

Figure 20. Performance of algorithm generated results against randomly generated electrode configurations
Performance comparison of MD, QP, and LP to one million random electrode configurations (gray normalized histogram), in efferent and afferent data. The three measures considered (Max Deviation, Sum of Squares, Sum) each indicate deviation from maximum possible activating function values. Thus, lower values correspond to better performance.

require massively large computational resources to calculate this solution. The computational efficiency of our approach arises from circumventing VTA prediction, while maintaining simplicity in user inputs: the power constraint (1 mA in this study), the target volume, and fiber orientations (in order to discretize the volume into grid points aligned in that orientation).

From Table 6, the mean AF values differed depending on the orientation of the fibers. However, this difference was not significant. Within VPLo (Fig. 18/Table 6), the LP solution achieved the highest mean AF values, but also resulted in the largest spread of data (about 2.5-4 times larger than the MD solution, and 1.5-2.3 times larger than the QP solution). Meanwhile, the QP solution produced slightly larger mean AF values than the

MD solution in both efferent and afferent cases, and only had a slightly larger spread. Based on this analysis, the LP criterion would be selected if one was interested in optimizing for the average AF value in the region of interest. Indeed, the LP solution converges on a single electrode, which has the greatest influence on the AF mean value. The LP criterion is mathematically equivalent to maximizing the mean AF values across all grid points. As such, it is expected that some grid points from the LP solution will lie on the Max Curve (as shown in Fig. 18) since all the current is applied to a single electrode and thus certain grid points will achieve their maximum AF and lie on the Max Curve by definition. On the other hand, if one considers generating a more uniform activating function value of the region of interest, the QP and MD criteria would be more appropriate. It is important to note that each criterion is meant to be used independently. What remains is performing the electrophysiological investigation to ascertain which criterion yields the most robust therapeutic effect with DBS.

There are other considerations to factor into this calculation. For one, charge density limits of stimulation at a given electrode may impact the LP approach more than the other two curve fitting approaches, since the LP solution converges on a single electrode. Additionally, the QP and MD criteria require multiple electrodes with independent current controlled stimulators that are not yet widespread clinically.

The optimization approach with MD, QP, and LP criteria each outperformed one million random electrode configurations in their respective measures of proximity to the Max Curve (Fig. 20). However, no single criterion solution yielded better-than-chance performance for all three measures. Indeed, while the LP solution clearly achieved the best performance for sum of deviations, it also had the worst performance for the other two measures. It is thus important to recognize that the efficiency and mathematical flexibility of these algorithms must be coupled with a clear goal of what are the desired criteria for the resulting AF values. These criteria may depend on patient-specific parameters (e.g. modulating a target uniformly or leveraging activation of a pathway that can have broad synaptic influence over the entire region [215].

The algorithm runtime for each of the MD, QP, and LP criteria was on the order of several seconds for the number of grid points used here, making it feasible for on-site

patient-specific clinical use. Runtime scaled nonlinearly with respect to number of grid points (i.e. halving the number of grid points reduced runtime by more than half). However, this nonlinear relation was not very strong. Randomly sampling half the grid points yielded a similar average height and angle of active electrodes, indicating that the algorithm is robust to changes in grid point resolution. However, very small samples (corresponding to low grid point resolutions) resulted in chance electrode configurations, since the spatial extent of the samples was sparse relative to the spatial features of the electric field. The algorithm presented here also allows for fast computation of multiple stimulating electrode configurations using the same DBSA to target different neuronal subpopulations within a target region, as in the case of coordinated reset stimulation [393], [394] to desynchronize pathological oscillations.

3.5.3 Study Limitations and Future Work

This study applied the optimization concept using relatively simplistic models to create a controlled environment. One important limitation to this study is the simplicity of the tissue model and its underlying neuron morphologies. For example, the volumes of VPLo and VPLc were discretized in two fixed directions, and the grid points were arranged in serial layers. A more realistic way to discretize the volumes would be to populate them with grid points that are more morphologically realistic [215], [161], [395], [396], [378]. Second, while the activating function was computed with potentials constrained to the approximate axonal trajectories within thalamus, the voltage distribution itself was obtained under the assumption of a homogeneous and isotropic tissue medium. This approximation is reasonable at the grid point spacing considered here [40], though a more realistic model would incorporate conductance inhomogeneity as well as anisotropy through diffusion tensor imaging [397]. The changes would take place in the initial construction of the FEM (e.g. extracting anisotropic and inhomogeneous tissue conductivities from diffusion tensor imaging data), but would not impact the overall efficiency of the algorithm. As such, this framework enables one to readily adapt the

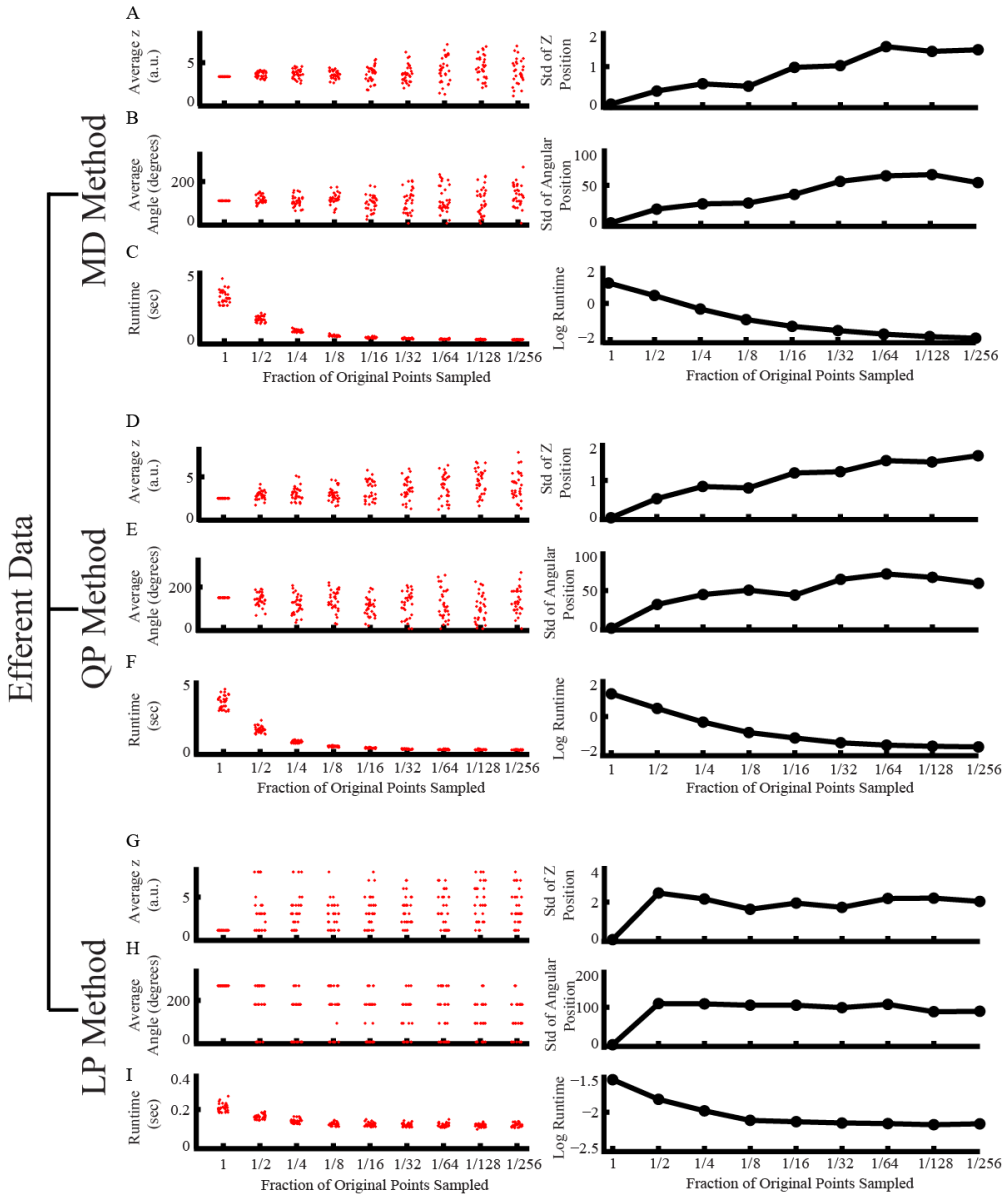

Figure 21. Comparison of runtime and sampling robustness for MD, QP, and LP algorithms
The original number of grid points for efferent data was 27,173. For each level of sampling (½, ¼, etc.) a random subset of the original points were selected. (**A, D, G**) Average height of active electrodes with respect to multiple sampled subsets. Standard deviation of height progressively increases as smaller subsets of original points are used. (**B, E, H**) Average angular direction of active electrodes. Similarly to average height, standard deviation increases toward random distribution. (**C, F, I**) Runtime and logarithm of runtime with respect to sampling.

model with changing implant environments (e.g. to model edema in acute implants vs. encapsulation in chronic implants). Third, we did not model the voltage drop or capacitance of the electrode-electrolyte interface. Such considerations are important

[398], and the optimization algorithms developed in this study are amenable to the inclusion of such complexities as part of future iterations of the algorithm. Another important consideration is that the algorithm in its current form does not include minimization of the AF values in regions deemed to elicit side effects when stimulated, such as VPLc [215], [201], [399]. Such an algorithm, which optimizes both cathodic and anodic currents delivered through the DBSA, is part of a subsequent study.

Validation studies exploring these parameters are needed to clarify this relation between the AF criteria and both electrophysiological changes in the brain and behavioral outcomes in the subject. Studies in the fields of cochlear and retinal implants have demonstrated that current steering can create 'virtual electrodes' by differential distribution of current between physical electrodes to elicit percepts intermediate to those produced using monopolar configurations [400], [401]. In DBS, clinical validation studies have shown that stimulation strategies based on computational models can be superior to clinically derived strategies to limit cognitive deficiencies [367] and improve therapeutic outcomes [369]. Electrophysiological studies to validate the model predictions are important and have been limited to date. For one, it is important to consider the spatial distribution of the modulated neuronal firing patterns around the DBS lead [402] [156] and how this varies amongst algorithm-generated stimulus settings and the setting derived from a clinical exam. It is also important to validate the models at a circuit level [403] to compare the ability for a given set of settings to modulate neuronal activity throughout the affected network. Ultimately, it is important to directly measure behavioral outcomes, such as motor capsule side effects [216] and symptom reduction [360] [238], in a clinical setting to determine if the algorithm generated stimulation is more effective and efficient.

3.6 Acknowledgements

This study was supported by the College of Science and Engineering, the Institute for Translational Neuroscience at the University of Minnesota, the Michael J. Fox Foundation and an NIH grant (R01-NS081118). We thank Drs. Noam Harel, Essa

Yacoub, and Gregor Adriany at the Center for Magnetic Resonance Research for help with the imaging.

Chapter 4

Spherical Statistics to Characterize the Spatial Distribution of Deep Brain Stimulation Effects on Neuronal Activity

This chapter reprinted with permission from Elsevier.

YiZi Xiao and Matthew D. Johnson, “Spherical statistics for characterizing the spatial distribution of deep brain stimulation effects on neuronal activity,” *J Neurosci Methods,* 255(2015): p.52-65.

4.1 Overview

4.1.1 Objective

Computational models of deep brain stimulation (DBS) have played a key role in understanding the physiological mechanisms of DBS therapies. By estimating a volume of tissue directly modulated by DBS, one can relate the neuronal pathways within those volumes to the therapeutic efficacy of a particular DBS setting. With the advent of DBS electrode arrays that can facilitate higher resolution current steering and sculpting, there is a need for a more systematic method to quantify the directional component of the morphology of these modulated volumes. Here, we describe a spherical statistical framework to quantify such morphologies.

4.1.2 Approach

This framework was demonstrated using a 3D computational model of stimulation of thalamocortical neurons surrounding a radially-segmented DBS array. Visualization techniques and empirical shape analysis were used to determine the salient features in the model data as well as formal hypothesis testing to determine the shape of each model distribution.

4.1.3 Main Results

We show that neuronal population volumes modulated by different electrode configurations can be characterized by parametric distribution models, such as the Kent and Watson girdle models. In addition, distribution parameters change with stimulus settings, including amplitude and radial distance from the DBS array. Increasing stimulation amplitude through a single contact resulted in more diffuse activation of neurons as well as increased rotational symmetry about the mean direction of the activated population. When stimulation amplitude is held constant, the activated neuronal population is more concentrated in distribution the further they are away from the DBS array, but also more rotationally asymmetric. We also show how data representation (e.g.

stimulus-entrained cell body vs. axon node) can significantly alter model distribution shape.

4.1.4 Significance

This statistical framework provides a quantitative method to analyze the spatial morphologies of DBS-induced effects on neuronal activity. The application of spherical statistics to assess spatial distributions of neuronal activity has potential usefulness for numerous other recording, labeling, and stimulation modalities.

4.2 Background

Electrical stimulation within the brain is known to modulate the rate and pattern of neuronal spike activity around an active electrode [156, 404-407]. Such effects are thought to stem from directly modulating a range of afferent and efferent neuronal processes as well as directly modulating nearby axonal fibers of passage [161, 208, 209], which together create a sparsely activated volume that is highly dependent on electrode placement [408, 409]. Characterizing the spatial distribution of modulation around an active electrode has importance for better understanding the neurophysiological mechanisms of electrical stimulation [170, 410] and has clinical relevance in the design of patient-specific strategies to improve the selectivity of targeting individual pathways within the brain [367-369]. In particular, assessing the spatial distribution of modulation is important for field-shaping capabilities of high-density electrode arrays for application in deep brain stimulation (DBS) [215, 357, 364] as well as characterizing the spatial precision of modulation for visual [411, 412] and auditory [400] neuroprostheses.

Currently, there does not exist a systematic and widely accepted method to quantify the spatial distribution of stimulus-induced changes in neuronal activity around an active electrode, be it from computational modeling [215] or experimental recordings using electrophysiological [409] or imaging-based [413] techniques. Commonly used metrics include: population center of mass (COM), total volume enclosing the population, or maximal radial extent of activation [390]. These metrics while useful do not provide a consistent way to account for important information about the underlying distribution of

the activated neuronal populations. As is the case with any data, it is important to use statistical approaches to analyze them and describe their distributions with parametric models.

Spherical statistics [414] provides a framework to analyze the directional distribution of data in space. This branch of statistics focuses on the analysis of orientation of lines/vectors in space and has applications in diverse disciplines, including the Earth sciences [415], remote sensing [416], and auditory psychophysics [417]. Three-dimensional data can be characterized into different distributions based solely on their directional components relative to a pre-specified origin. The radial component of the data generally does not play an important role and is normalized to the same value (e.g. unit radius). In cases in which radial distance needs to be taken into account, spherical statistics can then be applied to concentric shells of data, delineated by their radial distance from a pre-specified origin.

In this study, we develop a framework for applying spherical statistics to analyze the spatial distribution of neuronal spike activity around one or more active electrodes. The method is motivated by a computational model of deep brain stimulation using a population of thalamocortical neurons distributed around a DBS lead with four columns of elliptical electrodes arranged around the circumference of the lead. We show the process for making hypotheses on the shapes of neuronal data distributions, testing the data for hypothesized shapes, examining the importance of analytical perspective on interpretation of the results, and analyzing the effects of stimulus amplitude and electrode-neuron distance on the distribution of neuronal modulation.

4.3 Methods

4.3.1 Directionally-Segmented DBS Lead

A directionally-segmented DBS lead with 8 rows of 4 elliptical electrodes (semi-major axis: 0.265 mm; semi-minor axis: 0.14 mm) embedded on a 0.5 x 40 mm shaft (diameter x height) was generated in a finite-element model (FEM) (COMSOL Multiphysics, v4.3b) (Fig. 22A,B). The angular distance between adjacent contacts in the same row was

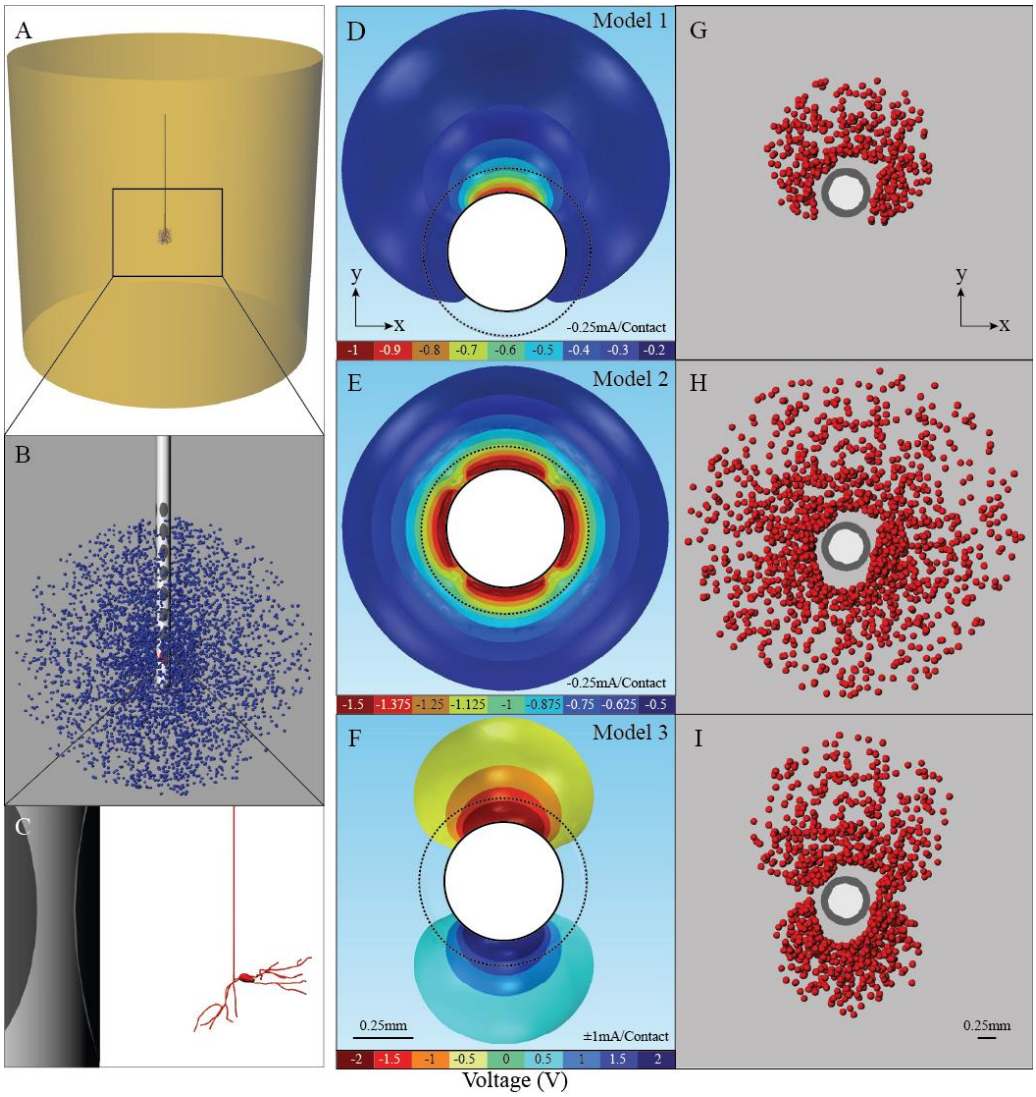

Figure 22. Computational model of neuronal activation by stimulation through a directionally-segmented DBS electrode array

(A) Volume conductor model with the DBS array in the center. **(B)** The blue spheres represent the cell bodies of 5000 thalamcortical relay neurons that were uniformly distributed about the center of bottom row of electrode contacts, in a sphere 5mm in radius. **(C)** Close up view of one of the neurons. The axon is oriented vertically and parallel to the shaft of the DBS array. **(D)-(F)** Cross sectional view of the voltage field in models 1,2 and 3. The dashed line represents the boundary of the encapsulation layer. **(G)-(I)** Top-down view of the neuronal activation profiles in models 1,2 and 3. The red spheres represent the cell bodies of neurons activated by stimulation.

45° and the distance between two rows of contacts was 0.75 mm. The lead was positioned such that the horizontal midline of the bottom row of electrodes was defined as the origin.

4.3.2 Tissue Conductance Model

A simplified inhomogeneous tissue conductance model was developed to simulate the tissue potential distribution resulting from current-controlled stimulation through one or more electrodes on the DBS array. For the purposes of this theoretical example, a 0.1 x 40 mm (thickness x height), 0.18 S/m homogeneous encapsulation layer and a 100 x 100 mm (diameter x height), 0.3 S/m cylinder of homogeneous bulk tissue surrounds the lead [375, 418] (Fig. 22B). The lead electrodes and insulation were assigned conductance values of 10^6 S/m and 10^{-12} S/m, respectively. The electrode surfaces were designated as boundary current sources with uniform normal current density (A/m^2). The walls of the bulk tissue cylinder were set to ground. The finite element model mesh contained 1116911 tetrahedral elements with finer mesh resolution near each electrode. The voltage distributions resulting from electrical stimulation through the electrodes were calculated via the finite element method (Fig. 22C) by solving Poisson's equation using the electrostatic solver.

4.3.3 Multi-Compartment Neuron Models

Multi-compartment thalamocortical (TC) relay neurons (n=5000) [161] were uniformly distributed within a 10 mm diameter sphere giving a spatial population density of approximately 10 neurons/mm^3 around the DBS lead. Model neuron axonal efferents were oriented vertically (parallel to lead shaft) (Fig. 22B,C). Current-controlled stimulation was applied using a waveform (130Hz, 90µs cathodic phase, 400 µs interphase delay, 3ms anodic phase) scaled from a constant-current pulse generator [419]. The FEM solution was scaled with the waveform, and the resulting time-varying voltage distribution was used to estimate activation, defined as the stimulus pulse train eliciting action potential(s) 3 ms after each stimulus pulse for at least 8 of 10 stimulus pulses.

4.3.4 Stimulation Configurations and Data Representation

Three stimulation configurations were considered in this study using the bottom row of electrodes: one contact monopolar cathodic stimulation (Model 1), four contact monopolar cathodic stimulation (Model 2), and bipolar stimulation using two opposing

	Model 1	***Model 2***	***Model 2****	***Model 3***
Data Type	Soma	Soma	Node of Ranvier	Soma
Origin	Model origin	Model origin	Model origin	Model origin
$\tau_1/\tau_2/\tau_3$	0.09/0.13/0.78	0.19/0.24/0.57	0.18/0.38/0.44	0.16/0.27/0.57
$\overline{R}$	0.872	0.6679	0.0805	0.4858
Hypothesized model	Unimodal	Unimodal	Girdle	Bimodal

Table 8. Summary of model information

contacts as cathode and anode (Model 3) (Fig. 22D-F). In Models 1 and 2, each contact delivered 0.25mA of current. In Model 3, each contact delivered ± 1mA. The locations of the somas relative to the center of the bottom row of contacts (FEM origin) in the models were used to represent activated neuronal soma locations in 3D. It is important to note that this is not the only way to represent the data. To demonstrate this, the locations of the axonal nodes of Ranvier that first elicited an action potential following a stimulus pulse were modeled for the stimulus configuration used in Model 2 relative the FEM origin (Model 2*). The details on data representation are listed in Table 8.

4.3.5 Spherical Statistical Hypothesis Testing and Parameter Estimation

In this study, the spherical statistical framework was used to quantify the directional distribution of neurons activated by each of the four model configurations. This framework followed a simplified version of the analysis put forth by Fisher et al. [414] (Fig. 23). Having identified the data points to use (i.e. soma/node locations), we next made initial hypotheses on the shape of their distributions. We first obtained the polar coordinates of colatitude (θ) and longitude ($\emptyset$) [414] of the data points (Fig. 24) and then projected these points onto the unit sphere. Projection was performed by setting the Euclidean distance between each data point and the origin to 1 while maintaining the orientation ($\theta, \emptyset$) of these points. For better visualization, we found the sample mean direction and rotated the data such that this direction pointed to the South Pole (Fig. 25A). In this new coordinate system, we used the Lambert azimuthal equal-area projection (EAP) (Fig. 24B) (1) of each data point (x_i, y_i, z_i) to obtain their projections (X_i, Y_i) in the 2D plane (Fig. 25B). No two data points in 3D will have the same

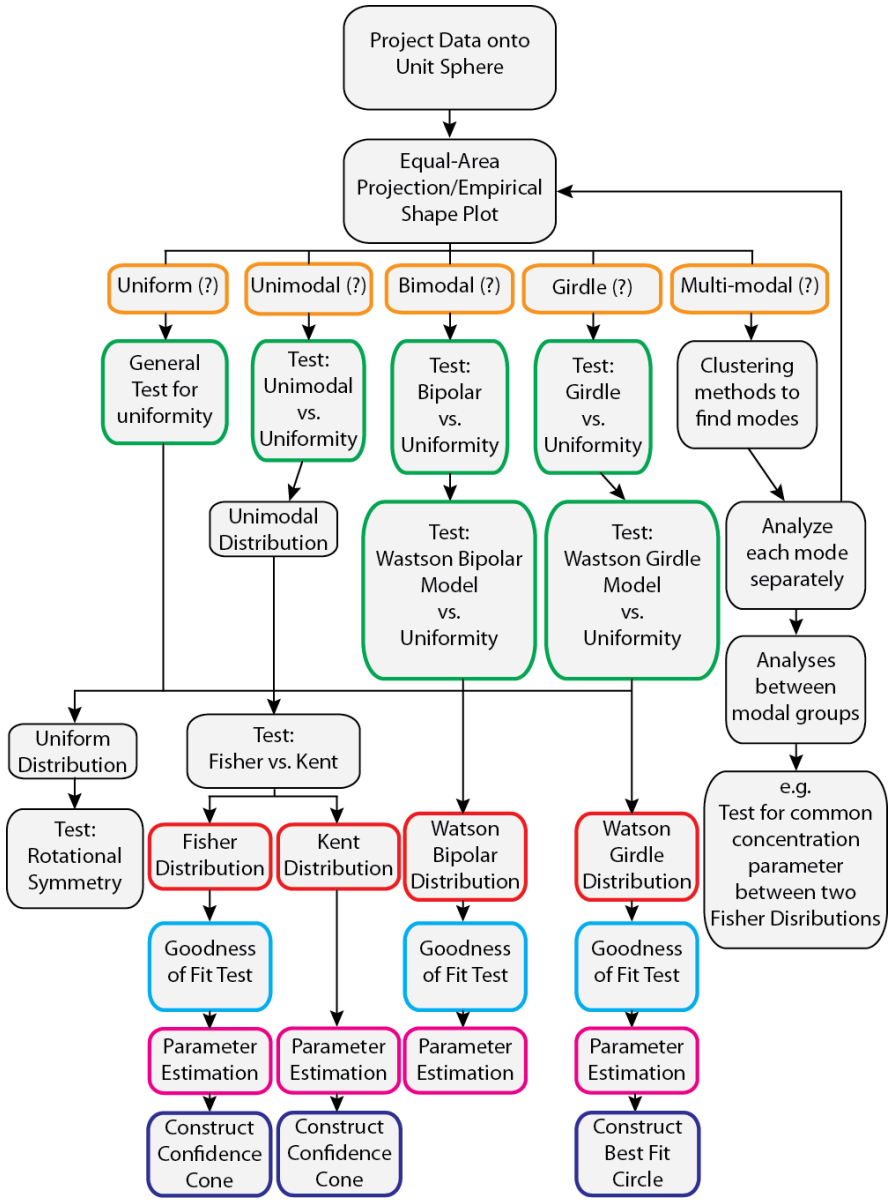

Figure 23. Spherical statistics workflow
Framework for hypothesis testing and parametric modeling of the spatial distribution of soma or axonal nodes affected by stimulation.

coordinates in 2D when projected in this manner. Data points will project progressively inwards on the 2D circle as their colatitudes vary from the North Pole to the South Pole.

$$(X_i, Y_i) = \left(\sqrt{\frac{2}{1-z_i}}x, \sqrt{\frac{2}{1-z_i}}y\right) \tag{4.1}$$

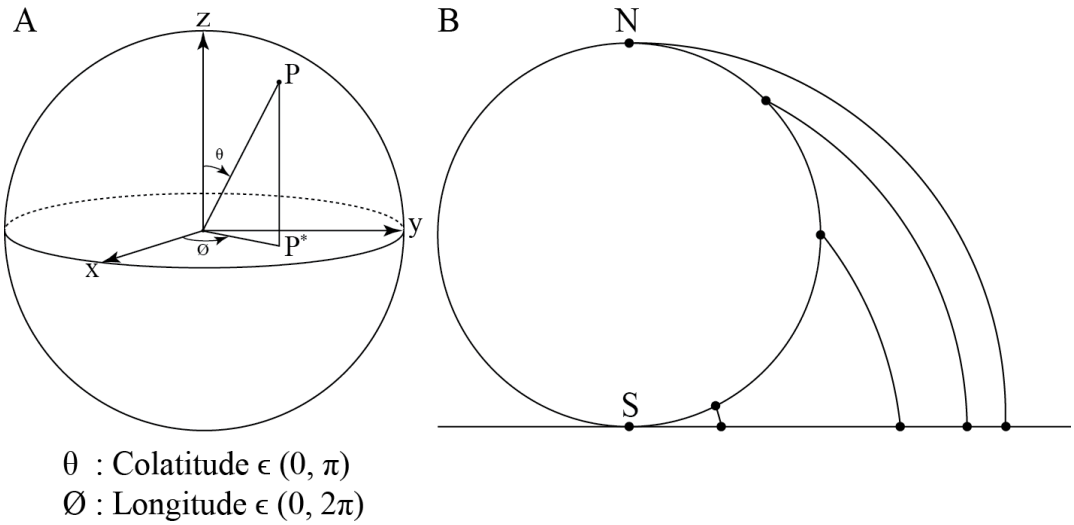

Figure 24. Data representation in 3D and projection onto 2D
(A) Data were transformed into polar coordinates with colatitude and longitude variables. **(B)** Illustration of Lambert azimuthal equal-area projection.

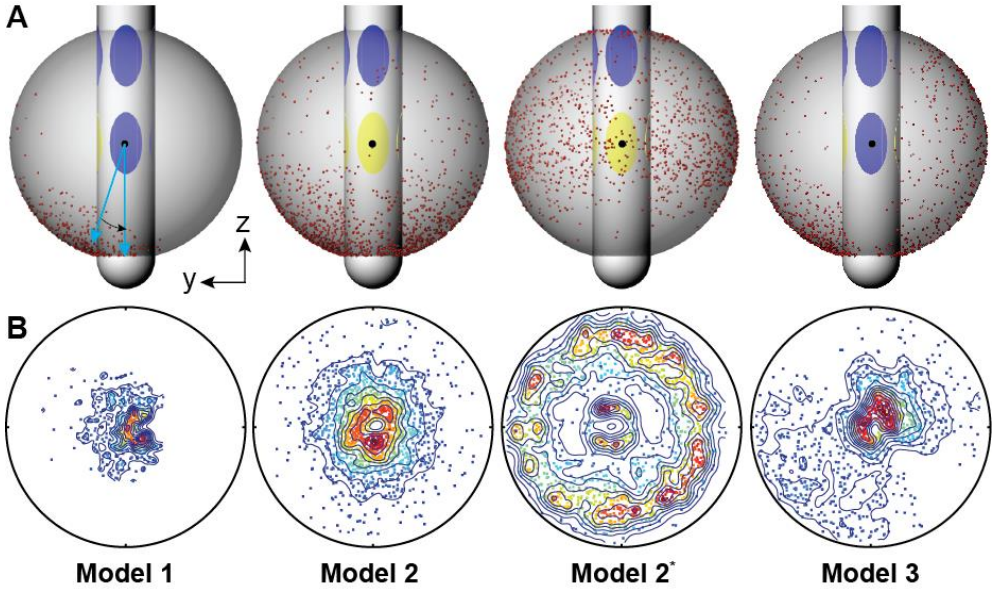

Figure 25. Model data representation in 3D and their projections onto 2D
(A) Multi-compartment, thalamocortical neuron model simulations were conducted in the context of three different stimulation configurations: monopolar cathodic stimulation through one electrode at -0.25mA (left column), monopolar cathodic stimulation through all four electrodes along a single row at -0.25mA/contact (middle two columns), and bipolar stimulation with opposing electrodes on a single row at ±1mA/contact (right column). For neuron models in which stimulation elicited stimulus-locked spike activity, the location of either the cell body (Models 1-3) or the first-activated node of Ranvier (Model 2*) was projected onto a sphere. **(B)** The mean direction of the distribution was then aligned to the South Pole (as shown in part A, left column) and then projected down to an equal area projection map to provide a basis for estimating the spatial distribution of the neuronal processes modulated by stimulation. Color indicates the density of the modulated neuronal processes.

The distribution of the projected data can be further visualized in terms of its density. A 200x200 2D histogram was constructed spanning the maximum width and height of the projected distribution and smoothed [420]. The smoothed density values at data locations were normalized to the maximum density value, assigned indexed colors, and plotted in terms of density contours (Fig. 25B). The normalized eigenvalues (τ_1, τ_2, τ_3) of the orientation matrix (2) [421] were computed, and the two-axis logarithmic plot (empirical shape plot or ESP) was constructed by plotting $\log(\tau_2/\tau_1)$ vs. $\log(\tau_3/\tau_2)$ (Fig. 26 G,H).

$$T = \begin{pmatrix} \sum x_i^2 & \sum x_i y_i & \sum x_i z_i \\ \sum x_i y_i & \sum y_i^2 & \sum y_i z_i \\ \sum x_i z_i & \sum y_i z_i & \sum z_i^2 \end{pmatrix} \tag{4.2}$$

According to Woodcock [421], points on the ESP that plot above, below the $y = x$ line, and near the origin represent cluster, girdle (equatorial/small circle), and uniform types of distributions, respectively. In addition, the mean resultant length $\overline{R}$ ($\overline{R} = R/n$, where R is the length of the resultant vector of all data point vectors on the unit sphere and n is the number of data points) and the relationship between the normalized eigenvalues can serve as further discriminators. Detailed information is listed in Table 9. Typically, uniform distributions tend to have $\tau_1 \approx \tau_2 \approx \tau_3 \approx 1/3$, clusters tend to have $\tau_3 \gg \tau_1, \tau_2$, while girdle distributions tend to have $\tau_1 \ll \tau_2, \tau_3$.

Relative magnitude of normalized eigenvalues			**Type of distribution**
$\tau_1 = \tau_2 = \tau_3 = 1/3$			*Uniform*
$\tau_3 \gg \tau_1, \tau_2$	$\tau_1 \neq \tau_2$	$\overline{R} = 1$	*Unimodal*
		Otherwise	*Bimodal*
	$\tau_1 \approx \tau_2$	$\overline{R} = 1$	*Unimodal*
		Otherwise	*Bipolar*
$\tau_1 \ll \tau_2, \tau_3$	$\tau_2 \neq \tau_3$		*Girdle*
	$\tau_2 \approx \tau_3$		*Symmetric Girdle (about polar axis)*

Table 9. Categorization of parametric distributions based on normalized eigenvalues of the orientation matrix

The procedures described above provided the basis for hypotheses on the shape of each model distribution. Based on those results, we performed a series of formal statistical tests on the datasets to determine the fit of their hypothesized models. Data hypothesized to be unimodal in distribution were tested against the null hypothesis of uniformity (H_0:

uniformity, H_A: unimodality) [422]. In the case of bimodal or multimodal distributions, the data were separated into modal groups, and each subpopulation was analyzed and tested separately. Unimodal distributions can be represented by the Kent distribution, which is very versatile because it is able to represent data with or without rotational symmetry about the sample mean direction. The Kent distribution can be characterized by 5 parameters: ξ_1, ξ_2, ξ_3, κ and total volume enclosing the population. The first three are unit vectors that represent the mean direction, major axis, and minor axis of the distribution. κ is termed the *concentration parameter,* and it is indicative of the tightness of data distribution about ξ_1. β is termed the *ovalness parameter,* and it is indicative of the amount of departure in the distribution profile from circular symmetry about ξ_1 [423]. Data that tested significant for the Kent distribution were fitted with the 5 parameters above. Assuming the data was sampled from a larger population, a 95% confidence cone was constructed by calculating the semi-vertical angle [423].

Hypothesized girdle type distributions were tested against the null hypothesis of uniformity (H_0: uniformity, H_A: girdle) [424]. Two types of girdle distributions can be distinguished based on symmetry properties. The first type is symmetry about the normal vector (polar axis) to the plane of the small circle/equator, which is characterized by the Watson girdle model [424]. The second type is symmetry about the plane of the small circle/equator itself, which is best characterized by the Bingham model [425, 426]. The first type of symmetry implies the second type, but not vice versa [414]. In this study, we focused on fitting girdle type data to the more generalized Watson girdle distribution. We performed both graphical and formal goodness of fit (GOF) tests [427] on the data fitted for the Watson girdle model to determine the adequacy of their representation. The Watson girdle distribution can be characterized by three parameters, κ, α, and β. (α, β) is the polar coordinate representation of the polar axis. κ is a concentration parameter that is negative in value. The larger the absolute value of κ, the more concentrated the data is about the polar axis. These parameters were determined for data distributions with sufficient symmetry about the polar axis as shown by the graphical and formal GOF tests.

4.3.6 Application of Parametric Spherical Statistical Models to Analyze Changes in External Stimulus Parameters

We investigated the effects of stimulation amplitude as well as the distance of the neuronal process from the active electrode on the spatial distribution of the activated neuronal population. We used the FEM of Model 1 and simulated it in two ways: 1) increased the amplitude of stimulation from 0.1 mA to 5 mA in steps of 0.1 mA, and 2) kept the stimulation amplitude constant at 5mA. In the first case, we quantified the distribution of activated neurons at each stimulation amplitude using the appropriate parametric model and analyzed the change in model parameters with increased amplitude. In the second case, we divided the space around the active electrode into concentric spherical shells centered about the FEM origin. Each shell was the difference between two consecutive spheres of radius r_1 and r_2, where $\Delta r = r_2 - r_1$ = 0.25 mm. The distribution of the activated neurons within each shell was quantified using the appropriate parametric model and the change in model parameters with respect to radial distance was analyzed.

4.4 Results

4.4.1 Graphical Interpretation of Data Distributions

All four models (using stimulation parameters described in Section 2.4) generated different distributions of activated neuronal processes (Fig. 25A). The colatitudes of most data points in Model 1 were concentrated in the $[\pi/2, \pi]$ range, while the longitudes were centered about $\pi/2$, which is the direction of the active electrode (positive y direction). Model 2 showed rather uniform distribution in the longitude of the data points, while the colatitudes were mostly concentrated in the in the $[\pi/2, \pi]$ range. In the case of Model 3, the colatitudes of most data points were centered about the $\pi/2$ and $3\pi/2$, or the axis of the active pair of electrodes. The longitudes of the data points in the hemisphere facing the cathode (positive y direction) were concentrated in the $[\pi/2, \pi]$ range, while those for data points in the direction of the anode were distributed more uniformly in the range $[0, \pi]$. The observations on these three models were consistent with our expectations. In all three

models, the data points were represented by the locations of somas, and the origin of the spherical system was the FEM origin. Since the neurons were oriented parallel to the lead with their somas at the bottom, the fact that most activated neurons had their somas located below and not above the plane of the active electrodes suggests that it was their axonal compartments that were activated directly. Model 2^* can be used to validate this observation because the locations of the first nodes of Ranvier to be activated by stimulation were used as data points. As expected, the data points in Model 2^* were concentrated around the equator of the sphere, indicating that the points of initiation for action potentials in neurons around the lead were located near the level of the plane of the active electrodes.

The EAP plots (Fig. 25B) further assisted us in identifying the salient features in the data distributions. Both Models 1 and 2 showed up as clusters on their EAP plots. The cluster was larger in Model 2, and there was a distinct mode of high concentration near the South Pole. For Model 2^*, the projected data formed a ring centered about a circle with a radius roughly half of the full 2D circle. This is the expected projection location for data points around the equator. In Model 3, the data was distinctly distributed in two groups, most likely representing neurons activated by either the cathode or the anode. We observed 2 modes of concentrated data points, albeit not completed separated. When compared to the spherical projection (Fig. 25A), we determined that the cathode (positive y direction) activated a population of neurons mostly concentrated below the plane of bottom row of electrodes. This was evident on the EAP plot as data points concentrated near the larger mode in the center. In contrast, the anode activated neurons in a more diffuse manner, as reflected by the uniformity in colatitudes. These data points appeared on the EAP plot in a large fan shape spanning half of the 2D circle. The data distribution from Model 3 suggested that the cathode most likely activated axon segments near the plane of the active electrode, while the anodal activation worked through a more distributed mechanism that may involve virtual cathodes.

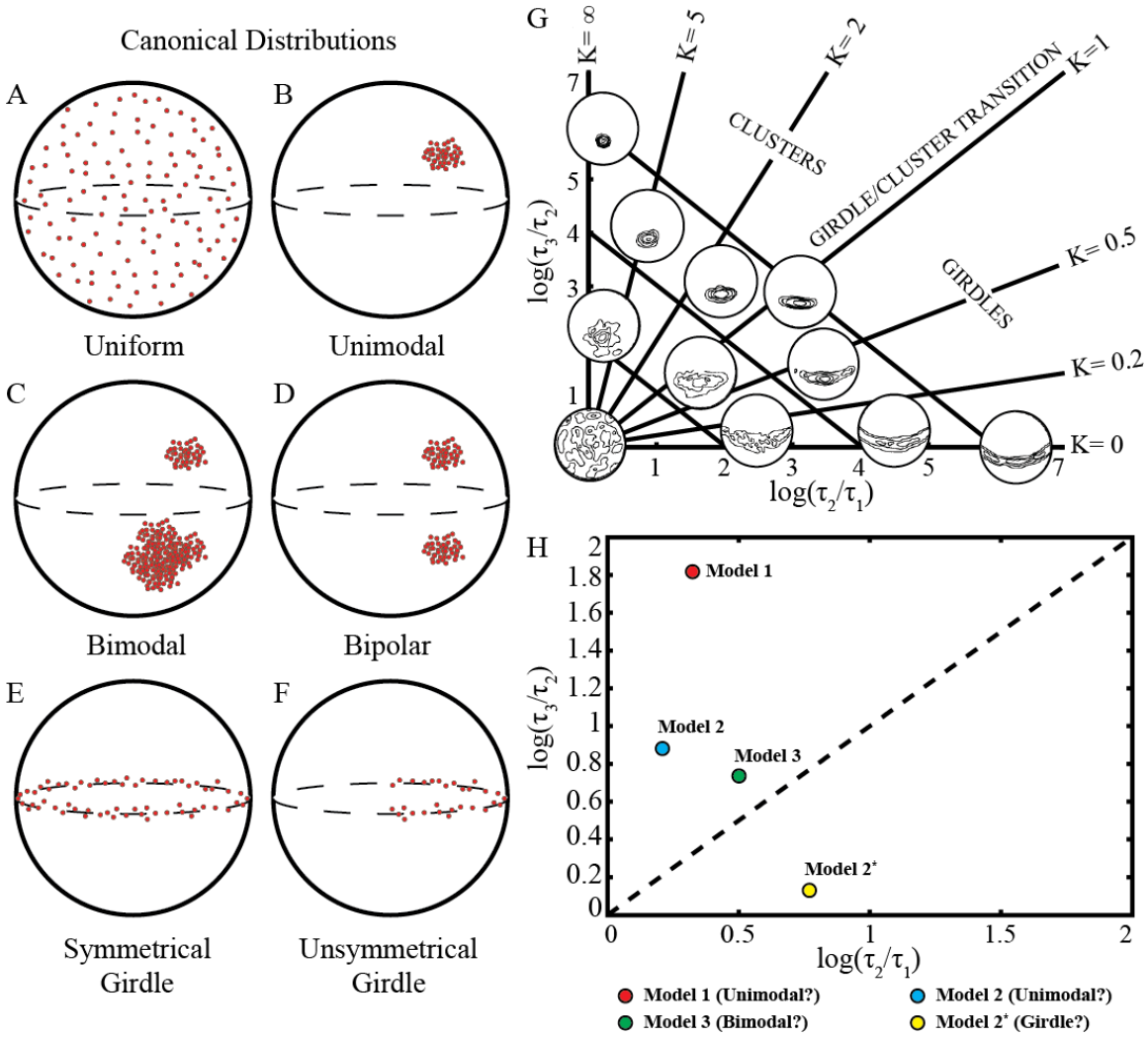

Figure 26. Canonical distributions and the empirical shape plot
(A) Uniform distribution **(B)** Unimodal distribution **(C)** Bimodal distribution **(D)** Bipolar distribution **(E)** Symmetrical girdle distribution **(F)** Unsymmetrical girdle distribution **(G)** Empirical shape plot showing the two-axis logarithmic eigenvalue ratio distributions for cluster, girdle, bimodal, and uniform distributions (adapted from Woodcock [421]). **(H)** Empirical shape plot for the thalamocortical neuron model data showing geometrical estimates for the distribution of each Model.

As described previously, the ESP can provide empirical guidelines on the shape of data distributions (Fig. 26G). Models 1, 2 and 3 all plotted above the line $y = x$ (Fig. 26H), which suggests that they are cluster type data distributions. Model 2* was situated below the line $y = x$, which indicates that it represents a girdle type distribution. Model 3 lied near the line $y = x$, which suggests that it is in a transition zone between cluster and girdle type distributions. The normalized eigenvalues had the relationship of $\tau_3 \gg \tau_1, \tau_2$,

$\tau_1 \neq \tau_2$ and $\overline{R} \neq 1$, which implies that the distribution could be bimodal, consistent with previous observation (Fig. 25). Taken together, the evidence from spherical projections, EAP plots, ESPs, normalized eigenvalues, and mean resultant lengths allowed us to make the following hypotheses on the shapes of the model distributions: Model 1 – unimodal, Model 2 – unimodal, Model 2* – girdle and Model 3 – bimodal (also listed in Table 8).

4.4.2 Spherical Statistical Testing

Models 1, 2, and 2* all tested significant for their respective alternative distributions to the uniform distribution ($p<0.05$) (Table 10). Model 1 had a smaller test statistic compared to models 2, which suggests a more diffuse distribution. In the case of Model 3, we dissected the data into two groups: data points in the hemisphere with positive y coordinates (facing cathode) were grouped into the +y cluster, while those with negative y coordinates (facing anode) were grouped into the –y cluster (Fig. 27A). The ESP (Fig. 27B) and EAP (Fig. 27C) of the +y cluster suggested a unimodal distribution, and this hypothesis was confirmed through formal statistical testing against the null hypothesis of uniform distribution ($p<0.05$) (Table 10). The ESP (Fig. 27B) for the –y cluster suggested a girdle type distribution; however, the EAP (Fig. 27D) showed a small concentrated core of data points near the South Pole while the other data points were spread over the entire hemisphere. The eigenvalues (τ_1= 0.1905, τ_2 = 0.3325, τ_3 = 0.4770) and mean resultant length ($\overline{R}$ = 0.5922) further indicated that the data was indicative of a non-symmetric girdle distribution. Statistical testing for the Watson girdle model failed to achieve significance (α = 0.05), indicating that there isn't strong symmetry of the data about its polar axis. This is a logical conclusion considering the –y cluster only consists of data from one hemisphere. Further analysis beyond the scope of this study is needed to determine if the Bingham distribution would be a more appropriate fit for the data.

	Model 1	***Model 2***	***Model 2****	***Model 3***	
Test against uniformity (H_0: uniformity)	(H_A: unimodal)	(H_A: unimodal)	(H_A: girdle)	+y cluster (H_A:unimodal)	-y cluster (H_A:girdle)
Test Statistic	1017.3436*	1985.8278*	0.1781*	1042.0512*	0.1905

Table 10. Hypothesis testing on the shape of model distributions
(* indicates test was significant at α= 0.05)

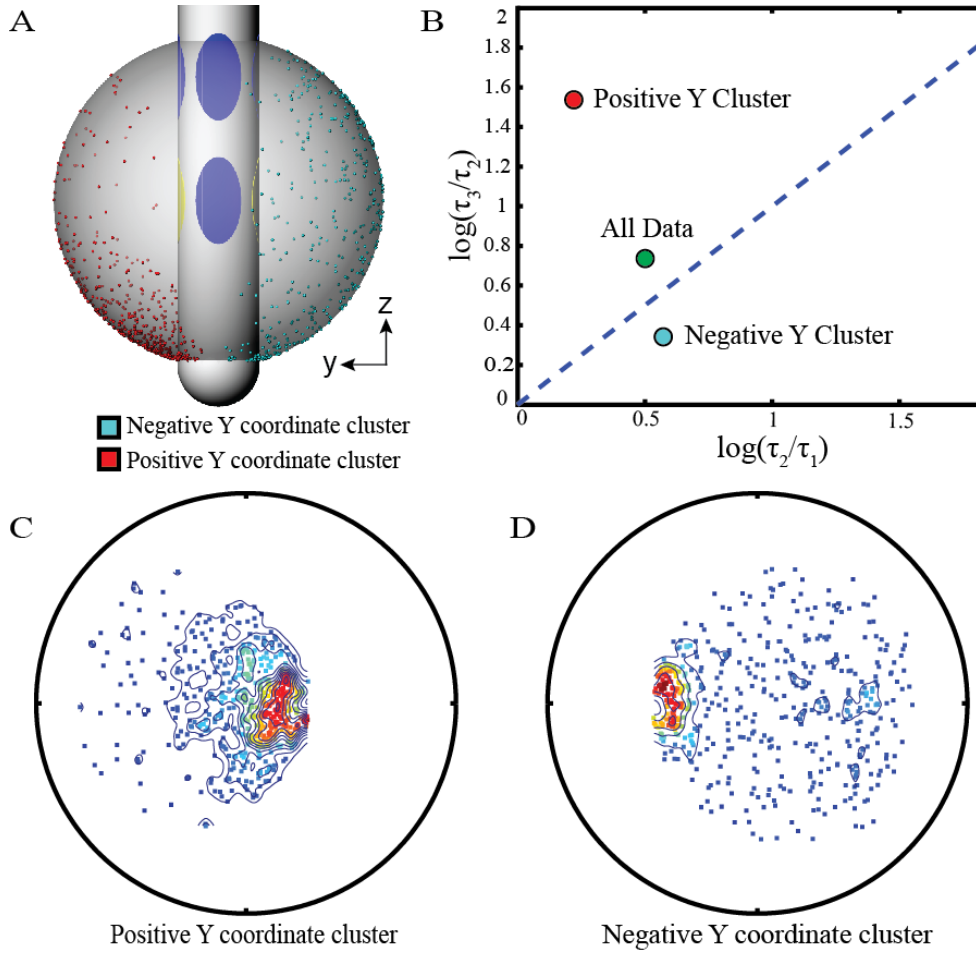

Figure 27. Analysis of bimodal distribution in Model 3
(A) Somas of neurons activated by bipolar stimulation in Model 3 projected onto the unit sphere. The red data points in the positive y hemisphere (facing the cathode) were grouped into the positive y coordinate cluster. The cyan data points in the negative y hemisphere (facing the anode) were grouped into the negative y coordinate cluster. Active electrode contacts are in yellow. **(B)** Empirical shape plot representation of all activated neurons, neurons in the positive y coordinate cluster and neurons in the negative y coordinate cluster. **(C)** Equal-area projection of data in the positive y coordinate cluster. **(D)** Equal-area projection of data in the negative y coordinate cluster.

4.4.3 Fitting Activation Data to Parametric Models

Models 1 and 2 both tested significant for the unimodal distribution, which can be well represented by the Kent distribution. The concentration and ovalness parameters κ and β are listed in Table 11. Model 1 was roughly 2.6 times more tightly concentrated about its mean direction compared to Model 2. Model 2 on the other hand was much more rotationally symmetrical about its mean direction, as indicated by the ovalness parameter β. These statistics were consistent with the fact that cathodic stimulation through one

	Model 1	*Model 2*	*Model 2**	
κ	7.9582	3.0247	-2.3161	
β	0.5408	0.1020	---	

Table 11. Kent distribution parameters for models 1,2 and 2*

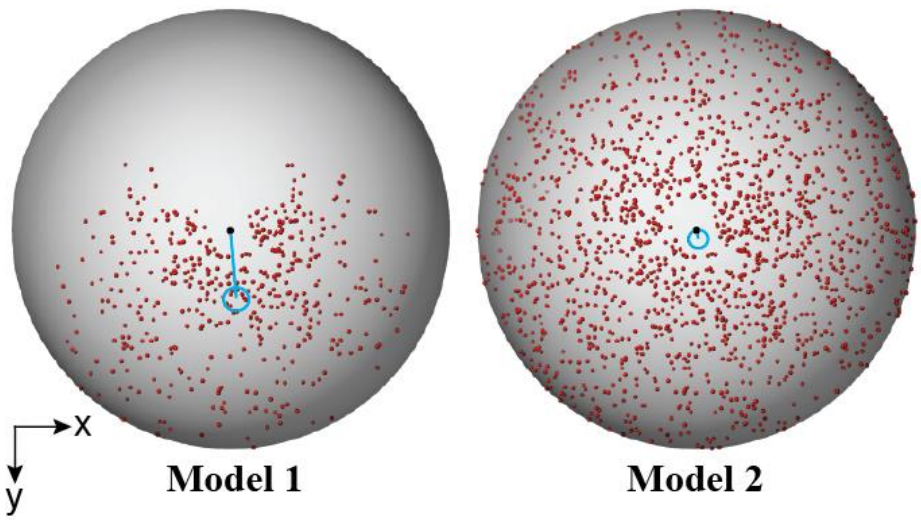

Figure 28. Projection of somas of activated neurons in models 1 and 2 onto the unit sphere
The blue line is the population mean direction in each model. The blue circle represents the 95% confidence cone.

contact confined activation to a smaller group of neurons compared to stimulation through four contacts. We have also illustrated that we can estimate 95% confidence cones [423] for these datasets, supposing that they represent samples from a larger, true population (Fig. 28).

Model 2* tested significant for the Watson girdle distribution. We performed both graphical and formal GOF tests to access the adequacy of using this parametric model. The graphical GOF test consists of the colatitude and longitude plots. The data was first arranged such that the polar axis was pointed to the North Pole and the corresponding colatitude and longitudes ($\theta_i, \emptyset_i$) were found. One can imagine that an ideal small circle/equatorial distribution should have the colatitudes of its data points concentrated in a narrow band centered about the plane of the small circle/equator, with few outliers outside of that range. The longitudes should be uniformly distributed in the range $[0, 2\pi]$. In the colatitude plot, the ordered values of $\cos^2\theta_i$ were plotted against the Chi-squared quantile, and a good fit was signified by an approximately linear line passing through the origin. In the longitude plot, the ordered values of $\emptyset_i/2\pi$ were plotted against the

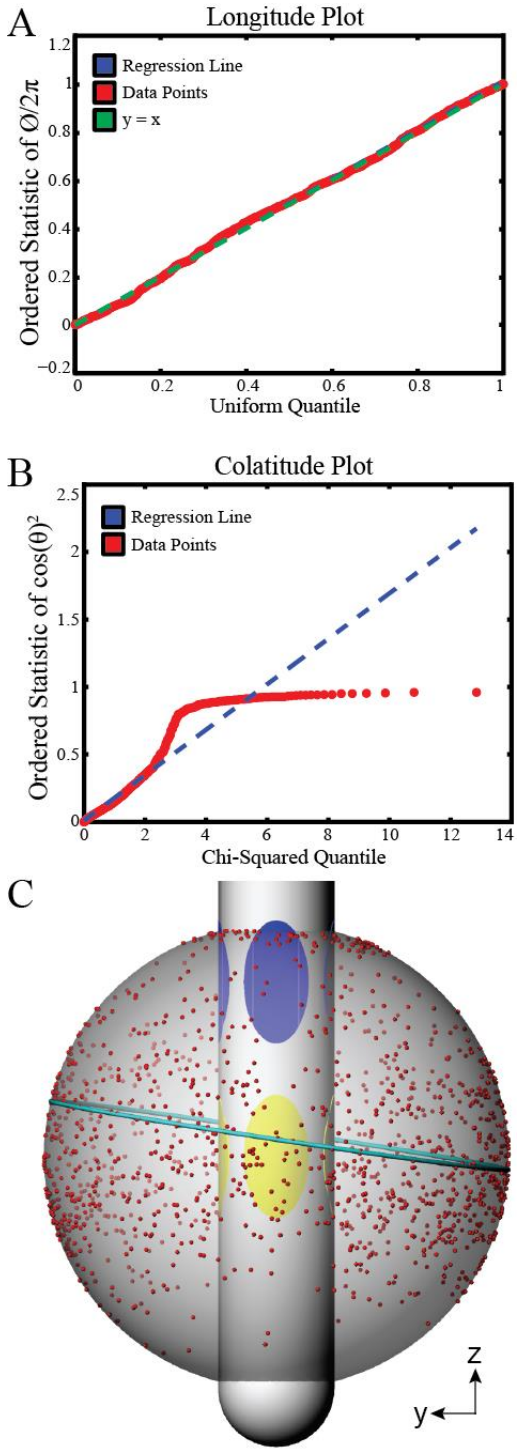

Figure 29. Analysis of the goodness of fit of Model 2* to the Watson girdle distribution
(A) Longitude plot graphically displaying the goodness of fit of Model 2* to the Watson girdle model. A good fit is signified by an approximately linear line, passing through the origin with a slope of approximately 1. **(B)** Colatitude goodness of fit plot. A good fit is signified by an approximately linear line passing through the origin. **(C)** Cell bodies of activated neurons in Model 2* projected onto the unit sphere. The cyan ring is the best-fit small circle for the data.

uniform quantile, and a good fit was signified by a line that was approximately linear, passing through the origin, with a slope of $45°$. For the data in model 2*, the longitude plot (Fig. 29A) showed an approximately linear line passing through the origin, the slope of which is 1.0131. This result indicated that longitudes of the data points are uniformly distributed in the range $[0, 2\pi]$. The colatitude plot (Fig. 29B), on the other hand, revealed some deviation from a linear line, especially towards higher $\cos^2\theta_i$ values. This was due to the presence of data points scattered away from the equator, especially those near the North Pole (Fig. 29C). The colatitude plot therefore illustrated the limitations of the Watson girdle model to accommodate the larger spread in the colatitude of the data. The formal GOF test consisted of both the colatitude test and the longitude test, and it further confirmed the interpretation of the graphical method. The colatitude test was not significant ($\alpha = 0.05$) to indicate a good fit for the Watson girdle model, while the longitude test did reach significance ($p<0.05$). We calculated the concentration parameter κ to be –2.3161 [424]. A best fit small circle was calculated [428] and it showed a slight tilt from the plane of the equator, which was most likely due to chance activation of axon nodes at lower colatitudes (Fig. 29C).

4.4.4 Effect of Stimulation Amplitude on Data Distributions

We studied the effects of stimulation amplitude on the distribution of activated neurons using the one contact monopolar cathodic stimulation model, by increasing the amplitude of stimulation from 0 to 5 mA in steps of 0.1 mA (Fig. 30C-D). The data points were represented using the locations of cell bodies of the activated neurons relative to the FEM origin. The number of activated neurons increased in a nonlinear fashion with stimulation amplitude until 1.6 mA, after which a step-like pattern of increase was observed (Fig. 30E). As shown with Model 1, the Kent distribution was adequate to model the neuronal cell population activated under this stimulation scheme. We observed that both κ and β decreased nonlinearly and eventually leveled off at higher stimulation amplitudes (Fig. 30F).

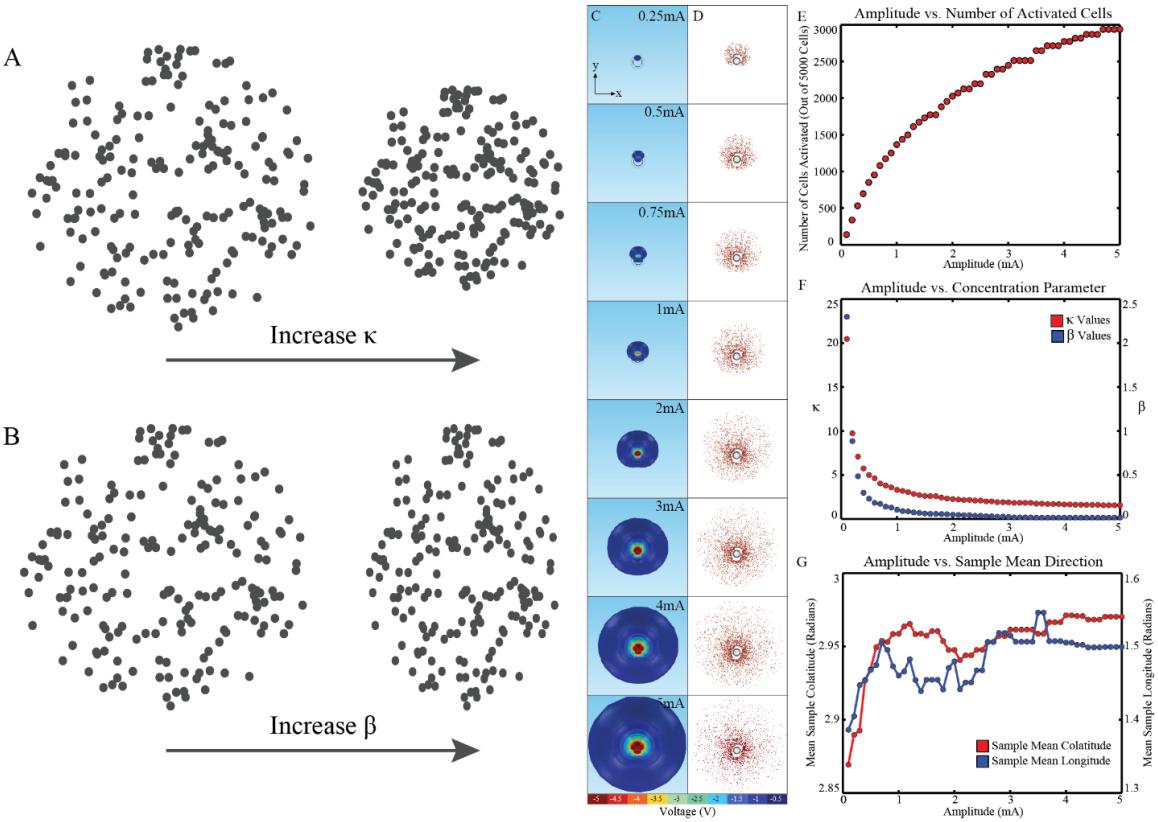

Figure 30. Analysis of activation profiles from single contact monopolar cathodic stimulation using the Kent distribution

(A) Idealized illustration of change in Kent distribution with increased concentration parameter κ. **(B)** Idealized illustration of change in Kent distribution with increased ovalness parameter β. **(C)** Top-down view of the voltage fields from single contact monopolar cathodic stimulation at eight example amplitudes. **(D)** Top-down view of the distribution of cell bodies of the corresponding activated neurons. **(E)** Number of activated neurons vs. stimulation amplitude. Stimulation amplitudes ranged from 0.1 – 5 mA at increments of 0.1 mA. **(F)** The distributions of activated neurons were characterized using the Kent model. The plot shows the change in Kent model parameters (κ, β) with stimulation amplitude. **(G)** Change in sample mean colatitude and longitude with stimulation amplitude.

4.4.5 Model Distribution along the Radial Direction

We modeled monopolar cathodic stimulation through one contact at 5 mA and analyzed the activated neuronal populations within spherical shells separated by 0.25 mm (Fig. 31A). The total number of cell bodies within each shell plateaued after the 6th shell (1.25 – 1.5 mm). The number of activated neurons within each shell reached a maximum of 257 in the 6th shell and then steadily decreased to 92 in the last shell (4.75mm – 5mm). The percent activation within each cell decreased from 100% in the first three shells to 30.26% in the last shell (Fig. 31C). EAP plots of activated populations within each shell suggested that the shape of the activated neuronal population tended to be more erratic in

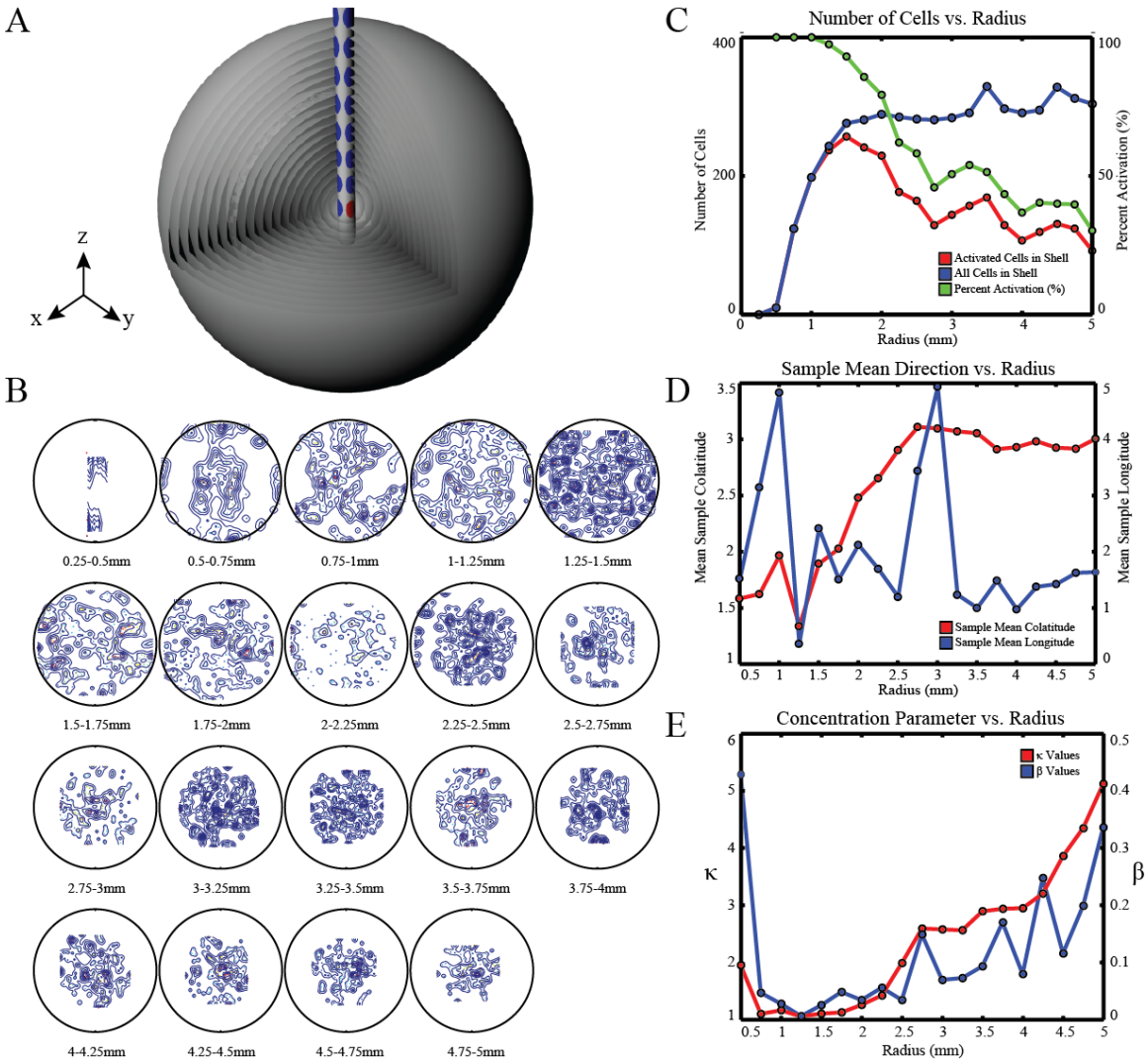

Figure 31. Analysis of activation profiles within concentric spherical shells using the Kent distribution

(A) Illustration of the concentric spherical shells about the center of the bottom row of electrodes. The thickness of each shell is 0.25 mm. The red electrode contact delivered cathodic stimulation at 5 mA. **(B)** Equal area projection of the cell bodies of activated neurons within each spherical shell. **(C)** Number of activated neurons vs. radius of spherical shell. **(D)** Sample mean colatitude and longitude of activated neurons vs. radius of spherical shell. **(E)** The distribution of activated neurons in each spherical shell was characterized using the Kent model. The plot shows the change in Kent model parameters (κ, β) with radius of spherical shells.

the first few shells close to the lead, which had fewer cells, and then gradually became more concentrated and rotationally symmetric (Fig. 31B). This was confirmed through analysis of the changes in mean colatitude and longitude along the radial dimension (Fig. 31D). The mean longitude remained relatively stable about $\pi/2$, which is the direction of

the active contact (Fig. 31A). Fluctuations in mean longitude were observed (shells 2, 3, 10, 11) and these could be attributed to sampling issues (i.e. more model neurons are needed to populate the model). The mean colatitude steadily increased from $\pi/2$ to π within the first 10 shells and remained at approximately that value in shells further away (Fig. 31D). This suggested that as distance away from the lead increased, the majority of the cell bodies of activated neurons were below the plane of the active contact. Finally, we fitted the Kent distribution to the activated neuronal populations within each shell and estimated the parameters κ and β. Both parameters fluctuated initially near the lead, but then steadily increased along the radial dimension, suggesting more focal and symmetrical activation profiles further from the lead despite a reduced probability of activation.

4.5 Discussion

In this study, we present a spherical statistics framework for quantifying the spatial distribution of modulated neuronal processes around a DBS lead. The framework included visualization techniques, empirical shape analysis, hypothesis testing, and data parameterization. We have demonstrated that the directional distribution of neurons activated by stimulation can be characterized by parametric models, and the model selection and parameterization can depend on the data representation (e.g. soma vs. axon node as the modulated process). In addition, we analyzed the change in model parameters with respect to external parameters, such as stimulation amplitude and radial distance away from the FEM origin.

4.5.1 Utility in Quantifying the Spatial Distribution of Neuronal Activation around a DBS Lead

There is a clinical need for DBS electrode arrays with the capability to provide directional stimulation via steering and shifting of the output electric field [354], [364]. Such capability is important in cases of off-target DBS implants [215], [232] and in avoiding inducing adverse side-effects for the patient [429], [254], [355]. Consequently, much research has gone into the development [430], [431], modeling [215], [213], [359]

and evaluation [191], [238] of high-density DBS arrays with circumferentially-segmented electrodes and independent current controlled stimulators [432]. A challenge when studying the effects of directional stimulation is to develop quantitative metrics for assessing the spatial distribution of neuronal activation around a DBS lead. Currently, the most widely used metric is the volume of tissue activated (VTA) [216], which is the volume enclosed by activated neurons or axons. Parameters such as the center of mass, total volume and maximal vertical/radial extent of activation can then be used to further characterize the VTA [235]. However, these measures only provide a fragmented picture of the data distribution making it difficult to generalize to compare different DBS settings. The advantage of spherical statistics lies in its ability to enable the user to understand the fundamental characteristics of the shape of a spatial distribution (e.g. unimodal, bimodal, girdle, etc.). In the case of DBS, it provides a number of parametric models that can be used to quantitatively describe the spatial distribution of modulated neuronal processes around a DBS lead. For example, in a recent study [433], researchers were able to use engineering optimization principles to design electrodes that preferentially activated neuronal elements in one orientation versus those in another. Stimulating the same neuronal population using two different electrodes would give different activation profiles (subject to certain definition of origin and data representation, e.g. first axon node that was activated) in space, which could potentially be represented by parametric spherical statistical models. Consider a scenario in which the Kent distribution was adequate to characterize the distribution of axon nodes that were first activated by stimulation in a neuronal population. Examining the differences in model parameters ξ_1, ξ_2, ξ_3, κ and β can provide the directions of most and least data density, the mean direction of activated nodes, as well as degree of symmetry about the sample mean direction. This information is much richer than simply knowing a percent activation level for each electrode. It can potentially give insight into inhomogeneities and anisotropies in tissue conductance (if modeled) as well as directional distributions of second spatial derivative of the extracellular voltage field. Researchers can also apply these parametric models to electrophysiological or optical recording data and study the spatial activation profiles of neurons under DBS in a quantitative manner. The results can then be used to

inform new DBS electrode array designs as well as programming algorithms. The results from such studies can also benefit clinicians by providing 1) quantitative data on the feasibility of radial directing of stimulation, 2) quantitative comparisons of neuronal activation profiles between different target brain structures, and 3) statistical description of their intuitions on shaping of the electric field.

4.5.2 Types of Spatial Distributions

We have demonstrated that spherical statistics is robust in quantifying spatial distributions of neurons activated by different stimulation configurations. Data representation (e.g. soma vs. axon node processes) is an important consideration and can significantly alter the shape of the resulting distribution. For instance, cathodic stimulation in all four directions (Model 2^*) activated axon nodes in a ring-like formation concentrated about the equator of the unit sphere (Fig. 25), which can be characterized by the Watson girdle model. However, the distribution of cell bodies of activated neurons in the same model (Model 2) displayed a unimodal formation centered about the South Pole (Fig. 25) and could be characterized by the Kent model. This discrepancy is explained by the fact that action potentials are thought to initiate first in the axons and propagate antidromically towards the soma [161] with DBS waveforms. Since the cells are oriented such that their somas are located beneath their axons in this example, it is logical that most activated cells would have their somas in the southern hemisphere of the unit sphere, below the level of the active contacts. Cathodic stimulation in one direction (Model 1) also resulted in a unimodal distribution of activated cell bodies. Compared with stimulation in all four directions (Model 2), stimulation in one direction resulted in activation that was more focused in direction (larger κ) and more oval (less rotationally symmetric) in shape (larger β). In the case of bipolar stimulation (Model 3), a bimodal distribution emerged from the cell bodies of the activated neurons. In the projected view (Fig. 27A), data in the hemisphere facing cathodic stimulation (+ y cluster) was mostly concentrated near the South Pole, indicating that action potential initiation in these neurons most likely occurred near the level of the cathode. On the other hand, the soma locations of activated neurons in the hemisphere facing anodic stimulation (– y cluster)

displayed much more variation in colatitude (Fig. 27D). There was a small concentration of data points with high colatitude values near the South Pole, while the rest were diffusely distributed over the entire range. This could be explained by anodic stimulation creating virtual depolarization [434] at locations along the axon that were further away from the plane of the anode. Together, the modeling results shown in this study (albeit using idealized model geometries) demonstrated that: 1) cathodic stimulation confined activation of axon nodes of Ranvier within a band centered about the plane of the active electrodes, which is suitable for focal activation; 2) anodic stimulation achieved broader activation in terms of direction and would be suitable for broadening activation of a given target; and 3) axonal projection morphologies play a critical role in determining the shape profile of the somatic population directly affected by the stimulation.

4.5.3 Empirical Analysis and Statistical Testing

Empirical analysis and statistical testing are complementary approaches that serve different functions. The ESP is able to provide a general outline of the data distribution and put it into perspective in a continuum of changing morphologies. Other empirical information listed in Table 9 allows for fast categorization of the shape of the data distribution and narrows the direction of further data analysis. However, formal statistical testing is needed to provide the confidence in confirming or rejecting a hypothesized shape. Ambiguities may arise in this process, when the shape of a distribution falls in a transition zone between two different categories (e.g. bimodal vs. girdle). In such a case, fitting the data to different parametric models and assessing the goodness of fit in each case becomes important. Discordancy tests are available to identify the outliers in the data that negatively affect the fit to a particular parametric model. These outliers can then be removed to achieve a better fit of the data. Once parametric models have been established for different stimulation settings, they can serve as quantitative metrics to describe and compare the spatial distributions of activated neuronal populations under these different settings.

4.5.4 Effect of Stimulation Settings on the Parametric Model Parameters

The parameters of parametric models reflect the characteristics of the underlying distribution and can be used for quantitative analysis of the effects of directional stimulation. For example, the concentration parameter κ of the Kent distribution, when analyzed in the context of neuronal activation profile, is reflective of the degree of focus in stimulation. A higher κ value indicates that in directional terms, neuronal activation is more confined about a certain mean direction, which in turn reflects a more focused effect in stimulation. Similarly, the ovalness parameter β is a reflection of the uniformity of stimulation. A lower β value is associated with more rotational symmetry of the distribution and vice versa for higher β values. The differences in the amount of rotational symmetry can be further indicative of either asymmetry in the distribution of the underlying neuronal population or a difference in the mechanism of activation (e.g. cathodic vs. anodic stimulation).

Unidirectional cathodic stimulation at increasing amplitudes resulted in unimodal distributions of activated neurons (soma) that were well characterized by the Kent model (Fig. 30). The model parameters of κ and β decreased in a nonlinear fashion and eventually flattened out at higher amplitudes of stimulation. The implication is that at lower stimulation amplitudes, the activated neuronal population is more concentrated about its mean direction while less rotationally symmetric in shape. At higher stimulation amplitudes, a larger population was activated, which was more diffusely distributed about the mean direction but more rotationally symmetric in shape (Fig. 30C,D). The decrease in κ and β largely happened within 1 mA of stimulation, suggesting that the shape profile of the activated population became mostly stable above this threshold. This reinforced the observation that the mean colatitudes and longitudes of the activated populations also became relatively stable after 1 mA.

This approach of using the Kent distribution to model the activation profile of monopolar stimulation can be used to assess the viability of directional stimulation in a region of interest. As shown previously, nodal activation directionality may not reflect somatic activation directionality. It is expected that effective current steering via monopolar stimulation through one electrode would yield an activated cell body

population that forms a Kent distribution, with mean direction close to the direction of stimulation. Distributions not described by the Kent model or have mean directions that largely deviate from the direction of stimulation would suggest that axonal projections are such that they render directional stimulation ineffective.

4.5.5 Limitations and Considerations

In this study, we constructed a simplified and idealized computational model to demonstrate the application of spherical statistics. Additions of inhomogeneous and anisotropic tissue conductivities, non-uniformity current density distributions across the electrode surface as well as voltage drop and capacitance at the electrode-electrolyte interface would make for a more realistic model and likely affect the model fits [398]. FEM mesh density is an important consideration to ensure convergence of action potential thresholds [435]. We did not validate convergence of action potential thresholds in this study because this work was meant to be a proof-of-concept demonstration of the application of spherical statistical analysis to computational models of DBS. Ensuring convergence of action potential thresholds is very important, but does not play as significant of a role in this study (compared to for example other studies that aim to use computation modeling to elucidate mechanisms of action in DBS), because the same principles and methods can be applied to analyze data on neuronal activation profiles even if they deviated from the absolute truth (obtained using more mesh elements). The axonal projection patterns and uniform distribution of neurons around the DBS lead that were modeled in this study were grossly idealized scenarios. Diffusion tensor imaging with probabilistic tractography methods [436], [268] as well as neuroanatomical tracing studies [437] could be used to construct realistic fiber tract morphologies, and the same analysis techniques and processes demonstrated in this study would apply.

Data representation in spherical statistical analysis can impact results and their interpretation. In this regard, the selection of coordinate systems is an important consideration and will vary depending on the particular application. Another consideration in data representation is the potential for different spatial profiles in the distributions as one extends in space from the DBS array. In this study, we analyzed the

shape profile of activated neurons within concentric spherical shells. However, this approach could be modified by adopting amorphous shells that conform to layered structures such as the layers of the cortex or segments within deep brain structures.

There are many other useful methods within the field of spherical statistics not described here, such as analyzing properties of rotational symmetry about an axis [438] or testing for common mean direction between two distributions [439]. Additionally, there are other parametric models including the Wood distribution (for bimodal distributions with two modes of equal strength) [440], the Bingham distribution (for symmetric/asymmetric girdle or bipolar distributions) [425] [426], as well as the multipurpose General Fisher-Bingham distribution [441]. In these cases, there is a trade-off between the complexity of a model and its range of applicability, which should be weighed by the user. In cases of multimodal distributions, as one would expect with neuronal populations activated by multipolar stimulation, clustering the data (e.g. using k-means clustering) into smaller unimodal or bimodal groups and analyzing them individually may be the most suitable and informative approach [414].

4.5.6 Applications to other Neurophysiological Recording Modalities

Advances in two-photon imaging have enabled *in-vivo* real-time imaging of large neuronal populations (with single-cell resolution) [442] [443] as well as simultaneous monitoring of different brain regions [444]. The spherical statistical approach used in the context of DBS has potential to be of value in quantifying network dynamics of neurons and constructing spatiotemporal maps of their activities. Studies have shown that spiking activities in rat neocortex are heterogeneous over time, generated by a continually changing subpopulation of active neurons [443]. Furthermore, microstimulation of the cat cortex has shown that neuronal populations are sparsely activated by stimulation, and patterns of activation are highly dependent on electrode location and likely arise from direct activation of axons in the vicinity [445]. Similar to what we have described in this paper, spherical statistics can be applied in these studies by introducing a reference origin via the stereotactic reference system. The origin of the reference system may be placed at a point on the cortical surface, in which case all imaged cells would reside in the

hemisphere below the cortex. This framework could provide a unified view of the distribution of neuronal dynamics in all cortical layers. Alternatively, the origin may be placed at a point in a particular cortical layer in the middle of the imaged volume (e.g. layer III, which contains projections to other cortical layers [446]), and neuronal activity would be analyzed from the perspective of this locus. Spherical statistics can also be useful in assessing whether two cortical regions are correlated by determining the correlation coefficient between two random vectors [447]. These vectors could represent time ordered population mean directions from two cortical areas. Correlation could be established if shifting the mean direction of neuronal activity in one region through stimulation induced a shift in the other region as well.

4.6 Acknowledgements

This study was supported by the College of Science and Engineering, the Institute for Translational Neuroscience at the University of Minnesota, the Michael J. Fox Foundation and an NIH grant (R01-NS081118).

Chapter 5

Spatial characterization of stimulation-induced neuronal activity around a chronically implanted thalamic deep brain stimulation array

5.1 Overview

5.1.1 Objective

The volume of tissue activated (VTA) is a key concept in computational models of DBS to measure the extent of modulation around the DBS lead. However, such models lack the morphological and network complexities that are present in the *in-vivo* brain. This study investigates the *in-vivo* VTA by examining spatial characteristics of stimulation-induced neuronal activity around chronically implanted thalamic DBS arrays (DBSAs) in two non-human primates.

5.1.2 Approach

In this study, two rhesus macaque monkeys were each implanted unilaterally with a 32-contact (8 rows × 4 contacts/row) DBSA in the cerebellar receiving area of the thalamus (nucleus ventralis posterior lateralis oralis or VPLo). Biphasic, charge-balanced (100μs cathodic pulse, 20μs interphase delay followed by a 100μs anodic phase, 100Hz at 150, 250, and 350μA) waveforms were delivered individually through each electrode from a particular row of electrodes on the DBSA. Single-unit microelectrode recordings were performed around the chronically implanted DBSA before, during and after DBS. Template subtraction was applied to remove the stimulus artifact, and unit-spikes were then sorted. Firing rates between the pre-DBS and DBS periods were compared for each neuron using the Mann-Whitney U test ($p<0.01$, 1s bins). Peri-stimulus time histograms (PSTHs) (100μs/bin) were generated for each cell. Entropies of the PSTHs during the pre-DBS and DBS-on periods were calculated and the difference between the two were assessed. Significant firing pattern modulation (FPM) was determined using a bootstrap statistical method.

5.1.3 Main Results

Neurons exhibiting firing pattern and/or rate modulation during VPLo-DBS were surprisingly sparse and distributed, and not confined to regions in the immediate proximity of the active electrode. The strengthening of modulatory effect with increased stimulation amplitude was only observed in a small group of cells. The majority of cells were not influenced by DBS in any way. For those that were modulated by DBS, their responses increasingly shifted from firing rate modulation (FRM) to FPM with increased stimulation amplitude. Interestingly, only 3.25% (±3.8%) of DBS pulses produced phase-locked spikes in cells exhibiting significant excitatory FPM. DBS also suppressed 81% ± 4.44% of phase-locked spikes in inhibitory FPM.

5.1.4 Significance

While computational models often predict uniform modulation of neuronal activity around a DBS lead, this study demonstrates that the *in-vivo* VTA consists of a small

fraction of neurons that are sparsely distributed within that volume. The response of these cells to DBS in terms of firing pattern and rate is amplitude dependent. Moreover, neuronal activity that is time-locked to DBS pulses does not follow the one-to-one pattern of entrainment often assumed in computational models. Instead, only a very small fraction of stimulus pulses actually result in phase-locked spike activity. Taken together, these findings outline the properties of neuronal response to DBS in-vivo, and highlight the need for computational models to incorporate realistic network connectivity and neuronal morphologies in order to reproduce these results.

5.2 Background

The VTA is a well-established computational metric to assess the extent of neuronal modulation via DBS [217], [216]. The second spatial derivative of the extracellular voltage potential along neuronal processes is also known as the Activating Function (AF). It is responsible for inducing transmembrane currents that result in direct depolarization of a neuron [448] (Fig. 32). In the case of unmyelinated axons:

$$\mathrm{AF} = \frac{d^2 V_e}{dx^2} \tag{5.1}$$

where x and V_e are positions and the extracellular voltage along the length of the axon, respectively. In the case of myelinated axons:

$$\mathrm{AF} = \frac{\Delta^2 V_e}{(\Delta x)^2} = \frac{V_{e,n-1} - 2V_{e,n} + V_{e,n+1}}{(\Delta x)^2} \tag{5.2}$$

where Δx is the distance between two adjacent nodes of Ranvier, $V_{e,n-1}$, $V_{e,n}$, $V_{e,n+1}$ are the extracelluar voltages at adjacent nodes $n-1$, n and $n+1$, respectively. This intermodal distance Δx scales linearly with the diameter of the axon.

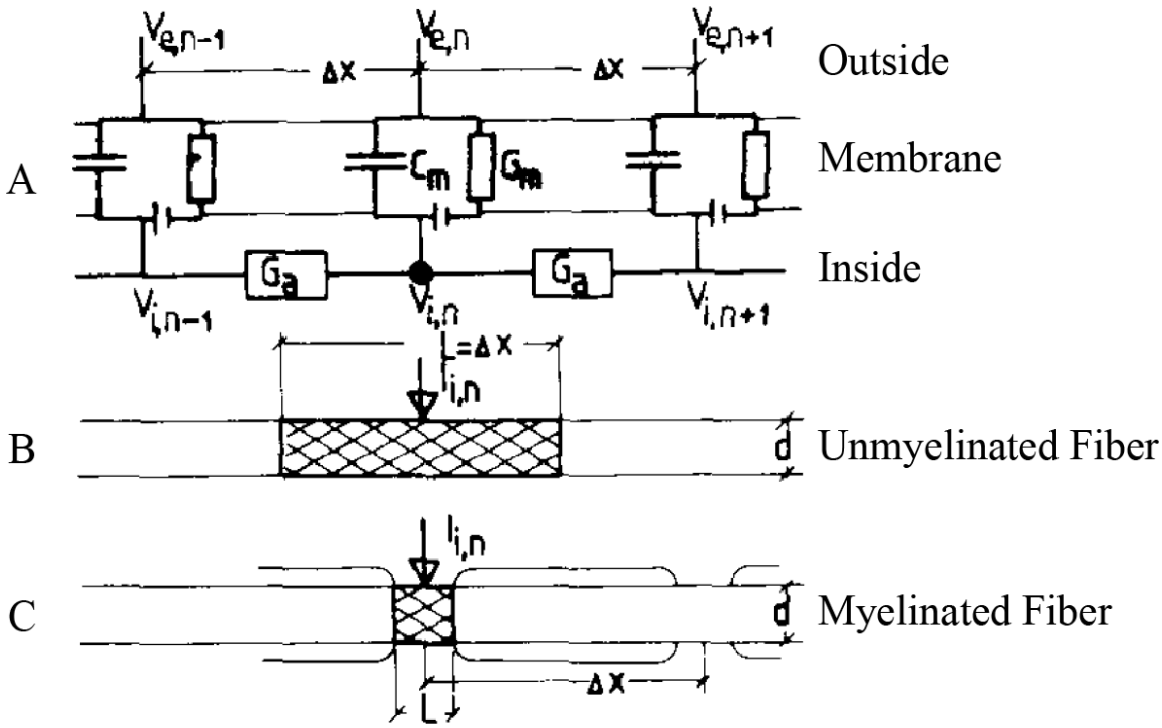

Figure 32. Equivalent circuit model of the axon and injection of transmembrane current
Unmyelinated as well as myelinated fibers are segmented into cylinders of length Δx**.** In the case of myelinated axons, Δx represents the intermodal distance. Within one segment the membrane is active in the cross-hatched area of length L. For the myelinated axons, this area is the gap in the myelin sheath and L is the nodal gap width. For the unmyelinated axon, L = Δx. (A) The membrane of every cylinder is simulated by an equivalent circuit. $C_m$is the capacity of the ionic voltage source, G_m is the nonlinear membrane conductance, G_a is the conductance of the axoplasm between two segments. $V_{e,n}$ and $V_{i,n}$ are the external and internal potential at the nth segment, respectively. $I_{i,n}$ is the induced transmembrane current through the nth segment. Adapted from [383].

Utilizing this principle of axonal activation, finite-element volume conductor models are used to extract the voltage field generated from DBS. The resulting AF map is then interpolated onto multi-compartment model neurons/axons that are distributed in some fashion around the DBS lead. The VTA at a certain stimulation amplitude (voltage controlled/current controlled stimulation) is comprised of the volume encompassed by all model neurons that generated stimulation induced action potentials. The VTA approach is great for visualizing the extent of modulation of a target of interest on a patient-specific basis [216], [398], [449] and helpful with guiding DBS programming [450], [451], [452], [453]. It is also an important research tool to investigate the current/field steering effects

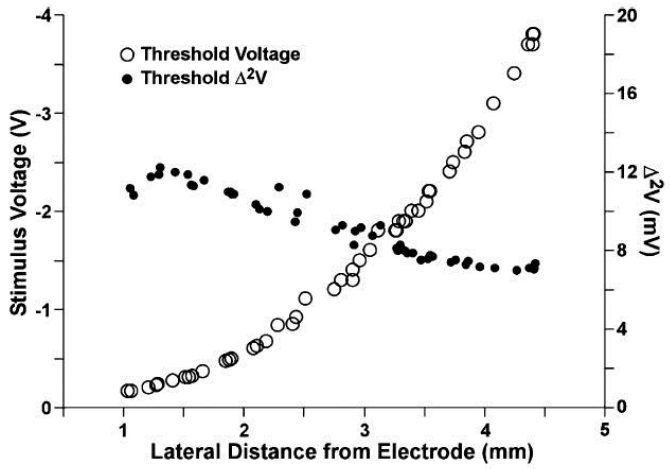

Figure 33. Voltage distance relationship for large diameter axons during DBS
Adapted from Figure 2 from [217]. The axons were positioned randomly in the model tissue medium and oriented parallel to the shaft of the DBS lead.

of directionally segmented DBSAs [454], [235], [232], [364]. However, it must be noted that the VTA method often involves certain simplifying assumptions and does not fully represent the complexities of the *in-vivo* brain. Firstly, most VTA studies [455], [217], [456] use multi-compartment axon models because axonal elements are presumed to be the most excitable components of neurons around the DBS lead [203], [457], [458], [459]. This ignores the dynamics of the soma, whose responses to DBS can be markedly different from the axon [161]. Secondly, these model axons are often arranged in idealized grid patterns either parallel [217] or perpendicular [455] to the shaft of the DBS lead. Thirdly, the complex networks of excitatory and inhibitory neuronal populations in DBS target structures [112], [460] and their connections to other regions of the brain [461], [462], [463], [464], [465] were not modeled. With isotropic tissue conductivities, the VTA has been shown to be spheres that increase in size with increased stimulation amplitude [217] (Fig. 33). However, studies in the *in-vivo* brain have shown that the activation profile by electrical stimulation is much more complex [445], [156]. Using two-photon calcium imaging, Histed et al. [445] visualized cortical neuronal activation under microstimultion and found that the in-vivo VTA around the intracortical electrode was sparsely populated with activated neurons. Stimulation did not bias towards activating neurons near the tip of the electrode. Contrary to conventional wisdom that

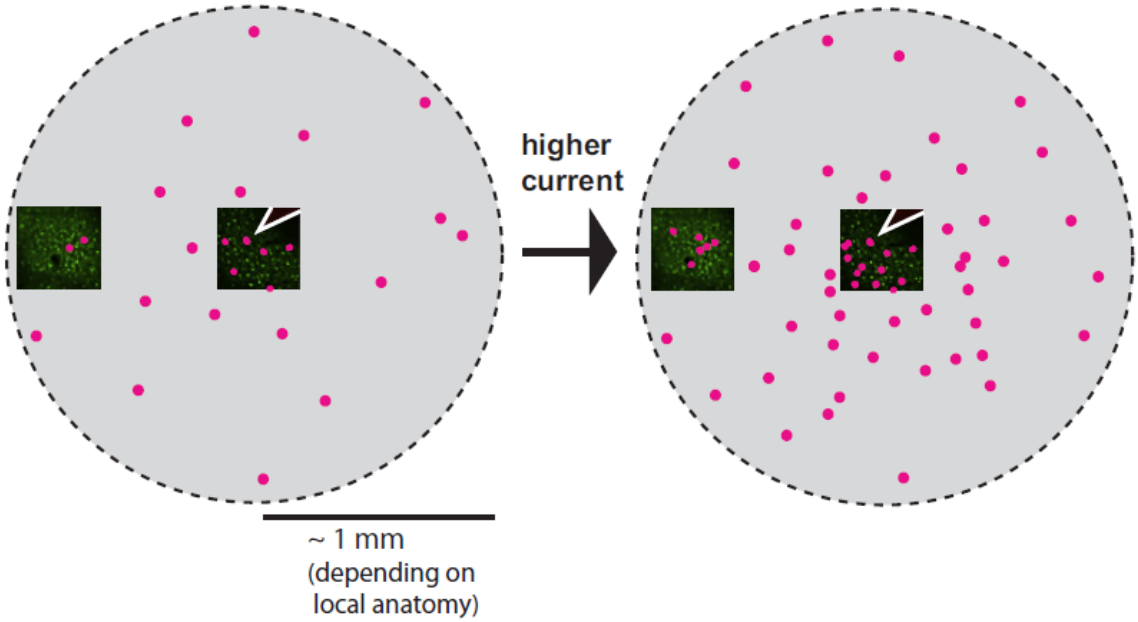

Figure 34. The in vivo VTA
Adapted from Figure 8B from [445], illustrating the change in the *in vivo* VTA with increased stimulation amplitude.

10μA of stimulation would only be capable of activating cell bodies within a radius of 65μm from the tip of the microelectrode [382], the researchers found that cells hundreds of microns away can be activated with as little as 4-9μA of stimulation. This finding is corroborated by studies in the globus pallidus internus (GPi), where cells 250-600μm away from the microelectrode tip were found to be suppressed with 10μA of stimulation [156]. Histed et al. [445] also found that increasing the amplitude of stimulation gradually fills in a large sphere of activated cells, instead of activating cells further away (Fig. 34). These findings suggest that the *in-vivo* VTA is more nuanced compared to the computational VTA. Better understanding of the properties of the *in-vivo* VTA will lead to the development of more accurate model VTAs. Here, we propose two main directions of investigation to understand the *in-vivo* VTA in the context of thalamic DBS: (1) characterize the spatial neuronal activation profile with varying stimulation amplitudes and (2) investigate the changes in the actual spike response of neurons within the VTA. Two non-human primates were chronically implanted with DBSAs in VPLo. Microelectrode recordings of thalamic neurons were made in a grid pattern around the

DBSA, before, during and after stimulation through the DBSA. Neuronal firing rate and pattern changes as a function of distance from the active contact and stimulation amplitude were analyzed using unit-spike data.

5.3 Methods

5.3.1 Subject

Two female rhesus macaque monkeys (*macaca mulatta*, Monkey K and Monkey U) were used in this study. All procedures were approved by the Institutional Animal Care and Use Committee of the University of Minnesota and complied with United States Public Health Service policy on the humane care and use of laboratory animals. The animals were housed individually with environmental enrichment, provided with water ad libitum, and given a range of food options including fresh fruit and vegetables. All efforts were made to provide good care and alleviate any discomfort for the animals during the study. Pre-operative 7T MRI was acquired at the Center for Magnetic Resonance Research (CMRR) at the University of Minnesota using a passively shielded 7T magnet (Magnex Scientific) for both animals. During the imaging sessions, the animals were anesthetized with isoflurane (2.5%) and monitored for depth of anesthesia. Susceptibility-weighted imaging was acquired with a 3D flow-compensated gradient echo sequence at 0.4 mm isotropic resolution using a field of view (FOV) of 128 × 96 × 48 mm^3. Under isoflurane anesthesia, each monkey was surgically implanted with a titanium headpost and cephalic chambers (Crist Instruments, Hagerstown, MD, USA) that were oriented in the sagittal plane in the same hemisphere [466] (Fig. 35). Following a 1–2 week recovery period, each animal received a computerized tomography scan to plan the DBSA implantation using *Monkey Cicerone* [241].

5.3.2 DBS Implant Procedure

Microelectrodes (25μm diameter, 0.8-1.2MΩ, FHC, Bowdoin, ME, USA) were advanced through the cephalic chamber in each monkey under the guidance of *Monkey Cicerone* to map the boundaries of VPLo. A combination of unit-spike responses to passive joint manipulation and microstimulation-evoked movements at thresholds less than 50μA

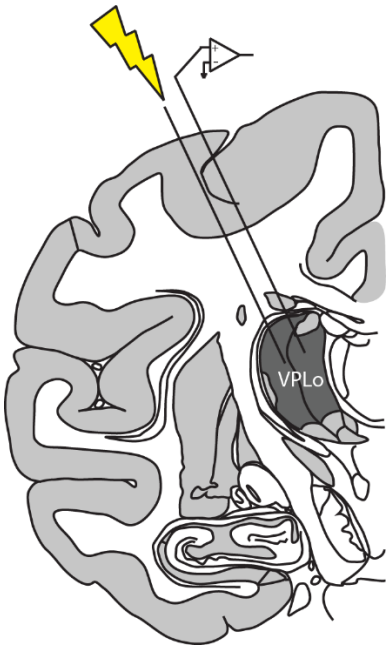

Figure 35. Illustration of the experimental procedure
Microelectrode recordings were performed in the cerebellar receiving area of thalamus (VPLo) while DBS was performed in the same nucleus.

[152] were used to identify VPLo. For each monkey, the mapping track that yielded a long stretch of VPLo was chosen for chronic implantation of the DBSA. The depth of implantation was chosen so that multiple rows of the DBSA would span the extent of VPLo. A radially segmented DBSA with 32 ellipsoidal ($360\mu m \times 470\mu m$) macroelectrodes (8 rows × 4 columns) arranged around a $600\mu m$ diameter shaft [233] was chronically implanted into the VPLo through the pre-planned track. The implantation procedure is described in a previous study [233]. Following DBSA implantation, a post-operative CT scan was performed under Ketamine and Dexdomitor anesthesia to visualize the implantation trajectory and depth in *Monkey Cicerone*. The preoperative SWI was co-registered with the postoperative CT to determine the DBSA lead location in VPLo.

5.3.3 DBS Protocols

After implantation of the DBSA, current controlled stimulations ($<350\mu A$) was delivered through each electrode to assess the magnitude of the evoked motor responses. The row

of electrodes with the lowest threshold responses was chosen for stimulation throughout the rest of the experiments. This was the fourth row from the tip of the DBSA in Monkey K and the bottom-most row in Monkey U. For each recorded neuron adjacent to the DBSA, 60s trains of monopolar, biphasic, charge-balanced (100µs cathodic phase, 20µs interphase interval, 100µs anodic phase) stimulation at 100Hz were delivered through each of the four electrodes from the chosen row, at 150μA, 250μA and 350μA. The order of the stimulation (selection of electrode) as well as the amplitude of stimulation were randomized.

5.3.4 Extracellular Recordings

Single-unit microelectrode recordings were performed using tungsten microelectrodes (25μm diameter, 0.8-1.2MΩ, FHC, Bowdoin, ME, USA) around the chronically implanted DBSA before (30-60s), during (60s), and after DBS (30-60s). Wideband recordings were collected (Alpha Omega SNR) and digitized at 44 KHz. Resting state unit-spike data were acquired with a high-pass filter cut off at 9000Hz (in reference to the titanium headpost). Stimulation artifacts were removed using a previously described template subtraction procedure [467] [169], reducing the period of recording obscured by stimulation artifacts to a small blanked period (average ~0.5ms). To prevent biasing the data, similarly blanked regions were introduced in the pre- and post-DBS recording epochs using “virtual stimulation” timestamps at the same stimulation pulse frequency. Template-subtracted spike recordings were thresholded and sorted in Offline Sorter (Plexon) to identify spike activity. While most neuronal recordings were stable enough to record effects of DBS through each of the four electrodes at three different amplitudes (12 recordings in total), it was not possible to achieve this with every neuron (n = 135/182 were recorded across all configurations in both animals).

5.3.5 Firing Pattern and Rate Analysis

Time-stamps of spike activity, stimulation pulses, and virtual stimulation pulses were imported into NeuroExplorer (NeuroExplorer, Littleton, MA, USA) to generate PSTHs (0.1ms bins) in the pre-DBS, DBS-on and post-DBS time periods to visualize the degree

of entrainment in spike activity to the stimulation (or virtual stimulation) pulses (Fig. 36). Previous studies have used either thresholding [468] or cumulative sum [469] methods to determine instances of significant FPM in PSTHs. However, these methods do not quantify the gradual and often subthreshold changes in the firing pattern behavior present in PSTHs. A new method is needed to capture these subthreshold effects, especially in the context of response to variable stimulation amplitudes. Therefore, a new entropy-based method was developed to quantify the degree of change in PSTHs between the pre-DBS and DBS states. The entropy (H) of a PSTH was computed using the following equation (based on the frequentist interpretation of H [470]):

$$H(x) = \sum_{i=1}^{m} p(x_i) log \frac{1}{p(x_i)} \tag{5.3}$$

Where m is the number of bins in the PSTH, x_i is the total number of spikes that fell in to PSTH bin i and $p(x_i)$ is the relative frequency that a spike falls in to PSTH bin i. This formulation of PSTH entropy dictates that entropy will be high when spikes fall randomly within the inter-pulse period (i.e. a flat PSTH), and it will be lower when either excitatory or inhibitory entrainment (i.e. peaks or troughs in the PSTH) occurs. The bin size in equation (5.3) was chosen to be 0.5ms under the following consideration: by studying H as a function of bin size, it was found that the bin size for should correspond to the length of the shortest observed period of entrainment (i.e. period of peaks or troughs in the PSTH). A smaller bin size would deprive equation (5.3) of the power to capture a decrease in H. Bin sizes that are much larger could also dilute this distinguishing power. The first 0.5ms in each PSTH were excluded from analysis to avoid false positives related to the blanking period from the stimulus subtraction algorithm. Excitatory or inhibitory FPM during DBS manifested in a drop in the H of the PSTH compared to the pre-DBS period. This drop is computed as a percentage decrease as follows:

$$\Delta H\% = \frac{H_{pre\_DBS} - H_{on\_DBS}}{H_{pre\_DBS}} \times 100 \tag{5.4}$$

Significant FPM is determined using a statistical methodology: sample with replacement n (where n equals the total number of spikes in the DBS-on period) spikes from the pre-DBS period, and calculate H using equation (5.3). Repeat this process 10,000 times to

generate a bootstrapped distribution of pre-DBS PSTH entropies: H_{pre_DBS}. Using all spikes from the DBS-on period, compute the DBS-on PSTH entropy: H_{on_DBS}. Statistically significant FPM is reached when the probability of observing values in the bootstrapped H_{pre_DBS} distribution that are lower than H_{on_DBS} is less than 5% ($\alpha = 0.05$). Firing rates calculated before, during and after DBS were compared for each recorded cell. A statistically significant difference in firing rate was established using the Mann-Whitney U test (1s bins, $p < 0.01$). A small fraction of recordings (<2%) were observed to have very sparse firing rates in either the pre-DBS or DBS-on periods, which led to inaccurate representations of the PSTH entropy. These recordings were excluded from further analysis.

5.3.6 Effective Pulse Fraction

The effective pulse fraction (EPF) was a concept developed by Agnesi et al. [468] to quantify how faithfully neurons are able to entrain to high frequency stimulation. In the case of excitatory FPM, we define the excitatory EPF (eEPF) as the fraction of stimulus pulses that effectively produced a spike within an entrained phase of the inter-pulse interval. This pulse fraction was normalized by subtracting the equivalent measure calculated from the pre-DBS baseline data. This is more succinctly described in the following equation:

$$eEPF = \frac{P_{On\_DBS} - P_{pre\_DBS}}{1 - P_{pre\_DBS}} \tag{5.5}$$

where P_{On_DBS} and P_{pre_DBS} are the percentages of stimulus (or virtual stimulus) pulses followed by a spike in the entrained phase of the DBS-on period and the corresponding phase in the pre-DBS period, respectively. The entrained phase during DBS was determined as follows. First, we located the PSTH bin with the highest firing rate (call it bin_High), then sample with replacement n spikes from the same period (n equals number of spikes in the DBS-on period) for 10,000 times to create 10,000 bootstrapped PSTHs. Next, we performed one-way analysis of variance (ANOVA) to test for a

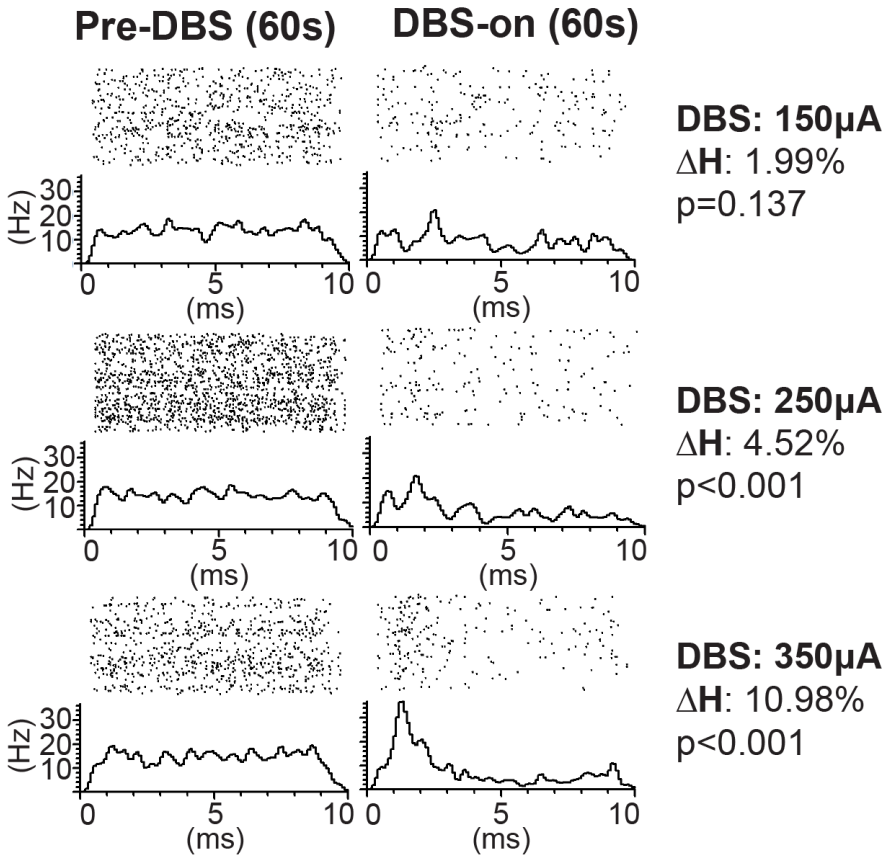

Figure 36. Examples of PSTH entropy
Examples peristimulus time histograms (PSTHs) from a recorded neuron before and during DBS at three different amplitudes. ΔH is the percentage change in PSTH entropy between the pre-DBS and DBS-on states. The p value indicates the likelihood of the observed PSTH entropy during DBS to occur by chance.

significant difference ($p<0.05$) in the average firing rate across all PSTH bins. If significance was reached, then we performed multiple comparison tests (pair-wise T test with Bonferroni correction, n =20 bins) to determine which bins do not have significantly different firing rates from bin_High. These bins, together with bin_High, form the entrained phase of the PSTH during DBS. An example PSTH is shown in Fig. 37(B), in which a neuron exhibited a higher probability of spiking between 1-1.5 ms from the onset of the DBS pulse. This entrained phase of the PSTH was used to calculate the eEPF. The inhibitory EPF (iEPF) is conceptually similar to the eEPF. It is defined as the fraction of pulses that effectively suppressed spike activity within an inter-pulse interval phase that probabilistically would have otherwise occurred with no stimulation present. This is described in the following equation:

$$iEPF=\frac{P_{pre\_DBS}-P_{On\_DBS}}{P_{pre\_DBS}} \quad (5.6)$$

where P_{On_DBS} and P_{pre_DBS} are the percentages of stimulus (or virtual stimulus) pulses followed by a spike in the inhibited phase of the DBS-on period and the corresponding phase in the pre-DBS period, respectively. The inhibited phase in the DBS-on period was determined as follows: locate the PSTH bin with the lowest firing rate (call it bin_Low), then sample with replacement n spikes from the same period (n equals number of spikes in the DBS-on period) for 10,000 times to create 10,000 bootstrapped PSTHs. Perform one-way analysis of variance (ANOVA) to test for a significant difference ($p<0.05$) in the average firing rate across all PSTH bins. If significance is reached, then perform multiple comparison tests (pair-wise T test with Bonferroni correction, n =20 bins) to determine which bins do not have significantly different firing rates from bin_Low. These bins, together with bin_Low, form the inhibited phase of the PSTH during DBS. An example PSTH is shown in Fig. 37(C), in which a neuron exhibited inhibition of spiking between 0.5 - 5ms from the onset of the DBS pulse. This inhibited phase of the PSTH was used to calculate the iEPF.

5.3.7 Stimulus artifact size as a measurement of distance

The size of the DBS stimulus artifact was used as a pseudo measure of distance in this study. Studies [471] [472] have shown that neurons will have to be within 50μm of the recording electrode in order to be reliable separated out in the spike sorting process. The recorded neurons in this study have all been shown to have good isolation in the spike sorting process. Therefore, we have reason to be believe that the recordings were performed in close proximity (on the order of tens of microns) to the neurons and the sizes of the stimulus artifacts are true reflections of the relative distances between the recorded neurons and the active electrode. The stimulus artifacts were detected via thresholding on the anodic phase of the waveform. For each recording session, the artifacts from each stimulation amplitude (150μA, 250 μA, or 350 μA) were averaged and the peak value (μV) of the anodic phase of the waveform was used as the pseudo measure for distance.

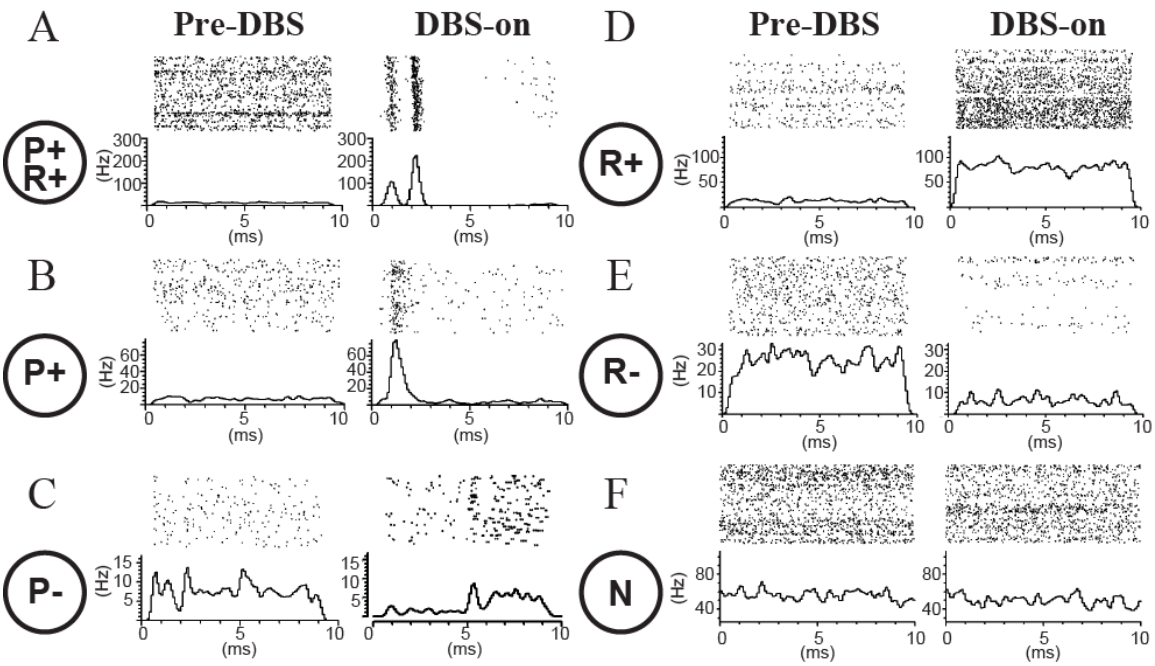

Figure 37. Example PSTHs of the various types of neuronal responses to VPLo-DBS
P: firing pattern modulation (FPM). R: firing rate modulation. '+': excitatory entrainment or firing rate increase. '−': inhibition or firing rate decrease. N: no response.

5.4 Results

5.4.1 Heterogeneity of Neuronal Responses to VPLo-DBS

The number of recorded neurons was 85 in Monkey K (21 recording tracks) and 97 in Monkey U (11 recording tracks). The neuronal responses to VPLo-DBS can be characterized by FPM and/or FRM. We have grouped these responses into 9 categories, shown in Fig. 37 FPM was

represented by the letter 'P' and FRM by the letter 'R'. Excitatory entrainment or rate increase were signified by '+', while inhibitory entrainment or rate decrease were signified by '−'. No response to DBS was represented by the letter 'N'. 12.94% (11/85) and 21.65% (21/97) of all recorded neurons in Monkey K and Monkey U, respectively, were exhibited FPM during DBS. The recordings were grouped by stimulation amplitude and divided into various types of responses (Fig. 38). In Monkey K, there were 273, 256 and 254 recordings at 350μA, 250μA and 150μA, respectively. Most recordings showed no response of any kind to DBS. The percentage of responsive recordings increased

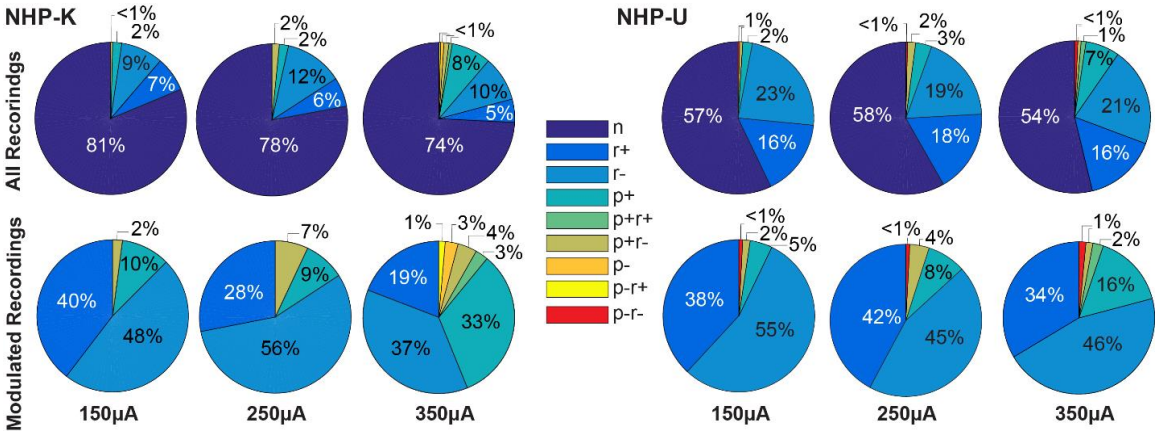

Figure 38. The percentage composition of recordings by type of response
Data from Monkey K and Monkey U are on the left and right side of the color legend, respectively. The top row of pie charts show the percentage makeup of different types of responses to DBS at 350μA, 250μA, and 150μA. The bottom row of pie charts show the corresponding percentage makeup of response subtypes only for those recordings that were modulated in some way by DBS. P: firing pattern modulation (FPM). R: firing rate modulation. '+': excitatory entrainment or firing rate increase. '−': inhibition or firing rate decrease. N: no response.

slightly from 19% at 150μA to 26% at 350μA. Within the fraction of recordings that were responsive to DBS in some way, there was a shift from mostly FRM to a more nuanced collection of responses. More specifically, 'R+' and 'R−' responses accounted for 88%, 84% and 56% of all responsive recordings at 150μA, 250μA and 350μA respectively. The decrease in the number of recordings with FRM at 350μA was accounted for with an increase in the number of recordings with FPM. In Monkey U, there were 290 recordings each at 350μA and 250μA and 292 recordings at 150μA. Out of these recordings, 57%, 58% and 54% of recordings were non-responsive to DBS. This represented a decrease compared to the corresponding percentages found in Monkey K. Similar to what was found in Monkey K, the composition of the responsive recordings showed a decrease in the proportion of FRM responses as the DBS amplitude increased: from 94% at 150μA to 80% at 350μA. This decrease was balanced by an increase in the proportion of FPM responses.

5.4.2 Neuronal Response as a Function of Distance

A total of 783 and 872 recordings (each recording corresponds to DBS with a single amplitude) were available from Monkey K and Monkey U respectively. PSTHs were

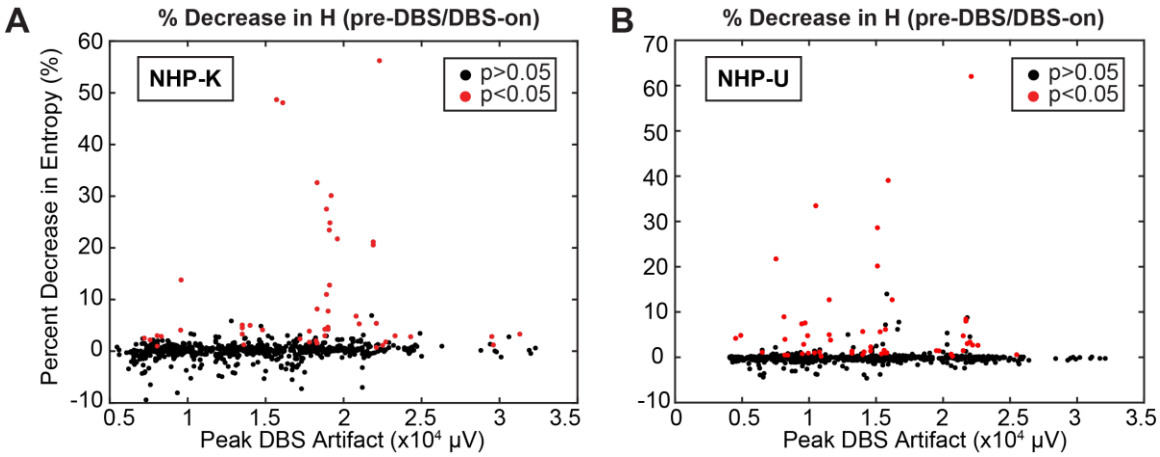

Figure 39. Change in PSTH entropy vs. stimulus artifact
The percentage decrease in PSTH entropy between the DBS-on and pre-DBS periods plotted against the peak amplitude of the recorded DBS artifact. Recordings that exhibited significant firing pattern modulation during DBS are labeled in red.

created for each recording and $\Delta H\%$ between the DBS-on and pre-DBS periods were calculated (see Methods section). The $\Delta H\%$ between the DBS-on and pre-DBS periods were plotted against the peak amplitude of the DBS artifact (Fig. 39). Recordings exhibiting significant FPM during DBS are labeled in red. The results showed that significant FPM can be associated with large decreases in PSTH entropy (>10%), but this was not necessarily always the case. Many instances of significant FPM had relatively small changes in PSTH entropy, but the neuronal responses during DBS were nevertheless highly unlikely to occur by chance. Furthermore, instances of significant FPM and large $\Delta H\%$ occurred over a wide range of 'distances', as measured by the size of the stimulus artifact. This range was found to be 4520μV at the farthest and 31300μV at the nearest, pointing to a sparse spatial activation profile. Using methods described previously, the recordings were also grouped by their response to DBS. Histograms illustrating the spatial distribution of each group are shown in Fig. 40. It is evident that the heterogeneous responses to DBS also occur over a wide range of distances.

5.4.3 Neuronal Response as a Function of Stimulus Amplitude

The degree of FPM as a function of stimulus amplitude was examined. Only those recording trials that have undergone DBS at all three amplitudes (150μA, 250μA, and

Monkey K					
Group nFPM			Group FPM		
150μA	250μA	350μA	150μA	250μA	350μA
-0.14 ± 1.47 %	0.08 ± 1.36 %	0.22 ± 1.47 %	1.43 ± 3.12 %	6.08 ± 14.18 %	11.36 ± 14.03 %
Monkey U					
Group nFPM			Group FPM		
150μA	250μA	350μA	150μA	250μA	350μA
-0.27 ± 0.67 %	-0.15 ± 1.23 %	-0.15 ± 0.84 %	1.02 ± 2.19 %	3.53 ± 7.97 %	7.21 ± 12.75 %

Table 12. The percentage decrease in PSTH entropy as a function of stimulus amplitude within Group nFPM and Group FPM

350μA) were chosen for this analysis. This amounted to 245 trials in Monkey K and 283 trials in Monkey U. The recording trials were grouped into two categories: 1) DBS failed to elicit FPM at any of the three stimulation amplitudes (Group nFPM), and 2) DBS elicited FPM with at least one stimulation amplitude (Group FPM). Monkey K had 21 and 224 recording trials in Group FPM and Group nFPM, respectively. Monkey U had 32 and 251 recording trials in Group FPM and Group nFPM, respectively. $\Delta H\%$ as a function of stimulus amplitude within each group are shown in Fig. 41. The average $\Delta H\%$ under three stimulus amplitudes are listed in Table 12. Within each group, one-way ANOVA was performed to test for a significant difference ($\alpha = 0.05$) in the average $\Delta H\%$ with stimulus amplitude as the explanatory variable. The analysis showed that for both Monkey K and Monkey U, there was no significant difference in the average $\Delta H\%$ between data recorded under the three DBS amplitudes (Monkey K: $p = 0.276$, Monkey U: $p = 0.247$). In contrast, a significant difference was found in Group FPM for both animals (Monkey K: $p = 0.028$, Monkey U: $p = 0.021$). Multiple-comparison tests (n=3, Mann-Whitney U test with Bonferroni correction, $\alpha=0.05/3=0.0167$) were subsequently performed on the data in Group FPM. In both animals, significant differences were found between the (150μA, 350μA) groups and the (250μA, 350μA) groups, but not between the (150μA, 250μA) groups (Fig. 41). The rate of increase in the average PSTH ΔH% as a function of the change in stimulus amplitude (i.e. slope) was calculated for

(5.7)

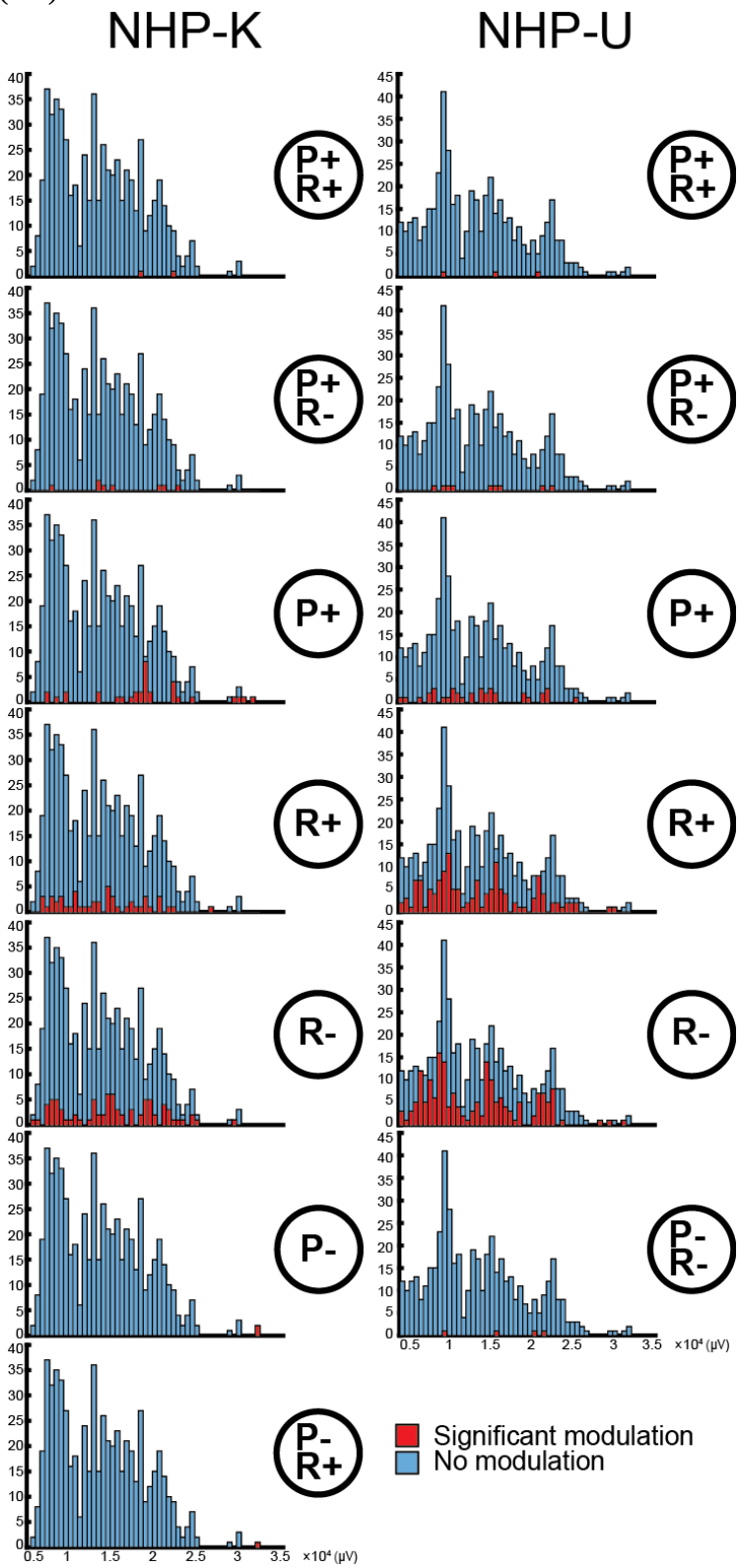

Figure 40. Spatial distribution of recordings grouped by their response to DBS

P: firing pattern modulation (FPM). R: firing rate modulation. '+': excitatory entrainment or firing rate increase. '−': inhibition or firing rate decrease. N: no response. The x-axis shows the peak amplitude of the recorded stimulus artifact (μV), used as a measure of distance from the active electrode. The y-axis is a count of the number of recordings. The blue histogram in the background of each plot shows the distribution of recordings in the non-responsive group N. All recordings belonging to other groups are shown in red histograms.

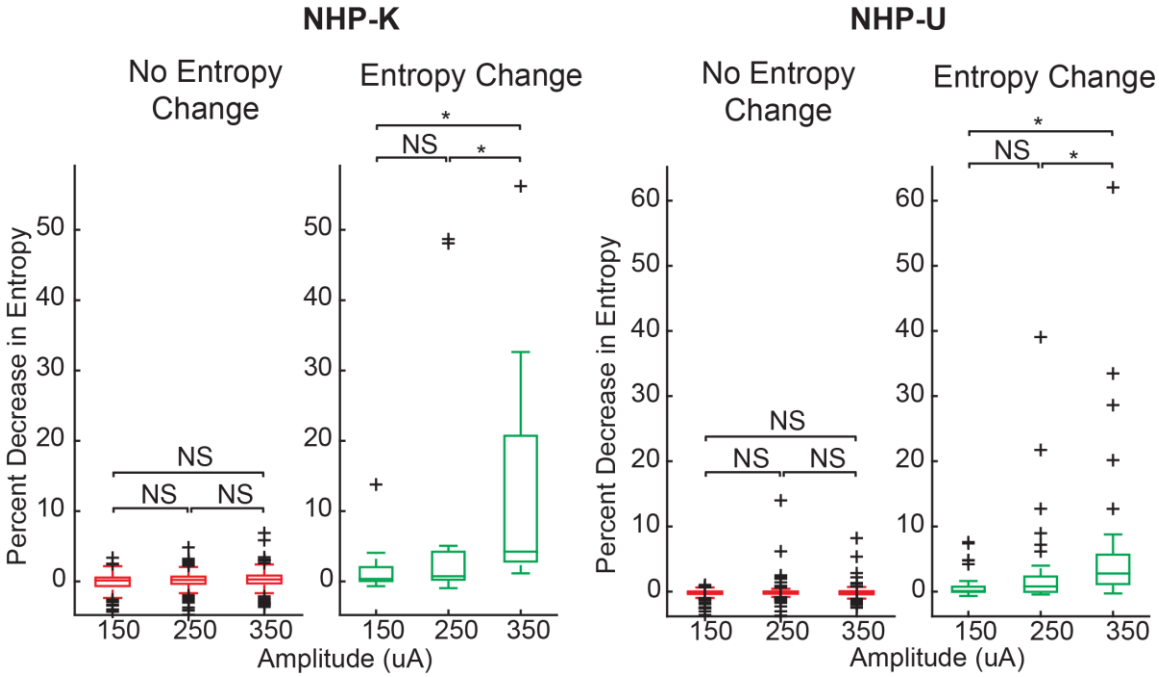

Figure 41. The percentage decrease in PSTH entropy as a function of stimulus amplitude within Group FPM and Group nFPM

NS: no significant difference by multiple comparison test. *: significant difference by multiple comparison test.

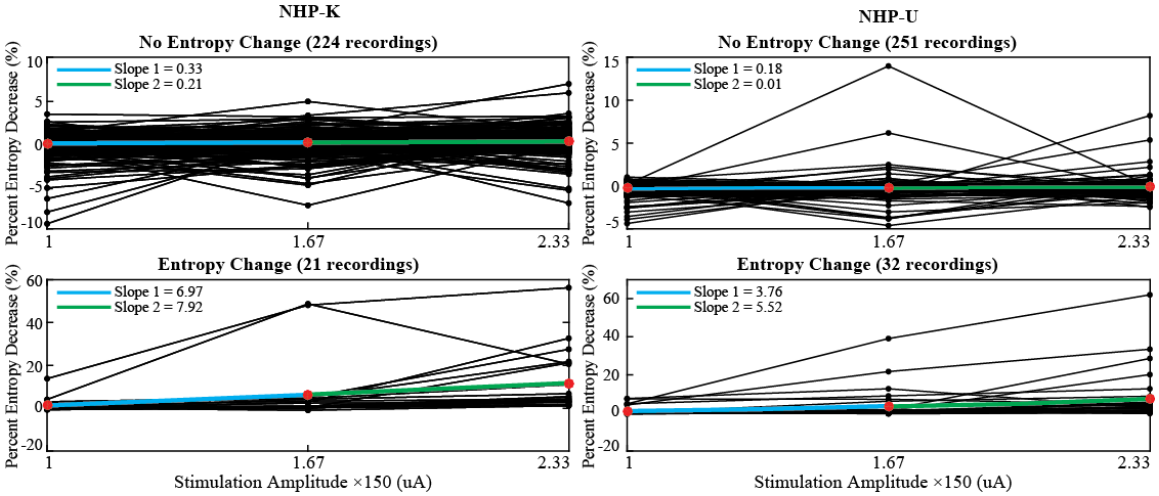

Figure 42. The rate of increase in the average change in PSTH entropy as a function of the change in stimulus amplitude

Data from groups nFPM and FPM are on the top and bottom rows, respectively. 'Slope 1' and 'slope 2' are the average rate of increase in PSTH ΔH% between (150μA, 250μA) and (250μA, 350μA), respectively. Note the different scalebars amongst the plots.

both Group nFPM and Group FPM, shown in Fig. 42. As an example, the rate of increase in the average PSTH ΔH% between data recorded under 350μA and 250μA can be calculated in the following way:

$$\text{Slope} = \frac{\Delta H\%_{350\mu A} - \Delta H\%_{250\mu A}}{\frac{350\mu A}{150\mu A} - \frac{250\mu A}{150\mu A}}$$

The fractions in the denominator in Equation 5.7 were meant to normalize all stimulus amplitudes by the lowest amplitude of 150μA. The average rate of increase in PSTH ΔH% between (150μA, 250μA) and (250μA, 350μA) were designated 'slope 1' and 'slope 2', respectively. The mean and standard deviation of the slopes are listed in Table 13. Two-way ANOVA with unbalanced sample sizes was performed on all the slope values (in each animal), using both response to DBS (i.e. Group FPM vs. Group nFPM) and slope segment (i.e. 'slope 1' vs. 'slope 2') as explanatory variables ($\alpha = 0.05$). In both animals, a significant difference in the average slope of PSTH ΔH% increase was only attributed to a difference in response to DBS ($p = 0$ in both animals), and not to slope segment, or the interaction of those two factors. Multiple-comparison tests (n=6, Mann-Whitney U test with Bonferroni correction, $\alpha = 0.05/6 = 0.0083$) were performed on the slope data in each animal (Fig. 45). For both animals, there was not a significant difference between slope 1 and slope 2 within the same response group (nFPM or FPM), but any comparison with a slope from another response group showed a significant difference (Fig. 43).

Lastly, pie charts were created to illustrate the likelihood of FPM to occur at different stimulus amplitudes (Fig. 44). The results showed that FPM was more likely to occur at higher stimulus amplitudes, 350μA in particular, which accounted for 48% and 41% of all recordings with FPM in Monkey K and Monkey U, respectively. The likelihood of FPM at 350μA and 250μA were 24% in Monkey K and 25% in Monkey U. The likelihood of FPM occurring at all three stimulus amplitudes was still significant, accounting for 19% in Monkey K and 22% in Monkey U.

Monkey K		Monkey U	
Group nFPM		Group nFPM	
Slope 1	0.33 ± 2.43	Slope 1	0.18± 2.08
Slope 2	0.21 ± 2.67	Slope 2	0.01± 2.26
Group FPM		Group FPM	
Slope 1	6.97 ± 17.66	Slope 1	3.76 ± 10.08
Slope 2	7.92 ± 16.88	Slope 2	5.52± 10.79

Table 13. Mean and standard deviation of the average rate of increase in PSTH between stimulation amplitudes

Mean and standard deviation of the average rate of increase in PSTH ΔH% between (150μA, 250μA) and (250μA, 350μA).

5.4.4 Effective Pulse Fraction during DBS

The eEPF was found to be 3.25% ± 3.8% in Monkey K (42 recordings) and 3.18% ± 3.99% in Monkey U (45 recordings). This result indicates that on average, only about 3% of DBS pulses introduced entrained spikes that would not have otherwise occurred. The iEPF was found to be 81.01% ± 4.44% in Monkey K (3 recordings) and 76.3% ± 20.61% in Monkey U (7 recordings). This result indicates that on average, approximately four-fifths of DBS pulses effectively suppressed spike activity within an interpulse interval phase that likely would have occurred with no stimulation present. The relationship of eEPF as a function of distance (from the active electrode) as well as PSTH ΔH% were examined and shown in Fig. 45. The same was not done for iEPF due to the small sample size in both animals. The eEPF was shown to be positively correlated (Pearson's correlation coefficient) with PSTH ΔH% (Fig. 45A) in both Monkey K (ρ = 0.77, p = 3.2×10^{-9}) and Monkey U (ρ = 0.59, p = 1.9×10^{-5}). Given this result, it was not surprising to notice the similarity in the shape of the data distribution when comparing eEPF vs. distance (Fig. 45B) and PSTH ΔH% vs. distance (Fig. 39).

5.5 Discussion

This study aimed to experimentally characterize 1) the spatial activation profile around a chronically implant DBSA during VPLo-DBS and 2) the neuronal responses in relation to

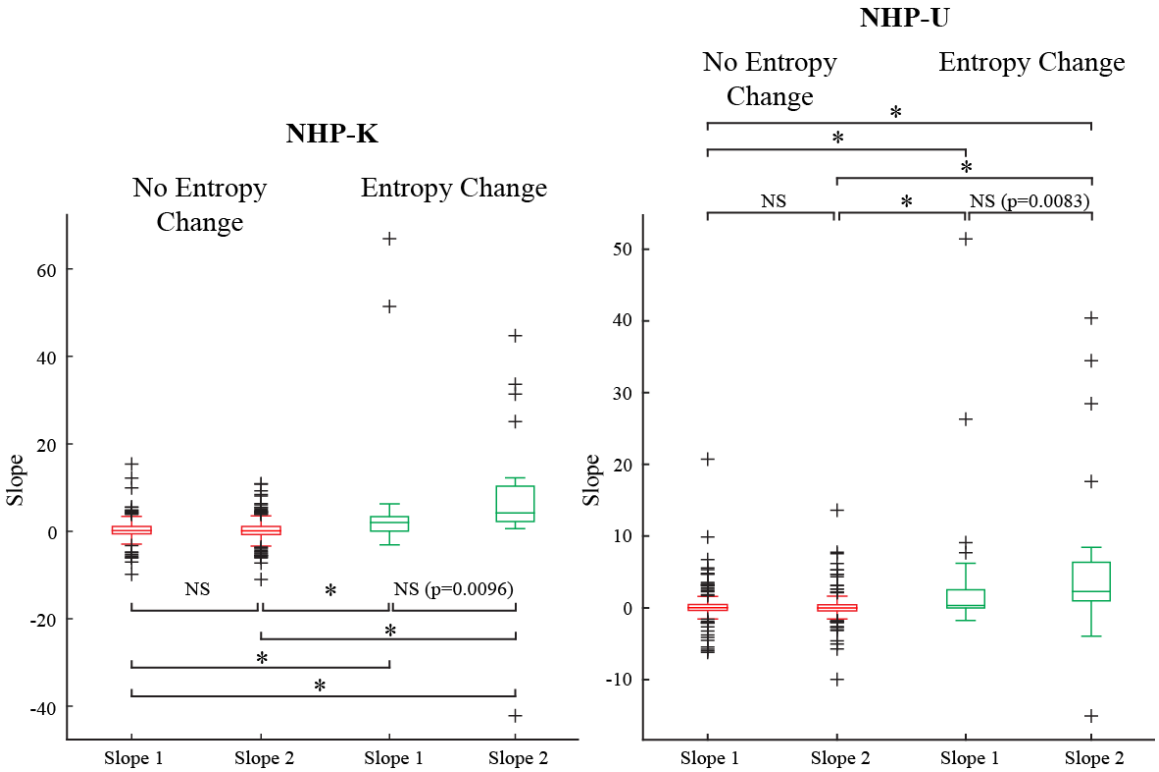

Figure 43. Average rate of change in PSTH entropy as a function of stimulation amplitude
Box whisker plots depicting the average rate of increase in PSTH ΔH% between (150μA, 250μA) ('slope 1') and (250μA, 350μA) ('slope 2'). NS: no significant difference by multiple comparison test. *: significant difference by multiple comparison test.

DBS amplitude. The results indicate that there is substantial heterogeneity in the neuronal response to DBS that included both FPM and FRM. Furthermore, the *in-vivo* VTA was sparsely populated and not confined to the immediate vicinity of the active electrode. Increasing the stimulation amplitude induced greater change in firing pattern only in a subset of recorded neurons. In addition, only a small fraction of DBS pulses were able to introduce entrained spiking activity in modulated neurons.

5.5.1 Heterogeneity of Neuronal Responses to VPLo-DBS

Studies in the past have mostly characterized thalamic neuronal responses to short duration intrathalamic stimulation [473], [152], [474], [475], [476] that ranged from 0.5ms [473] – 2s [474] in length. A longer stimulation duration of 10 – 60s was used in [477], [478]. The focus of these studies were to understand somatotopic organization of

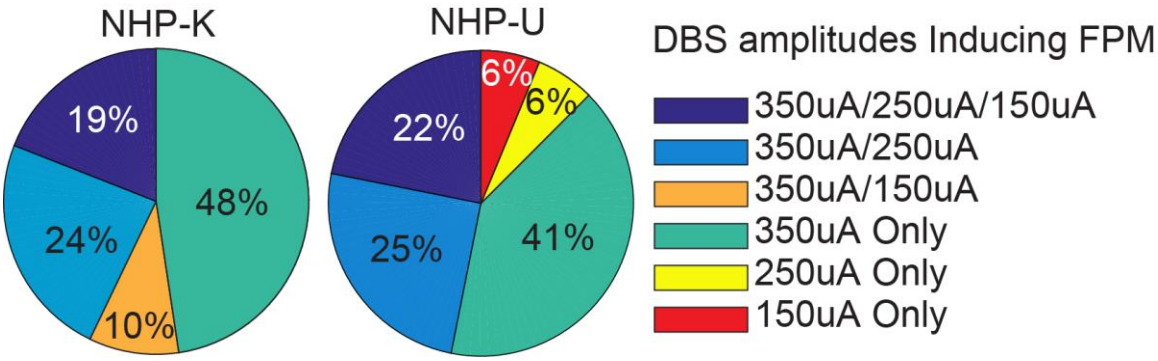

Figure 44. Likelihood of firing pattern modulation at various stimulation amplitudes
Likelihood of FPM to occur at different stimulus amplitudes or combination of stimulus amplitudes.

the motor thalamus [152], the temporal patterns of response proceeding stimulation across different neuronal populations [473], [474], [475] and the neural origins of the stimulation-evoked potentials [477]. The study described in this chapter is different in that it is focused on understanding changes in neuronal firing behavior during longer (up to 60s) DBS-ON periods and quantifying the spatial profile of where these changes are taking place. The majority of recordings showed that neuronal activity was not influenced by DBS in any way (Fig. 38). The proportion of unaffected recordings ranged from 74% - 81% in Monkey K and 54%-58% in Monkey U. This is consistent with reports from previous studies, where 55% (330/600) [475] and 51% (51/100) [473] of recorded neurons in the motor thalamus were unaffected by stimulation. The higher percentage of non-responding recordings found in Monkey K could be due to tissue damage and microelectrode recordings farther from the active electrodes in comparison to previous studies. A previous study also noted that the proportion of non-responsive neurons varied appreciably from animal to animal [473]. Most responses to DBS were in the form of FRM, with rate decrease being the majority. This is supported by the observation in [479] that the major effect of thalamic stimulation is local depression of neuronal activity. That study found two types of cells that were inhibited following 0.5ms of stimulation with amplitudes ranging from 120-200μA. The inhibitory behavior of these cells was characterized as a complete silencing of activity for periods of time at differing latencies following a single shock. The study estimated that 42% of all responsive neurons within a 4mm radius sphere would be silenced by stimulation. This is generally consistent with

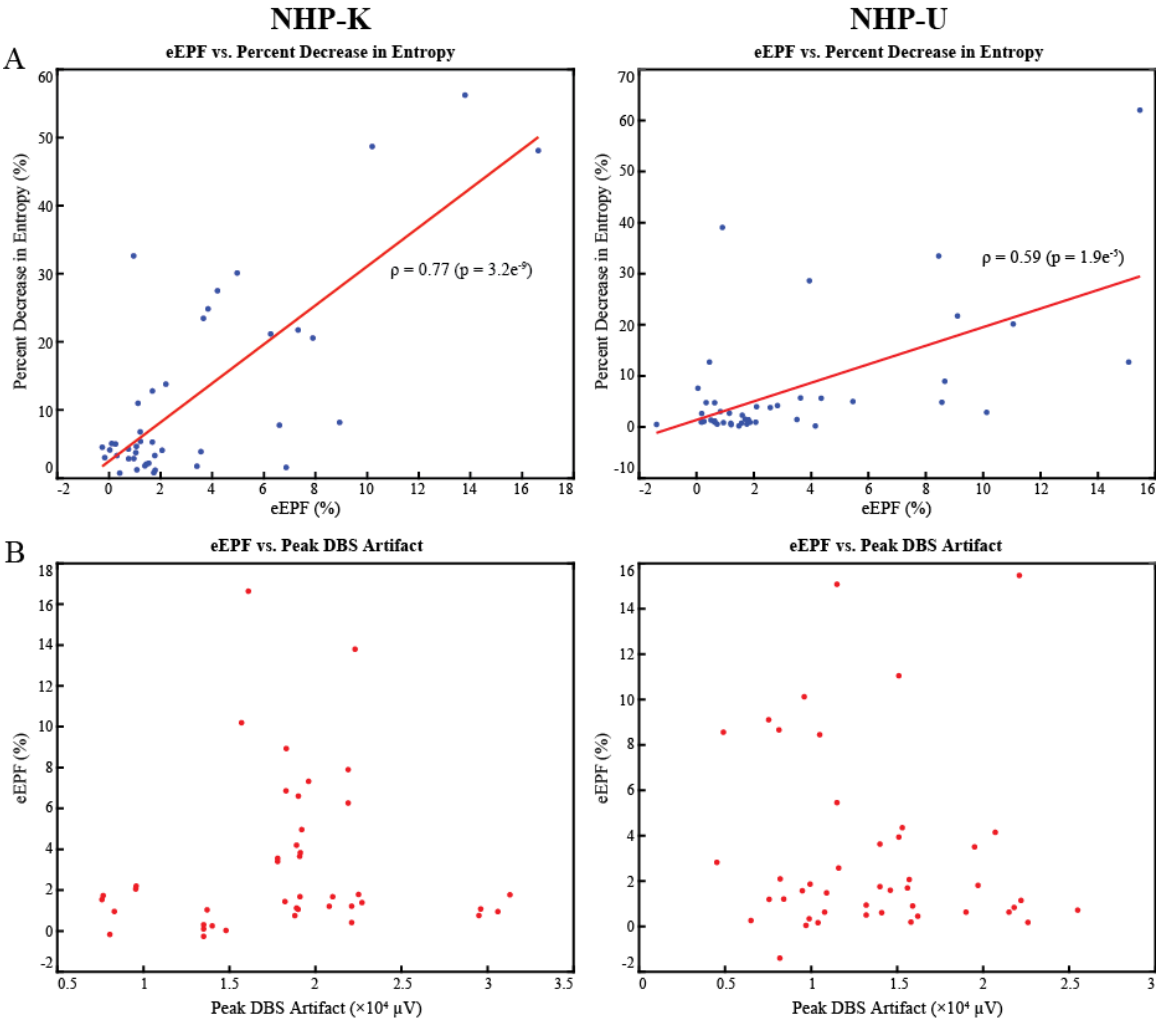

Figure 45. Excitatory effective pulse fraction (eEPF) in relation to strength of modulation under DBS and distance away from the stimulating electrode
(A) Correlation between eEPF and ΔH. ρ is the Pearson's correlation coefficient. **(B)** eEPF as a function of the peak amplitude of the recorded DBS artifact.

our findings, where 37% - 56% (Monkey K) and 45% -55% (Monkey U) of responses were in the 'r−' category. However, it is important to note that in the absence of chronically applied DBS, it is possible that the inhibitory response described will differ from the 'r−' and 'p−' categories of responses in the current study. Similarly, a 'Class III' group of cells was found by the same group [473] with a neuronal response characterized by an initial burst following a single shock. These cells accounted for 36% (36/100) of recorded neurons. This percentage is higher than the 5% -7% and 16% - 18% of 'r+' type responses found in Monkey K and Monkey U, respectively (Fig. 38, first

row). Again, it is difficult to predict the response of the 'Class III' neurons to prolonged stimulation ($\geq 30s$). FPM was rarer compared to FRM, making up 12% - 44% of all responsive recordings in Monkey K and 7% - 20% in Monkey U. Inhibitory FPM was especially rare, accounting for at maximum only 4% and 1% of all responses in Monkey K and Monkey U respectively. This is likely attributed to the preponderance of excitatory inputs relative to inhibitory inputs in the thalamus [480], [460]. Taken together, the results in this study provide a more refined classification of neuronal response to DBS based on both FPM and FRM.

5.5.2 Entropy-Based Method to Quantify Changes in PSTH

The entropy-based method developed in this study was effective at identifying instances of significant FPM and characterizing the graded changes in the PSTHs (Fig. 36). Visual inspection of all PSTHs with FPM have shown that there were no gross misclassifications (i.e. PSTHs that clearly did not exhibit FPM). Studies in the past have also used entropy as a quantitative measure of neuronal output. However, the focus of these methods were to either measure neuronal information from inter-spike intervals [481], [482], [483] or spike train data [484]. The method used in this study was tailored for characterizing changes in PSTHs, which only pertains to a cell's firing behavior in relation to the onset of the stimulus pulses. This method is effective at capturing both excitatory and inhibitory FPM and provides a quantitative measure of the change in PSTH between the DBS-on and pre-DBS states. Moreover, the method presents a less biased approach to define statistical significance in PSTHs than the conventional approaches using a preset number of standard deviations above the mean [468], [169].

5.5.3 Neuronal Response as a Function of Distance

In the absence of histology to verify the exact location of the recorded neurons relative to the active electrode contacts, we have used the average peak amplitude of the stimulus artifact as a pseudo measure of the distance away from the stimulating electrode. The results revealed that instances of significant FPM occurred over a wide range of distances and were not confined to the immediate vicinity of the stimulating electrode (Fig. 39). In

a simplified scenario where DBS is produced by a point charge Q on the surface of the stimulating electrode, the electrical potential V at a distance R from the point charge is given by $V = \frac{kQ}{R}$, where k is Couloumb's constant. The confounding factor of variable DBS amplitude (i.e. varying Q) present in this study can be transformed into a scenario of constant Q by varying the distance R. For example, the size of the DBS artifact from 350 μA of stimulation recorded at a distance of R is the same as the artifact resulting from 150 μA of stimulation, recorded at a distance of $\frac{150}{350}R$. Employing this concept, the relative distances between recording sites can be determined as $\frac{R_1}{R_2} = \frac{V_2}{V_1}$. The ratio between the largest and smallest DBS artifact amplitudes at which significant FPM occurred was 4.34 ($3.13 \times 10^4 \mu V / 7220 \mu V$) in Monkey K and 5.64 ($2.55 \times 10^4 \mu V / 4520 \mu V$) in Monkey U. Therefore, effectively speaking, the furthest location of FPM occurrence was 4.34 and 5.64 times more distant than the nearest location in Monkey K and Monkey U, respectively. Inspecting the occurrences of all response subtypes also indicates that 1) activation was sparse (the majority of recordings did not show response to stimulation) and 2) the occurrences of modulation were distributed (Fig. 40) with no noticeable spatial bias. This sparse distribution of modulated neurons echoes observations from other studies. Schlag et al. [479] noted that during stimulation in the ventrolateral nucleus (VPLo homologue) in cats that non-responsive cells can be found everywhere, even very close ($< 1mm$) to the stimulating electrode. Vitek et al. [152] have also reported on micoexcitable zones within the thalamus that ranged from 500 – 1500μm, where the same response was observed at several adjacent stimulation sites within the zone. This sparse and distributed profile of the *in-vivo* VTA was also clearly demonstrated in the rodent and cat cortex using two-photon calcium imaging [445]. The same study demonstrated compelling evidence to suggest that direct activation of axons near the stimulating electrode (within tens of microns) coupled with local axonal projection patterns were the reasons for the sparse distribution of modulated cells (whose somas we recorded from [485], [472]). The variation in the ΔH% observed amongst the modulated cells (Fig. 41) was reminiscent of the differences in fluorescence of activated cells observed in [445]. The strongly modulated cells likely had axons that

were directly modulated by stimulation, while the weakly modulated ones were possibly driven via postsynaptic activation, or had axons that were further away from the stimulating electrode [445]. It is interesting to note in Monkey K's data, there appears to be a 'hot spot' for cells with large ΔH% values, which is between 1.5 – 2$\times 10^4\ \mu V$ (Fig. 39). This is likely due to the axonal projection patterns within the recorded region. This phenomenon was less pronounced in Monkey U.

5.5.4 Neuronal Response as a Function of Stimulus Amplitude

The majority of recordings showed that increase in stimulation amplitude did not influence neuronal activity (Fig. 38). However, within the fraction of data that did show modulation (Fig. 38, bottom row), a transition took place where FRM was gradually replaced with FPM as the stimulation amplitude increased. In Monkey K, FPM account for 12% of all modulated recordings at 150μA**,** 16% at 250μA and 44% at 350μA. The rate of increase in the percentage of FPM recordings is 6% ($\frac{16\% - 12\%}{\frac{250\mu A}{150\mu A} - \frac{150\mu A}{150\mu A}}$) between 150$\mu A$ and 250μA and 42% (($\frac{44\% - 16\%}{\frac{350\mu A}{150\mu A} - \frac{250\mu A}{150\mu A}}$)) between 250$\mu A$ and 350μA. This change from FRM to FPM was less prominent in Monkey U, where FPM accounted for 7% of all responsive recordings at 150μA and 20% at 350μA. The rate of increase in the percentage of FPM recordings is 9% between 150μA and 250μA and 10.5% between 250μA and 350μA. The results also show that there is a propensity for FPM to occur at higher stimulation amplitudes (Fig. 44). This increase in the firing probability (FPM) with successive increase in stimulation amplitude is likely the result of a non-synaptic mechanism where direct current effects alters the membrane excitability of axons [486]. The implication for DBS is that at lower stimulation amplitudes, the mechanism of 'de-rhythmication' [478] is mainly through 'masking' of the rhythmic tremor activity [487] by creating randomness in spike activity via FRM. At higher amplitudes, the mechanism shifts to disruption via entrainment (FPM) of spike activity. Increasing stimulation amplitude exhibited a differential modulatory effect on a minority of cells (i.e. Group FPM, 12.94% and 21.65% in Monkey K and Monkey U, respectively). Within this group, a difference

in modulatory effect was found between 250μA and 350μA and not between 150μA and 250μA (Fig. 43), suggesting a nonlinear effect. The average rate of change in modulatory effect (ΔH%) as a function of stimulus amplitude were both practically zero in Group nFPM (Fig. 43), and not found to be significantly different. In contrast, the rates of increase in Group FPM were significantly different from zero. Slope 2 was on average larger than slope 1. It should be noted that although the two slopes were found not to be significantly different in the context of a multiple comparisons test, the p values in both animals were very small (0.0096 in Monkey K and 0.0083 in Monkey U) and would have reached significance without Bonferroni correction. This again echoes the nonlinear effect that increasing stimulation amplitude has on the degree of FPM. The separation of all recorded neurons into two distinct groups, one that can be influenced by electrical stimulation, and another that altogether cannot, is a very interesting phenomenon. Taking the perspective that direct activation of axons is the main modulatory effect in DBS [445], and axonal activation is dependent on the AF at nodal compartments [448], it is likely that axonal projection patterns and the resulting relative orientation to the electric field plays an important role in a neuron's response to stimulation. To illustrate this point, an example of AF maps surrounding a DBSA under three different stimulation configurations [353] is shown in Fig. 46. The AF maps can take on complex profiles, even under idealized axonal trajectories. Taken together, the results point to the need to further characterize network connectivity and axonal projection patterns of neuronal processes at a much more detailed level than currently available, and incorporate the findings into computational models.

5.5.5 Fidelity of Entrainment of Neuronal Activity During DBS

DBS has been shown to low-pass filter circuit-level entrainment during DBS in glutamatergic pathways [468], where entrained spike activity does not faithfully follow stimulus pulses in a one-to-one fashion. This is consistent with results from the current study, where only less than 4% of all DBS pulses produced spikes within the entrained phase of the interpulse interval. This is roughly half of the eEPF reported from motor cortex during VPLo DBS (7.5%) and from the

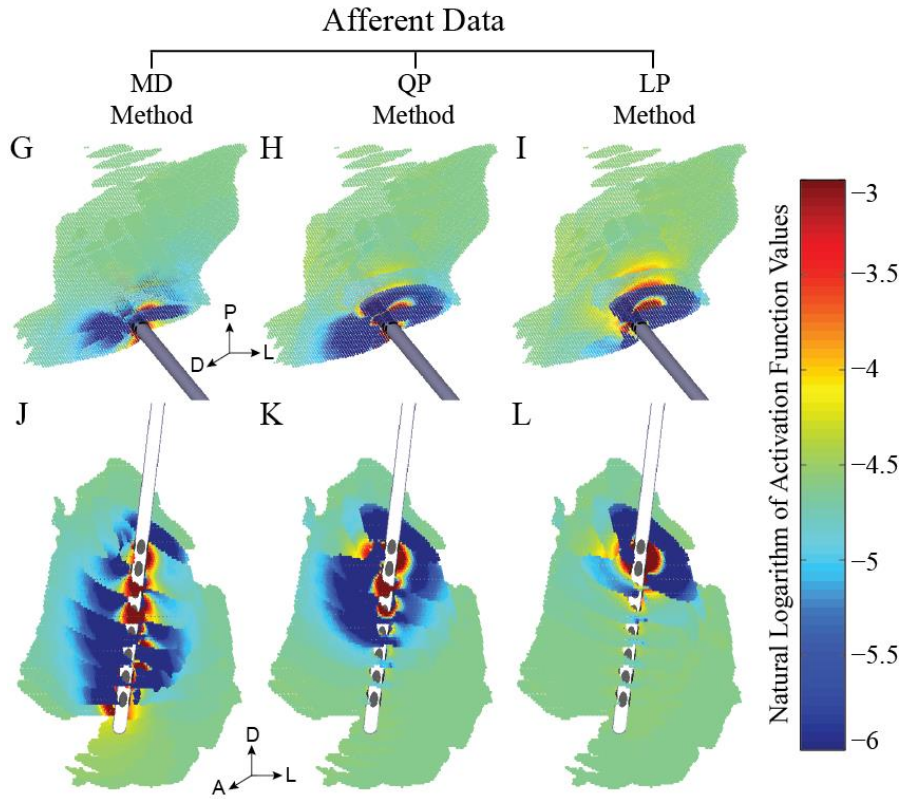

Figure 46. Examples of activating function maps
Adapted from Figure 7 in [353]. The figure illustrates the complex activating function map that resulted from stimulation through a DBS array under three different active electrode configurations.

globus pallidus (GP) during subthalamic nucleus (STN) DBS (8.7%). This discrepancy is likely due to a difference in 1) the selection of recordings exhibiting significant FPM and 2) calculation of entrained phases within the PSTH. Agnesi et al., [468] employed a thresholding method that's more stringent than the one used in the current study to detect instances of significant FPM. It is more stringent because thresholding on the PSTH is an absolute measure on the strength of entrainment to DBS and would miss instances of weaker FPM that are nevertheless significant because they are highly unlikely to occur by chance. Therefore, selecting from the current study only the data with strong entrainment would likely have resulted in higher eEPF values. The iEPF data in the current study aligned closely with reported values from the STN (82%) and the pallidal-receiving area of thalamus (VLo) (86%) during GP DBS, indicating that DBS was effective at suppressing spike activity. Agnesi et al. computed the EPFs using data from structures downstream from the stimulated structure, whereas the current study stimulated and

recorded in the same structure. The similarity in eEPF results from the two studies suggests that the low-pass filtering effect on the glutamatergic transmission began within the stimulated structure (VPLo in this study). This is consistent with results from 100Hz stimulation in the cat ventrolateral nucleus of thalamus (VL) showing the response of VL neurons to DBS tended to drop off after the third pulse or often followed the pulses in a partial or alternating fashion [475]. Another study in motor thalamic brain slices showed that high frequency stimulation could only entrain antidromic activity within corticothalamic axons firing at less than 50Hz [488]. Similarly, the iEPF data suggests that the effective suppression of spiking activity also began in the stimulated structure. The specific mechanism behind these findings is unclear. Possible factors are discussed in detail in [468] and are not elaborated here. In addition, there's strong statistical evidence to suggest that eEPF is correlated with the degree of FPM (ΔH%). In other words, strong modulation is correlated with higher rates of success of DBS pulses in inducing entrained spikes. Taken together, we have shown through EPF analysis that within VPLo, 1) DBS pulse have a high success rate in suppressing spiking activity (as indicated by high iEPF values, see definition of equation 5.6) and low success rate in inducing entrained spike activity (as indicated by low eEPF values, see definition of equation 5.5). 2) A higher success rate of DBS pulses in inducing entrained spike activity likely plays an important role in producing strong modulatory effects. More studies are needed to understand the mechanisms of this low-pass filtering effect on entrainment during DBS, and these mechanisms should be incorporated into the computational models of neuronal activation to make them more realistic.

The results from this study found that the majority of modulated neuronal responses to DBS happened in the form rate changes, especially at lower stimulation amplitudes (Fig. 38). The implication for DBS treatment of ET is that when under low intensity stimulation, noise is introduced into the rhythmic discharge of 'tremor' cells in the thalamus [487] via random changes firing rate, masking their synchronized activities and thus producing a 'de-rhythmication' effect [478]. At higher amplitudes, a transition in neuronal response to DBS takes place from FRM to FPM, with excitatory entrainment of spike activity being the most prominent. This entrainment to the stimulus is in effect

regularizing neuronal activity, consistent with the 'informational lesion' [164] hypothesis on the mechanism of therapeutic DBS. However, the low eEPF values found in this study (also reported in [468]) suggests that this regularizing mechanism is not very effective. In other words, if an informational lesion effect is taking place, this effect would be incomplete. This interpretation is supported by a study from Agnesi et al. [169], which showed that despite losing kinematic tuning, cells in the GP and VLo still responded to one or more aspects of joint movement during GP-DBS. Furthermore, the data has shown significant positive correlation between stronger FPM and higher eEPF values (Fig. 45). This suggests that the more complete the informational lesion (associated with higher eEPF, as discussed above), the stronger the modulatory effects and hence better therapy. Finally, it has been suggested that effective DBS in ET works by disrupting pathological activity in the CTT [68] or TCT [153]. Stimulation of the PSA has been demonstrated to produce good tremor control at lower stimulation intensities (compared to the Vim proper) [175]. This is presumably because the afferent CTT fibers are bundled together as they enter the ventrolateral thalamus and therefore stimulation is able to activate a larger proportion of these fibers. The larger intensities required to stimulate the Vim proper is supported by the finding of topographically organized 'tremor clusters' within that nucleus [176]. Therefore it is possible that stimulation in the Vim involves a volumetric effect in which tremor suppression results from electrical current sufficiently capturing these tremor clusters via either the 'informational lesion' or 'de-rhythmication' mechanisms.

5.6 Acknowledgements

This work was supported by the National Institutes of Health under grant R01-NS081118. We thank Rio Vetter, Jamie Hetke, and Rob Shoemaker from Neuronexus for helping with the design and fabrication of the DBS arrays. We also thank Noam Harel, Essa Yacoub, and Gregor Adriany at the Center for Magnetic Resonance Research. In addition, we thank Filippo Agnesi, Simeng Zhang, Edward Bello, Alexandra Doyle, Edgar Pena, Julia Slopsema and Logan Grado for help with data collection.

Chapter 6

Conclusions and Future Directions

This doctoral dissertation made the following contributions to advancing DBS technology for the treatment of ET: 1) Coupled high-field imaging data with image processing tools to generate subject-specific atlases of individual thalamic nuclei, thus improving the ability to visualize DBS targets. 2) Developed an efficient computational model-based algorithm to program high-density DBSAs. 3) Applied spherical statistical tools to quantify computational VTA models of DBS. (4) Characterized the stimulation-induced neuronal activity around chronically implanted thalamic DBSAs.

6.1 Summary of Findings

In Chapter 2, 7T SWI (n = 7) and DWI (n = 3) data from NHPs were used to create subject-specific atlases of the thalamus. The process involved the simultaneous use of a nonlinear image warping algorithm [313] and probabilitistic fiber tractography to segment individual thalamic nuclei and reconstruct the afferent fibers pathways. High-field SWI revealed that several regions of the thalamus (especially in the posterior regions) exhibited increased contrast relative to other regions within and external to thalamus. These borders with a difference in image contrast can then be used to guide manual segmentation or help provide landmarks for image deformation algorithms. Posterior thalamic nuclei including VPLc, Pulvinar and MGN exhibited significant trends of image hypointensity with age. Various studies in the past have described the use of

atlas deformation techniques [332, 489] and probabilistic fiber tractography [230, 268] separately, but their combined use in a multimodal approach have not been reported. The accuracy of thalamic nuclei segmentation was validated using electrophysiological recording data, blockface tissue sections as well as reconstructed afferent fibers. The results from the *in vivo* recording data showed good alignment between the locations of recorded VPLo and VPLc cells with their respective segmented volumes. Similarly, tissue sections also registered well with corresponding deformed atlas images, both in terms of the alignment of the borders of thalamus as well as regions such as MD, pulvinar and MGN that displayed hypointensity in the MRI. Furthermore, afferent ML, SCP and PF tracts all reached their respective destinations in the VPLc, VPLo and VLo/Va. Thus we have demonstrated in this study the feasibility to reconstruct from multimodal high-field imaging data both brain nuclei and their afferent fibers with good anatomical accuracy. This is important both for DBS target localization as well as building accurate subject-specific computational models. For example, it has been suggested that effective DBS therapy for ET acts through disruption of pathological activity in the CTT [68] or TCT [154] going to and from the Vim nucleus. The multimodal imaging approach described in this study is well-suited to locate the intersection of these fibers and the Vim, direct stimulation of which have been shown to achieve therapeutic effects with lower stimulation intensities [175] (as compared to stimulation of Vim proper).

In Chapter 3, we developed an efficient programming algorithm for DBSAs based on finite-element electric field models and the principles of convex optimization. The goal of the algorithm was to achieve optimal stimulation of a target volume by maximizing the AF values of axonal nodes of Ranvier within that volume. The conceptual innovation of the algorithm is that it breaks away from the traditional approach of pre-computing and storing numerous VTA solutions and searching through a database to find the solution that best captures a volume of interest [218, 219]. Instead, our approach only requires pre-computing as many finite-element simulations as there are electrodes on the DBSA (n = 32 for the study in Chapter 3) and storing the voltage field results. Given these results, the algorithm is able to deduce the maximum possible AF value at each axon node location within the volume of interest. Simultaneously achieving the highest possible AF

value for every node is not feasible because the second spatial difference of the extracellular voltage is dependent on the location and orientation of axons relative the voltage field. Therefore, the problem of maximization was further specified using three different objective function criteria: (1) linear programming (LP), (2) quadratic programing (QP) and (3) maximum deviation (MD). The algorithm was then able to leverage the principle of voltage superposition and forward compute the current output solutions that will satisfy each criterion in a matter of seconds. The results showed that the LP method produced the largest average AF values among the axon nodes, followed by the QP and then MD methods. However, the size of the spread of the AF values also followed in that order, with the LP method producing the most spread, and MD method the least. These characteristics of the three methods can be tailored to suit different needs, for example focal stimulation vs. broad excitation.

In Chapter 4, we modeled directional stimulation of 5000 thalamocortical relay neurons surrounding a 32 channel DBSA and utilized the tools of spherical statistics to quantitatively describe the profile of their activation. Spherical statistics has wide applications in analyzing directional data [415-417], but has not been introduced into the field of DBS to characterize the spatial effects of directional stimulation. The study described in detail the procedures from creation of a directional dataset (from 3D Cartesian data), to forming a hypothesis of a model to fit its shape, statistically testing that hypothesis and finally fitting the dataset to the appropriate parametric model. The study also demonstrated how parametric model parameters changed as a function of both stimulation amplitude and distance from the active electrode, using unidirectional stimulation as an example and fitting the distribution of activated neurons to the unimodal Kent Model. Interpretation of the change in model parameters indicated: 1) as stimulation amplitude increased, the shape of activated neurons became progressively more diffuse about the direction of stimulation and more symmetrical in shape. (2) More focal and symmetrical neuronal activation profiles were observed in concentric shells further away from the active electrode, despite reduced probabilities of activation. The approach and methods described in this study are well-suited to characterize the effects of directional stimulation and can be applied to data from a variety of modalities, including

computational modeling [213, 215], electrophysiological recording [407, 473] and optical imaging [442, 445].

In Chapter 5, we investigated the *in vivo* VTA by examining spatial characteristics of stimulation-induced neuronal activity around chronically implanted thalamic DBSAs in two NHPs. The study examined both neuronal firing rate and pattern changes as a function of stimulation amplitude and distance away from the source of stimulation. A novel entropy-based method was developed to quantify the degree and significance of firing pattern modulation based on PSTHs. The results showed that the majority of neurons were not modulated by stimulation, which is consistent with previous findings [473, 475]. The responses of the modulated neurons, on the other hand, were heterogeneous, ranging from firing rate increase and decrease to excitatory or inhibitory entrainment to the stimulus pulses, or a mixture of those responses. The majority of recordings showed that neurons were not influenced by increases in stimulation amplitude. However, within the fraction of data that did show modulation, a transition took place where FRM was gradually replaced with FPM as the stimulation amplitude increased. The results also showed that there was a propensity for FPM to occur at higher stimulation amplitudes. The implication for DBS is that at lower stimulation amplitudes, the mechanism of 'de-rhythmication' [478] is mainly through 'masking' of the rhythmic tremor activity [487] by creating randomness in spike activity via firing rate increasing, or raising the threshold for tremor burst propagation via firing rate decrease. At higher amplitudes, the mechanism shifts to disruption via entrainment (FPM) of spike activity. Increasing stimulation amplitude exhibited a differential modulatory effect only on a minority of cells. Within this group, a difference in modulatory effect was found between $250\mu A$ and $350\mu A$ and not between $150\mu A$ and $250\mu A$, suggesting a nonlinear effect. The data clearly showed that the recorded neurons can be divided into two groups: one that can be influenced by electrical stimulation, and another that altogether cannot at the stimulation levels tested. Taking the perspective that direct activation of axons is the main modulatory effect in DBS [445], and axonal activation is dependent on the AF at nodal compartments [448], it is likely that axonal projection patterns and the resulting relative orientation to the voltage field plays an important role in a neuron's response to

stimulation. This finding points to the importance of continued research to characterize network connectivity and projection patterns of neuronal processes, and incorporating them into computational models. Contrary to the traditional belief that stimulation leads to a sphere of activated neurons around the electrode tip which increases in size with increasing current [408, 410, 490], the results in Chapter 5 indicated that neuronal activation occurs over a wide range of distances and is not confined to the immediate vicinity of the active electrode. This was true regardless of the type of neuronal response to DBS. This finding is consistent with reported results from two-photon calcium imaging of neuronal responses to stimulation in the rodent and cat cortex, which demonstrated compelling evidence to suggest it was direct activation of axons near the stimulating electrode (within tens of microns) coupled with local axonal projection patterns that were the reasons for the sparse distribution of modulated cells [445]. The eEPF and iEPF values computed from the data in Chapter 5 were in close agreement with those reported by Agnesi et al. [468]. The eEPF values were less than 4% in both NHPs, suggesting that there was a strong low-pass filtering effect on excitatory entrainment taking place in the stimulated nucleus. This low-pass filtering effect is not at all accounted for in the majority of computational models of DBS, where entrained neurons will fire in a one-to-one fashion to the stimulus pulse. In addition, there's strong statistical evidence to suggest that eEPF is correlated with the degree of FPM (ΔH%), indicating that stronger modulation is due to higher rates of success of DBS pulses in inducing entrained spikes. Taken together, the findings described in Chapter 5 illustrate the reality and complexities of the *in vivo* VTA. The result of sparse and distributed neuronal activation is in strong agreement with previous findings [445] and likely reflects on local projection patterns of neuronal processes [445]. Understanding and reconstructing network connections of neurons near the site of stimulation will be important and necessary for the accurate modeling of the effects of DBS. Similarly, mechanisms of the low-pass filtering effect on excitatory entrainment should also be studied and incorporated into computational models.

The studies included in this dissertation developed computational tools and methodologies to address three challenges in the field of DBS: 1) accuracy of lead

placement, 2) complexity of DBS programming and 3) validation of computational models. The image processing tools developed in Chapter 2 and programming algorithms developed in Chapter 3 can have direct applications in DBS surgical planning and stimulator programming. The two areas can even be integrated into a single integrated package. The spherical statistics tools implemented in Chapter 4 can be applied directly to analyze the data from Chapter 5. Those tools can serve as a 'common language' to describe neuronal activation profiles resulting from directional stimulation. Finally, the results from Chapter 5 can serve as a reference for developing more accurate models of VTA during DBS and also highlights areas of model inaccuracies for further research.

6.2 Future Directions

6.2.1 Development of DBS Programming Algorithms and Their Translation to the Clinic

The optimization algorithm developed in Chapter 3 is a good starting point for efficient and automated programming of DBSAs. The objective of that algorithm was to maximize activation of axons in a region of interest. However, it does not take into account avoiding stimulation of regions that might induce adverse side-effects, as well as minimization of power consumption. In addition, algorithm predicted axonal activation based on AF values should be tested against results from stimulation of biophysical neuron models. These features were incorporated into a new study (spearheaded by colleagues in our laboratory) that was recently submitted for publication. The study developed a particle swarm optimization (PSO) algorithm to program DBSAs using a swarm of individual particles representing electrode configurations and stimulation amplitudes. Using a finite-element model of motor thalamic DBS, we demonstrate how the PSO algorithm can efficiently optimize a multi-objective function that maximizes predictions of axonal activation in regions of interest (cerebellar-receiving area of motor thalamus), minimizes predictions of axonal activation in regions of avoidance (somatosensory thalamus), and minimizes power consumption.

The infrastructure (including those developed in this dissertation) already exists for the subject-specific application of these programming algorithms in a clinical setting. Studies in the past have used motor and perceptual observations related to the side-effects of stimulation to validate model predicted effects of DBS. These include the use of EMG recordings of distal muscle groups to measure DBS activation of the internal capsule [210], as well as using patient reports sensory paresthesias to measure Vc activation [201]. Imaging modalities such as functional MRI [491] and positron emission tomography [492] can also be used to measure neuronal activation by DBS in target areas. A similar approach can be taken in a future study, in which both the target for stimulation (e.g. Vim or STN) and region of side-effects to avoid stimulation (e.g. Vc or IC) are defined and reconstructed with the multimodal imaging methods described in Chapter 2, using patient-specific high-field imaging data. These reconstructed nuclei and fiber pathways along with the finite-element models of the implanted DBS lead (e.g. Medtronic 3387 or 3389 models) are then input for the programming algorithms (convex optimization or PSO) to compute for the optimal stimulation setting. A test can then be performed in the following way: several experienced neurologists are shown the placement of the DBS lead relative to the reconstructed target nuclei/fiber pathways, and are asked to provide their programming solutions with the aim to achieve maximum therapy while minimizing adverse side-effects. The settings from the neurologists and the algorithms are then individually programmed into the patient's stimulator device in a series of test sessions, and the level of therapy and side-effects are measured using the above described methodologies. In this way, the programming algorithms can be directly compared against the experience and intuition of clinical neurologists, and their effectiveness can be evaluated in an objective manner. This test can also be performed in a simulated setting as well, in which the metrics for comparison of performance are the percentage activation of model neurons within the region of interest as well as the region of side-effect.

Furthermore, the imaging methods (nuclei segmentation coupled with fiber tractography) described in Chapter 2 and the programming algorithms can be integrated into a single software package to provide real-time insights into potential DBS therapy

during the surgical planning stage. The software will have a storage of 1) pre-computed finite-element voltage field solutions (equaled to the number of available electrodes, as described in Chapter 3) from various clinically available DBSAs, and 2) reconstructed DBS target nuclei and fiber pathways from the patient's high-field imaging data. Some development is needed to equip the software with the capability to populate target fiber tracts with 'virtual axons'. In rudimentary terms, this may consist of parallel line representations of fiber bundles (complete with axonal node points distributed along their lengths) that conform to the trajectory of the reconstructed pathways. Clinicians can then choose their placement of the DBSA, and the software will run the programming algorithm and predict the outcome of activation. This will allow the clinicians to test and compare multiple implant trajectories based on their predicted modulatory effects and aide in their decision-making process.

6.2.2 Studying the Effects of Directional Stimulation

The study described in Chapter 5 performed directional DBS in the VPLo of two NHPs. The analysis was focused on the effect of DBS on neuronal activity as a function of stimulation amplitude and distance. However, the directional effects of stimulation were not evaluated at this point. The data from Chapter 5 illustrated that the *in vivo* VTA was sparsely populated with modulated neurons, which were arranged in a distributed fashion amongst other neurons that were unresponsive to stimulation. Similar observations were made during stimulation in the cortex [445]. The likely explanation for this phenomenon is that stimulation directly activated local neuronal processes which have complex patterns of projections to cell bodies located further away [445]. Given our understanding that axonal activation is driven by the AF at nodes of Ranvier (a quantity that is dependent on the relative orientation of the axons to the extracellular voltage field), it is likely that we will observe a difference in the activities of recorded neurons based on the direction of stimulation. A more implicit approach to analyzing the effects of directional stimulation is to 'rank' the directions in terms of the magnitude of the recorded DBS artifact. More specifically, for each recorded neuron that has undergone stimulation from each of the four active electrodes, sort the recorded DBS artifacts by magnitude such that

the stimulated electrode producing the largest artifact is considered to most closely face that neuron, while the one with the smallest artifact faces away from it. In this way, each recorded neuron is located at the center of this reference frame while the DBSA rotates relative to it. The direction of stimulation can now be used as an independent variable with four values, and the metrics of neuronal modulation developed in Chapter 5 can be evaluated as a function of direction. These metrics can include the percentage change in PSTH entropy and neuronal firing rate between DBS-off and DBS-on states as well as the eEPF or iEPF. This analysis will determine how much change in modulatory effects is produced via directional stimulation. Taking another perspective, we can view the DBSA as immobile with recorded neurons distributed around it in space. In this scenario, the spherical statistics tools described in Chapter 4 are well-suited to characterize the distribution of modulated neurons in 3D. More specifically, for each stimulating electrode, find all the neurons that were modulated by its stimulation at 350μA, 250 μA and 150 μA. The results from Chapter 4 demonstrated that unidirectional stimulation will activate neurons whose spatial distribution can be represented by the unimodal Kent Model. Increase in the stimulation amplitude was predicted to result in the decrease of both model parameters κ and β, implying that the distribution will become more diffusely distributed about the population mean direction and more rotationally symmetric in shape. Results from the *in vivo* data can be directly compared against model predicted results and trends. If the conjecture that local axonal projections play an important role in shaping the *in vivo* VTA, then it is likely that spherical statistical characterization of that volume will deviate from a well-defined unimodal distribution. It is important to note that this process of reconstructing the 3D distribution of recorded neurons will require accurate localization of their positions relative to the DBSA and the active electrodes.

6.2.3 Development of Realistic Computational Models of DBS

Results from Chapter 5 pointed to two major discrepancies between the *in vivo* VTA and the computational model-predicted VTA. First, neurons modulated by DBS were sparsely distributed around the DBSA, and increasing stimulation amplitude was only able to differentially influence a minority group of neurons. This is in contrast to the model

predictions of a sphere of activation that increases in size with stimulation amplitude [217]. Secondly, the eEPF results indicated that entrainment of neuronal activity to DBS pulses does not occur in a one-to-one fashion, contrary to most computational model predictions. In fact the success rate of entrainment is very low, at less than 4%.

To bridge the first discrepancy, it is important that we have a realistic model of the connectivity patterns of neuronal processes in the target region. This can be done via tracing stained cells in tissue histology slices, as described in [205, 493]. In the Vim nucleus for example, the tracing effort should focus on studying as many relay neurons and interneurons as possible, and map on each cell the synaptic connections coming from the cerebellum, cortex, the reticular nucleus of thalamus, as well as other local interneurons. With this data we can ask a series of questions on connectivity patterns within the Vim. For example, how many interneurons on average are within a certain radius of a relay neuron? On average, how many afferent synapses does reach relay neuron receive from the cerebellum, cortex, reticular nucleus and other interneurons respectively and how are they distributed along the somatodendritic processes? What are those corresponding numbers for an interneuron? The answers to these questions will lead to the development of a set of general 'rules' for neuronal connectivity within the Vim, much like those employed in the network model in [494]. Integration of these rules with detailed morphological models of thalamic relay [205] and interneurons [493], as well as knowledge of broad projection trajectories of afferent [121, 378] and efferent [379] fibers to and from the Vim will form the foundations for the development of very realistic models of the Vim DBS. More specifically, it is conceivable to dynamically 'grow' a model neuronal network using the information listed above. Using a simplified version of the cerebellothalamocortical network for example, researchers can segment out the Vim, reticular nucleus of thalamus and the motor cortex from MRI, and also reconstruct the CTT and TCT using fiber tractography. Neurons native to each area are placed in sufficient numbers, their axons project via the reconstructed pathways to their respective target areas. Once within the target regions, these axons will dynamically extend out collaterals and seek to make synaptic connections with the appropriate target cells, in a manner consistent with the 'rules' of connectivity discussed previously.

Hypothetically, the axon from a neuron in the reticular nucleus of thalamus would actively seek out and synapse with X number of thalamic relay neurons before stopping, X being the average number of distinct relay neurons that a reticular neuron will synapse on to. In this way, an entire network may grow and form realistic connections on its own, until each element in the network has satisfied a series of connectivity constraints. The complex network of excitatory and inhibitory connections within the *in vivo* thalamus might play an important role in the observed neuronal responses to DBS as well as the spatial profile of the VTA. Researchers have begun to employ models of neurons with network connectivities [123, 166, 494]. Kent et al. [123] reported the use of a network model of thalamocortical relay neurons and found the simulated DBS evoked compound action potentials were comparable with those measured *in vivo*, both in terms of the shape of the waveforms as well as the way they change with stimulation amplitude. In order to replicate neuronal responses to DBS, we must also reconstruct ever more accurate models of the underlying neuronal networks. The idea of 'rule-based' growth of neuronal networks could possibly be a step in that direction.

To bridge the second discrepancy, it is necessary that we understand the exact mechanisms producing the observed low-pass filtering effect on excitatory transmission in the thalamus. One possibility is due to the stochastic nature of axonal action potential generation [495] that not all axons projecting through the stimulated area will follow the stimuli faithfully. Other possible mechanisms include depolarization block [496], membrane hyperpolarization due to activation of calcium-dependent potassium channels from an accumulation of intracellular calcium [497], accumulation of extracellular potassium within the periaxonal space [498], difficulties for axonal branches to conduct action potentials at high frequencies [497, 499] and vesicle depletion in synaptic transmission at high frequencies of stimulation [500]. Reports have also shown that interneurons are better able to sustain higher firing rates [501] and are less prone to conduction failure [502] compared to glutamatergic neurons. Therefore inhibitory projections from the reticular nucleus of thalamus as well as from local interneurons onto thalamic relay neurons might play an important role in reducing the extent of spike

entrainment for a given thalamo-cortical cell. These complex network effects will likely only emerge when the underlying neuronal networks are replicated.

Taken together, building more realistic computational models of DBS will require 1) replication of complex neuronal network connections and 2) identification and incorporation of potential mechanisms of conduction failure.

6.2.4 Development of a Tremor Model of VPLo DBS

The experiments in Chapter 5 were performed in the naïve state and did not establish a relationship between the degree of neuronal modulation in VPLo and therapy. What is needed is the development of a tremor model of ET, which is most commonly induced via the administration of harmaline [22]. Accelerometers placed on the limbs of the NHP can be used to measure tremor and evaluate the effects of DBS, similar to the methods performed on human ET patients in [165]. The goal will be to understand the quantitative differences in neuronal response to stimulation between therapeutic DBS and ineffective DBS. It is conceivably best to perform VPLo stimulation through a single electrode for ease of comparison between results. It will be important to establish the threshold stimulation amplitude (I_{Th}) for therapy, which for example can be defined as the amplitude that results in 50% reduction in tremor magnitude. Once this value is established, a set of subthreshold stimulation values can also be defined to provide a gradient of intensities for ineffective DBS (e.g. 25%I_{Th}, 50%I_{Th} and 75%I_{Th}). The experimental protocol will be to perform microelectrode recordings of unit spike activity from neurons adjacent to the implanted DBSA, before, during and after DBS. For each recorded neuron, stimulate through the single electrode using the four amplitudes listed above (duration and wash-in/wash-out times similar to those in Chapter 5) in a randomized fashion. We can then compute the change in PSTH entropy between DBS-off/DBS-on states ($\Delta H\%$, which is a measure of firing pattern regularity) as well as the eEPF, for every stimulation amplitude. Applying the 'informational lesion' hypothesis of DBS [164], we would expect to observe more regularized firing in more neurons during therapeutic DBS (I_{Th}) compared to during ineffective DBS (25%I_{Th}, 50%I_{Th} and 75%I_{Th}). To see if this is true, we can ask the following questions: (1) what percentage of

cells shows significant FPM at each stimulation amplitude? (2) What is the average $\Delta H\%$ across all neurons with significant FPM at each stimulation amplitude? Is there a significant difference between them? (3) Is there a significant correlation between stimulation amplitude and the average $\Delta H\%$ in cells with significant FPM? (4) What is the average eEPF across all neurons with significant FPM at each stimulation amplitude? Is there a significant difference between them? (5) Is there a significant correlation between stimulation amplitude and the average eEPF of cells with significant FPM? The answers to these questions will give insights on the differences in the strength of neuronal modulation and successfulness of entrainment (or informational lesion) between therapeutic DBS and ineffective DBS. Furthermore, the experiment can be modified to keep the stimulation amplitude constant while varying the frequency, and the same questions can be asked only with respect to the frequency of stimulation.

Overall, many challenges and opportunities remain in the field of DBS. The tools/methodologies and findings discussed in this dissertation will hopefully inform and help others further our understanding of the mechanisms of DBS as well as making improvements in its application for helping individuals with tremor reclaim control over their motor function.

References

1. Louis, E.D., R. Ottman, and W. Allen Hauser, *How common is the most common adult movement disorder? Estimates of the prevalence of essential tremor throughout the world.* Movement Disorders, 1998. **13**(1): p. 5-10.
2. Kurtzke, J.F., *The current neurologic burden of illness and injury in the United States.* Neurology, 1982. **32**(11): p. 1207-1207.
3. Hubble, J.P., K.L. Busenbark, and W.C. Koller, *Essential tremor.* Clin Neuropharmacol, 1989. **12**(6): p. 453-82.
4. Louis, E.D., et al., *Differences in the prevalence of essential tremor among elderly African Americans, whites, and Hispanics in northern Manhattan, NY.* Arch Neurol, 1995. **52**(12): p. 1201-5.
5. Rautakorpi, I., et al., *Essential tremor in a Finnish population.* Acta Neurologica Scandinavica, 1982. **66**(1): p. 58-67.
6. Louis, E.D. and R. Ottman, *Study of possible factors associated with age of onset in essential tremor.* Mov Disord, 2006. **21**(11): p. 1980-6.
7. Louis, E.D., L.S.t. Dure, and S. Pullman, *Essential tremor in childhood: a series of nineteen cases.* Mov Disord, 2001. **16**(5): p. 921-3.
8. Zesiewicz, T.A., et al., *Overview of essential tremor.* Neuropsychiatr Dis Treat, 2010. **6**: p. 401-8.
9. Whaley, N., et al., *Essential tremor: phenotypic expression in a clinical cohort.* Parkinsonism Relat Disord, 2007. **13**(6): p. 333-339.
10. Singer, C., J. Sanchez-Ramos, and W.J. Weiner, *Gait abnormality in essential tremor.* Mov Disord, 1994. **9**(2): p. 193-6.
11. Rautakorpi, I., *Essential tremor: an epidemiological, clinical and genetic study*. 1978: I. Rautakorpi.
12. Louis, E.D., *Functional correlates of lower cognitive test scores in essential tremor.* Mov Disord, 2010. **25**(4): p. 481-5.
13. Louis, E.D., et al., *Risk of tremor and impairment from tremor in relatives of patients with essential tremor: a community-based family study.* Ann Neurol, 2001. **49**(6): p. 761-9.
14. Louis, E.D., *Etiology of essential tremor: should we be searching for environmental causes?* Mov Disord, 2001. **16**(5): p. 822-9.
15. Louis, E.D., et al., *Torpedoes in Parkinson's disease, Alzheimer's disease, essential tremor, and control brains.* Mov Disord, 2009. **24**(11): p. 1600-5.
16. Louis, E.D., et al., *Neuropathological changes in essential tremor: 33 cases compared with 21 controls.* Brain, 2007. **130**(Pt 12): p. 3297-307.
17. Guillain, G., *The Syndrome of Synchronous and Rhythmic Palato-Pharyngo-Laryngo-Oculo-Diaphragmatic Myoclonus: (Section of Neurology).* Proc R Soc Med, 1938. **31**(9): p. 1031-8.

18. Eccles, J., R. Llinas, and K. Sasaki, *Excitation of cerebellar Purkinje cells by the climbing fibres.* 1964.
19. Ruigrok, T.J. and J. Voogd, *Cerebellar influence on olivary excitability in the cat.* Eur J Neurosci, 1995. **7**(4): p. 679-93.
20. Llinas, R. and K. Sasaki, *The Functional Organization of the Olivo-Cerebellar System as Examined by Multiple Purkinje Cell Recordings.* Eur J Neurosci, 1989. **1**(6): p. 587-602.
21. Llinas, R. and M. Muhlethaler, *Electrophysiology of guinea-pig cerebellar nuclear cells in the in vitro brain stem-cerebellar preparation.* J Physiol, 1988. **404**: p. 241-58.
22. Elble, R.J., *Animal models of action tremor.* Mov Disord, 1998. **13 Suppl 3**: p. 35-9.
23. Jankovic, J. and J.L. Noebels, *Genetic mouse models of essential tremor: are they essential?* The Journal of clinical investigation, 2005. **115**(3): p. 584-586.
24. Lorenz, D. and G. Deuschl, *Update on pathogenesis and treatment of essential tremor.* Curr Opin Neurol, 2007. **20**(4): p. 447-52.
25. Sugihara, I., E.J. Lang, and R. Llinas, *Serotonin modulation of inferior olivary oscillations and synchronicity: a multiple-electrode study in the rat cerebellum.* Eur J Neurosci, 1995. **7**(4): p. 521-34.
26. Wiklund, L., *Serotonergic innervation of the inferior olive and tremor generated in the olivocerebellar climbing fiber system*, in *Serotonin, the Cerebellum, and Ataxia*. 1993, Raven Press New York. p. 113-119.
27. Shaikh, A.G., et al., *Hypothetical membrane mechanisms in essential tremor.* J Transl Med, 2008. **6**: p. 68.
28. Busby, L. and Y. Lamarre, *Effect of diazepam on the neuronal rhythmic activity and tremor induced by harmaline.* The Inferior Olivary Nucleus: Anatomy and Physiology, edited by J. Courville, C. DeMontigny, and Y. Lamarre. New York: Raven, 1980: p. 315-320.
29. Sinclair, J.G., G.F. Lo, and D.P. Harris, *Ethanol effects on the olivocerebellar system.* Can J Physiol Pharmacol, 1982. **60**(5): p. 610-4.
30. Rappaport, M.S., et al., *Ethanol effects on harmaline-induced tremor and increase of cerebellar cyclic GMP*. Life Sci, 1984. **34**(1): p. 49-56.
31. Sarem-Aslani, A. and K. Mullett, *Industrial perspective on deep brain stimulation: history, current state, and future developments.* Front Integr Neurosci, 2011. **5**: p. 46.
32. Lyons, K.E. and R. Pahwa, *Pharmacotherapy of essential tremor : an overview of existing and upcoming agents.* CNS Drugs, 2008. **22**(12): p. 1037-45.
33. Cleeves, L. and L.J. Findley, *Propranolol and propranolol-LA in essential tremor: a double blind comparative study*. J Neurol Neurosurg Psychiatry, 1988. **51**(3): p. 379-84.
34. Koller, W.C., *Long-acting propranolol in essential tremor.* Neurology, 1985. **35**(1): p. 108-10.

35. Zesiewicz, T., et al., *Practice parameter: therapies for essential tremor report of the quality standards subcommittee of the American Academy of Neurology.* Neurology, 2005. **64**(12): p. 2008-2020.
36. Shahzadi, S., R.R. Tasker, and A. Lozano, *Thalamotomy for essential and cerebellar tremor.* Stereotact Funct Neurosurg, 1995. **65**(1-4): p. 11-7.
37. Jankovic, J., et al., *Outcome after stereotactic thalamotomy for parkinsonian, essential, and other types of tremor.* Neurosurgery, 1995. **37**(4): p. 680-6; discussion 686-7.
38. Asanuma, C., W.T. Thach, and E.G. Jones, *Distribution of Cerebellar Terminations and Their Relation to Other Afferent Terminations in the Ventral Lateral Thalamic Region of the Monkey.* Brain Research Reviews, 1983. **5**(3): p. 237-265.
39. Haber, S. and N.R. McFarland, *The place of the thalamus in frontal cortical-basal ganglia circuits.* Neuroscientist, 2001. **7**(4): p. 315-24.
40. Jones, E.G., S.P. Wise, and J.D. Coulter, *Differential thalamic relationships of sensory-motor and parietal cortical fields in monkeys.* J Comp Neurol, 1979. **183**(4): p. 833-81.
41. Schuurman, P.R., et al., *A comparison of continuous thalamic stimulation and thalamotomy for suppression of severe tremor.* N Engl J Med, 2000. **342**(7): p. 461-8.
42. Nagaseki, Y., et al., *Long-term follow-up results of selective VIM-thalamotomy.* J Neurosurg, 1986. **65**(3): p. 296-302.
43. Zirh, A., et al., *Stereotactic thalamotomy in the treatment of essential tremor of the upper extremity: reassessment including a blinded measure of outcome.* J Neurol Neurosurg Psychiatry, 1999. **66**(6): p. 772-5.
44. Akbostanci, M.C., K.V. Slavin, and K.J. Burchiel, *Stereotactic ventral intermedial thalamotomy for the treatment of essential tremor: results of a series of 37 patients.* Stereotact Funct Neurosurg, 1999. **72**(2-4): p. 174-7.
45. Benabid, A.L., et al., *Chronic VIM thalamic stimulation in Parkinson's disease, essential tremor and extra-pyramidal dyskinesias.* Acta Neurochir Suppl (Wien), 1993. **58**: p. 39-44.
46. Hassler, R., et al., *Physiological observations in stereotaxic operations in extrapyramidal motor disturbances.* Brain, 1960. **83**: p. 337-50.
47. Gildenberg, P.L., *Evolution of neuromodulation.* Stereotact Funct Neurosurg, 2005. **83**(2-3): p. 71-9.
48. Heath, R.G. and W.A. Mickle, *Evaluation of Seven Years< Experience with Depth Electrode Studies in Human Patients.* 1960.
49. Hosobuchi, Y., J.E. Adams, and B. Rutkin, *Chronic thalamic stimulation for the control of facial anesthesia dolorosa.* Arch Neurol, 1973. **29**(3): p. 158-61.
50. Bechtereva, N., et al., *Method of electrostimulation of the deep brain structures in treatment of some chronic diseases.* Stereotact Funct Neurosurg, 1975. **37**(1-3): p. 136-140.

51. Benabid, A.L., et al., *Combined (thalamotomy and stimulation) stereotactic surgery of the VIM thalamic nucleus for bilateral Parkinson disease.* Appl Neurophysiol, 1987. **50**(1-6): p. 344-6.
52. Siegfried, J. and J. Shulman, *Deep brain stimulation.* Pacing Clin Electrophysiol, 1987. **10**(1 Pt 2): p. 271-2.
53. Benabid, A.L., et al., *Long-term suppression of tremor by chronic stimulation of the ventral intermediate thalamic nucleus.* Lancet, 1991. **337**(8738): p. 403-6.
54. Siegfried, J. and B. Lippitz, *Chronic electrical stimulation of the VL-VPL complex and of the pallidum in the treatment of movement disorders: personal experience since 1982.* Stereotact Funct Neurosurg, 1994. **62**(1-4): p. 71-5.
55. Limousin, P., et al., *Effect of parkinsonian signs and symptoms of bilateral subthalamic nucleus stimulation.* Lancet, 1995. **345**(8942): p. 91-5.
56. Limousin, P., et al., *Multicentre European study of thalamic stimulation in parkinsonian and essential tremor.* J Neurol Neurosurg Psychiatry, 1999. **66**(3): p. 289-96.
57. The Deep-Brain Stimulation for Parkinson's Disease Study, G., *Deep-brain stimulation of the subthalamic nucleus or the pars interna of the globus pallidus in Parkinson's disease.[comment]*. New England Journal of Medicine., 2001. **345**(13): p. 956-63.
58. Coubes, P., et al., *Treatment of DYT1-generalised dystonia by stimulation of the internal globus pallidus.* Lancet, 2000. **355**(9222): p. 2220-1.
59. Kupsch, A., et al., *Pallidal deep-brain stimulation in primary generalized or segmental dystonia.* N Engl J Med, 2006. **355**(19): p. 1978-90.
60. Temel, Y. and V. Visser-Vandewalle, *Surgery in Tourette syndrome.* Mov Disord, 2004. **19**(1): p. 3-14.
61. Porta, M., et al., *Thalamic deep brain stimulation for treatment-refractory Tourette syndrome Two-year outcome.* Neurology, 2009. **73**(17): p. 1375-1380.
62. Nuttin, B., et al., *Electrical stimulation in anterior limbs of internal capsules in patients with obsessive-compulsive disorder.* Lancet, 1999. **354**(9189): p. 1526.
63. Malone, D.A., Jr., et al., *Deep brain stimulation of the ventral capsule/ventral striatum for treatment-resistant depression.* Biol Psychiatry, 2009. **65**(4): p. 267-75.
64. Bewernick, B.H., et al., *Nucleus accumbens deep brain stimulation decreases ratings of depression and anxiety in treatment-resistant depression.* Biol Psychiatry, 2010. **67**(2): p. 110-6.
65. Velasco, F., et al., *Electrical stimulation of the centromedian thalamic nucleus in the treatment of convulsive seizures: a preliminary report.* Epilepsia, 1987. **28**(4): p. 421-30.
66. Hodaie, M., et al., *Chronic anterior thalamus stimulation for intractable epilepsy.* Epilepsia, 2002. **43**(6): p. 603-8.
67. Flora, E.D., et al., *Deep brain stimulation for essential tremor: a systematic review.* Mov Disord, 2010. **25**(11): p. 1550-9.
68. Groppa, S., et al., *Physiological and anatomical decomposition of subthalamic neurostimulation effects in essential tremor.* Brain, 2014. **137**(Pt 1): p. 109-21.

69. Plaha, P., N.K. Patel, and S.S. Gill, *Stimulation of the subthalamic region for essential tremor*. J Neurosurg, 2004. **101**(1): p. 48-54.
70. Blomstedt, P., U. Sandvik, and S. Tisch, *Deep brain stimulation in the posterior subthalamic area in the treatment of essential tremor.* Mov Disord, 2010. **25**(10): p. 1350-6.
71. Klein, J.C., et al., *The tremor network targeted by successful VIM deep brain stimulation in humans.* Neurology, 2012. **78**(11): p. 787-95.
72. Sandvik, U., et al., *Thalamic and Subthalamic DBS for Essential Tremor: WhereIs the Optimal Target?[published online ahead of print Sep 27 2012] Neurosurgery 2011*.
73. Macchi, G. and E.G. Jones, *Toward an agreement on terminology of nuclear and subnuclear divisions of the motor thalamus.* J Neurosurg, 1997. **86**(1): p. 77-92.
74. Elble, R.J., *Tremor disorders.* Curr Opin Neurol, 2013. **26**(4): p. 413-9.
75. Hassler, R., *Anatomy of the thalamus*, in *Introduction to Stereotaxis with an Atlas of the Human Brain*, G. Schaltenbrand and P. Bailey, Editors. 1959, Thieme: Stuttgart. p. 230-290.
76. Walker, A.E., *The primate thalamus.* 1938.
77. Olszewski, J., *The thalamus of the Macaca, mulatta. An atlas for use with the stereotaxic instrument.* The thalamus of the Macaca, mulatta. An atlas for use with the stereotaxic instrument., 1952.
78. Friedman, D.P. and E.G. Jones, *Thalamic input to areas 3a and 2 in monkeys.* J Neurophysiol, 1981. **45**(1): p. 59-85.
79. Jones, E.G. and D.P. Friedman, *Projection pattern of functional components of thalamic ventrobasal complex on monkey somatosensory cortex.* J Neurophysiol, 1982. **48**(2): p. 521-44.
80. Ilinsky, I. and K. Kultas-Ilinsky, *Sagittal cytoarchitectonic maps of the macaca mulatta thalamus with a revised nomenclature of the motor-related nuclei validated by observations on their connectivity.* J.Comp.Neurol., 1987. **262**: p. 331-364.
81. Percheron, G., C. François, and J. Yelnik, *Relations entre les ganglions de la base et le thalamus du primate. Nouvelles données morphologiques. Nouvelles interprétations physiopathologiques.* Rev. Neurol, 1986. **142**: p. 337-353.
82. Walker, A., *Normal and pathological physiology of the human thalamus*, in *Stereotaxy of the Human Brain. Anatomical, Physiological and Clinical Applications*, S. G and W. AE, Editors. 1982, Stuttgart: Thieme. p. 181–217.
83. Hirai, T. and E.G. Jones, *A new parcellation of the human thalamus on the basis of histochemical staining.* Brain Res Brain Res Rev, 1989. **14**(1): p. 1-34.
84. Hirai, T. and E. Jones, *Distribution of tachykinin-and enkephalin-immunoreactive fibers in the human thalamus.* Brain Research Reviews, 1989. **14**(1): p. 35-52.
85. Ohye, C., *Thalamus*, in *The Human Nervous System*, P. G, Editor. 1990, Academic Press: San Diego. p. 439–468.
86. Ilinsky, I. and K. Kultas-Ilinsky, *Sagittal cytoarchitectonic maps of the Macaca mulatta thalamus with a revised nomenclature of the motor-related nuclei*

validated by observations on their connectivity. Journal of Comparative Neurology, 1987. **262**(3): p. 331-364.

87. Kultas-Ilinsky, K. and I.A. Ilinsky, *Fine structure of the magnocellular subdivision of the ventral anterior thalamic nucleus (VAmc) of Macaca mulatta: II. Organization of nigrothalamic afferents as revealed with EM autoradiography.* J Comp Neurol, 1990. **294**(3): p. 479-89.
88. Percheron, G., et al., *The primate motor thalamus analysed with reference to subcortical afferent territories.* Stereotact Funct Neurosurg, 1993. **60**(1-3): p. 32-41.
89. DeVito, J.L. and M.E. Anderson, *An autoradiographic study of efferent connections of the globus pallidus in Macaca mulatta.* Exp Brain Res, 1982. **46**(1): p. 107-17.
90. Schmahmann, J.D. and D.N. Pandya, *Anatomical investigation of projections from thalamus to posterior parietal cortex in the rhesus monkey: a WGA-HRP and fluorescent tracer study.* J Comp Neurol, 1990. **295**(2): p. 299-326.
91. Tracey, D.J., et al., *Thalamic relay to motor cortex: afferent pathways from brain stem, cerebellum, and spinal cord in monkeys.* J Neurophysiol, 1980. **44**(3): p. 532-54.
92. Schell, G.R. and P.L. Strick, *The origin of thalamic inputs to the arcuate premotor and supplementary motor areas.* J Neurosci, 1984. **4**(2): p. 539-60.
93. Mikula, S., et al., *Internet-enabled high-resolution brain mapping and virtual microscopy.* Neuroimage, 2007. **35**(1): p. 9-15.
94. Benabid, A.L., et al., *Deep brain stimulation for movement disorders*, in *Youmans Neurological Surgery*, H.R. Winn, Editor. 2004, Saunders: Philadelphia.
95. Alexander, G.E. and M.D. Crutcher, *Functional architecture of basal ganglia circuits: neural substrates of parallel processing.* Trends Neurosci, 1990. **13**(7): p. 266-71.
96. DeLong, M.R., *Primate models of movement disorders of basal ganglia origin.* Trends Neurosci, 1990. **13**(7): p. 281-5.
97. Kurata, K. and S.P. Wise, *Premotor and supplementary motor cortex in rhesus monkeys: neuronal activity during externally- and internally-instructed motor tasks.* Exp Brain Res, 1988. **72**(2): p. 237-48.
98. Mushiake, H., M. Inase, and J. Tanji, *Neuronal activity in the primate premotor, supplementary, and precentral motor cortex during visually guided and internally determined sequential movements.* J Neurophysiol, 1991. **66(3)**: p. 705-718.
99. Kurata, K., *Premotor cortex of monkeys: set- and movement-related activity reflecting amplitude and direction of wrist movements.* ournal of Neurophysiology, 1993. **69**: p. 187-200.
100. Haber, S.N., E. Lynd-Balta, and W.P.J.M. Spooren, *Integrative aspects of basal ganglia circuitry*, in *The Basal Ganglia IV. New ideas and data on structure and function*, G. Percheron, J.S. McKenzie, and J. Feger, Editors. 1994, Plenum Press: New York and London. p. 71-80.

101. Parent, A. and L.N. Hazrati, *Functional anatomy of the basal ganglia. I. The cortico-basal ganglia-thalamo-cortical loop.* Brain Res Brain Res Rev, 1995. **20**(1): p. 91-127.
102. Passingham, R.E., *The frontal lobes and voluntary action*. 1993: Oxford University Press.
103. Levy, R. and P.S. Goldman-Rakic, *Association of storage and processing functions in the dorsolateral prefrontal cortex of the nonhuman primate.* J Neurosci, 1999. **19**(12): p. 5149-58.
104. Selemon, L.D. and P.S. Goldman-Rakic, *Longitudinal topography and interdigitation of corticostriatal projections in the rhesus monkey.* J Neurosci, 1985. **5**(3): p. 776-94.
105. Rolls, E.T., et al., *Orbitofrontal cortex neurons: role in olfactory and visual association learning.* J Neurophysiol, 1996. **75**(5): p. 1970-81.
106. Tremblay, L. and W. Schultz, *Modifications of reward expectation-related neuronal activity during learning in primate orbitofrontal cortex.* J Neurophys, 2000. **83**(4): p. 1877-1885.
107. Haber, S.N., et al., *The Orbital and Medial Prefrontal Circuit through the Primate Basal Ganglia.* Journal of Neuroscience, 1995. **15**(7): p. 4851-4867.
108. Caracalos, A., E. Levita, and I. Cooper, *A study of roentgeno-anatomic lesion location and results in cryosurgery of the basal ganglia.* St. Barnabas Hospital Medical Bulletin, 1961. **1**: p. 24-32.
109. Carpenter, M.B. and G.R. Hanna, *Effects of thalamic lesions upon cerebellar dyskinesia in the rhesus monkey.* Journal of Comparative Neurology, 1962. **119**(2): p. 127-147.
110. Wiesendanger, R. and M. Wiesendanger, *The thalamic connections with medial area 6 (supplementary motor cortex) in the monkey (macaca fascicularis).* Exp Brain Res, 1985. **59**(1): p. 91-104.
111. Matelli, M. and G. Luppino, *Thalamic input to mesial and superior area 6 in the macaque monkey.* J Comp Neurol, 1996. **372**(1): p. 59-87.
112. Sherman, S.M. and R.W. Guillery, *Functional organization of thalamocortical relays.* J Neurophysiol, 1996. **76**(3): p. 1367-95.
113. Deschenes, M., P. Veinante, and Z.W. Zhang, *The organization of corticothalamic projections: reciprocity versus parity.* Brain Res Brain Res Rev, 1998. **28**(3): p. 286-308.
114. Jones, E.G. and S.P. Wise, *Size, laminar and columnar distribution of efferent cells in the sensory-motor cortex of monkeys.* J Comp Neurol, 1977. **175**(4): p. 391-438.
115. Giguere, M. and P. Goldman-Rakic, *Mediodorsal nucleus: areal, laminar, and tangential distribution of afferents and efferents in the frontal lobe of rhesus monkeys.* Journal of Comparative Neurology, 1988. **277**(2): p. 195-213.
116. Kurata, K., *Site of origin of projections from the thalamus to dorsal versus ventral aspects of the premotor cortex of monkeys.* Neurosci Res, 1994. **21**(1): p. 71-6.

117. Kunzle, H., *An autoradiographic analysis of the efferent connections from premotor and adjacent prefrontal regions (areas 6 and 9) in macaca fascicularis.* Brain Behav Evol, 1978. **15**(3): p. 185-234.
118. Fenelon, G., et al., *Topographic distribution of the neurons of the central complex (centre median-parafascicular complex) and of other thalamic neurons projecting to the striatum in macaques.* Neuroscience, 1991. **45**(2): p. 495-510.
119. Gimenez-Amaya, J.M., et al., *Organization of thalamic projections to the ventral striatum in the primate.* J Comp Neurol, 1995. **354**(1): p. 127-49.
120. McFarland, N.R. and S.N. Haber, *Organization of thalamostriatal terminals from the ventral motor nuclei in the macaque.* J Comp Neurol, 2001. **429**(2): p. 321-36.
121. Gallay, M.N., et al., *Human pallidothalamic and cerebellothalamic tracts: anatomical basis for functional stereotactic neurosurgery.* Brain Structure and Function, 2008. **212**(6): p. 443-463.
122. Asanuma, C., W.T. Thach, and E.G. Jones, *Anatomical evidence for segregated focal grouping of efferent cells and their terminal ramifications in the cerebellothalamic pathway of the monkey.* Brain Res.Rev., 1983. **5**: p. 267-297.
123. Kent, A.R. and W.M. Grill, *Neural origin of evoked potentials during thalamic deep brain stimulation.* J Neurophysiol, 2013. **110**(4): p. 826-43.
124. Darian-Smith, C., I. Darian-Smith, and S.S. Cheema, *Thalamic projections to sensorimotor cortex in the macaque monkey: use of multiple retrograde fluorescent tracers.* J Comp Neurol, 1990. **299**(1): p. 17-46.
125. Kievit, J. and H.G. Kuypers, *Organization of the thalamo-cortical connexions to the frontal lobe in the rhesus monkey.* Exp Brain Res, 1977. **29**(3-4): p. 299-322.
126. Matelli, M., et al., *Thalamic input to inferior area 6 and area 4 in the macaque monkey.* J Comp Neurol, 1989. **280**(3): p. 468-88.
127. Sakai, S.T., M. Inase, and J. Tanji, *Comparison of cerebellothalamic and pallidothalamic projections in the monkey (Macaca fuscata): a double anterograde labeling study.* J Comp Neurol, 1996. **368**(2): p. 215-28.
128. Middleton, F.A. and P.L. Strick, *Anatomical evidence for cerebellar and basal ganglia involvement in higher cognitive function.* Science, 1994. **266**(5184): p. 458-61.
129. Nakano, K., et al., *Cortical connections of the motor thalamic nuclei in the Japanese monkey, Macaca fuscata.* Stereotact Funct Neurosurg, 1993. **60**(1-3): p. 42-61.
130. Rouiller, E.M., et al., *Cerebellothalamocortical and pallidothalamocortical projections to the primary and supplementary motor cortical areas: a multiple tracing study in macaque monkeys.* J Comp Neurol, 1994. **345**(2): p. 185-213.
131. Burton, H. and E.G. Jones, *The posterior thalamic region and its cortical projection in New World and Old World monkeys.* J Comp Neurol, 1976. **168**(2): p. 249-301.
132. Jones, E., *Some aspects of the organization of the thalamic reticular complex.* Journal of Comparative Neurology, 1975. **162**(3): p. 285-308.

133. Guillery, R.W. and J.K. Harting, *Structure and connections of the thalamic reticular nucleus: Advancing views over half a century.* J Comp Neurol, 2003. **463**(4): p. 360-71.
134. Ohara, P.T. and A. Lieberman, *The thalamic reticular nucleus of the adult rat: experimental anatomical studies.* Journal of Neurocytology, 1985. **14**(3): p. 365-411.
135. Jones, E.G., *The thalamus*. 2012: Springer Science & Business Media.
136. Ahlsen, G. and S. Lindstrom, *Mutual Inhibition between Perigeniculate Neurons.* Brain Research, 1982. **236**(2): p. 482-486.
137. SanchezVives, M.V., T. Bal, and D.A. McCormick, *Inhibitory interactions between perigeniculate GABAergic neurons.* Journal of Neuroscience, 1997. **17**(22): p. 8894-8908.
138. Shosaku, A. and I. Sumitomo, *Auditory neurons in the rat thalamic reticular nucleus.* Exp Brain Res, 1983. **49**(3): p. 432-42.
139. Shosaku, A., Y. Kayama, and I. Sumitomo, *Somatotopic organization in the rat thalamic reticular nucleus.* Brain Res, 1984. **311**(1): p. 57-63.
140. Gonzalo-Ruiz, A. and A.R. Lieberman, *GABAergic projections from the thalamic reticular nucleus to the anteroventral and anterodorsal thalamic nuclei of the rat.* J Chem Neuroanat, 1995. **9**(3): p. 165-74.
141. Gonzalo-Ruiz, A. and A.R. Lieberman, *Topographic organization of projections from the thalamic reticular nucleus to the anterior thalamic nuclei in the rat.* Brain Res Bull, 1995. **37**(1): p. 17-35.
142. Guillery, R.W., S.L. Feig, and D.A. Lozsadi, *Paying attention to the thalamic reticular nucleus.* Trends Neurosci, 1998. **21**(1): p. 28-32.
143. Bourassa, J. and M. Deschenes, *Corticothalamic Projections from the Primary Visual-Cortex in Rats - a Single-Fiber Study Using Biocytin as an Anterograde Tracer*. Neuroscience, 1995. **66**(2): p. 253-263.
144. Fitzpatrick, D., et al., *The sublaminar organization of corticogeniculate neurons in layer 6 of macaque striate cortex.* Vis Neurosci, 1994. **11**(2): p. 307-15.
145. Hale, P.T., et al., *Interrelations of the rat's thalamic reticular and dorsal lateral geniculate nuclei.* Exp Brain Res, 1982. **45**(1-2): p. 217-29.
146. Pinault, D., *The thalamic reticular nucleus: structure, function and concept.* Brain Res Brain Res Rev, 2004. **46**(1): p. 1-31.
147. Guillery, R.W., *Patterns of fiber degeneration in the dorsal lateral geniculate nucleus of the cat following lesions in the visual cortex.* J Comp Neurol, 1967. **130**(3): p. 197-221.
148. Golshani, P., X.B. Liu, and E.G. Jones, *Differences in quantal amplitude reflect GluR4-subunit number at corticothalamic synapses on two populations of thalamic neurons.* Proceedings of the National Academy of Sciences of the United States of America, 2001. **98**(7): p. 4172-4177.
149. Pinault, D. and M. Deschenes, *Voltage-dependent 40-Hz oscillations in rat reticular thalamic neurons in vivo.* Neuroscience, 1992. **51**(2): p. 245-58.

150. Ohara, P.T., G. Chazal, and H.J. Ralston, 3rd, *Ultrastructural analysis of GABA-immunoreactive elements in the monkey thalamic ventrobasal complex.* J Comp Neurol, 1989. **283**(4): p. 541-58.
151. Vitek, J.L., et al., *Physiologic properties and somatotopic organization of the primate motor thalamus.* J Neurophysiol, 1994. **71**(4): p. 1498-513.
152. Vitek, J.L., et al., *Microstimulation of primate motor thalamus: Somatotopic organization and differential distribution of evoked motor responses among subnuclei.* J Neurophysiol, 1996. **75**(6): p. 2486-2495.
153. Miocinovic, S., et al., *History, applications, and mechanisms of deep brain stimulation.* JAMA Neurol, 2013. **70**(2): p. 163-71.
154. Benazzouz, A., et al., *Effect of high-frequency stimulation of the subthalamic nucleus on the neuronal activities of the substantia nigra pars reticulata and ventrolateral nucleus of the thalamus in the rat.* Neuroscience, 2000. **99**(2): p. 289-95.
155. Welter, M.L., et al., *Effects of high-frequency stimulation on subthalamic neuronal activity in parkinsonian patients.* Arch Neurol, 2004. **61**(1): p. 89-96.
156. Dostrovsky, J.O., et al., *Microstimulation-induced inhibition of neuronal firing in human globus pallidus.* J Neurophysiol, 2000. **84**(1): p. 570-4.
157. Hashimoto, T., et al., *Stimulation of the subthalamic nucleus changes the firing pattern of pallidal neurons.* J Neurosci, 2003. **23**(5): p. 1916-23.
158. Anderson, M.E., N. Postupna, and M. Ruffo, *Effects of high-frequency stimulation in the internal globus pallidus on the activity of thalamic neurons in the awake monkey.* J Neurophysiol, 2003. **89**(2): p. 1150-60.
159. Montgomery, E.B., Jr., *Effects of GPi stimulation on human thalamic neuronal activity.* Clin Neurophysiol, 2006. **117**(12): p. 2691-702.
160. Vitek, J.L., et al., *External pallidal stimulation improves parkinsonian motor signs and modulates neuronal activity throughout the basal ganglia thalamic network.* Exp Neurol, 2012. **233**(1): p. 581-6.
161. McIntyre, C.C., et al., *Cellular effects of deep brain stimulation: model-based analysis of activation and inhibition.* J Neurophysiol, 2004. **91**(4): p. 1457-69.
162. Xu, W., et al., *Subthalamic nucleus stimulation modulates thalamic neuronal activity.* J Neurosci, 2008. **28**(46): p. 11916-24.
163. Johnson, M.D., J.L. Vitek, and C.C. McIntyre, *Pallidal stimulation that improves parkinsonian motor symptoms also modulates neuronal firing patterns in primary motor cortex in the MPTP-treated monkey.* Experimental Neurology, 2009. **219**(1): p. 359-362.
164. Grill, W.M., A.N. Snyder, and S. Miocinovic, *Deep brain stimulation creates an informational lesion of the stimulated nucleus.* Neuroreport, 2004. **15**(7): p. 1137-40.
165. Kuncel, A.M., et al., *Amplitude- and frequency-dependent changes in neuronal regularity parallel changes in tremor With thalamic deep brain stimulation.* IEEE Trans Neural Syst Rehabil Eng, 2007. **15**(2): p. 190-7.
166. Dorval, A.D., et al., *Deep brain stimulation alleviates parkinsonian bradykinesia by regularizing pallidal activity.* J Neurophysiol, 2010. **104**(2): p. 911-21.

167. Dorval, A.D., et al., *Deep brain stimulation reduces neuronal entropy in the MPTP-primate model of Parkinson's disease.* J Neurophysiol, 2008. **100**(5): p. 2807-18.
168. Couto, J. and W.M. Grill, *Kilohertz Frequency Deep Brain Stimulation Is Ineffective at Regularizing the Firing of Model Thalamic Neurons.* Frontiers in Computational Neuroscience, 2016. **10**.
169. Agnesi, F., et al., *Deep brain stimulation imposes complex informational lesions.* PLoS One, 2013. **8**(8): p. e74462.
170. Johnson, M.D., et al., *Mechanisms and targets of deep brain stimulation in movement disorders.* Neurotherapeutics, 2008. **5**(2): p. 294-308.
171. Guo, Y., et al., *Thalamocortical relay fidelity varies across subthalamic nucleus deep brain stimulation protocols in a data-driven computational model.* J Neurophys, 2008. **99**(3): p. 1477-1492.
172. Zheng, F., et al., *Axonal failure during high frequency stimulation of rat subthalamic nucleus.* J Physiol, 2011. **589**(Pt 11): p. 2781-93.
173. Herzog, J., et al., *Kinematic analysis of thalamic versus subthalamic neurostimulation in postural and intention tremor.* Brain, 2007. **130**(Pt 6): p. 1608-25.
174. Stover, N.P., et al., *Stimulation of the subthalamic nucleus in a patient with Parkinson disease and essential tremor.* Arch Neurol, 2005. **62**(1): p. 141-3.
175. Barbe, M.T., et al., *Deep brain stimulation of the ventral intermediate nucleus in patients with essential tremor: stimulation below intercommissural line is more efficient but equally effective as stimulation above.* Exp Neurol, 2011. **230**(1): p. 131-7.
176. Pedrosa, D.J., et al., *Essential tremor and tremor in Parkinson's disease are associated with distinct 'tremor clusters' in the ventral thalamus.* Exp Neurol, 2012. **237**(2): p. 435-43.
177. Bekar, L., et al., *Adenosine is crucial for deep brain stimulation-mediated attenuation of tremor.* Nature Medicine, 2008. **14**(1): p. 75-80.
178. Papavassiliou, E., et al., *Thalamic deep brain stimulation for essential tremor: relation of lead location to outcome.* Neurosurgery, 2004. **54**(5): p. 1120-29; discussion 1129-30.
179. Yu, H., et al., *Confined stimulation using dual thalamic deep brain stimulation leads rescues refractory essential tremor: report of three cases.* Stereotact Funct Neurosurg, 2009. **87**(5): p. 309-313.
180. Montgomery Jr, E.B., *Deep brain stimulation programming: principles and practice*. 2010: Oxford University Press.
181. Vitek, J.L., et al., *Microelectrode-guided pallidotomy: technical approach and its application in medically intractable Parkinson's disease.* J Neurosurg, 1998. **88**(6): p. 1027-43.
182. Ashby, P., et al., *Immediate motor effects of stimulation through electrodes implanted in the human globus pallidus.* Stereotact Funct Neurosurg, 1998. **70**(1): p. 1-18.

183. Ackermann, H., W. Ziegler, and D. Petersen, *Dysarthria in bilateral thalamic infarction. A case study.* J Neurol, 1993. **240**(6): p. 357-62.
184. Kobayashi, K., et al., *Effects of electrode implantation angle on thalamic stimulation for treatment of tremor.* Neuromodulation, 2010. **13**(1): p. 31-6.
185. Hoover, J.E. and P.L. Strick, *The organization of cerebellar and basal ganglia outputs to primary motor cortex as revealed by retrograde transneuronal transport of herpes simplex virus type 1.* J Neurosci, 1999. **19**(4): p. 1446-63.
186. Strick, P.L., *How do the basal ganglia and cerebellum gain access to the cortical motor areas?* Behav Brain Res, 1985. **18**(2): p. 107-23.
187. Foote, K.D. and M.S. Okun, *Ventralis intermedius plus ventralis oralis anterior and posterior deep brain stimulation for posttraumatic Holmes tremor: two leads may be better than one: technical note.* Neurosurgery, 2005. **56**(2 Suppl): p. E445; discussion E445.
188. Hirai, T., et al., *The correlation between tremor characteristics and the predicted volume of effective lesions in stereotaxic nucleus ventralis intermedius thalamotomy.* Brain, 1983. **106 (Pt 4)**: p. 1001-18.
189. McClelland, S., 3rd, et al., *Subthalamic stimulation for Parkinson disease: determination of electrode location necessary for clinical efficacy.* Neurosurg Focus, 2005. **19**(5): p. E12.
190. Volkmann, J., et al., *Introduction to the programming of deep brain stimulators.* Mov Disord, 2002. **17 Suppl 3**: p. S181-7.
191. Pollo, C., et al., *Directional deep brain stimulation: an intraoperative double-blind pilot study.* Brain, 2014. **137**(Pt 7): p. 2015-26.
192. Kumar, R., *Methods for programming and patient management with deep brain stimulation of the globus pallidus for the treatment of advanced Parkinson's disease and dystonia.* Movement Disorders, 2002. **17**(S3): p. S198-S207.
193. Hunka, K., et al., *Nursing time to program and assess deep brain stimulators in movement disorder patients.* J Neurosci Nurs, 2005. **37**(4): p. 204-10.
194. Krauss, J.K., et al., *Deep brain stimulation for dystonia.* J Clin Neurophysiol, 2004. **21**(1): p. 18-30.
195. Houeto, J.L., et al., *Tourette's syndrome and deep brain stimulation.* J Neurol Neurosurg Psychiatry, 2005. **76**(7): p. 992-5.
196. Moro, E., et al., *Subthalamic nucleus stimulation: improvements in outcome with reprogramming.* Arch Neurol, 2006. **63**(9): p. 1266-72.
197. Hariz, M.I., et al., *Tolerance and tremor rebound following long-term chronic thalamic stimulation for Parkinsonian and essential tremor.* Stereotact Funct Neurosurg, 1999. **72**(2-4): p. 208-18.
198. Kumar, R., et al., *Long-term follow-up of thalamic deep brain stimulation for essential and parkinsonian tremor.* Neurology, 2003. **61**(11): p. 1601-4.
199. Shih, L.C., et al., *Loss of benefit in VIM thalamic deep brain stimulation (DBS) for essential tremor (ET): How prevalent is it?* Parkinsonism Relat Disord, 2013. **19**(7): p. 676-679.
200. Ruiz, P.J.G., et al., *Deep brain stimulation holidays in essential tremor.* Journal of Neurology, 2001. **248**(8): p. 725-726.

201. Kuncel, A.M., S.E. Cooper, and W.M. Grill, *A method to estimate the spatial extent of activation in thalamic deep brain stimulation.* Clin Neurophysiol, 2008. **119**(9): p. 2148-58.
202. Rattay, F., *The basic mechanism for the electrical stimulation of the nervous system.* Neuroscience, 1999. **89**(2): p. 335-46.
203. McIntyre, C.C. and W.M. Grill, *Excitation of central nervous system neurons by nonuniform electric fields.* Biophys J, 1999. **76**(2): p. 878-88.
204. Grill, W.M. and C.C. Mclntyre, *Extracellular excitation of central neurons: implications for the mechanisms of deep brain stimulation.* Thalamus & Related Systems, 2001. **1**(03): p. 269-277.
205. Destexhe, A., et al., *Dendritic low-threshold calcium currents in thalamic relay cells.* J Neurosci, 1998. **18**(10): p. 3574-88.
206. Hines, M.L. and N.T. Carnevale, *The NEURON simulation environment.* Neural Computation, 1997. **9**(6): p. 1179-1209.
207. McIntyre, C.C., et al., *Uncovering the mechanism(s) of action of deep brain stimulation: activation, inhibition, or both.* Clin Neurophysiol, 2004. **115**(6): p. 1239-48.
208. Johnson, M.D. and C.C. McIntyre, *Quantifying the neural elements activated and inhibited by globus pallidus deep brain stimulation.* J Neurophysiol, 2008. **100**(5): p. 2549-63.
209. Miocinovic, S., et al., *Computational analysis of subthalamic nucleus and lenticular fasciculus activation during therapeutic deep brain stimulation.* J Neurophysiol, 2006. **96**(3): p. 1569-80.
210. Butson, C.R., et al., *Probabilistic analysis of activation volumes generated during deep brain stimulation.* Neuroimage, 2011. **54**(3): p. 2096-104.
211. Johnson, M.D., et al., *Neural targets for relieving parkinsonian rigidity and bradykinesia with pallidal deep brain stimulation.* J Neurophysiol, 2012. **108**(2): p. 567-77.
212. Lujan, J.L., et al., *Axonal pathways linked to therapeutic and nontherapeutic outcomes during psychiatric deep brain stimulation.* Hum Brain Mapp, 2012. **33**(4): p. 958-68.
213. Zitella, L.M., et al., *Computational modeling of pedunculopontine nucleus deep brain stimulation.* J Neural Eng, 2013. **10**(4): p. 045005.
214. Zitella, L.M., et al., *Subject-specific computational modeling of DBS in the PPTg area.* Front Comput Neurosci, 2015. **9**: p. 93.
215. Keane, M., et al., *Improved spatial targeting with directionally segmented deep brain stimulation leads for treating essential tremor.* J Neural Eng, 2012. **9**(4): p. 046005.
216. Butson, C.R., et al., *Patient-specific analysis of the volume of tissue activated during deep brain stimulation.* Neuroimage, 2007. **34**(2): p. 661-70.
217. McIntyre, C.C., et al., *Electric field and stimulating influence generated by deep brain stimulation of the subthalamic nucleus.* Clin Neurophysiol, 2004. **115**(3): p. 589-95.

218. Butson, C.R., et al., *StimExplorer: deep brain stimulation parameter selection software system.* Acta Neurochir Suppl, 2007. **97**(Pt 2): p. 569-74.
219. Frankemolle, A.M.M., et al., *Reversing cognitive-motor impairments in Parkinson's disease patients using a computational modelling approach to deep brain stimulation programming.* Brain, 2010. **133**: p. 746-761.
220. Larson, P.S., et al., *An optimized system for interventional magnetic resonance imaging-guided stereotactic surgery: preliminary evaluation of targeting accuracy.* Neurosurgery, 2012. **70**(1 Suppl Operative): p. 95-103; discussion 103.
221. Starr, P.A., et al., *Subthalamic nucleus deep brain stimulator placement using high-field interventional magnetic resonance imaging and a skull-mounted aiming device: technique and application accuracy.* J Neurosurg, 2010. **112**(3): p. 479-90.
222. Abosch, A., et al., *An assessment of current brain targets for deep brain stimulation surgery with susceptibility-weighted imaging at 7 tesla.* Neurosurgery, 2010. **67**(6): p. 1745-56; discussion 1756.
223. Lenglet, C., et al., *Comprehensive in vivo mapping of the human basal ganglia and thalamic connectome in individuals using 7T MRI.* PLoS One, 2012. **7**(1): p. e29153.
224. Kerl, H.U., et al., *Imaging for deep brain stimulation: The zona incerta at 7 Tesla.* World J Radiol, 2013. **5**(1): p. 5-16.
225. Kanowski, M., et al., *Direct visualization of anatomic subfields within the superior aspect of the human lateral thalamus by MRI at 7T.* AJNR Am J Neuroradiol, 2014. **35**(9): p. 1721-7.
226. Keuken, M.C., et al., *Ultra-high 7T MRI of structural age-related changes of the subthalamic nucleus.* J Neurosci, 2013. **33**(11): p. 4896-900.
227. Zitella, L.M., et al., *In Vivo 7T MRI of the Non-Human Primate Brainstem.* PLoS One, 2015. **10**(5): p. e0127049.
228. McEvoy, J., et al., *Electrophysiological validation of STN-SNr boundary depicted by susceptibility-weighted MRI.* Acta Neurochir (Wien), 2015. **157**(12): p. 2129-34.
229. Wolberg, G., *Image morphing: a survey.* Visual Computer, 1998. **14**(8-9): p. 360-372.
230. Behrens, T.E., et al., *Non-invasive mapping of connections between human thalamus and cortex using diffusion imaging.* Nat Neurosci, 2003. **6**(7): p. 750-7.
231. Wiegell, M.R., et al., *Automatic segmentation of thalamic nuclei from diffusion tensor magnetic resonance imaging.* Neuroimage, 2003. **19**(2 Pt 1): p. 391-401.
232. Martens, H.C.F., et al., *Spatial steering of deep brain stimulation volumes using a novel lead design.* Clinical Neurophysiology, 2011. **122**(3): p. 558-566.
233. Connolly, A.T., et al., *A Novel Lead Design for Modulation and Sensing of Deep Brain Structures.* IEEE Trans Biomed Eng, 2016. **63**(1): p. 148-57.
234. Chaturvedi, A., T.J. Foutz, and C.C. McIntyre, *Current steering to activate targeted neural pathways during deep brain stimulation of the subthalamic region.* Brain Stimul, 2012. **5**(3): p. 369-77.

235. Toader, E., M.M.J. Decre, and H.C.F. Martens, *Steering deep brain stimulation fields using a high resolution electrode array.* 2010 Annual International Conference of the Ieee Engineering in Medicine and Biology Society (Embc), 2010: p. 2061-2064.
236. Teplitzky, B.A., et al. *Sculpting neural activation using deep brain stimulation leads with radially segmented contacts*. in *Neural Engineering (NER), 2013 6th International IEEE/EMBS Conference on*. 2013. IEEE.
237. Teplitzky, B.A., et al., *Model-Based Comparison of Deep Brain Stimulation Array Functionality with Varying Number of Radial Electrodes and Machine Learning Feature Sets.* Front Comput Neurosci, 2016. **10**: p. 58.
238. Contarino, M.F., et al., *Directional steering: A novel approach to deep brain stimulation.* Neurology, 2014. **83**(13): p. 1163-9.
239. McIntyre, C.C., et al., *Customizing Deep Brain Stimulation to the Patient Using Computational Models.* 2009 Annual International Conference of the Ieee Engineering in Medicine and Biology Society, Vols 1-20, 2009: p. 4228-4229.
240. McIntyre, C.C., et al., *Improving postural stability via computational modeling approach to deep brain stimulation programming.* Conf Proc IEEE Eng Med Biol Soc, 2011. **2011**: p. 675-6.
241. Miocinovic, S., et al., *Cicerone: stereotactic neurophysiological recording and deep brain stimulation electrode placement software system.* Acta Neurochir Suppl, 2007. **97**(Pt 2): p. 561-7.
242. Lemaire, J.J., et al., *Brain mapping in stereotactic surgery: a brief overview from the probabilistic targeting to the patient-based anatomic mapping.* Neuroimage, 2007. **37 Suppl 1**: p. S109-15.
243. Larson, P.S., et al., *An optimized system for interventional MRI guided stereotactic surgery: preliminary evaluation of targeting accuracy.* Neurosurgery, 2012. **70**(OPERATIVE): p. ons95.
244. Starr, P.A., et al., *Magnetic resonance imaging-based stereotactic localization of the globus pallidus and subthalamic nucleus.* Neurosurgery, 1999. **44**(2): p. 303-13; discussion 313-4.
245. Schlaier, J., et al., *Reliability of atlas-derived coordinates in deep brain stimulation.* Acta Neurochir (Wien), 2005. **147**(11): p. 1175-80; discussion 1180.
246. Levy, R.M., S. Lamb, and J.E. Adams, *Treatment of chronic pain by deep brain stimulation: long term follow-up and review of the literature.* Neurosurgery, 1987. **21**(6): p. 885-93.
247. Lipsman, N., et al., *MR-guided focused ultrasound thalamotomy for essential tremor: a proof-of-concept study.* Lancet Neurol, 2013. **12**(5): p. 462-8.
248. Fisher, R., et al., *Electrical stimulation of the anterior nucleus of thalamus for treatment of refractory epilepsy.* Epilepsia, 2010. **51**(5): p. 899-908.
249. Takase, K., et al., *Efficacy of mediodorsal thalamic nucleus stimulation in a rat model of cortical seizure.* Fukuoka Igaku Zasshi, 2009. **100**(8): p. 274-80.
250. Visser-Vandewalle, V., et al., *Chronic bilateral thalamic stimulation: a new therapeutic approach in intractable Tourette syndrome. Report of three cases.* J Neurosurg, 2003. **99**(6): p. 1094-100.

251. Schiff, N.D., et al., *Behavioural improvements with thalamic stimulation after severe traumatic brain injury.* Nature, 2007. **448**(7153): p. 600-3.
252. Klein, J., et al., *Mapping brain regions in which deep brain stimulation affects schizophrenia-like behavior in two rat models of schizophrenia.* Brain Stimul, 2013. **6**(4): p. 490-9.
253. Ewing, S.G., B. Porr, and J.A. Pratt, *Deep brain stimulation of the mediodorsal thalamic nucleus yields increases in the expression of zif-268 but not c-fos in the frontal cortex.* Journal of Chemical Neuroanatomy, 2013. **52**: p. 20-24.
254. Papavassiliou, E., et al., *Thalamic deep brain stimulation for essential tremor: Relation of lead location to outcome.* Neurosurgery, 2004. **54**(5): p. 1120-1129.
255. Yu, H., et al., *Confined stimulation using dual thalamic deep brain stimulation leads rescues refractory essential tremor: report of three cases.* Stereotact Funct Neurosurg, 2009. **87**(5): p. 309-13.
256. Talairach, J. and P. Tournoux, *Coplanar Stereotaxic Atlas of the Human Brain*. Thieme Medical Publishers. 1988, New York.
257. Villemure, J.G., et al., *Magnetic resonance imaging stereotaxy: recognition and utilization of the commissures.* Appl Neurophysiol, 1987. **50**(1-6): p. 57-62.
258. Lunsford, L.D., *Magnetic resonance imaging stereotactic thalamotomy: report of a case with comparison to computed tomography.* Neurosurgery, 1988. **23**(3): p. 363-7.
259. Kall, B.A., S.J. Goerss, and P.J. Kelly, *A new multimodality correlative imaging technique for VOP/VIM (VL) thalamotomy procedures.* Stereotact Funct Neurosurg, 1992. **58**(1-4): p. 45-51.
260. Schaltenbrand, G. and W. Wahren, *Atlas for Stereotaxy of the Human Brain: Architectonic Organisation of the Thalamic Nuclei by Rolf Hassler*, 1977, Thieme, Stuttgart.
261. Baker, S.C., et al., *Neural systems engaged by planning: a PET study of the Tower of London task.* Neuropsychologia, 1996. **34**(6): p. 515-26.
262. Davis, K.D., et al., *Functional MRI study of thalamic and cortical activations evoked by cutaneous heat, cold, and tactile stimuli.* J Neurophysiol, 1998. **80**(3): p. 1533-46.
263. Krams, M., et al., *The preparation, execution and suppression of copied movements in the human brain.* Exp Brain Res, 1998. **120**(3): p. 386-98.
264. Samuel, M., et al., *Evidence for lateral premotor and parietal overactivity in Parkinson's disease during sequential and bimanual movements: A PET study.* Brain, 1997. **120**: p. 963-976.
265. Calamante, F., et al., *Super-resolution track-density imaging studies of mouse brain: comparison to histology.* Neuroimage, 2012. **59**(1): p. 286-96.
266. Calamante, F., et al., *Super-resolution track-density imaging of thalamic substructures: Comparison with high-resolution anatomical magnetic resonance imaging at 7.0T.* Hum Brain Mapp, 2013. **34**(10): p. 2538-2548.
267. Tourdias, T., et al., *Visualization of intra-thalamic nuclei with optimized white-matter-nulled MPRAGE at 7T.* Neuroimage, 2014. **84**: p. 534-45.

268. Johansen-Berg, H., et al., *Functional-anatomical validation and individual variation of diffusion tractography-based segmentation of the human thalamus.* Cereb Cortex, 2005. **15**(1): p. 31-9.
269. Deoni, S.C., et al., *Visualization of thalamic nuclei on high resolution, multi-averaged T1 and T2 maps acquired at 1.5 T.* Human Brain Mapping, 2005. **25**(3): p. 353-359.
270. Gringel, T., et al., *Optimized High-Resolution Mapping of Magnetization Transfer (MT) at 3 Tesla for Direct Visualization of Substructures of the Human Thalamus in Clinically Feasible Measurement Time.* Journal of Magnetic Resonance Imaging, 2009. **29**(6): p. 1285-1292.
271. Gee, J.C., et al. *Evaluation of multiresolution elastic matching using MRI data*. in *Medical Imaging V: Image Processing*. 1991. International Society for Optics and Photonics.
272. Mesulam, M.-M., et al., *Atlas of cholinergic neurons in the forebrain and upper brainstem of the macaque based on monoclonal choline actyltransferase immunohistochemistry and acetylcholinesterase histochemistry.* Neuroscience, 1984. **12**: p. 669-686.
273. Lanciego, J.L. and A. Vazquez, *The basal ganglia and thalamus of the long-tailed macaque in stereotaxic coordinates. A template atlas based on coronal, sagittal and horizontal brain sections.* Brain Struct Funct, 2012. **217**(2): p. 613-66.
274. Morel, A., M. Magnin, and D. Jeanmonod, *Multiarchitectonic and stereotactic atlas of the human thalamus.* J Comp Neurol, 1997. **387**(4): p. 588-630.
275. Eidelberg, D. and A.M. Galaburda, *Symmetry and asymmetry in the human posterior thalamus. I. Cytoarchitectonic analysis in normal persons.* Arch Neurol, 1982. **39**(6): p. 325-32.
276. Galaburda, A.M., et al., *Right-left asymmetrics in the brain.* Science, 1978. **199**(4331): p. 852-6.
277. Good, C.D., et al., *Cerebral asymmetry and the effects of sex and handedness on brain structure: a voxel-based morphometric analysis of 465 normal adult human brains.* Neuroimage, 2001. **14**(3): p. 685-700.
278. Bertrand, G., A. Oliver, and C.J. Thompson, *The computerized brain atlas: its use in stereotaxic surgery.* Trans Am Neurol Assoc, 1973. **98**: p. 233.
279. Evans, A.C., et al., *Anatomical-functional correlation using an adjustable MRI-based region of interest atlas with positron emission tomography.* J Cereb Blood Flow Metab, 1988. **8**(4): p. 513-30.
280. Marrett, S., et al. *A volume of interest (VOI) atlas for the analysis of neurophysiological image data*. in *1989 Medical Imaging*. 1989. International Society for Optics and Photonics.
281. Ganser, K.A., et al., *A deformable digital brain atlas system according to Talairach and Tournoux.* Med Image Anal, 2004. **8**(1): p. 3-22.
282. Bohm, C., et al., *Adjustable Computerized Stereotaxic Brain Atlas for Transmission and Emission Tomography.* American Journal of Neuroradiology, 1983. **4**(3): p. 731-733.

283. Dann, R., et al. *Three-Dimensional Computerized Brain Atlas For Elastic Matching: Creation And Initial Evaluation*. 1988.
284. Dauguet, J., et al., *Generation of a 3D atlas of the nuclear division of the thalamus based on histological sections of primate: Intra- and intersubject atlas-to-MRI warping.* Irbm, 2009. **30**(5-6): p. 281-291.
285. Greitz, T., et al., *A computerized brain atlas: construction, anatomical content, and some applications.* J Comput Assist Tomogr, 1991. **15**(1): p. 26-38.
286. Sadikot, A.F., et al., *Creation of Computerized 3D MRI-Integrated Atlases of the Human Basal Ganglia and Thalamus.* Front Syst Neurosci, 2011. **5**: p. 71.
287. Yelnik, J., et al., *A three-dimensional, histological and deformable atlas of the human basal ganglia. I. Atlas construction based on immunohistochemical and MRI data.* Neuroimage, 2007. **34**(2): p. 618-38.
288. Chakravarty, M.M., et al., *The creation of a brain atlas for image guided neurosurgery using serial histological data.* Neuroimage, 2006. **30**(2): p. 359-76.
289. Finnis, K.W., et al., *Three-dimensional database of subcortical electrophysiology for image-guided stereotactic functional neurosurgery.* IEEE Trans Med Imaging, 2003. **22**(1): p. 93-104.
290. Nowinski, W.L., G.L. Yang, and T.T. Yeo, *Computer-aided stereotactic functional neurosurgery enhanced by the use of the multiple brain atlas database.* IEEE Trans Med Imaging, 2000. **19**(1): p. 62-9.
291. St-Jean, P., et al., *Automated atlas integration and interactive three-dimensional visualization tools for planning and guidance in functional neurosurgery.* IEEE Trans Med Imaging, 1998. **17**(5): p. 672-80.
292. Maintz, J. and M.A. Viergever, *A survey of medical image registration.* Medical Image Analysis, 1998. **2**(1): p. 1-36.
293. Pham, D.L., C. Xu, and J.L. Prince, *Current methods in medical image segmentation.* Annu Rev Biomed Eng, 2000. **2**: p. 315-37.
294. McInerney, T. and D. Terzopoulos, *Deformable models in medical image analysis: a survey.* Medical Image Analysis, 1996. **1**(2): p. 91-108.
295. Pitiot, A., et al., *Piecewise affine registration of biological images for volume reconstruction.* Med Image Anal, 2006. **10**(3): p. 465-83.
296. Gross, R.E., et al., *Electrophysiological mapping for the implantation of deep brain stimulators for Parkinson's disease and tremor.* Mov Disord, 2006. **21 Suppl 14**: p. S259-83.
297. Hamani, C., et al., *Correspondence of microelectrode mapping with magnetic resonance imaging for subthalamic nucleus procedures.* Surg Neurol, 2005. **63**(3): p. 249-53; discussion 253.
298. Adriany, G., et al., *A 21 channel Transceiver Array for Non-human Primate Applications at 7 Tesla*, in *Proceedings of the 18th Annual Meeting of ISMRM*2010: Stockholm, Sweden.
299. Haacke, E.M., et al., *Susceptibility-weighted imaging: technical aspects and clinical applications, part 1.* AJNR Am J Neuroradiol, 2009. **30**(1): p. 19-30.
300. Schenck, J.F. and E.A. Zimmerman, *High-field magnetic resonance imaging of brain iron: birth of a biomarker?* NMR Biomed, 2004. **17**(7): p. 433-45.

301. LeVine, S.M. and W.B. Macklin, *Iron-enriched oligodendrocytes: a reexamination of their spatial distribution.* J Neurosci Res, 1990. **26**(4): p. 508-12.
302. Dwork, A.J., E.A. Schon, and J. Herbert, *Nonidentical distribution of transferrin and ferric iron in human brain.* Neuroscience, 1988. **27**(1): p. 333-45.
303. Francois, C., J. Nguyen-Legros, and G. Percheron, *Topographical and cytological localization of iron in rat and monkey brains.* Brain Res, 1981. **215**(1-2): p. 317-22.
304. Haacke, E.M., et al., *Characterizing Iron Deposition in Multiple Sclerosis Lesions Using Susceptibility Weighted Imaging.* Journal of Magnetic Resonance Imaging, 2009. **29**(3): p. 537-544.
305. Ogg, R.J., et al., *The correlation between phase shifts in gradient-echo MR images and regional brain iron concentration.* Magn Reson Imaging, 1999. **17**(8): p. 1141-8.
306. Hopp, K., et al., *Brain iron detected by SWI high pass filtered phase calibrated with synchrotron X-ray fluorescence.* J Magn Reson Imaging, 2010. **31**(6): p. 1346-54.
307. Stejskal, E.O. and J.E. Tanner, *Spin Diffusion Measurements: Spin Echoes in the Presence of a Time-Dependent Field Gradient.* J. Chem. Phys., 1965. **42**: p. 288-292.
308. Deriche, R., J. Calder, and M. Descoteaux, *Optimal real-time Q-ball imaging using regularized Kalman filtering with incremental orientation sets.* Medical image analysis, 2009. **13**(4): p. 564-79.
309. Andersson, J.L.R., S. Skare, and J. Ashburner, *How to correct susceptibility distortions in spin-echo echo-planar images: application to diffusion tensor imaging.* Neuroimage, 2003. **20**(2): p. 870-888.
310. Paxinos, G., X.F. Huang, and A.W. Toga, *The rhesus monkey brain in stereotaxic coordinates*. 2000, San Diego, CA: Academic Press. 163 p.
311. Sorlie, C., et al., *Matching of digitised brain atlas to magnetic resonance images.* Med Biol Eng Comput, 1997. **35**(3): p. 239-45.
312. Castro, F.J.S., et al., *Cross validation study of deep brain stimulation targeting: From experts to atlas-based, segmentation-based and automatic registration algorithms.* IEEE Trans Med Imaging, 2006. **25**(11): p. 1440-1450.
313. Schaefer, S., T. McPhail, and J. Warren, *Image deformation using moving least squares.* Acm Transactions on Graphics, 2006. **25**(3): p. 533-540.
314. Tiddeman, B., N. Duffy, and G. Rabey, *A general method for overlap control in image warping.* Computers & Graphics-Uk, 2001. **25**(1): p. 59-66.
315. Jenkinson, M., et al., *Fsl.* Neuroimage, 2012. **62**(2): p. 782-90.
316. Woolrich, M.W., et al., *Bayesian analysis of neuroimaging data in FSL.* Neuroimage, 2009. **45**(1 Suppl): p. S173-86.
317. Smith, S.M., et al., *Advances in functional and structural MR image analysis and implementation as FSL.* Neuroimage, 2004. **23 Suppl 1**: p. S208-19.
318. Smith, S.M., *Fast robust automated brain extraction.* Hum Brain Mapp, 2002. **17**(3): p. 143-55.

319. Jenkinson, M., et al., *Improved optimization for the robust and accurate linear registration and motion correction of brain images.* Neuroimage, 2002. **17**(2): p. 825-841.
320. Jenkinson, M. and S. Smith, *A global optimisation method for robust affine registration of brain images.* Medical Image Analysis, 2001. **5**(2): p. 143-156.
321. Greve, D.N. and B. Fischl, *Accurate and robust brain image alignment using boundary-based registration.* Neuroimage, 2009. **48**(1): p. 63-72.
322. Gallay, M.N., et al., *Human pallidothalamic and cerebellothalamic tracts: anatomical basis for functional stereotactic neurosurgery.* Brain Struct Funct, 2008. **212**(6): p. 443-63.
323. Vitek, J.L., et al., *Microstimulation of primate motor thalamus: somatotopic organization and differential distribution of evoked motor responses among subnuclei.* J Neurophysiol, 1996. **75**(6): p. 2486-95.
324. Sandor, S. and R. Leahy. *Matching deformable atlas models to preprocessed magnetic resonance brain images*. in *Image Processing, 1994. Proceedings. ICIP-94., IEEE International Conference*. 1994. IEEE.
325. Davatzikos, C., *Spatial transformation and registration of brain images using elastically deformable models.* Computer Vision and Image Understanding, 1997. **66**(2): p. 207-222.
326. Cuisenaire, O., et al., *Automatic registration of 3D MR images with a computerized brain atlas.* Medical imaging, 1996. **2710**: p. 438-448.
327. Bajcsy, R., R. Lieberson, and M. Reivich, *A Computerized System for the Elastic Matching of Deformed Radiographic Images to Idealized Atlas Images.* Journal of Computer Assisted Tomography, 1983. **7**(4): p. 618-625.
328. MacDonald, D., D. Avis, and A.C. Evans. *Multiple surface identification and matching in magnetic resonance images*. in *Visualization in Biomedical Computing 1994*. 1994. International Society for Optics and Photonics.
329. Thompson, P. and A.W. Toga, *A surface-based technique for warping three-dimensional images of the brain.* IEEE Trans Med Imaging, 1996. **15**(4): p. 402-17.
330. Alexa, M., D. Cohen-Or, and D. Levin. *As-rigid-as-possible shape interpolation*. in *Proceedings of the 27th annual conference on Computer graphics and interactive techniques*. 2000. ACM Press/Addison-Wesley Publishing Co.
331. Igarashi, T., T. Moscovich, and J.F. Hughes, *As-rigid-as-possible shape manipulation.* Acm Transactions on Graphics, 2005. **24**(3): p. 1134-1141.
332. Gee, J.C., M. Reivich, and R. Bajcsy, *Elastically Deforming 3d Atlas to Match Anatomical Brain Images.* Journal of Computer Assisted Tomography, 1993. **17**(2): p. 225-236.
333. Bookstein, F.L., *Principal Warps - Thin-Plate Splines and the Decomposition of Deformations.* Ieee Transactions on Pattern Analysis and Machine Intelligence, 1989. **11**(6): p. 567-585.
334. Connor, J.R. and S.L. Menzies, *Relationship of iron to oligodendrocytes and myelination.* Glia, 1996. **17**(2): p. 83-93.

335. Hallgren, B. and P. Sourander, *The effect of age on the non-haemin iron in the human brain.* J Neurochem, 1958. **3**(1): p. 41-51.
336. Chen, J.C., et al., *MR of human postmortem brain tissue: correlative study between T2 and assays of iron and ferritin in Parkinson and Huntington disease.* AJNR Am J Neuroradiol, 1993. **14**(2): p. 275-81.
337. Dexter, D.T., et al., *Alterations in the Levels of Iron, Ferritin and Other Trace-Metals in Parkinsons-Disease and Other Neurodegenerative Diseases Affecting the Basal Ganglia.* Brain, 1991. **114**: p. 1953-1975.
338. Griffiths, P.D. and A.R. Crossman, *Distribution of iron in the basal ganglia and neocortex in postmortem tissue in Parkinson's disease and Alzheimer's disease.* Dementia, 1993. **4**(2): p. 61-5.
339. Loeffler, D.A., et al., *Transferrin and iron in normal, Alzheimer's disease, and Parkinson's disease brain regions.* J Neurochem, 1995. **65**(2): p. 710-24.
340. Small, S.A., et al., *Differential regional dysfunction of the hippocampal formation among elderly with memory decline and Alzheimer's disease.* Annals of Neurology, 1999. **45**(4): p. 466-72.
341. Small, S.A., et al., *Evaluating the function of hippocampal subregions with high-resolution MRI in Alzheimer's disease and aging.* Microsc Res Tech, 2000. **51**(1): p. 101-8.
342. Cook, R.D., *Detection of influential observation in linear regression.* Technometrics, 1977. **19**(1): p. 15-18.
343. Deoni, S.C., et al., *Visualization of thalamic nuclei on high resolution, multi-averaged T1 and T2 maps acquired at 1.5 T.* Hum Brain Mapp, 2005. **25**(3): p. 353-9.
344. Anthofer, J., et al., *The variability of atlas-based targets in relation to surrounding major fibre tracts in thalamic deep brain stimulation.* Acta Neurochir (Wien), 2014.
345. Zakszewski, E., et al., *A diffusion-tensor-based white matter atlas for rhesus macaques.* PLoS One, 2014. **9**(9): p. e107398.
346. Lujan, J.L., et al., *Automated 3-dimensional brain atlas fitting to microelectrode recordings from deep brain stimulation surgeries.* Stereotact Funct Neurosurg, 2009. **87**(4): p. 229-40.
347. Dauguet, J., et al., *Three-dimensional reconstruction of stained histological slices and 3D non-linear registration with in-vivo MRI for whole baboon brain.* J Neurosci Methods, 2007. **164**(1): p. 191-204.
348. Macchi, G. and E.G. Jones, *Toward an agreement on terminology of nuclear and subnuclear divisions of the motor thalamus.* J Neurosurg, 1997. **86**(4): p. 670-85.
349. diPierro, C.G., et al., *Optimizing accuracy in magnetic resonance imaging-guided stereotaxis: a technique with validation based on the anterior commissure-posterior commissure line.* J Neurosurg, 1999. **90**(1): p. 94-100.
350. Dormont, D., et al., *Chronic thalamic stimulation with three-dimensional MR stereotactic guidance.* AJNR Am J Neuroradiol, 1997. **18**(6): p. 1093-107.
351. Kamiryo, T. and E.R. Laws, Jr., *Stereotactic frame-based error in magnetic-resonance-guided stereotactic procedures: a method for measurement of error*

and standardization of technique. Stereotact Funct Neurosurg, 1996. **67**(3-4): p. 198-209.
352. Xiao, Y. and M.D. Johnson, *Spherical statistics for characterizing the spatial distribution of deep brain stimulation effects on neuronal activity.* J Neurosci Methods, 2015. **255**: p. 52-65.
353. Xiao, Y., E. Pena, and M. Johnson, *Theoretical Optimization of Stimulation Strategies for a Directionally Segmented Deep Brain Stimulation Electrode Array.* IEEE Trans Biomed Eng, 2015.
354. Johnson, M.D., et al., *Neuromodulation for brain disorders: challenges and opportunities.* IEEE Trans Biomed Eng, 2013. **60**(3): p. 610-24.
355. Tamma, F., et al., *Anatomo-clinical correlation of intraoperative stimulation-induced side-effects during HF-DBS of the subthalamic nucleus.* Neurol Sci, 2002. **23 Suppl 2**: p. S109-10.
356. Krack, P., et al., *Postoperative management of subthalamic nucleus stimulation for Parkinson's disease.* Movement Disorders., 2002. **17**(Suppl 3): p. S188-97.
357. Martens, H.C., et al., *Spatial steering of deep brain stimulation volumes using a novel lead design.* Clin Neurophysiol, 2011. **122**(3): p. 558-66.
358. Mazzone, P., et al., *Implantation of human pedunculopontine nucleus: a safe and clinically relevant target in Parkinson's disease.* Neuroreport, 2005. **16**(17): p. 1877-81.
359. Buhlmann, J., et al., *Modeling of a segmented electrode for desynchronizing deep brain stimulation.* Front Neuroeng, 2011. **4**: p. 15.
360. Pollo, C., et al., *Directional deep brain stimulation: an intraoperative double-blind pilot study.* Brain, 2014.
361. Barbe, M.T., et al., *Individualized current-shaping reduces DBS-induced dysarthria in patients with essential tremor.* Neurology, 2014. **82**(7): p. 614-9.
362. Volkmann, J., et al., *Introduction to the programming of deep brain stimulators.* Movement Disorders, 2002. **17**(S3): p. S181-S187.
363. Kumar, R., *Methods for programming and patient management with deep brain stimulation of the globus pallidus for the treatment of advanced Parkinson's disease and dystonia.* Mov Disord, 2002. **17 Suppl 3**: p. S198-207.
364. Butson, C.R. and C.C. McIntyre, *Current steering to control the volume of tissue activated during deep brain stimulation.* Brain Stimul, 2008. **1**(1): p. 7-15.
365. Phibbs, F.T., et al., *Use of efficacy probability maps for the post-operative programming of deep brain stimulation in essential tremor.* Movement Disorders, 2014. **29**: p. S464-S464.
366. Plaha, P., et al., *Stimulation of the caudal zona incerta is superior to stimulation of the subthalamic nucleus in improving contralateral parkinsonism.* Brain, 2006. **129**(Pt 7): p. 1732-47.
367. Frankemolle, A.M., et al., *Reversing cognitive-motor impairments in Parkinson's disease patients using a computational modelling approach to deep brain stimulation programming.* Brain, 2010. **133**(Pt 3): p. 746-61.

368. McIntyre, C.C., et al. *Customizing deep brain stimulation to the patient using computational models*. in *Engineering in Medicine and Biology Society, 2009. EMBC 2009. Annual International Conference of the IEEE*. 2009. IEEE.
369. McIntyre, C.C., et al. *Improving postural stability via computational modeling approach to deep brain stimulation programming*. in *Engineering in Medicine and Biology Society, EMBC, 2011 Annual International Conference of the IEEE*. 2011. IEEE.
370. Rattay, F., *Analysis of models for external stimulation of axons.* IEEE Trans Biomed Eng, 1986. **33**(10): p. 974-7.
371. McIntyre, C.C., et al., *Electric field and stimulating influence generated by deep brain stimulation of the subthalamic nucleus.* Clinical Neurophysiology, 2004. **115**(3): p. 589-595.
372. Butson, C.R. and C.C. McIntyre, *Role of electrode design on the volume of tissue activated during deep brain stimulation.* J Neural Eng, 2006. **3**(1): p. 1.
373. McIntyre, C.C., A.G. Richardson, and W.M. Grill, *Modeling the excitability of mammalian nerve fibers: influence of afterpotentials on the recovery cycle.* J Neurophysiol, 2002. **87**(2): p. 995-1006.
374. Hines, M.L. and N.T. Carnevale, *The NEURON simulation environment.* Neural Comput, 1997. **9**(6): p. 1179-209.
375. Ranck, J.B., Jr., *Analysis of specific impedance of rabbit cerebral cortex.* Exp Neurol, 1963. **7**: p. 153-74.
376. Stances, A.L., S. J., *Impedance and Current Density Studies*, in *Electroanesthesia: Biomedical and Biophysical Studies*, C.A. Caceres, Editor. 1975, Academic Press: New York, New York. p. 114-147.
377. Miocinovic, S., et al., *Experimental and theoretical characterization of the voltage distribution generated by deep brain stimulation.* Exp Neurol, 2009. **216**(1): p. 166-76.
378. Kakei, S., J. Na, and Y. Shinoda, *Thalamic terminal morphology and distribution of single corticothalamic axons originating from layers 5 and 6 of the cat motor cortex.* J Comp Neurol, 2001. **437**(2): p. 170-85.
379. Crouch, R.L. and J.K. Thompson, *The efferent fibers of the thalamus of Macacus rhesus. I. Lateral ventral nuclei.* Journal of Comparative Neurology, 1938. **69**(2): p. 255-271.
380. Grant, M. and S. Boyd, *CVX: Matlab software for disciplined convex programming.*
381. Whiten, D.M., *Electro-anatomical models of the cochlear implant*, 2007, Massachusetts Institute of Technology.
382. Ranck, J.B., Jr., *Which elements are excited in electrical stimulation of mammalian central nervous system: a review.* Brain Res, 1975. **98**(3): p. 417-40.
383. Rattay, F., *Analysis of models for extracellular fiber stimulation.* IEEE Trans Biomed Eng, 1989. **36**(7): p. 676-82.
384. McNeal, D.R., *Analysis of a model for excitation of myelinated nerve.* IEEE Trans Biomed Eng, 1976. **23**(4): p. 329-37.

385. Yousif, N., et al., *Evaluating the impact of the deep brain stimulation induced electric field on subthalamic neurons: a computational modelling study.* J Neurosci Methods, 2010. **188**(1): p. 105-12.
386. Schmidt, C., et al., *Influence of uncertainties in the material properties of brain tissue on the probabilistic volume of tissue activated.* IEEE Trans Biomed Eng, 2013. **60**(5): p. 1378-87.
387. Peterson, E.J., O. Izad, and D.J. Tyler, *Predicting myelinated axon activation using spatial characteristics of the extracellular field.* Journal of Neural Engineering, 2011. **8**(4).
388. Chaturvedi, A., J.L. Lujan, and C.C. McIntyre, *Artificial neural network based characterization of the volume of tissue activated during deep brain stimulation.* J Neural Eng, 2013. **10**(5): p. 056023.
389. Litvak, L.M., A.J. Spahr, and G. Emadi, *Loudness growth observed under partially tripolar stimulation: model and data from cochlear implant listeners.* J Acoust Soc Am, 2007. **122**(2): p. 967-81.
390. Toader, E., M.M. Decre, and H.C. Martens, *Steering deep brain stimulation fields using a high resolution electrode array.* Conf Proc IEEE Eng Med Biol Soc, 2010. **2010**: p. 2061-4.
391. Townshend, B. and R.L. White, *Reduction of electrical interaction in auditory prostheses.* IEEE Trans Biomed Eng, 1987. **34**(11): p. 891-7.
392. Ross, R.C., *Channel interaction cancellation within a multichannel neural stimulation system*, 2006, Google Patents.
393. Tass, P.A., *A model of desynchronizing deep brain stimulation with a demand-controlled coordinated reset of neural subpopulations.* Biol Cybern, 2003. **89**(2): p. 81-8.
394. Tass, P., et al., *Long-lasting desynchronization in rat hippocampal slice induced by coordinated reset stimulation.* Physical Review E, 2009. **80**(1): p. 011902.
395. Darian-Smith, C., A. Tan, and S. Edwards, *Comparing thalamocortical and corticothalamic microstructure and spatial reciprocity in the macaque ventral posterolateral nucleus (VPLc) and medial pulvinar.* Journal of Comparative Neurology, 1999. **410**(2): p. 211-234.
396. Kultas-Ilinsky, K., E. Sivan-Loukianova, and I.A. Ilinsky, *Reevaluation of the primary motor cortex connections with the thalamus in primates.* Journal of Comparative Neurology, 2003. **457**(2): p. 133-158.
397. Coenen, V.A., et al., *Individual fiber anatomy of the subthalamic region revealed with diffusion tensor imaging: a concept to identify the deep brain stimulation target for tremor suppression.* Neurosurgery, 2011. **68**(4): p. 1069-75; discussion 1075-6.
398. Chaturvedi, A., et al., *Patient-specific models of deep brain stimulation: influence of field model complexity on neural activation predictions.* Brain Stimul, 2010. **3**(2): p. 65-7.
399. Lenz, F.A., et al., *Thermal and pain sensations evoked by microstimulation in the area of human ventrocaudal nucleus.* J Neurophysiol, 1993. **70**(1): p. 200-12.

400. Bonham, B.H. and L.M. Litvak, *Current focusing and steering: modeling, physiology, and psychophysics.* Hear Res, 2008. **242**(1-2): p. 141-53.
401. Dumm, G., et al., *Virtual Electrodes by Current Steering in Retinal Prostheses.* Invest Ophthalmol Vis Sci, 2014.
402. Schlag, J. and J. Villablanca, *A quantitative study of temporal and spatial response patterns in a thalamic cell population electrically stimulated.* Brain Res, 1968. **8**(2): p. 255-270.
403. Johnson, L.A., et al., *Modulation of motor cortex neuronal activity and motor behavior during subthalamic nucleus stimulation in the normal primate.* J Neurophysiol, 2015: p. jn 00997 2014.
404. Bar-Gad, I., et al., *Complex locking rather than complete cessation of neuronal activity in the globus pallidus of a 1-methyl-4-phenyl-1,2,3,6-tetrahydropyridine-treated primate in response to pallidal microstimulation.* J Neurosci, 2004. **24**(33): p. 7410-9.
405. Boraud, T., et al., *High frequency stimulation of the internal Globus Pallidus (GPi) simultaneously improves parkinsonian symptoms and reduces the firing frequency of GPi neurons in the MPTP-treated monkey.* Neurosci Lett, 1996. **215**(1): p. 17-20.
406. Filali, M., et al., *Stimulation-induced inhibition of neuronal firing in human subthalamic nucleus.* Exp Brain Res, 2004. **156**(3): p. 274-81.
407. Meissner, W., et al., *Subthalamic high frequency stimulation resets subthalamic firing and reduces abnormal oscillations.* Brain, 2005. **128**(Pt 10): p. 2372-82.
408. Tolias, A.S., et al., *Mapping cortical activity elicited with electrical microstimulation using fMRI in the macaque.* Neuron, 2005. **48**(6): p. 901-911.
409. Histed, M.H., V. Bonin, and R.C. Reid, *Direct activation of sparse, distributed populations of cortical neurons by electrical microstimulation.* Neuron, 2009. **63**(4): p. 508-22.
410. Tehovnik, E.J., et al., *Direct and indirect activation of cortical neurons by electrical microstimulation.* J Neurophysiol, 2006. **96**(2): p. 512-21.
411. Matteucci, P.B., et al., *Current steering in retinal stimulation via a quasimonopolar stimulation paradigm.* Invest Ophthalmol Vis Sci, 2013. **54**(6): p. 4307-20.
412. Jepson, L.H., et al., *Spatially patterned electrical stimulation to enhance resolution of retinal prostheses.* J Neurosci, 2014. **34**(14): p. 4871-81.
413. Lim, D.H., et al., *In vivo Large-Scale Cortical Mapping Using Channelrhodopsin-2 Stimulation in Transgenic Mice Reveals Asymmetric and Reciprocal Relationships between Cortical Areas.* Front Neural Circuits, 2012. **6**: p. 11.
414. Fisher, N.I., *Statistical analysis of spherical data*. 1993: Cambridge University Press.
415. Borradaile, G.J. and B. Henry, *Tectonic applications of magnetic susceptibility and its anisotropy.* Earth-Science Reviews, 1997. **42**(1-2): p. 49-93.

416. Allen, T.R. and J.A. Kupfer, *Application of spherical statistics to change vector analysis of Landsat data: Southern Appalachian spruce-fir forests.* Remote Sensing of Environment, 2000. **74**(3): p. 482-493.
417. Leong, P. and S. Carlile, *Methods for spherical data analysis and visualization.* J Neurosci Methods, 1998. **80**(2): p. 191-200.
418. Grill, W.M. and J.T. Mortimer, *Electrical properties of implant encapsulation tissue.* Ann Biomed Eng, 1994. **22**(1): p. 23-33.
419. Lempka, S.F., et al., *Current-controlled deep brain stimulation reduces in vivo voltage fluctuations observed during voltage-controlled stimulation.* Clin Neurophysiol, 2010. **121**(12): p. 2128-33.
420. Eilers, P.H.C. and J.J. Goeman, *Enhancing scatterplots with smoothed densities.* Bioinformatics, 2004. **20**(5): p. 623-U82.
421. Woodcock, N.H., *Specification of Fabric Shapes Using an Eigenvalue Method.* Geological Society of America Bulletin, 1977. **88**(9): p. 1231-1236.
422. Rayleigh, L., *XXXI. On the problem of random vibrations, and of random flights in one, two, or three dimensions.* The London, Edinburgh, and Dublin Philosophical Magazine and Journal of Science, 1919. **37**(220): p. 321-347.
423. Kent, J.T., *The Fisher-Bingham Distribution on the Sphere.* Journal of the Royal Statistical Society Series B-Methodological, 1982. **44**(1): p. 71-80.
424. Watson, G., *Equatorial distributions on a sphere.* Biometrika, 1965: p. 193-201.
425. Bingham, C., *Distributions on the sphere and on the projective plane*. 1964: Yale University.
426. Bingham, C., *An antipodally symmetric distribution on the sphere.* The Annals of Statistics, 1974: p. 1201-1225.
427. Best, D. and N. Fisher, *GOODNESS-OF-FIT AND DISCORDANCY TESTS FOR SAMPLES FROM THE WATSON DISTRIBUTION ON THE SPHERE.* Australian Journal of Statistics, 1986. **28**(1): p. 13-31.
428. Mardia, K. and R. Gadsden, *A small circle of best fit for spherical data and areas of vulcanism.* Applied Statistics, 1977: p. 238-245.
429. Krack, P., et al., *Postoperative management of subthalamic nucleus stimulation for Parkinson's disease.* Mov Disord, 2002. **17 Suppl 3**: p. S188-97.
430. Gijsbers, J.T.M., F.L.H. Gielen, and H.M. Knuth, *High resolution brain stimulation lead and method of use*, 1998, Google Patents.
431. Hetke, J.F., et al., *Modular multichannel microelectrode array and methods of making same*, 2011, Google Patents.
432. Lempka, S.F., et al., *Current-controlled deep brain stimulation reduces in vivo voltage fluctuations observed during voltage-controlled stimulation.* Clinical Neurophysiology, 2010. **121**(12): p. 2128-33.
433. Howell, B., B. Huynh, and W.M. Grill, *Design and in vivo evaluation of more efficient and selective deep brain stimulation electrodes.* J Neural Eng, 2015. **12**(4): p. 046030.
434. Roth, B.J., *Mechanisms for electrical stimulation of excitable tissue.* Crit Rev Biomed Eng, 1994. **22**(3-4): p. 253-305.

435. Howell, B., S. Naik, and W.M. Grill, *Influences of interpolation error, electrode geometry, and the electrode-tissue interface on models of electric fields produced by deep brain stimulation.* IEEE Trans Biomed Eng, 2014. **61**(2): p. 297-307.
436. Behrens, T.E.J., et al., *Non-invasive mapping of connections between human thalamus and cortex using diffusion imaging.* Nature Neuroscience, 2003. **6**(7): p. 750-757.
437. Hampel, S., et al., *Drosophila Brainbow: a recombinase-based fluorescence labeling technique to subdivide neural expression patterns.* Nat Methods, 2011. **8**(3): p. 253-9.
438. Stephens, M.A., *Edf Statistics for Goodness of Fit and Some Comparisons.* Journal of the American Statistical Association, 1974. **69**(347): p. 730-737.
439. Watson, G.S., et al., *Statistics on spheres*. Vol. 6. 1983: Wiley New York.
440. Wood, A., *A Bimodal Distribution on the Sphere.* Applied Statistics-Journal of the Royal Statistical Society Series C, 1982. **31**(1): p. 52-58.
441. Kent, J.T., *The Fisher-Bingham distribution on the sphere.* Journal of the Royal Statistical Society. Series B (Methodological), 1982: p. 71-80.
442. Stosiek, C., et al., *In vivo two-photon calcium imaging of neuronal networks.* Proc Natl Acad Sci U S A, 2003. **100**(12): p. 7319-24.
443. Kerr, J.N., D. Greenberg, and F. Helmchen, *Imaging input and output of neocortical networks in vivo.* Proc Natl Acad Sci U S A, 2005. **102**(39): p. 14063-8.
444. Lecoq, J., et al., *Visualizing mammalian brain area interactions by dual-axis two-photon calcium imaging.* Nat Neurosci, 2014. **17**(12): p. 1825-9.
445. Histed, M.H., V. Bonin, and R.C. Reid, *Direct activation of sparse, distributed populations of cortical neurons by electrical microstimulation.* Neuron, 2009. **63**(4): p. 508-522.
446. Burkhalter, A. and K.L. Bernardo, *Organization of corticocortical connections in human visual cortex.* Proc Natl Acad Sci U S A, 1989. **86**(3): p. 1071-5.
447. Jupp, P.E. and K.V. Mardia, *A General Correlation-Coefficient for Directional-Data and Related Regression Problems.* Biometrika, 1980. **67**(1): p. 163-173.
448. Rattay, F., *Analysis of models for external stimulation of axons.* IEEE Transactions on Biomedical Engineering, 1986(10): p. 974-977.
449. Yousif, N., et al., *Evaluating the impact of the deep brain stimulation induced electric field on subthalamic neurons: A computational modelling study.* J Neurosci Methods, 2010. **188**(1): p. 105-112.
450. Frankemolle, A.M., et al., *Reversing cognitive–motor impairments in Parkinson's disease patients using a computational modelling approach to deep brain stimulation programming.* Brain, 2010. **133**(3): p. 746-761.
451. McIntyre, C.C., et al. *Customizing deep brain stimulation to the patient using computational models*. in *2009 Annual International Conference of the IEEE Engineering in Medicine and Biology Society*. 2009. IEEE.
452. McIntyre, C.C., et al. *Improving postural stability via computational modeling approach to deep brain stimulation programming*. in *2011 Annual International*

Conference of the IEEE Engineering in Medicine and Biology Society. 2011. IEEE.
453. Butson, C., et al., *StimExplorer: deep brain stimulation parameter selection software system*, in *Operative Neuromodulation*. 2007, Springer. p. 569-574.
454. Chaturvedi, A., T.J. Foutz, and C.C. McIntyre, *Current steering to activate targeted neural pathways during deep brain stimulation of the subthalamic region.* Brain Stimul, 2012. **5**(3): p. 369-377.
455. Butson, C.R. and C.C. McIntyre, *Role of electrode design on the volume of tissue activated during deep brain stimulation.* J Neural Eng, 2006. **3**(1): p. 1-8.
456. Chaturvedi, A., J.L. Luján, and C.C. McIntyre, *Artificial neural network based characterization of the volume of tissue activated during deep brain stimulation.* J Neural Eng, 2013. **10**(5): p. 056023.
457. McIntyre, C.C. and W.M. Grill, *Selective microstimulation of central nervous system neurons.* Ann Biomed Eng, 2000. **28**(3): p. 219-33.
458. Nowak, L. and J. Bullier, *Axons, but not cell bodies, are activated by electrical stimulation in cortical gray matter I. Evidence from chronaxie measurements.* Experimental Brain Research, 1998. **118**(4): p. 477-488.
459. Nowak, L. and J. Bullier, *Axons, but not cell bodies, are activated by electrical stimulation in cortical gray matter II. Evidence from selective inactivation of cell bodies and axon initial segments.* Experimental Brain Research, 1998. **118**(4): p. 489-500.
460. Jones, E.G., *The Thalamus*. 1985, New York: Plenum Press. 5-935.
461. Asanuma, C., T. Thach, and E.G. Jones, *Distribution of cerebellar terminations in the ventral lateral thalamic region of the monkey.* Brain Res.Rev., 1983. **5**: p. 237-265.
462. Friedman, D.P. and E.G. Jones, *Thalamic input to areas 3a and 2 in monkeys.* J.Neurophysiol., 1981. **45**: p. 59-86.
463. Jones, E.G. and D.P. Friedman, *Projection pattern of functional components of thalamic ventrobasal complex on monkey somatosensory cortex.* J.Neurophysiol., 1982. **48(2)**: p. 521-543.
464. Kievit, J. and H.G.J.M. Kuypers, *Organization of the thalamo-cortical connexions to the frontal lobe in the rhesus monkey.* Exp.Brain Res., 1977. **29**: p. 299-322.
465. Schell, G.R. and P.L. Strick, *The origin of thalamic inputs to the arcuate premotor and supplementary motor areas.* J.Neurosci., 1984. **4**: p. 539-560.
466. Elder, C.M., et al., *Chronic implantation of deep brain stimulation leads in animal models of neurological disorders.* J Neurosci Methods, 2005. **142**(1): p. 11-6.
467. Hashimoto, T., C.M. Elder, and J.L. Vitek, *A template subtraction method for stimulus artifact removal in high-frequency deep brain stimulation.* J Neurosci Methods, 2002. **113**(2): p. 181-6.
468. Agnesi, F., et al., *Fidelity of frequency and phase entrainment of circuit-level spike activity during DBS.* J Neurophysiol, 2015. **114**(2): p. 825-34.
469. Dorrscheidt, G.H., *The statistical significance of the peristimulus time histogram (PSTH).* Brain Res, 1981. **220**(2): p. 397-401.

470. Shannon, C.E. and W. Weaver, *The mathematical theory of communication*. 2015: University of Illinois press.
471. Harris, K.D., et al., *Accuracy of tetrode spike separation as determined by simultaneous intracellular and extracellular measurements.* Journal of Neurophysiology, 2000. **84**(1): p. 401-414.
472. Henze, D.A., et al., *Intracellular features predicted by extracellular recordings in the hippocampus in vivo.* J Neurophysiol, 2000. **84**(1): p. 390-400.
473. Schlag, J. and J. Villablanca, *A quantitative study of temporal and spatial response patterns in a thalamic cell population electrically stimulated.* Brain Res, 1968. **8**(2): p. 255-70.
474. Birdno, M.J., et al., *Response of human thalamic neurons to high-frequency stimulation.* PLoS One, 2014. **9**(5): p. e96026.
475. Marco, L., T. Brown, and M. Rouse, *Unitary responses in ventrolateral thalamus upon intranuclear stimulation.* J Neurophys, 1967. **30**(3): p. 482-493.
476. Sakata, H., T. Ishijima, and Y. Toyoda, *Single unit studies on ventrolateral nucleus of the thalamus in cat: its relation to the cerebellum, motor cortex and basal ganglia.* Jpn J Physiol, 1966. **16**(1): p. 42-60.
477. Kent, A.R. and W.M. Grill, *Neural origin of evoked potentials during thalamic deep brain stimulation.* J Neurophys, 2013. **110**(4): p. 826-843.
478. Kiss, Z.H., et al., *Neuronal response to local electrical stimulation in rat thalamus: physiological implications for mechanisms of deep brain stimulation.* Neuroscience, 2002. **113**(1): p. 137-43.
479. Schlag, J. and J. Villablanca, *Thalamic inhibition by thalamic stimulation.* Psychonomic Science, 1967. **8**(9): p. 373-374.
480. Dostrovsky, J., et al. *Microstimulation-induced effects on neurons in human globus pallidus and motor thalamus*. in *Soc. Neurosci. Abstr*. 1999.
481. Selinger, J.V., et al., *Methods for characterizing interspike intervals and identifying bursts in neuronal activity.* J Neurosci Methods, 2007. **162**(1-2): p. 64-71.
482. Dorval, A.D., *Probability distributions of the logarithm of inter-spike intervals yield accurate entropy estimates from small datasets.* J Neurosci Methods, 2008. **173**(1): p. 129-39.
483. Dorval, A.D., *Estimating Neuronal Information: Logarithmic Binning of Neuronal Inter-Spike Intervals.* Entropy (Basel), 2011. **13**(2): p. 485-501.
484. Strong, S.P., et al., *Entropy and information in neural spike trains.* Physical Review Letters, 1998. **80**(1): p. 197-200.
485. Johnston, D. and S.M.-S. Wu, *Foundations of cellular neurophysiology*. 1994: MIT press.
486. Anderson, T., et al., *Mechanisms of deep brain stimulation: an intracellular study in rat thalamus.* J Physiol, 2004. **559**(Pt 1): p. 301-13.
487. Lenz, F.A., et al., *Single unit analysis of the human ventral thalamic nuclear group. Tremor-related activity in functionally identified cells.* Brain, 1994. **117 (Pt 3)**: p. 531-43.

488. Iremonger, K.J., et al., *Cellular mechanisms preventing sustained activation of cortex during subcortical high-frequency stimulation.* J Neurophysiol, 2006. **96**(2): p. 613-21.
489. Evans, A.C., et al., *Warping of a Computerized 3-D Atlas to Match Brain Image Volumes for Quantitative Neuroanatomical and Functional-Analysis.* Medical Imaging V : Image Processing, 1991. **1445**: p. 236-246.
490. Murasugi, C.M., C.D. Salzman, and W.T. Newsome, *Microstimulation in visual area MT: effects of varying pulse amplitude and frequency.* J Neurosci, 1993. **13**(4): p. 1719-29.
491. Min, H.K., et al., *Deep brain stimulation induces BOLD activation in motor and non-motor networks: an fMRI comparison study of STN and EN/GPi DBS in large animals.* Neuroimage, 2012. **63**(3): p. 1408-20.
492. Perlmutter, J.S., et al., *Blood flow responses to deep brain stimulation of thalamus.* Neurology, 2002. **58**(9): p. 1388-94.
493. Huguenard, J.R. and D.A. Prince, *A novel T-type current underlies prolonged Ca(2+)-dependent burst firing in GABAergic neurons of rat thalamic reticular nucleus.* J Neurosci, 1992. **12**(10): p. 3804-17.
494. Santaniello, S., et al., *Therapeutic mechanisms of high-frequency stimulation in Parkinson's disease and neural restoration via loop-based reinforcement.* Proc Natl Acad Sci U S A, 2015. **112**(6): p. E586-95.
495. Segev, I. and E. Schneidman, *Axons as computing devices: Basic insights gained from models.* Journal of Physiology-Paris, 1999. **93**(4): p. 263-270.
496. Beurrier, C., et al., *High-frequency stimulation produces a transient blockade of voltage-gated currents in subthalamic neurons.* J Neurophysiol, 2001. **85**(4): p. 1351-6.
497. Debanne, D., *Information processing in the axon.* Nat Rev Neurosci, 2004. **5**(4): p. 304-16.
498. Bellinger, S.C., G. Miyazawa, and P.N. Steinmetz, *Submyelin potassium accumulation may functionally block subsets of local axons during deep brain stimulation: a modeling study.* Journal of Neural Engineering, 2008. **5**(3): p. 263-274.
499. Grill, W.M., M.B. Cantrell, and M.S. Robertson, *Antidromic propagation of action potentials in branched axons: implications for the mechanisms of action of deep brain stimulation.* J Comput Neurosci, 2008. **24**(1): p. 81-93.
500. Anderson, T.R., et al., *Selective attenuation of afferent synaptic transmission as a mechanism of thalamic deep brain stimulation-induced tremor arrest.* Journal of Neuroscience, 2006. **26**(3): p. 841-850.
501. Martina, M. and P. Jonas, *Functional differences in Na+ channel gating between fast-spiking interneurones and principal neurones of rat hippocampus.* Journal of Physiology-London, 1997. **505**(3): p. 593-603.
502. Meeks, J.P. and S. Mennerick, *Selective effects of potassium elevations on glutamate signaling and action potential conduction in hippocampus.* Journal of Neuroscience, 2004. **24**(1): p. 197-206.